The Defect Modes of MoS_2:

Indirect Double Resonance Raman Spectroscopy in Transition Metal Dichalcogenides

A thesis submitted in partial fulfillment of the requirements for the degree of

Doctor of Philosophy

in

Nanoscience

at Massey University, Manawatū, New Zealand

Samuel James BROOKE

2022

Declaration of Authorship

I, Samuel James BROOKE, declare that this thesis titled, "The Defect Modes of MoS_2: Indirect Double Resonance Raman Spectroscopy in Transition Metal Dichalcogenides", and the work presented in it are my own.

Note in the use of personal pronouns, "we" implies collectively myself and the reader during explanations and discussion sections, or mine and my supervisor Prof. Mark Waterland's joint conclusions based on lengthy discussions and many whiteboard diagrams. The situation should be clear based on the context and grammar.

I confirm that:

- This work was done wholly or mainly while in candidature for a research degree at this University.
- Where any part of this thesis has previously been submitted for a degree or any other qualification at this University or any other institution, this has been clearly stated.
- Where I have consulted the published work of others, this is always clearly attributed.
- Where I have quoted from the work of others, the source is always given. With the exception of such quotations, this thesis is entirely my own work.
- I have acknowledged all main sources of help.
- Where the thesis is based on work done by myself jointly with others, I have made clear exactly what was done by others and what I have contributed myself.

Signed: Samuel Brooke

Date: 02/05/2022

Abstract

The Defect Modes of MoS_2: Indirect Double Resonance Raman Spectroscopy in Transition Metal Dichalcogenides

by Samuel James BROOKE

Molybdenum disulfide (MoS_2) is a layered two-dimensional (2D) semiconducting crystal which has been a focal point of 2D materials research since the isolation and characterisation of graphene in 2005, owing to its relative abundance and a wide range of potential applications in thin film electronics, photovoltaics, information storage, and catalysis to name a few. It has unique layer-dependent electronic properties, demonstrating intense photoluminescence in single-layers and tightly-bound excitons at room temperature.

The excitonic properties of MoS_2 lead to an optical phenomenon known as double resonance Raman (DRR), whereby the excited state charge carriers of excitons can interact with lattice vibrations (phonons) to scatter throughout the Brillouin zone during optical absorption and Raman spectroscopy measurements. These processes reveal signatures of electron and hole scattering dynamics that govern the complex electronic and physical properties of the material.

At the nanoscale, the edges of MoS_2 have significant influence over the material's properties, altering the electronic structure and contributing to doping effects for semiconductor performance and photoluminescence tuning. In addition, these edges (and defects) are also the sites of catalytic reactions, leading to intense efforts in literature to optimise MoS_2 as a catalyst for the production of clean hydrogen fuels. Consequently, understanding the edges of these materials is of great interest.

This work demonstrates the design of a home-built low-frequency scanning Raman microscope, used to probe DRR features in MoS_2, revealing for the first time a defect-mediated indirect DRR mechanism which allows the quantification of defects and determination of zigzag and armchair edge structures in MoS_2 materials. This mechanism reveals indirect scattering pathways in the Brillouin zone, and appears to be applicable to similar materials in the family of transition metal dichalcogenides (TMDs).

This indirect resonance mechanism has immediate application in facilitating the development of catalytic materials and novel nanomaterial architectures, as well as potential applications in the characterisation of exotic TMD materials and next-generation spin-valley coupled information storage devices.

Acknowledgements

Firstly, I would like to thank the MacDiarmid Institute for funding my study and research, and Massey University for providing additional funding and the facilities to do the research.

I would like thank my supervisors - Mark Waterland, Richard Haverkamp, and Geoff Waterhouse for their guidance throughout my research. I'm particularly grateful to my primary supervisor, Mark Waterland, for his enormous support, as this project was by no means linear in its progression and without his attention and enthusiasm during long whiteboard discussions, I could not have learnt and achieved as much as I have. In addition, his willingness to let me guide my own path and delve deep into rabbit holes for weeks and months on end has led to some of the most fascinating research discoveries I couldn't have even imagined at the onset of the project.

Many colleagues have contributed to my research in one way or another - through either experimental assistance or rich discussions. In particular, Tyson Dais has been generous in his willingness to help me troubleshoot computational issues, and in deep discussions of wild theories, which no doubt gave inspiration for some of these results. In a similar vein, my friends in the rest of the Waterland, Plieger, Rowlands, Williams and Telfer groups (past and present) have endured my ramblings and assisted in troubleshooting some of my more tedious synthetic endeavours. In addition, these same friends have been greatly beneficially to my mental health over the last four years – keeping me grounded and entertained during coffee breaks and various social excursions - including many essential "networking" events at the local.

I must also acknowledge the technical services of the mechanical engineering team in the School of Natural Sciences, including Steve Denby, Olaf Griewaldt, Stan Hyde, and Garry Collins, who have been invaluable throughout this research providing technical advice and various machined goods for the microscope parts, which has no doubt been critical to its success. Moreover, they're a great bunch of guys, and I've thoroughly enjoyed our entertaining discussions over the years.

I would also like to thank the greater MacDiarmid community – particularly the MESA cohort for being a generally awesome group of people whenever we get together at events and workshops, and the Science Executive of MacDiarmid for their willingness to help foster this community.

A special thanks goes to my family, who have supported my endeavours throughout all my studies. Last and certainly not least is a special thanks to Annie Reid – who has more than anyone supported me every step of the way through all the late nights and rough patches, and without whom this PhD wouldn't have been the same.

Contents

List of Figures

List of Tables

List of Abbreviations

0D	Zero-dimensional
1D	One-dimensional
2D	Two-dimensional
3D	Three-dimensional
1L	One-layer
2L	Two-layer
3L	Three-layer
AFM	Atomic force microscopy
BZ	Brillouin zone
CAD	Computer aided design
CB	Conduction band
DOS	Density of states
DRR	Double resonance Raman
EPC	Electron phonon coupling
FDM	Fused deposition modelling
FWHM	Full-width-at-half-maximum
HER	Hydrogen evolution reaction
HT	High-temperature
irrep.	Irreducible representation
LT	Low-temperature
MFD	Mode field diameter
pDOS	Phonon density of states
QD	Quantum dot
QE	Quantum ESPRESSO
RT	Room-temperature
SORS	Spatially-offset Raman spectroscopy
TA	Transverse acoustic (phonon)
TEM_{00}	Transverse electromagnetic mode (fundamental)
TIR	Total internal reflection
TMD	Transition metal dichalcogenide
TRR	Triple resonance Raman
VB	Valence band
VBG	Volume Bragg grating
ZA	Out-of-plane acoustic (phonon)

Chapter 1

Introduction to Molybdenum Disulfide (MoS_2)

1.1 General Properties and Applications

Layered two-dimensional (2D) materials have received burgeoning interest since the isolation and characterisation of single-layer graphene in 2005.[1–3] MoS_2 in particular has become a prominent feature of materials research, owing to a diverse range of remarkable properties. As a semiconductor MoS_2 shows promise as a transistor material for ultra-thin electronic devices,[4,5] and its photoluminescent properties yield applications in optoelectronic devices, including photo-transistors,[6] detectors,[7,8] and photovoltaic devices for solar energy harvesting.[9–11]

It also shows promise as a cathode material for lithium ion batteries,[12–14] and is capable of catalysing a range of chemical processes,[15] including the hydrogen evolution reaction (HER) for generating environmentally clean hydrogen fuels.[16]

MoS_2 is part of the family of transition metal dichalcogenides (TMDs), which take the form of MX_2, where M is a transition element from groups IV, V, and VI of the periodic table and X represents one of the chalcogens S, Se, and Te.[16]

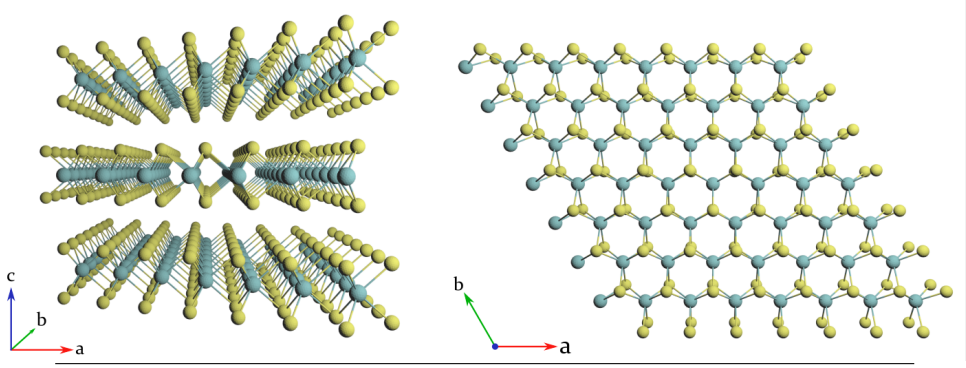

FIGURE 1.1: Ball and stick models of a section of 2H-MoS_2 crystal, showing (left) a side view along the in-plane b crystallographic axis, and (right) a top-down view of the plane along the out-of-plane c crystallographic axis. Molybdenum atoms are in cyan, sulfur atoms are in yellow.

Each layer of MoS_2 is 6-7 Å thick, and consists of a plane of molybdenum atoms sandwiched between two planes of sulfur atoms (see Figure 1.1). Van der Waals interactions drive the stacking of layers along the axis perpendicular to the atomic planes (c-axis). Two polytypes of MoS_2 can be found in nature, and are labelled 2H-MoS_2 and 3R-MoS_2, corresponding to hexagonal and rhombohedral stacking symmetries respectively. Sulfur atoms coordinate to the molybdenum atoms in a trigonal prismatic geometry in both these polytypes, but 2H is the most thermodynamically favourable, belonging to the $P6_3/mmc$ space group with D_{6h} symmetry in the bulk.[17]

A third meta-stable phase known as 1T-MoS_2 can be generated,[18] which exhibits a distorted octahedral geometry and shows promise in catalytic applications due to its electrically-conductive metallic nature.[19]

The weak interlayer interactions result in low in-plane shear resistance, making MoS_2 useful as a dry lubricant, similar to graphite.[20–22] It is commonly utilised in combustion-engine oils,[23] and has found specialised use in aerospace applications, showing superlubricity in the inert environment of space.[24]

These weak interactions also enable mechanical exfoliation all the way to single layers, using techniques such as simply rubbing on a flat substrate[1] or the infamous "scotch tape" method.[7,25] The scotch tape method involves taking a crystal and repeatedly pressing a piece of scotch tape into it, then peeling away layers until a sufficiently thin sample remains. This is then pressed and rubbed firmly into a flat substrate (polished silicon chip, sapphire, mica etc.), and when pulled away leaves flakes on its surface.

MoS_2 can also be chemically exfoliated, using methods such as solvent intercalation and sonication,[26,27] aqueous stabilisation with surfactants,[28] and interlayer expansion via lithium intercalation.[19,29,30] Lithium intercalation causes a violent expansion of layers during exposure to water, typically resulting in the phase transition to 1T-MoS_2, which makes it useful in catalytic studies.[31]

1.1.1 Catalytic Properties

The catalytic properties of MoS_2 have been exploited for decades in the hydrodesulfurization processes of petroleum refining,[28,32–34] and as a general catalyst in a variety of organic reactions.[35] Due to increasing efforts to move away from fossil fuels, MoS_2 has been identified as a potential earth-abundant replacement for the currently ideal but expensive platinum catalysts in the the electrochemical generation of hydrogen fuels.[36–38] It has been shown that the defects and edges of MoS_2 are efficient catalysts for the HER, while the basal plane remains relatively inert.[39] As such, there's extensive literature focused on the optimisation of MoS_2-based catalysts for the HER. These include attempts to maximise the ratio of edges and defect catalytic sites,[40–42] improve the inherently low electrical conductivity of MoS_2 by using the

metallic 1T-MoS_2 polytype or conductive supports,[19,43–46] and lower the overpotential required through the use of amorphous allotropes[47–49] or co-catalyst adatoms and alloys.[50]

There have also been examples of photo-catalytic hybrid systems which use photo-excited charge-carriers from another semiconductor to provide the electrochemical potential needed to drive the catalytic processes in MoS_2 systems.[51–53]

1.1.2 Electronic Properties

MoS_2 and other TMDs display unique emergent electronic properties, owing to a shifting band gap with layer number. Bulk MoS_2 is an indirect band gap semiconductor, with a gap energy of around 1.3 eV.[54] As layer number decreases, the band gap begins to increase as the valence band maximum (Γ) and conduction band minimum (Q) recede into their respective bands (see Figure 1.2). This is a consequence of strong contributions from the sulfur p_z orbitals to the states at these points in the band structure, resulting in a high sensitivity to interlayer distance, as reducing layer number weakens these long-range interactions.[55,56] Conversely, the states at the K point are mostly constructed of contributions from the Mo d-orbitals, which are relatively sheltered in the middle of the MoS_2 layer. In two-layer (2L) MoS_2, the indirect band gap is around 1.5 eV,[57] and in single layer (1L) MoS_2 a cross-over between these states and the states at the K point occurs, resulting in a direct band gap at the K point of about 1.9 eV.[58]

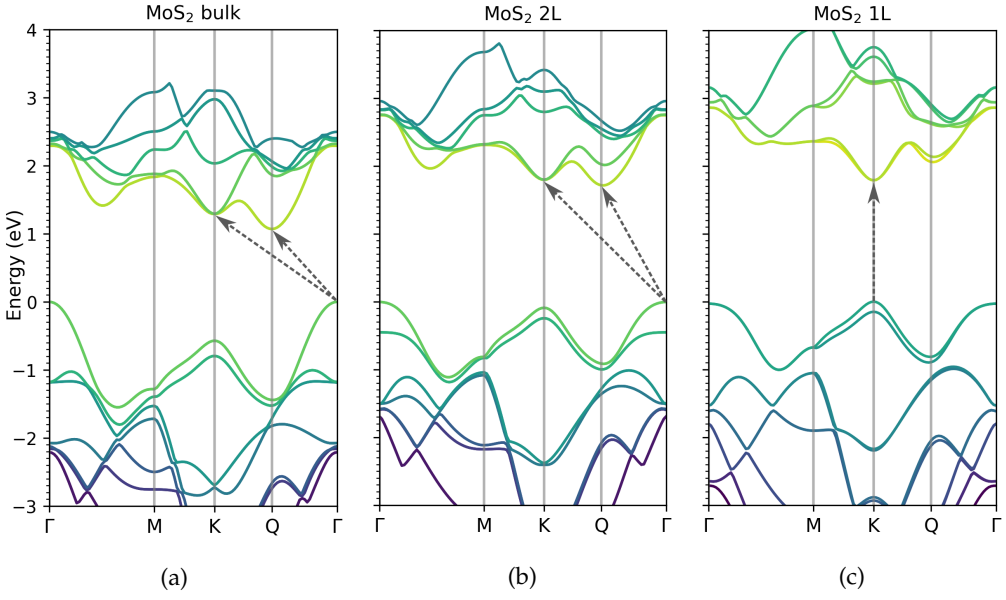

FIGURE 1.2: Calculated band structures using Quantum ESPRESSO (QE) for MoS_2: (a) bulk, (b) bilayer (2L), and monolayer (1L), plotted along the high symmetry points of the Brillouin zone.

The direct-gap crossover results in a significant enhancement (up to 4 orders of magnitude) to photoluminescent yields from radiative recombination of excited-state charge carriers at the K-point.[58,59] The photoluminescent properties in MoS_2 and the other TMDs are dominated by strong excitonic interactions, yielding specific A, B, and C bright (optically allowed) excitons, as well as charged trions and dark (optically forbidden) excitons, adding fine-structure to the exciton spectrum.[60–63] The energies and relative intensities of these excitons can be tailored to specific applications through band gap engineering,[64] doping,[65] and controlled defect introduction.[66,67] In addition, various kinds of strain can be used to alter the electronic properties and band structure of MoS2 materials, resulting in changes to electron mobility and excitonic energies.[68–70]

The capacity for band gap modulation is due in part to the reduced dimensionality of MoS_2, and its subsequent sensitivity to the surrounding environment. For instance, chemical sensory capability have been demonstrated through the observation of changes in electronic conductivity[71] and photoluminescence peaks, brought about simply by the doping effects of electron-donating and electron withdrawing analytes in both gaseous and aqueous media.[72–75]

A common method for the deliberate doping MoS_2 materials is to utilise the various crystal defects (which include under-coordinated Mo atoms at sulfur vacancies) to attach adatoms[50,76] or thiol-containing (C-SH) organic molecules.[77] Unlike the non-covalent interactions of the gaseous and aqueous dopants, the thiol linkers typically attach covalently and impart electron donating or withdrawing effects through the ligand chemical structure.[78] For instance, Sim *et al.* report using the charge-transfer interactions of amine-containing ligands as n-dopants, and polyfluorinated ligands as p-dopants to enhance or reduce electron mobility respectively, whilst also observing red and blue-shifts in the photoluminescence spectra.[79] Another study demonstrated enhanced catalytic activity as a result of functionalisation-induced metallic behaviour.[80]

Further functionality can be imparted to the MoS_2 through the chemical groups found on the thiol ligands. For instance, enhanced solubility has been reported using thioglycolic acid for basic fluorescent cell labelling,[81] thiolated polyethylene glycols for drug loading and cancer treatment,[82–84] and thionine for ultra-sensitive detection of DNA.[85]

The band gap of MoS_2 can also be modified through quantum confinement effects, producing one-dimensional (1D) nanoribbons and zero-dimensional (0D) quantum dots (QDs).[86,87] QDs of MoS_2 are favoured for their chemical stability, low-toxicity, and resistance to photobleaching, and find extensive application in luminescent tagging of biological molecules.[88–90] In addition, their relatively high edge-to-basal-plane ratios make them suitable for catalytic applications.[91,92]

Nanoribbons of MoS_2 are typically more difficult to make than QDs, owing to the highly-ordered structure and high degree of anisotropy on the nanoscale. As such, examples of genuine pristine nanoribbons are relatively rare.[93–97] They have,

however, been extensively investigated in computational literature, and will be discussed in the defects section below (1.2).

1.1.3 Spin-Valley Polarization

MoS_2 also exhibits spin-coupled valley-polarization in single layers, which leads to potential applications in high-density information storage devices using spintronics and valleytronics.[98,99] The hexagonal symmetry in MoS_2 is provided by a screw axis, and each of the six corners of the hexagonal lattice contain alternating Mo and S atoms. This leads to degeneracy lifting of the K and adjacent K' points in the Brillouin Zone (BZ).[17] In single-layer MoS_2, inversion symmetry from the screw axis is broken, which along with strong spin-orbit coupling leads to coupled spin and valley physics. Time-reversal symmetry requires different spins in the K and K' valleys, which allows spin states and valley polarizations to be selected for through the valley-dependent selection rule using left and right-handed circularly-polarized excitation sources.[100] The spin-valley coupling means individual spin or valley relaxation is suppressed - they must relax simultaneously, resulting in long excited-state lifetimes and the possibility of information storage using circularly-poalrized light.

Each TMD has a similar but unique band structure, and understanding their complex electronic properties may lead to a host of fascinating applications.[17] For instance, while in bilayer MoS_2 the inversion symmetry is restored and spin-valley coupling is lost,[101] Zhu *et al.* show that the significantly stronger spin-orbit coupling in tungsten disulfide (WS_2) weakens the inversion symmetry in bilayers, which not only allows spin-valley coupling to persist, but enhances it.[102] Standard values for spin-valley polarization in monolayer WS_2 are around 30 %, while in the bilayer system the polarization can reach up to 95 %. This is a consequence of additional coupling to a third degree of freedom provided by the upper and lower layers, where the stacking symmetry means the K point on one layer corresponds to the K' point on the other layer.

Thermal fluctuations (phonons) are responsible for the depolarization of spin-valley states (known as valley-depolarization), and therefore represent a physical limitation on the ability to maintain stored information.[98] Recent double resonant Raman (DRR) studies have revealed that the phonons responsible for valley-depolarization in MoS_2 are LA(K) phonons through an intervalley scattering event from the K to Q valleys of the valence band (i.e. hole scattering).[103] The theory of DRR in TMDs is still in its infancy, but is already capable of revealing intricate physical details of these systems, and will likely facilitate the development of such technologies (see section 3.1.3 for an introduction of DRR).

1.2 Defects

Defects in semiconductors often work to the detriment of device performances. However in some cases, such in the catalytic processes above, defects introduce

new functionality that can be exploited, and understanding what changes they bring about and how to identify them is of paramount importance for the development of nanomaterials and next-generation electronic devices.

For instance, defects and grain boundaries have been shown to possess one-dimensional (1D) magnetic properties,[104,105] while prismatic coordination geometries at edges have been shown to confer bulk magnetic properties in nanosheet films.[106] In addition, magnetic coupling of substitutional dopant clusters has been shown to induce valley-pseudospin Zeeman splitting effects,[107,108] while defect states can induce enhanced spin-orbit splitting and lead to magnetic manipulation of the valley-pseudospins in defect-bound excitons.[109,110]

Additional defect-activated photoluminescence features can be obtained due to bound/trapped excitons at defect states in MoS_2 and other TMDs.[111–114] Defects have been used to bind excitons and trions locally, and in some cases enhance lifetimes above those of the unbound A and B excitons.[66]

The study of defects is particularly important for nanoribbons, where the edges have a major influence over the material properties. As mentioned above, MoS_2 nanoribbons have been extensively investigated in computational literature, comparing the effects of width, edge structure, strain and electric and magnetic field interactions.[97,115–120] These studies have predicted that ribbons with zigzag edges exhibit magnetic behaviour with metallic properties, suggesting possible applications in ultra-thin electronics and information storage. Importantly, armchair ribbons do not share the same properties, instead being non-magnetic and semiconducting.[115,117]

Strain has been shown to increase the magnetic moment at zigzag edges up to three fold by decreasing intra-edge interactions of the Mo-S bonds and allowing more electrons to become spin polarised,[118] which may have follow-on effects for valley-pseudospin coupling.

Currently, there are few convenient methods for characterising defects and edges of MoS_2 materials, as they typically revolve around atomic-resolution imaging of localised defects or specialised optical instruments.

Many researchers use atomic-resolution scanning transmission electron microscopes (STEM) or scanning tunnelling microscopy (STM) to individually view atomic displacements.[121–123] Aryeetey *et al.* go one step further, using STEM and ion-beam bombardment techniques to calibrate the broad defect-associated acoustic phonon features in the Raman spectrum at 532 nm excitation.[124]

Song *et al.* use a specialised noise-correlated atomic-force microscopy (AFM) technique to observe single defects in the AFM scans.[125]

Yang *et al.* use magneto-Raman measurements to observe defects indirectly, by measuring the polarized Raman response of the fundamental phonons under magnetic fields up to 9 T.[126] They show that the magnetic-field induced electron motion, which affects Raman intensities through electron-phonon coupling, is perturbed in

the presence of defects, which act to reduce induced electron mobility through the scattering of mobile charge-carriers.[127]

Tip-enhanced Raman spectroscopy uses the surface plasmon enhancement from a gold-coated AFM probe to preferentially enhance Raman signals from nanoscale regions of the sample. Huang *et al.* use this to show that edges and defects have short range doping effects on the sample, which causes the fundamental A_{1g} mode to shift subtly shift up ($0.3\,cm^{-1}$) or down ($1\,cm^{-1}$) in wavenumbers at armchair and zigzag features respectively.[128]

Guo *et al.* present a Raman study of some TMDs including MoS_2, WS_2 and WSe_2, and use a combination of incident and scattered polarization analysis to show that the E_{1g} mode, which is normally forbidden in the backscatter geometry, becomes weakly allowed under certain combinations of polarization configurations.[129] They show that armchair and zigzag edges have unique and opposite E_{1g} intensity responses to the polarization combinations. Using theoretical modelling they describe a strong polarization and orientation dependent distortion of the induced electric fields at the edges of these materials, which results in a distortion of the incident and scattered polarization vectors into non-backscattering directions. However, they note that they are only able to observe these effects in materials thicker than 30 nm ($>$ 40 layers for MoS_2), which is likely due to a diminishing induced electric field strength in thinner materials.

Graphitic materials such a graphene and carbon nanomaterials are known to have defect-specific vibrational modes in the Raman spectrum, which is described by the theory of DRR[130](see section 3.1.3). These modes not only reveal defect densities, but also provide detailed electronic information, and a polarization dependence which can be used to quantify the amount of zigzag and armchair edges.[131] However, the analagous process is not typically resonant in MoS_2, and such features present in the spectrum are a consequence of great loss of crystallinity ($q \approx 0$ selection rule),[132] and do not provide much more information than an estimate of defect density.[133] That being said, the contents of Chapter 3 demonstrates for the first time a set resonant defect modes analagous to those in graphene, which are just as useful - if not more so. Chapter 2 covers the optics principles and construction of a low-frequency microscope used to observe these modes.

Chapter 2

Raman Microscope Design

2.1 Raman Spectroscopy

The theory of Raman spectroscopy will be explained in detail in 3, but is briefly explained here to provide context for the instrument design.

Raman scattering is a process whereby incident electromagnetic radiation (typically visible wavelengths) is inelastically scattered following interaction with vibrational modes of a molecule or material.[134] This interaction results in the exchange of a quantum of vibrational energy with the photon, which can either add to or subtract from the incident photon energy. Photons which lose energy to the system do so by exciting a vibration from an initial state (usually ground) to an excited state, and are called Stokes scattered photons. Photons which gain energy from the system cause a vibration to relax from some excited state to a lower energy state (usually ground), and are called anti-Stokes scattered photons. Accompanying these inelastic processes is the elastic process, Rayleigh scattering, where no energy is exchanged and the scattered photon has the same energy as the incident photon.

As such, Raman spectroscopy is a vibrational spectroscopy technique, which uses the change in scattered photon energy to identify vibrational motion in a sample, reported as Raman Shift in units of cm^{-1}. For much of the 20^{th} century, Raman spectroscopy was held back by the limited technology of the time, mainly used in physical and crystallographic characterisation.[135] However, the development of high-intensity coherent laser sources, sensitive multi-channel detectors, and efficient and sophisticated optical filters has made Raman spectroscopy a common and accessible characterisation technique across a wide range of scientific industrial disciplines, including but not limited to: chemical and biological imaging,[136] materials characterisation,[137] food-technology,[138] pharmaceutical development,[139] chemical analysis,[140,141] spatially-offset Raman spectroscopy (SORS),[142] and border security and defence.[143,144]

In general, there are two main technical challenges to overcome in a basic Raman spectroscopy instrument. Firstly, Raman scattering is a very weak process, requiring sensitive detection elements to observe spectra on reasonable timescales. In addition, Raman scattering is about 10^4 to 10^6 times less intense than the accompanying

Rayleigh scattering. Moreover, other elastic scattering and diffuse reflections off solid samples, optical elements, and dust particles can easily exceed Rayleigh scattering by orders of magnitude, exacerbating this contrast. These additional elastic scatterings typically radiate light from a point and are not collimated, which contributes to stray light - which is any light in the optical setup that is travelling in a direction it shouldn't. In the context of a Raman spectrum, we typically describe the combined effects of stray light, reflections, and other unshifted photons as the "laser line" or simply "Rayleigh line".

Stray light is a problem for Raman spectrographs, as these wayward photons no not necessarily follow the optical path, and can end up reflecting and scattering around the internals of the spectrograph. An intense Rayleigh beam will also contribute to stray light within the spectrograph by increasing the probability of scattering off dust and imperfections in the internal spectrograph optics. Eventually, some of this stray light ends up reaching the detector, and appearing in the spectrum as a baseline which slopes upwards in intensity as the spectral region approaches the laser frequency (see Figure 2.1). Since Raman scattering is so weak, and our detectors are very sensitive, this stray light can quickly overshadow the entire Raman spectrum, preventing any information from being obtained.

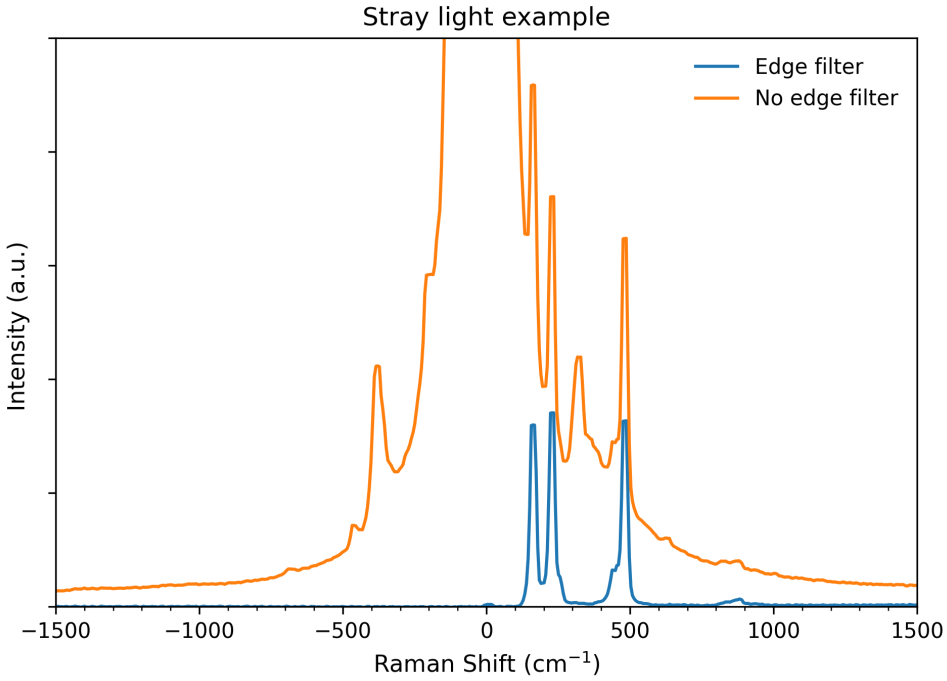

FIGURE 2.1: An example of how excess stray light in the spectrograph leads do spectral broadening and artefacts. At its worst, stray light can completely obscure the Raman signals. The orange spectrum is a sample of sulfur powder with no edge filter in place, and the blue spectrum is the same sample with an edge filter.

Therefore we need to filter this intense laser light before it reaches the spectrograph. This leads us to the second main challenge: since the Raman shifts are relatively small and the frequencies of our inelastically and elastically scattered light are so close together, any filters need to change from completely blocking to completely transmitting over as small a frequency range as possible (i.e. "sharp" or "steep" filters), so that we don't filter our Raman scattered photons as well as the Rayleigh. As Figure 2.1 demonstrates, efficient laser line rejection is even more important for studying low-frequency modes ($< 200\,\mathrm{cm}^{-1}$), since the effects of stray light become exponentially stronger as the frequency approaches the Rayleigh peak.

These days the most common method is to use appropriate optical filters for the laser of choice, placed in the optical path of the collected light to reject the laser line and allow the Raman scattered light to pass. Another method is to use a double monochromator or triple spectrograph as a tunable filter.

Triple spectrographs are ideal for low-frequency work, as they provide excellent Rayleigh line and stray light rejection allowing clear observation of vibrational modes very close to the laser line ($4\,\mathrm{cm}^{-1}$)[145,146]. They operate by using a first grating to disperse the light onto a wide slit, which allows the spectrum (stokes or anti-stokes) to be transmitted but blocks the laser line. This light is then refocused onto a second grating which is matched to reverse the dispersive effects of the first grating and re-collimate the light. These two sections or stages can be considered a double-monochromator or tunable filter. This filtered light is focused onto the slit of the final stage, which contains the last grating, optics, and the detector. Since there are effectively two narrow slits confining the optical path of the beam at the first and third stages, the stray light has a much harder time reaching the detector. The overall attenuation is quantified by the product of the attenuation at each slit, the amount of Rayleigh and stray light reaching the detector becomes very small - on the order of 10^{-10} - 10^{-12} of the original photons (compared to 10^{-5} - 10^{-6} for single stage (single grating) spectrographs).

However, the use of three diffraction gratings results in painfully low throughput, since even at the optimised operation wavelengths gratings are typically at most 70-80 % efficient, and the losses at each grating are multiplicative.

Therefore, as optical filter technology has developed, these triple spectrograph systems have generally been replaced by single stage (single grating) spectrographs and optical filters for standard spectroscopic work, with the exception of specialised applications such as tunable excitation studies which would otherwise require an impractical assortment of optical filters.

The first generation of filter-enabled single stage spectrographs used absorptive or dielectric reflective edge and notch filters. Edge filters have a wavelength cutoff, below which light is reflected and above is transmitted (for Stokes scattering observation, long-pass), and the sharpness or steepness of this cutoff determines how close to the laser line Raman features can be observed. Notch filters are designed to reflect a small band or "notch" of wavelengths, and have edges either side of this

region. Early filters had relatively soft/broad edges, precluding Raman observation below 100-250 cm^{-1}, depending on the excitation wavelength.

While this frequency cutoff is acceptable for most common chemical characterisation using Raman spectroscopy, there is an entire realm of useful vibrational information that can be found in the "low-frequency" region below 250 cm^{-1}, such as rotational information, vibrations of heavy atoms or groups of atoms, long-range vibrations resulting from packing arrangements of molecules and inter-molecular interactions,[139,141,147] and interlayer vibrations of low-dimensional materials.[148–150]

High-quality edge filters today can be made remarkably sharp, and can be used to observe features as low as 25-50 cm^{-1}(Iridian Spectral Technologies filters).[151] Holographic notch filters, also known as Volume Bragg Gratings (VBGs), offer another filtering solution using an alternating refractive index embedded into a photosensitive glass to establish a Bragg grating which reflects a specific wavelength or set of wavelengths, while allowing a large percentage of the remaining light to be transmitted (up to 95 %). These filters have benefited greatly from advancements in technology, and with spectral bandwidths (FWHM) reaching below 5 cm^{-1} can be used to observe ultra-low-frequency shifts in the terahertz region, as well as both Stokes and anti-Stokes scattering simultaneously (see Figure 2.2).

Having such a narrow bandwidth, however, means these filters are incredibly sensitive to angle of incidence and beam divergence, requiring high-quality lasers, optics, and optomechanical mounts to get the most out of a Raman spectrum. Even with all these considerations, it can still be challenging to achieve satisfactory results.

This chapter covers the design of a low-frequency scanning Raman microscope utilising VBG filters to observe low-frequency defect-mediated vibrational modes (phonons) in MoS_2 nanomaterials.

2.2 Theory of Optics

This section covers the basics of light propagation required to understand the reasons for choices of optics in the microscope design. A basic understanding of Geometrical optics and ray-tracing diagrams is assumed, but a brief introduction can be found in Appendix G. For brevity, basic concepts are discussed in passing, and the reader should follow references to gain further understanding as required. An excellent resource for fundamental and advanced optical theories is "Optics" by Eugene Hecht,[152] while the RP-Photonics Encyclopedia[153,154] provides a collection of technical resources and theory for optical applications. Another excellent resource in an applied sense are the ThorLabs technical resources (thorlabs.com),[155] which does as this section aims to - provide basic overview of the critical principles required to understand how to use their products. Their content is typically dense, so reading around may be required in some cases.

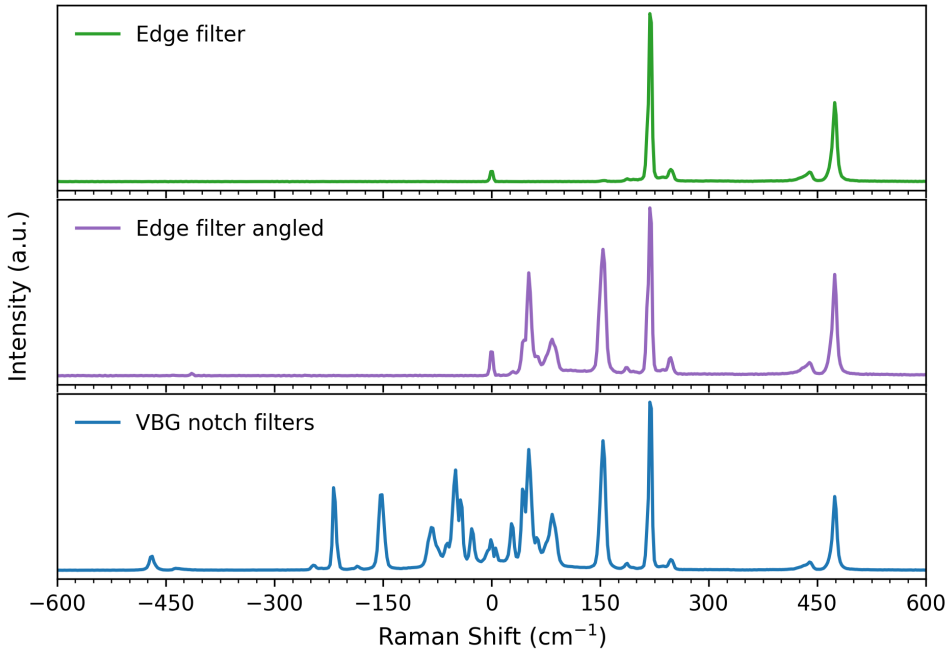

FIGURE 2.2: Raman spectra of sulfur powder demonstrating the effects of edge and notch filters. The top spectrum uses an edge filter at normal incidence to the beam, blocking light below ∼200 cm^{-1}. Note a residual amount of laser light at 0 cm^{-1} still makes it through. The middle spectrum uses the same filter, rotated at an angle to the beam, which shifts the cut-off edge closer to the laser in exchange for filtering efficiency (see laser line is more intense). The bottom spectrum uses VBG notch filters, and allows the observation of both Stokes and anti-Stokes scattering simultaneously, while effectively attenuating the laser.

2.2.1 Volume Bragg Gratings

At the heart of our low-frequency microscope is a series of volume Bragg gratings (VBGs) used as spectral filters, for both input laser and collected scattered radiation. VBGs are transparent filters with a periodic modulation of refractive index which establishes a Bragg grating to reflect a very specific wavelength of light through diffraction and constructive interference, while maintaining high transmission efficiency for the rest of the spectrum.[156,157]

The Bragg condition for constructive interference in a VBG is given by the relation

$$m\lambda = 2\Lambda sin(\theta + \phi) \tag{2.1}$$

where m is the Bragg order, λ is the wavelength of diffracted light, Λ is the grating period, θ is the angle between the filter surface normal and the incident photon, and ϕ is the angle between the surface normal and the grating vector. The grating vector is the direction in which the periodicity occurs, which can be at different

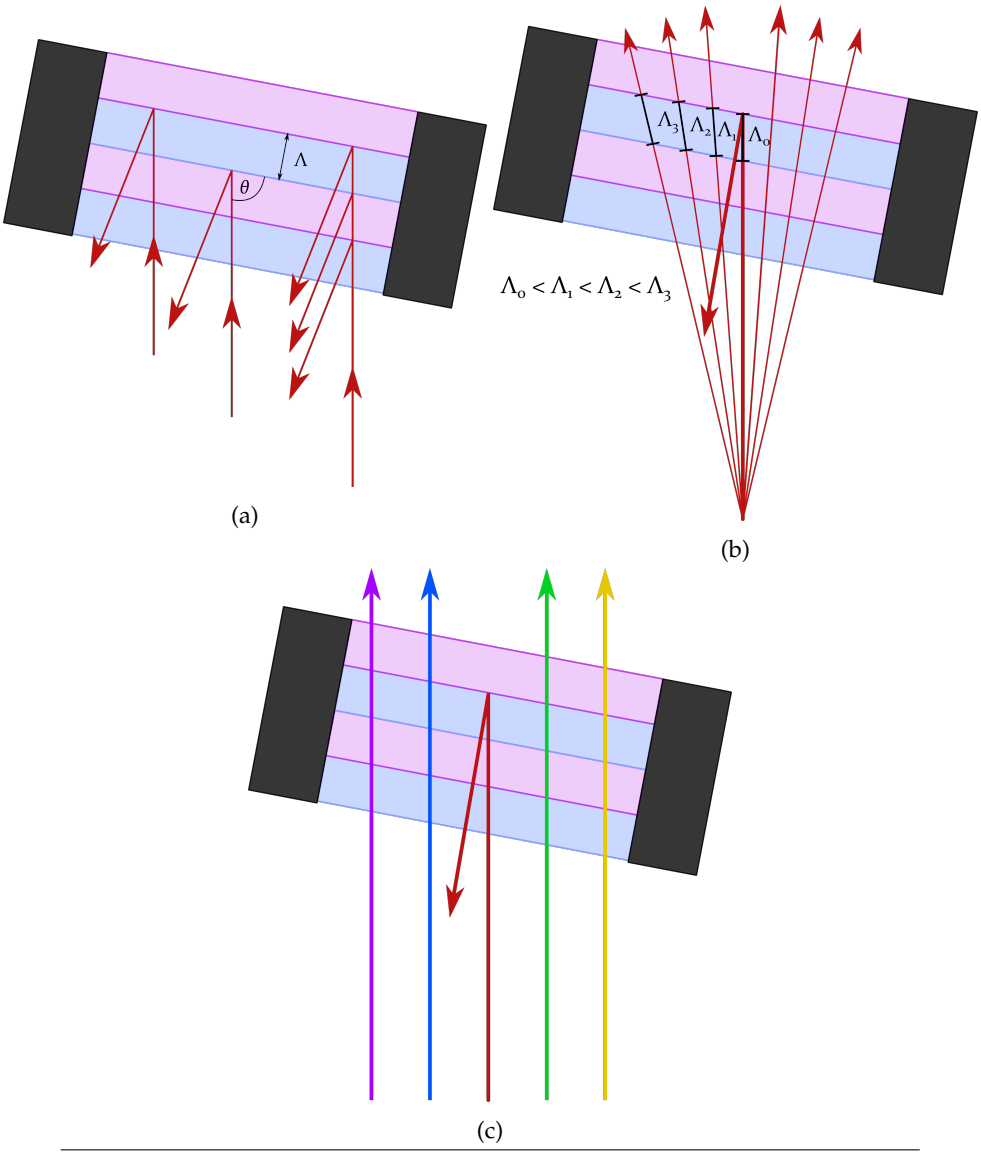

FIGURE 2.3: Schematic representation of reflections in VBGs. The alternating blue and purple wedges represent alternating regions of different refractive indicies. Wavelengths which meet the Bragg condition for the spacing between planes constructively interfere and result in reflection. (a) shows the ideal case, where a single wavelength of collimated light meets this condition for the angle of incidence and reflection occurs. (b) shows that for a divergent beam (spread arrows) one angle will meet the Bragg condition, but the other angles travel slightly further before reaching a reflection plane, which brings them out-of-phase at the reflection plane. (b) shows that for collimated broadband radiation, only one wavelength (indicated by colour) is reflected, while the rest are transmitted.

angles to the filter surface normal depending on the final application of the filter (e.g. high-angle filter, normal-incidence filter, reflection or transmission gratings etc.). Equation 2.1 shows that a filter with a given grating angle and period will establish a Bragg condition for a very specific wavelength, and that changing the angle of incidence changes the wavelength that meets the condition and is reflected.

At the same time, light which does not meet the wavelength requirement will be transmitted, mostly un-attenuated.

VBGs are used in two ways to achieve our low-frequency setup. Firstly, VBGs on the input side spectrally filter the input laser. This is a good idea whenever the laser is fiber coupled (even if the laser is high quality), as the fiber core glass undergoes Raman scattering which is collimated with the laser and can appear in the collected Raman spectrum.[158] Reflecting off a VBG causes the laser to be redirected while the unwanted fiber Raman scattering is lost.

Secondly, we use three VBGs on the collection optics to filter out the laser line (only) from the Raman spectrum. Each filter has an optical density (OD, the negative logarithm of its transmission) at the laser wavelength near 4, which corresponds to a rejection of 99.99 % of the laser light. Three of these in series multiplies their ODs together, giving a final reduction of laser light by 10^6 - bringing the Rayleigh line down to the same order of magnitude as the Raman scattering. This allows access to low-frequency modes, and simultaneous observation of Stokes and Anti-Stokes scattering, which provides additional insights discussed in Chapter 4.

The high-sensitivity of VBGs to angle of incidence also applies to beam divergence. Figure 2.3(b) shows that light rays from a diverging beam travel further than co-axial rays, so they will not arrive at the next reflection plane in phase and therefore do not meet the Bragg condition for reflection. As such, they are transmitted through the filter, and can be collected by the collection optics and contribute to stray light, which then obscures the Raman spectrum. Therefore, it is an absolute requirement to have a laser beam with low divergence and high-quality optics to observe low-frequency modes in our setup, and this motivates many of the design decisions in this chapter.

2.2.2 Divergence

In practice, no beam is perfectly collimated and will typically increase in diameter with distance from the source, which we quantify as beam divergence (angle) θ. Divergence is a consequence of two factors: having a finite source size, and the effects of diffraction. Minimising divergence wherever possible is the most important condition for the design of our low-frequency Raman microscope. In addition to poor Rayleigh rejection, divergence results in larger spot sizes, meaning our sample point-resolution is limited by the divergence of the beam (among other factors). A larger spot size at the sample has knock-on effects for every event following - a larger spot will be collimated less effectively by the microscope objective into a more divergent beam, which is less effectively filtered by the low-frequency filters, and is harder to focus into a small spot again for the collection fiber.

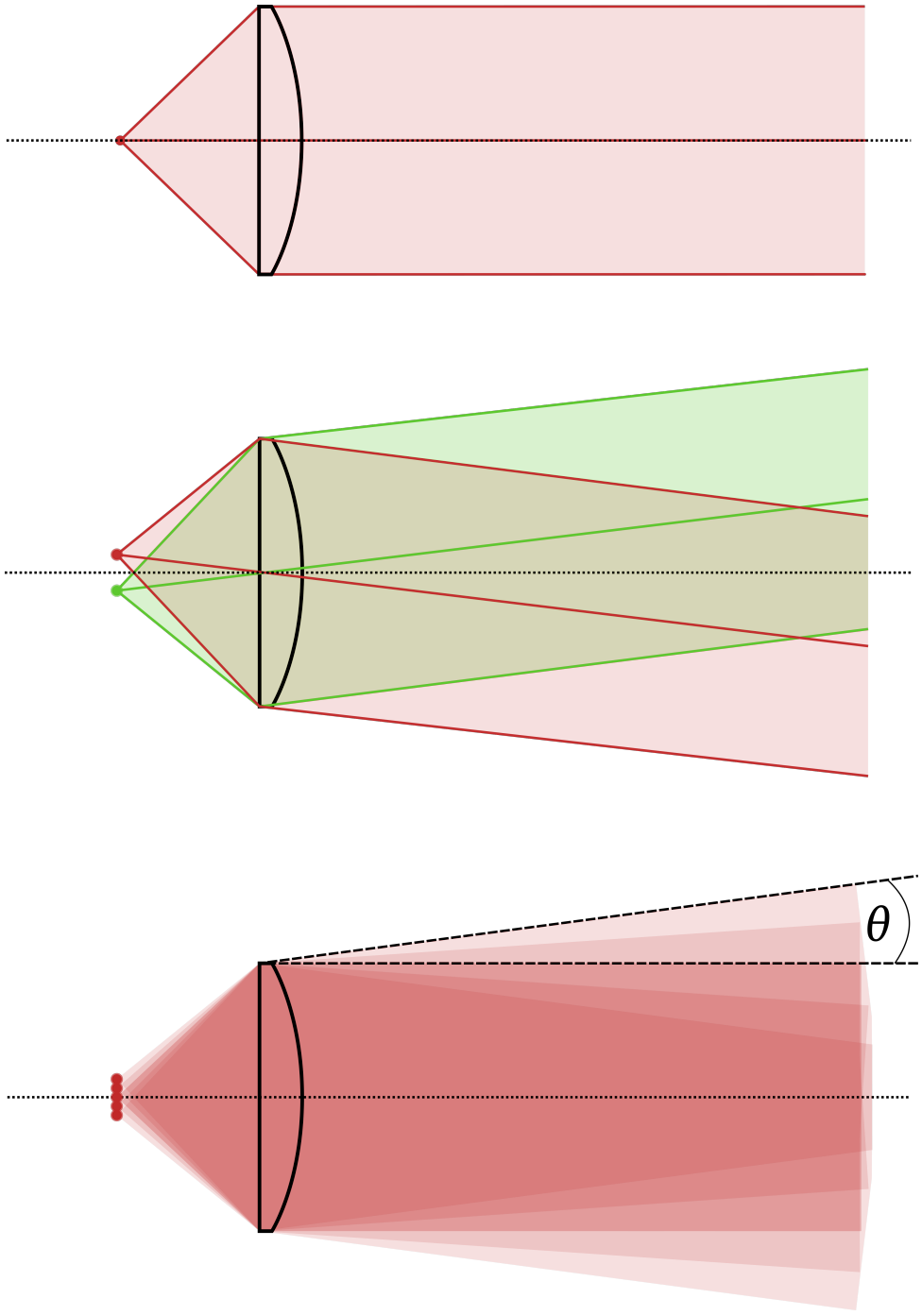

FIGURE 2.4: The top image shows an ideal case for a spot size of zero, exactly at the focal point, which exhibits diffraction-limited divergence. The middle image shows how points offset from the optical axis are collimated at separate angles. The bottom image shows this for a finite spot size which is actually a finite area/volume. Light from each point is collected and contributes to a beam of light with a divergence defined by the angle θ.

We can understand schematically how divergence arises from finite spot sizes in Figure 2.4. If we imagine our source is a single point, the top schematic illustrates how for a single point of zero size, the perfect aspheric lens will result in the lowest

possible divergence for a beam. Note the effects of diffraction prevent this from being zero, so we refer to this as diffraction-limited divergence. The middle image shows what happens to the beam if we consider two points, offset by some distance either side of the principal axis - which gives two beams travelling in non-parallel directions to one another. Therefore if we consider a finite point source of some size to be a large number of point sources in a line, we end up with a series of overlapping beams with most of the light concentrated near the principal axis, but diverging as it travels further from the lens. The divergence is then the angle created by the ideal beam diameter and the edge of the diverging beams, θ.

2.2.3 Gaussian Beam Optics

Lasers

Lasers generate light via stimulated emission in a resonant laser cavity. Electrons in an excited state are stimulated into emission of a photon by other photons propagating in the cavity, and consequently adopt the direction, polarization, and phase of the stimulating photon. This creates an amplification or gain of photons with coherent phase, propagation direction, and polarization - all of which are desirable properties that can be exploited by the modern spectroscopist. The resonant characteristics of the cavity support certain standing waves which become enhanced over all others (others tend to destructively interfere), and thereby quantize the wavelengths of the photons to those with nodes at either end of the cavity. These quantized wavelengths are typically referred to as "modes" as they describe the spatial mode of propagation. Many high-quality lasers are "mode-locked", or include optics or lasing techniques which select for a single spatial mode only. These are referred to as single-mode lasers, and have properties of an ideal coherent wave. Note that no laser source is genuinely perfect, so there will always be some amount of multi-mode and divergent behaviour from the device design.

For single mode lasers, the primary source of divergence comes from the diffraction of light, which is not described by Geometric Optics.

Since an ideal single-mode beam has an amplitude envelope perpendicular to the direction of propagation described by a Gaussian function, we can use Gaussian beam optics to provide a suitable model for single-mode wave propagation in lasers. This ideal laser mode is often the fundamental transverse mode (TEM_{00}), as a beam of this mode provides the smallest focused spot.[159,160] The irradiance profile $I(r)$ across a TEM_{00} beam is described by the Gaussian function:

$$I(r,z) = \frac{2P}{\pi w(z)^2} \exp\left(\frac{-2r^2}{w(z)^2}\right) \tag{2.2}$$

where P is the total power of the beam, r denotes radial distance away from the propagation (z) axis, z denotes distance along the z axis, and $w(z)$ is the beam radius at each point along z - defined as the radius at which the intensity drops

to $1/e^2$ ($\sim$13.5 %) of the maximum value (see Figure 2.5(b)). The above equation 2.2 shows irradiance as a function of radial distance and position along the propagation/principal axis z, and the change of beam radius with z being due to the diffraction of light. The beam radius along z is described by the hyperbolic function:

$$w(z) = w_0\sqrt{1+\left(\frac{z}{z_R}\right)^2} \tag{2.3}$$

where w_0 is the beam waist. z_R is known as the Rayleigh range, and is given by

$$z_R = \frac{\pi w_0^2 n}{\lambda} \tag{2.4}$$

where n is the refractive index of the medium. The diagram in Figure 2.5 shows the shape of the beam described by equation 2.3, with each of the important variables labelled.

For a diffraction limited Gaussian beam, the divergence is defined as the far-field approximation of $\partial w(z)/\partial z$, and the divergence half angle θ can be approximated by

$$\theta \approx \frac{\lambda}{\pi n w_0} \tag{2.5}$$

where n is the refractive index and w_0 is the beam waist, which is the beam radius at its smallest point. Importantly, we see that for a single-mode beam the divergence is inversely proportional to the beam diameter. This means that we can minimise divergence in our beam by expanding its radius (i.e. beam waist) using optical elements. For multi-mode sources the diffraction properties are still present and beam expansion is still useful for controlling divergence, it is just not the only source of divergence.

Other useful parameters shown in Figure 2.5 include the Rayleigh length, z_R, which is the distance from the beam waist where the cross-sectional area of the beam is twice that of the beam waist (half the power-density). We typically consider the focal depth to be one Rayleigh length either side of the beam waist. Therefore, when we talk about the focal volume we are really considering a three-dimensional hourglass shape about w_0 aligned on the propagation axis.

It should be noted that Gaussian beam optics are only valid for relatively shallow beam angles with respect to the principal axis (the paraxial approximation),[162] so it does not accurately describe a strongly converging/diverging beam, except near the focal point where the beam shallows out due to diffraction effects.

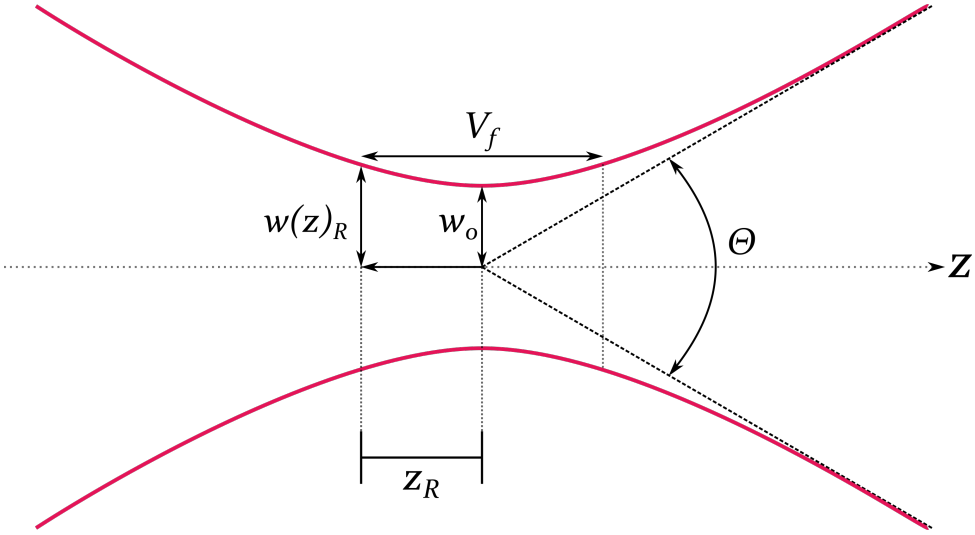

(a)

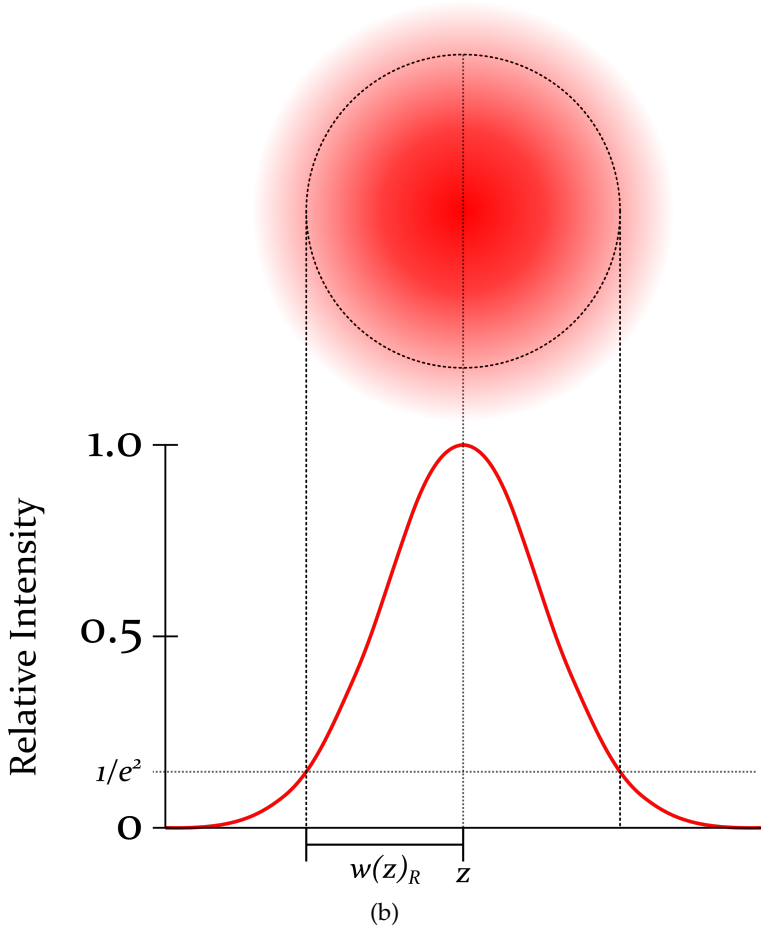

(b)

FIGURE 2.5: The top diagram shows a beam waist, and how divergence arising from diffraction is defined as the full-cone angle Θ. The bottom diagram shows the ideal cross-sectional profile for a Gaussian beam. Labels are defined in the text. Figure adapted from the Edmund Optics Laser Optics Resource Guide.[161]

2.2.4 Fiber Coupling

Fiber optic cables allow the transmission of light through a waveguided medium, which is typically an insulated core of optical glass fiber. Optical fibers achieve their waveguide properties through the principle of total internal reflection (TIR), which is a consequence of Snell's law at high angles.[163] When light crosses the the boundary from one medium to the other, Snell's law (equation G.2) shows that if the second medium has a lower refractive index, the angle of the refracted ray of light (between it and the surface normal) is greater than the angle of incidence. As such, there exists some shallow angle of incidence where the angle of refraction is greater than 90°, and the ray is unable to escape the first medium (see Figure 2.6). At this point, reflection becomes the main optical process at the boundary, and the ray is confined in the medium by TIR.

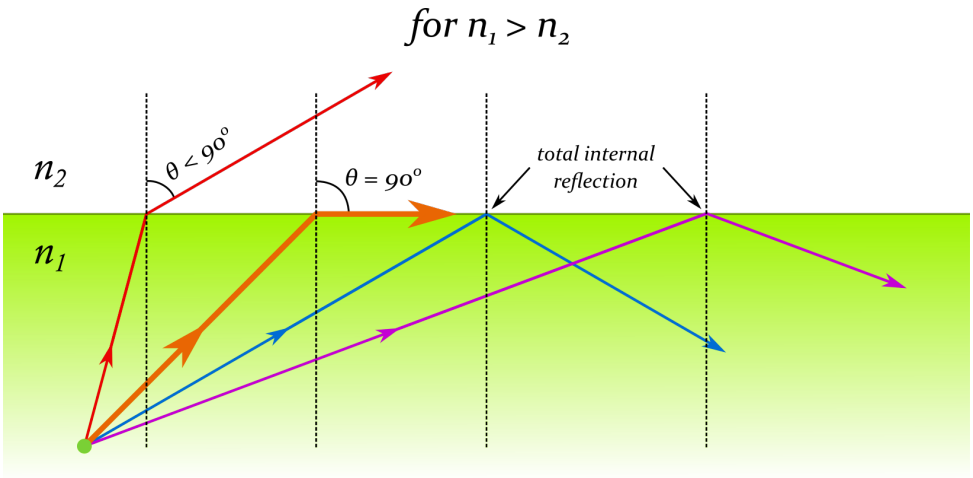

FIGURE 2.6: Schematic representation showing total internal reflection. When a ray of light light encounters an interface where the other medium has a lower refractive index, it refracts away from the surface normal, and there are some angles of incidence for which the refracted beam is not able to escape the medium. Thus reflection becomes the dominant process.

Multi-mode fibers have large enough cores that they can support multiple propagation modes, while single-mode fibers only support the one mode, and coupling to each requires different considerations.

For multi-mode fibers, the walls of the fiber are typically far enough away from a focal point that we consider wave propagation in the far-field, so we can use ray-tracing and Snell's law to describe coupling of light to the fiber. There is a maximum acceptance angle (or NA) for rays to enter and become trapped in the fiber, and is given by

$$NA \approx nsin\theta_{max} \approx \sqrt{n_{core}^2 - n_{clad}^2} \tag{2.6}$$

where n_{core} and n_{clad} are the refractive indexes of the fiber optic core and cladding material respectively. Sending light into a fiber at too high an angle (too large NA) is called overfilling, and causes the high-angle light to leave the fiber as losses. Figure 2.7(a) shows this schematically, and the red shaded region indicates the light which is captured by the fiber, while the blue shading indicates light which is lost. This NA also describes how rapidly light diverges from the end of a fiber by setting a maximum divergence angle θ, shown in Figure 2.7(b). By changing the focal length of the lens used to collimate a fiber, one can control the resulting beam diameter, since longer focal length lenses give the light exiting the fiber more distance to expand before being collimated.

Under-filling a fiber is when the NA_{eff} of incident light is smaller than the fiber NA, and is only a problem if the spot size - reduced due to the lower NA - does not fit inside the fiber core, and therefore results in losses. For multi-mode fibers, there is often a comfortable amount of freedom between small spot size and fiber NA that their alignment is trivial, and therefore are a useful choice for polychromatic Raman collection optics. However the improvement to divergence provided by single-mode

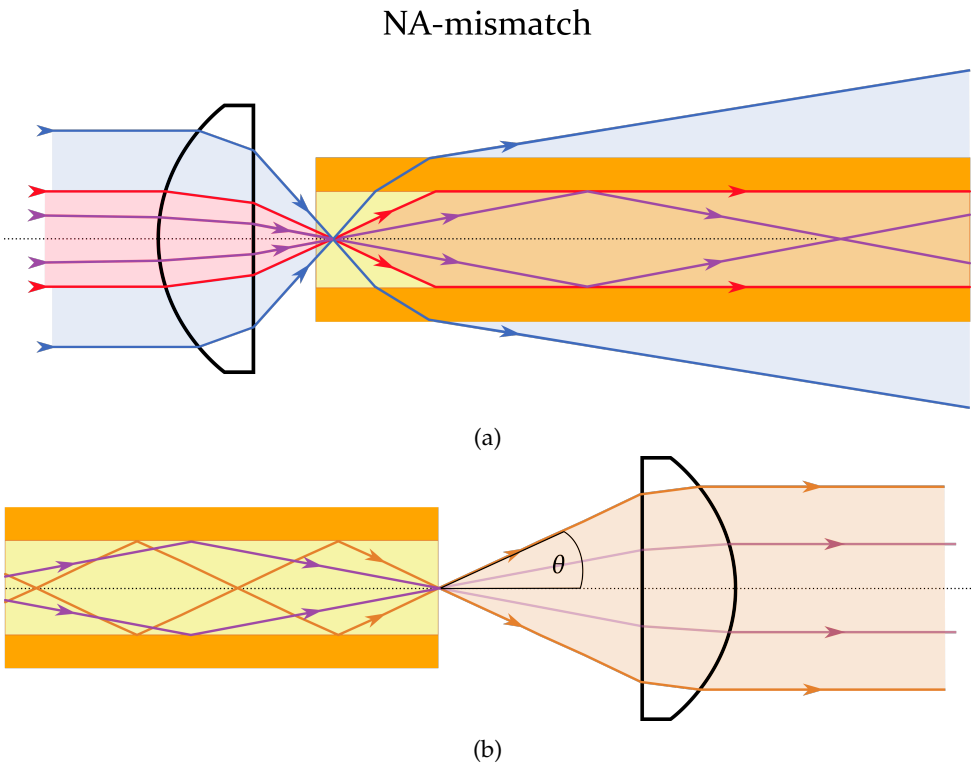

FIGURE 2.7: (a) When coupling to a multi-mode fiber, it is important to match the NA of the focusing lens to the NA of the fiber, otherwise TIR cannot be satisfied for the peripheral rays of light which strike the core-cladding interface high angles, which refract and escape the fiber. (b) The highest angle modes supported by the fiber define a cone of light with angle θ upon exit - which can be collimated to different beam diameters by selecting the appropriate focal length lenses.

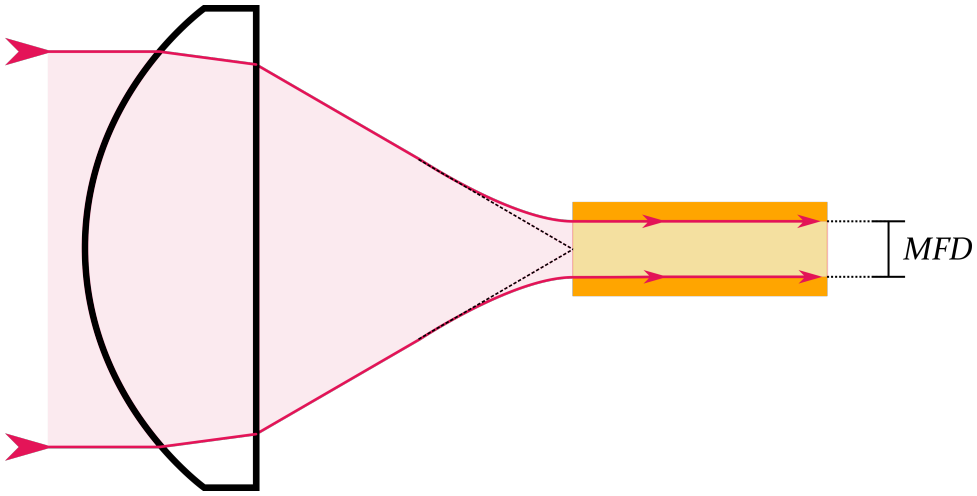

(a)

FIGURE 2.8: Fiber coupling is different for single-mode fibers, which require consideration of Gaussian wave propagation. In single-mode fibers, the only mode of propagation is in-line with the fiber axis. Therefore, when focusing to the fiber, the beam waist should match the effective propagating diameter of the fiber, known as the mode field diameter (MFD). Coupling efficiency is determined by how well the beam intensity profile at the fiber end matches the approximately Gaussian MFD profile.

optics necessitates their use as the input source in our low-frequency setups.

For single mode fibers, we do not consider the NA of the fiber, as mode propagation is described by Gaussian beam optics. This is in part because of the shape of the wavefront, which flattens out smoothly as the radius approaches the beam waist at the focal point. Instead, the efficiency of coupling is determined by how well the beam profile at the beam waist matches the approximately Gaussian profile of the single-mode fiber. The mode field diameter (MFD) is the width of the fiber's Gaussian profile, and assuming we have an ideal Gaussian beam profile, we need only match the focused spot size to the MFD. While this may initially sound simple, to effectively couple to a single-mode fiber requires positioning accuracy on a sub-micron scale for x, y, and z translation, *and* three axes of tilt control, whilst matching the beam diameter to the NA of an aspheric lens to achieve the ideal spot size at the focal point. In addition, a lens used to focus laser light of one wavelength into a single mode fiber cannot be used for another wavelength, as the dispersion from wavelength-dependent refractive index means the focal point is different for each wavelength. Single-mode optics are not suitable for guiding broadband radiation for the same reason. To minimise alignment efforts we often use dedicated single-mode optics for each wavelength, pre-aligned in their housings. This also ensures that the collimated beam on the output end of the fiber has the lowest possible divergence.

2.3 Low-Frequency Raman Microscope Design

Throughout this PhD work, I have designed and implemented several unique Raman microscope configurations through constant iteration for various purposes. Ultimately, two designs have become standards in the laboratory, and I will use this section to outline their design and discuss their technical aspects. These are referred to colloquially as the "modular" and "scanning microscope" designs, and both are capable of providing high-quality low-frequency Raman spectra at a range of wavelengths for resonant Raman studies.

In our lab we heavily utilise the 30 mm and 60 mm optical cage systems from ThorLabs (ThorLabs), which facilitate alignment of optics on a common optical axis. In addition, 3D printed parts using a Prusa i3 MK3S fused-deposition modelling (FDM) printer are used extensively, and it is remarkable how effective these parts are - even as end-use components in sensitive optical configurations.

Both microscope designs utilise a dual-cage configuration shown in Figure 2.9, containing both the input and collection optics. A separate cage is built and pre-aligned for each actively-used laser, and the dovetail adapter allows rapid swapping of laser wavelengths for resonant Raman studies. Each wavelength uses a dedicated fixed-focus aspheric lens fiber collimator and a single mode fiber, to ensure the collimated laser beam has the lowest possible divergence and spot sizes. For our free-space lasers, this means we must first couple into the single mode fiber using another of these fixed focus collimators. Even with these collimators, the correct alignment can be difficult to achieve due to the required precision of both position and angle of the incoming beam, and it best performed at low laser power initially to minimise accidental laser-induced damage to the fiber end. After the correct alignment has been found, the power can be slowly increased to an appropriate level for Raman spectroscopy (a few milliwatts at the output). Keeping in mind there will be some losses due to imperfections in the alignment and incoming beam quality, incident laser power on the input end of fiber end should not exceed the threshold for laser induced damage of $\sim$1 MW cm^{-2}, which for a fiber of $\sim$1.5 µm diameter and visible wavelengths is $\sim$70 mW (see ThorLabs "Damage Threshold" tabs in fiber cable product sections[164]).

Each of the optics holders in 2.9 has fine adjustment as either X/Y translation, Z translation/focus (along optical axis), or on-axis tilt (gimbal). The dovetail adapter also has a matching mount on the side of the inverted microscope, which means either microscope can be used with any of the laser lines (see Figure 2.10). This is advantageous for accommodating a wide variety of sample morphologies and preparation methods. The top two optics in the schematic in Figure 2.9 labelled "Collection fiber alignment" are responsible for focusing and aligning the collected Raman scattered light to the collection fiber optic cable. When operating on the side of the inverted microscope, these can be removed to allow the collected light to

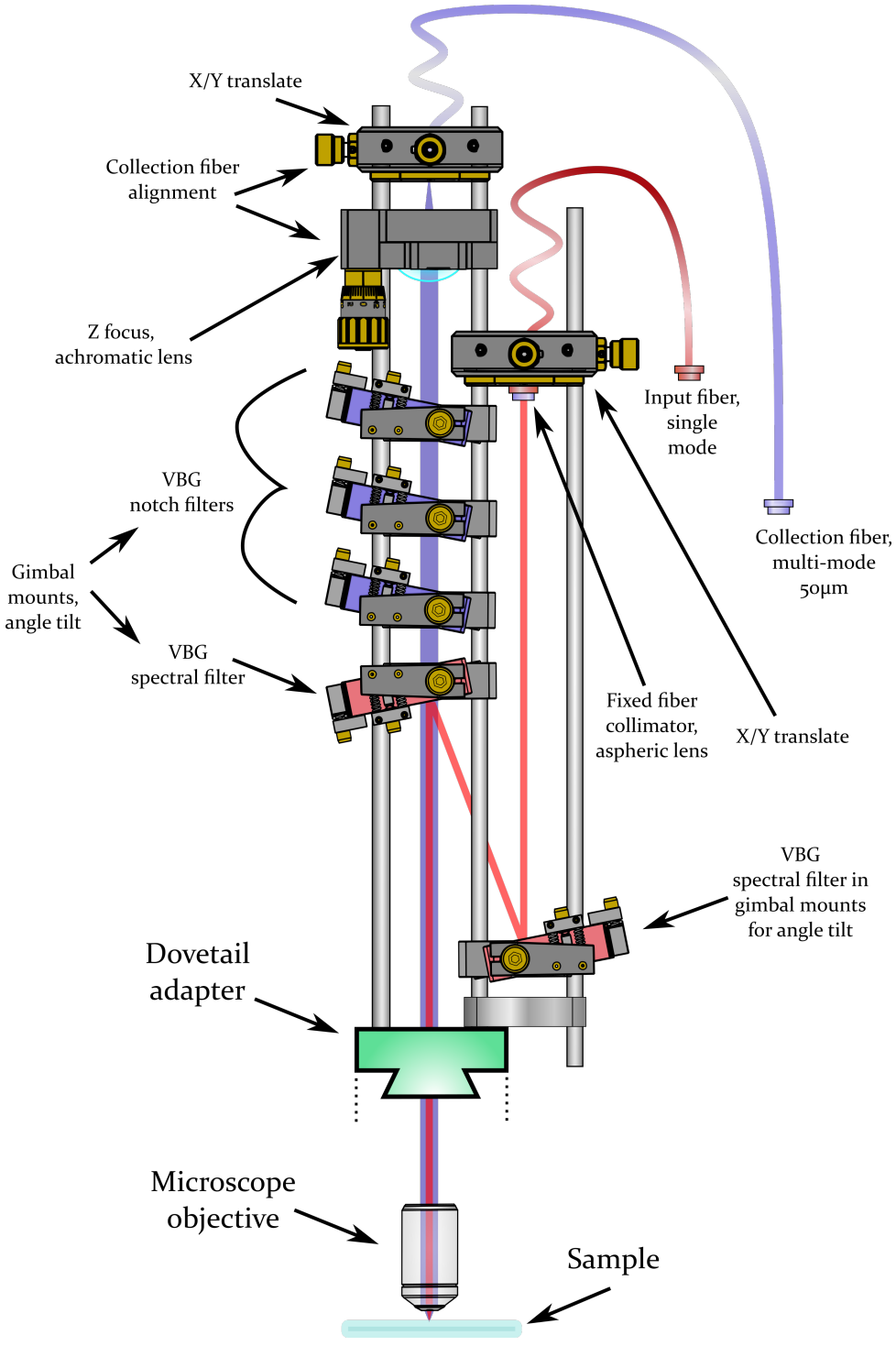

FIGURE 2.9: Schematic representation of the dual-cage design, with labels indicating each part.

continue in free-space to the detector, and be further manipulated if required.

Having two VBG filters on the input line is not always necessary but significantly reduces the amount of Rayleigh scattered light in the spectrum. This is primarily because the laser light which is not reflected by the filter (rejected) then passes through the optic, during which time it can elastically scatter off the optic itself (see Figure

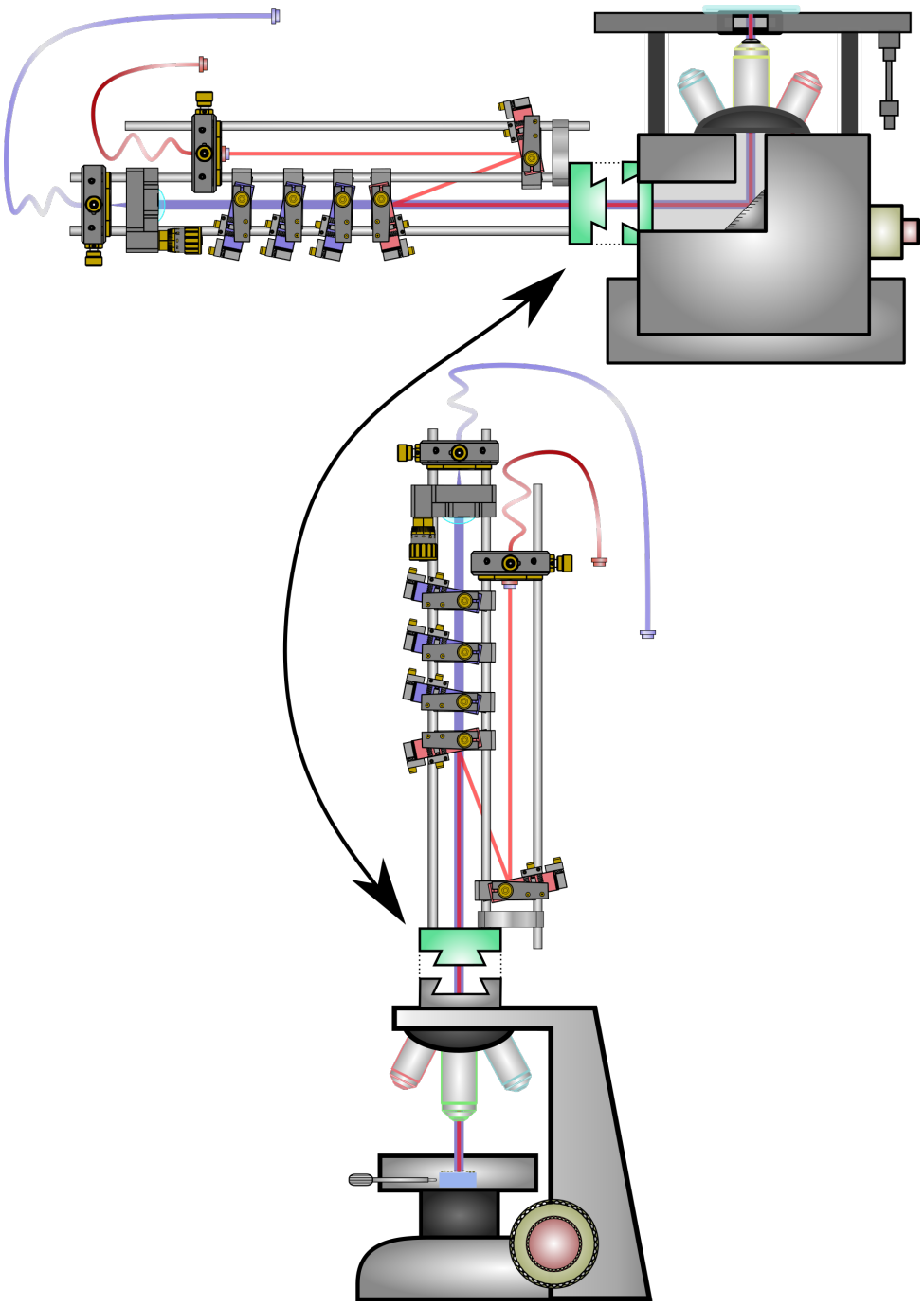

FIGURE 2.10: Schematic representation of the swappable nature of the dual-cage desing, using dovetail adapters to quickly change from an inverted microscope (top) to an upright microscope (bottom) configuration.

2.11). While the scattering rate is relatively low, it is still enough to be observed as a visible glow of the glass (see Figure A.1), which means some will scatter in directions close enough to the principal axis to be collected and observed in the spectrum. With two VBGs, the initial spectral filtering is done by the first filter on the right of

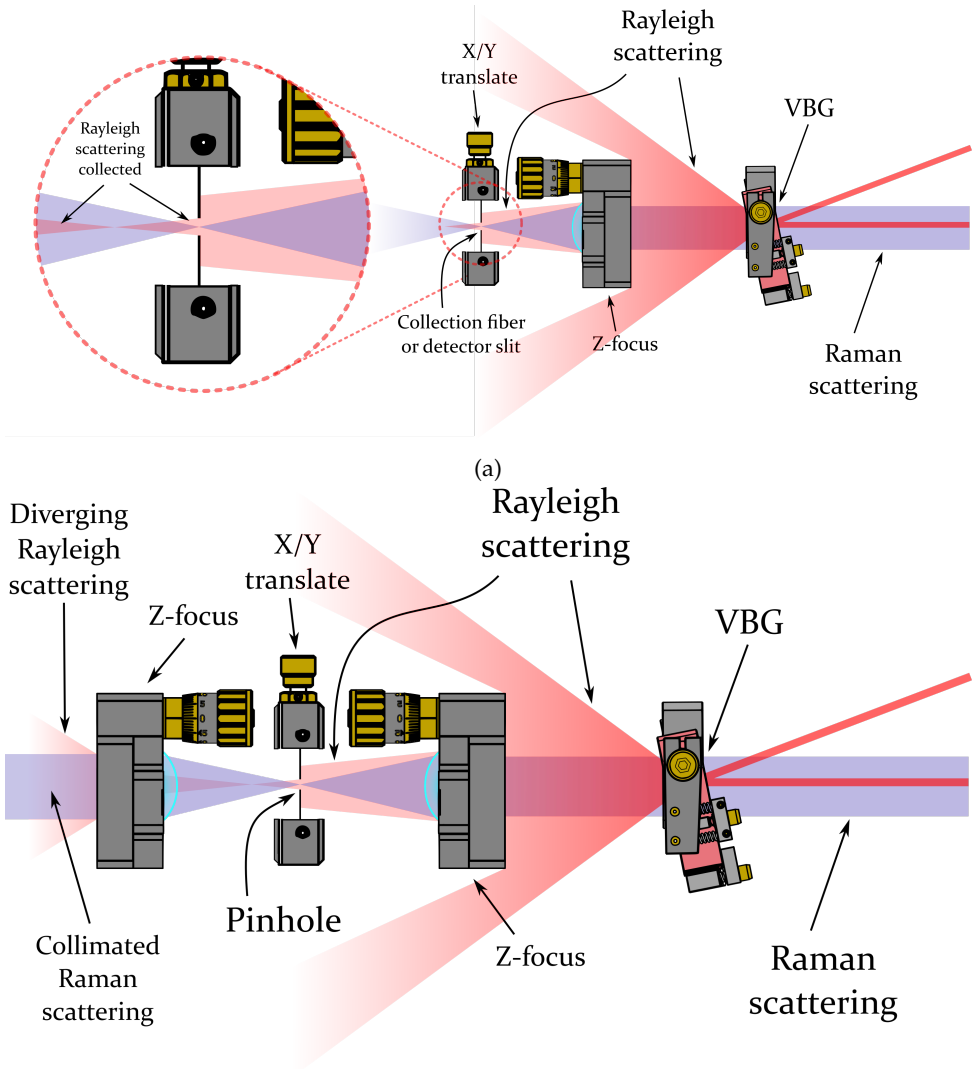

FIGURE 2.11: Schematics of elastic scattering in the VBGs under the Geometrical optics model. (a) Rayleigh scattering in the VBGs, which is highly divergent, is still partially focused into the detector slit or fiber optic cable, ending up in the spectrum. (b) Addition of a pinhole filtering setup which re-collimates the Raman scattering on the other side, but the Rayleigh scattering continues diverging.

Figure 2.9, which is not on the principal axis and thus rejected (transmitted) scattering cannot reach the detector. Then when the laser reaches the second filter, most of the light meets the Bragg condition and only a small amount is rejected on the principal axis, resulting in a much smaller Rayleigh line.

The problem is actually worse for the free-space configuration, as the 50 µm fiber acts as a pinhole spatial filter, which minimises the contribution from divergent scattering (see Figure 2.11 and 2.12). Therefore it is often necessary to construct a pinhole spatial filtering module for free-space designs (Figure 2.11) - which takes away the high-throughput advantage of staying in free-space, since the pinhole restricts the collection volume to a thin slice of the sample (essentially making it confocal). Note

the interpretation in 2.11 is appropriate for relatively large apertures (slits, pinholes, and fibers) showing far-field effects in a Geometrical optics model. For small apertures, diffraction effects begin to dominate, and the aperture behaves as a new point source, which can be collimated and re-filtered by VBGs (see Figure 2.12). A similar effect of re-collimating from a multi-mode fiber also results in improved Rayleigh rejection.

Given the complexity of aligning to/from a pinhole, when basic spatial filtering is required during Raman collection it is often easier to couple to a fiber. Note that an edge filter can be placed before the detector in the free-space setup to immediately improve the spectral quality by sacrificing the low-frequency and anti-Stokes modes. The filter can actually be carefully rotated to optimise the spectral cut-off closer to the laser frequency, and in some cases can allow the observation of low-frequency Stokes modes (see Figure 2.2). Given that anti-Stokes is not required by most other users, this is a common configuration for high-throughput Raman on the inverted microscope.

Given the spatial filtering provided by the pinhole, it can be better to send the Raman scattered light through a fiber before it reaches the VBG notch filters, as shown in Figure 2.13. This is because when the collected light emerges from the fiber, it does so from a spot the size of the fiber core - in this case 50 µm. This means scattered light from the VBG spectral filter can be re-collimated to reduce its divergence so it is better rejected by the VBG notch filters. In addition, our VBG notch filters have a significantly larger clear aperture than the limiting apertures in the setup (see Figure 2.14). By re-collimating with a longer focal length lens, we end up with a

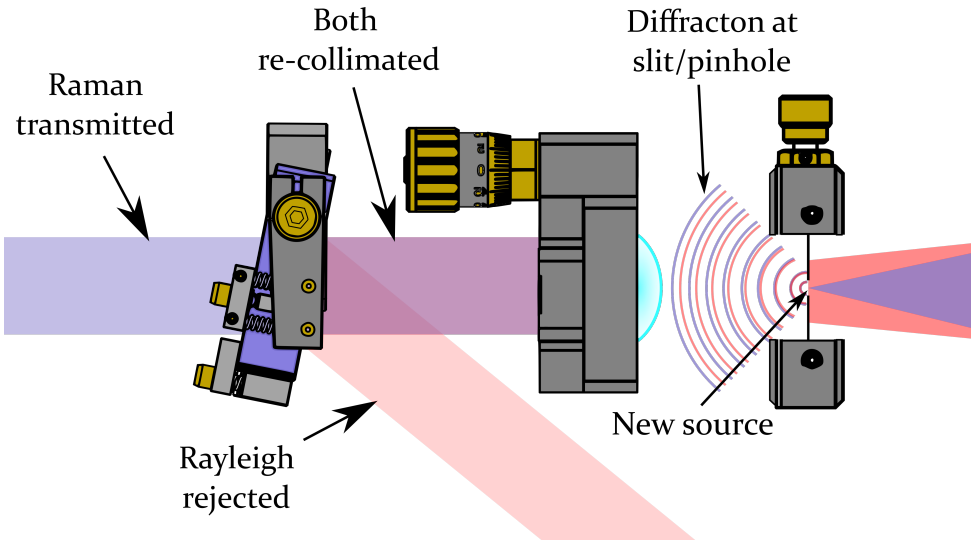

(a)

FIGURE 2.12: For pinholes of sufficiently small size (<50 µm) diffraction at the pinhole/slit becomes significant, and this aperture begins to act as a new point source, with the Rayleigh and Raman scattered light propagating radially. This can then be re-collimated and the Rayleigh light filtered by VBGs.

lower divergence than the initial beam (i.e. we have effectively expanded the beam for the filters). This again improves the Rayleigh rejection and spectral quality. Note that in 2.13 one VBG notch filter is used before the fiber. This is because at high laser powers the back-scattered Rayleigh light collected at the sample and reflected laser light is sufficiently intense that it can produce a detectable amount of Raman scattering of the collection fiber, which reduces the spectral quality - particularly in the low-frequency region. One filter before the fiber is enough to prevent this.[158]

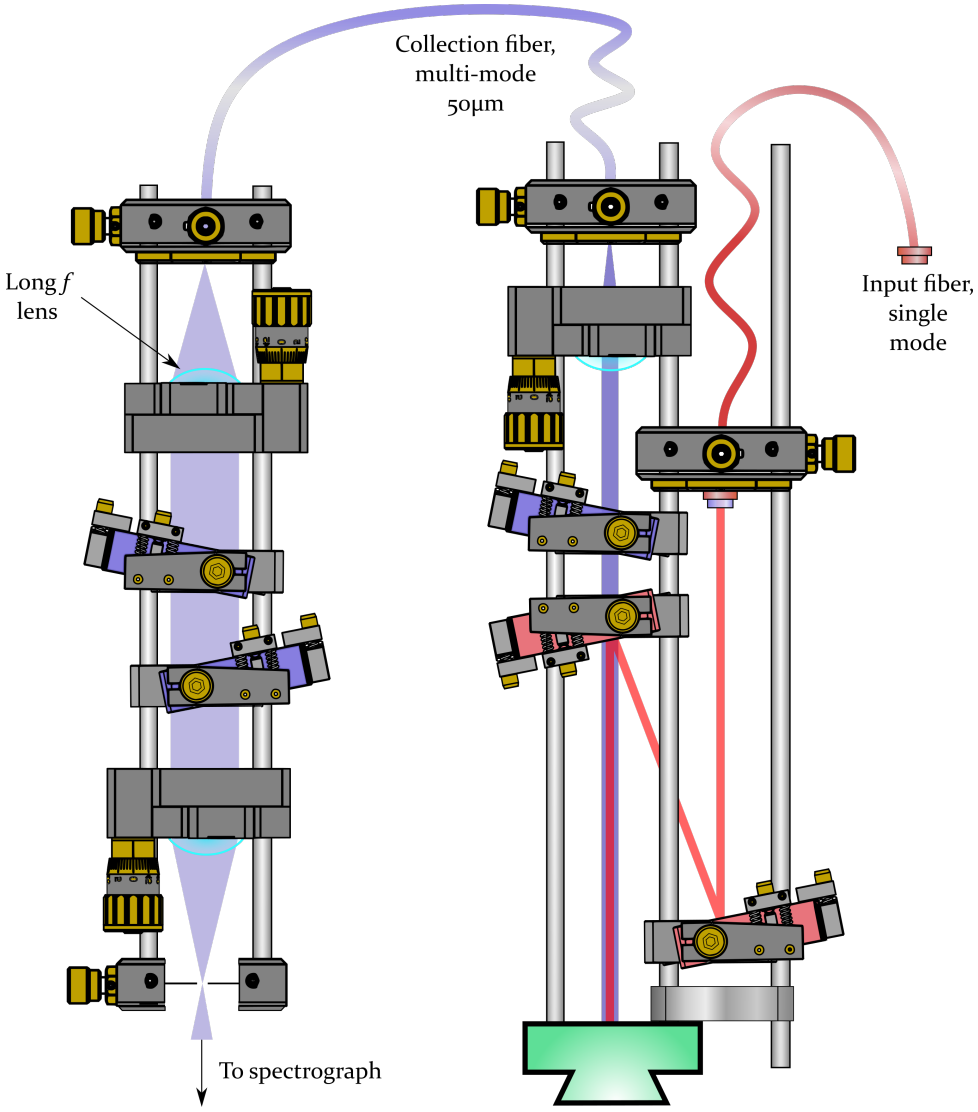

FIGURE 2.13: Split-collection method. It is often beneficial to filter with VBGs after collecting with a fiber, since the VBG Rayleigh scattering is re-collimated or spatially filtered out. Note that one filter is used before the fiber to prevent residual laser light from Raman scattering within the fiber.

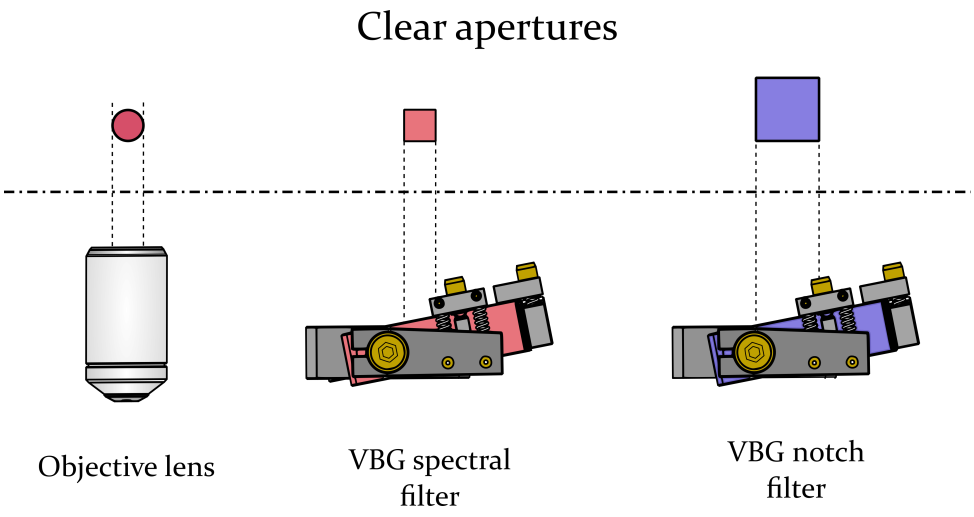

FIGURE 2.14: The clear aperture is the size of the optic through which light can actually pass without being obstructed. In our setup, the clear apertures for the input spectral VBGs and microscope objective (∼5 mm) are about half the size of the collection notch VBGs. This means we can expand the collected beam upon collection fiber re-collimation to reduce divergence and improve Rayleigh rejection.

Stability

These cages are typically very stable, but the added mass of the VBG gimbal mounts and X/Y and Z translation mounts can cause the cage to flex under its own weight. This is typically not an issue in the split-collection configuration in Figure 2.13, but can be problematic when working in free space with lots of optics on the cage. One solution is to mount a post to the table under the cage, set at a height for the cage to rest on. Another solution is to run a bracing bracket along the side or back of the cage, reducing the amount of flexion (see Figure A.3).

2.3.1 Scanning Raman Microscope

In order to to precisely map samples at sub-micron resolutions, the scanning microscope needs to be structurally stable. In addition, it must remain stable over the length of the collection period, which for imaging maps of 2D materials can be up to several days, otherwise artefacts and distortions will appear in the reconstructed images (example shown later in Figure 2.54). It must be rigid so that is does not easily move or flex - and however much it does move or flex, it must not have any hysteresis. That is to say if a force is applied somewhere then released, all parts need to return to their rest positions. Getting this right turned out to be a significant challenge, and was part of the motivation for moving away from the commercial microscope bases and building an entirely separate microscope from ThorLabs components. This gave me complete control over the structural elements to trial different designs and optimise stability.

An ideal stage for sub-micron Raman mapping would be an amplified piezoelectric stage with X, Y, and Z travel, with a closed-loop feedback mechanism to accurately measure position. ThorLabs offer similar stages and controllers, but they get very expensive very quickly, and ultimately suffer from small total travel ranges. As a starting point, and since we like the idea of salvaging components from old equipment for a new life elsewhere, we used a high-precision fine-pitch leadscrew stage from an old optical instrument (origin unknown, see Figure 2.15). This is heavy and sturdy, with vernier scales reading down to 1 µm increments. With a bit of gearing, it is also capable making accurate sub-micron steps. This gives X and Y translation control, while Z focus and depth would be controlled with a Z-translation cage-mount holding the microscope objective. Using this stage requires the microscope to be in an upright geometry (microscope objective pointing down towards the sample). It was also decided early on to leave some amount of accessible space above the stage to allow the mounting of additional apparatus, such as a Linkam THMS600 cold-stage for low-temperature measurements (see section 2.3.6). This meant the main assembly was relatively high above the table, so in order to maintain stability the assembly was mounted on the end of several 200 mm long, 1.5 inch diameter steel posts along the optical axis. The microscope also needed a camera and light source mounted near the objective lens.

Figure 2.16 shows an optical schematic demonstrating generally how light is manipulated in the design, and Figures 2.17 and 2.18 show computer-aided design (CAD) renders and photos of the of the final build of the microscope. There are four main sub-assemblies to this microscope, indicated in Figure 2.19, and each will discussed in the following sections. The backbone of the cage assembly is connected through each section by various cage plates and 6 mm stainless-steel cage

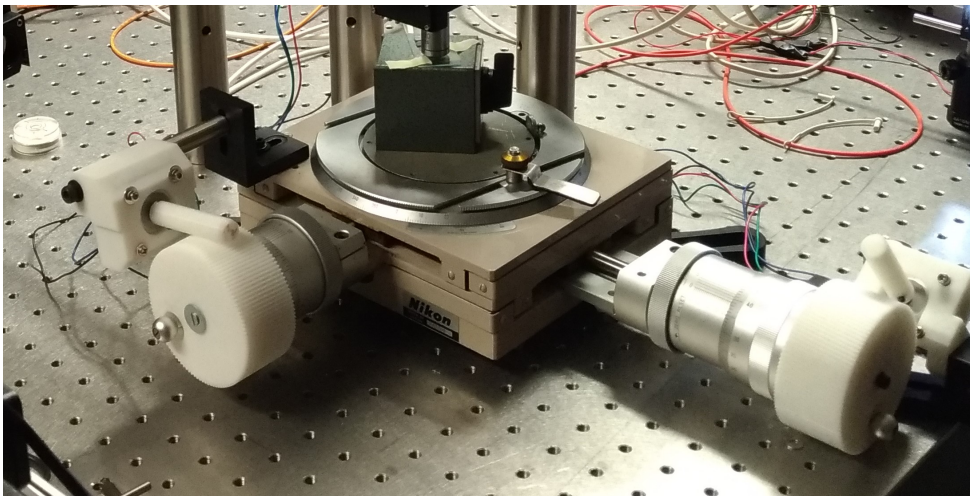

FIGURE 2.15: Photo of the sturdy Nikon stage, with large vernier micrometer lead screw drives on each axis. This photo shows prototype 3D printed worm-gear drives (discussed below) attached to the micrometer knobs.

rods, which can be threaded together with internal grub-screws. At either side of the sections are cage-plates tightly mounted on half-inch stainless-steel optical posts. These posts sit in optical post holders (black cylinders in the figures) which are firmly screwed through their base to the 1.5-inch steel posts standing upright on the table. The 1.5-inch posts are firmly tightened directly to the optical table holes via an internal M6 grub screw. The result is a ridiculously rigid structure, which is justified by the need to ensure that the optics stay aligned over the relatively long distance from laser source, to sample, and to collection fiber. It also provides peace of mind that any additional sub-assemblies added to the backbone are unlikely to introduce structural issues.

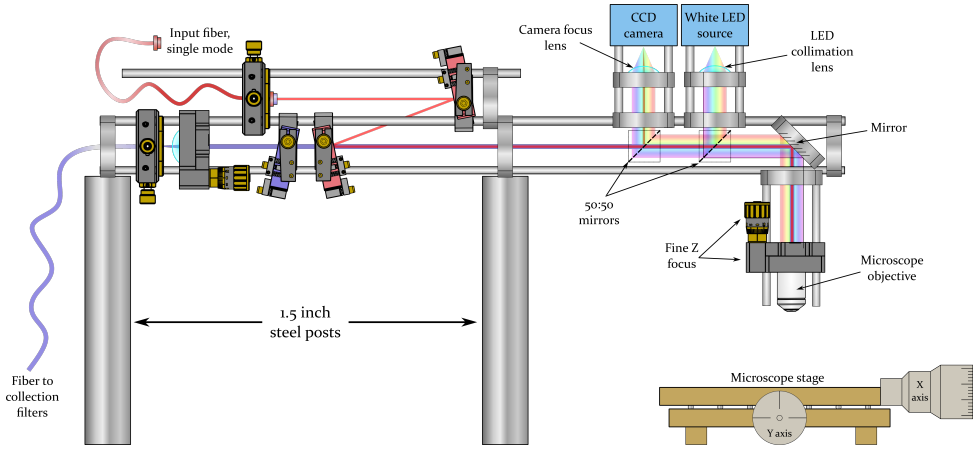

FIGURE 2.16: Schematic representation of the design of a raised upright microscope. Note the positions of the 50:50 cubes are designed to bring a white light illumination source on-axis, and allow the reflected sample image to be sent off the optical axis to the camera.

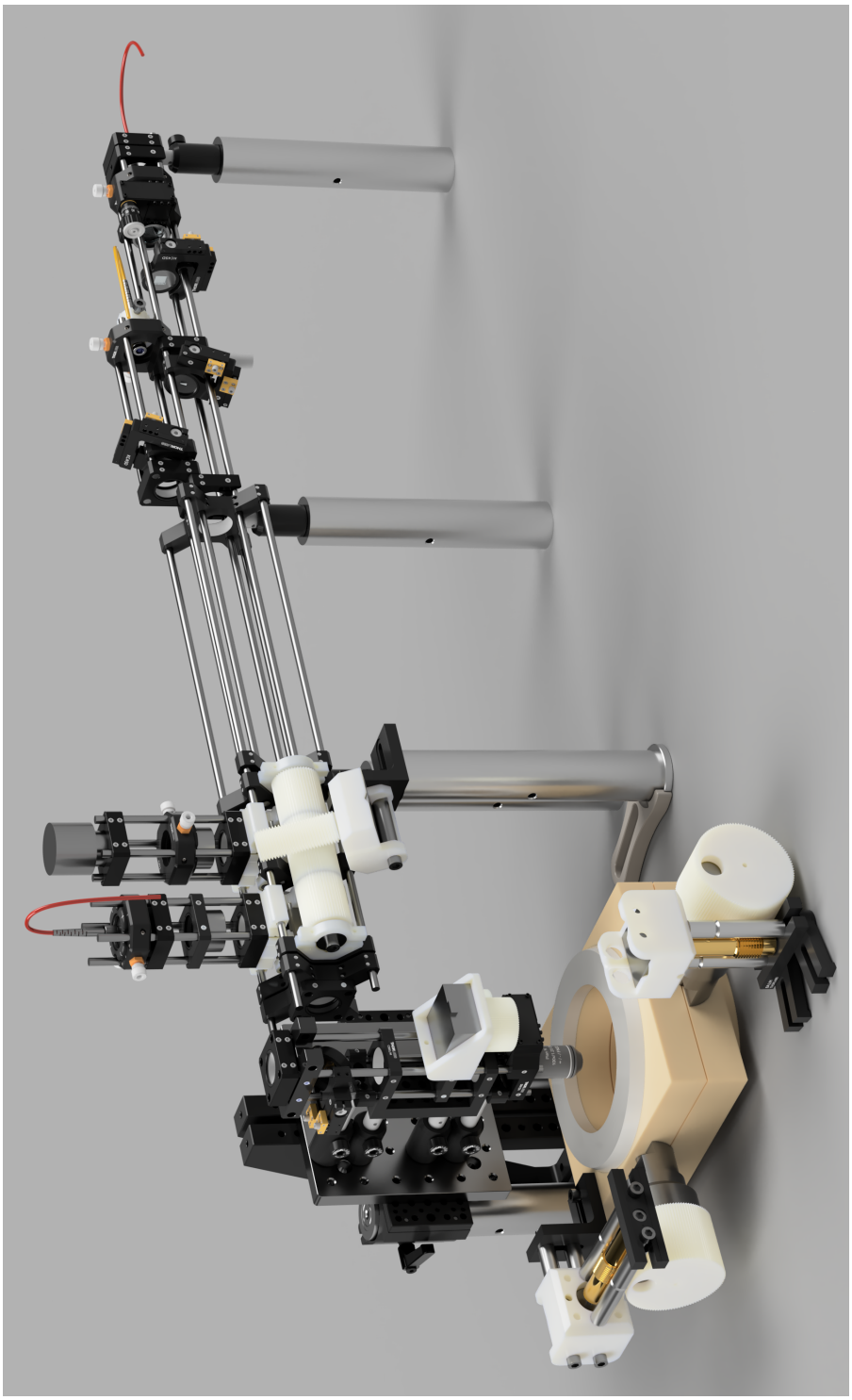

FIGURE 2.17: CAD render of the final microscope design from the front.

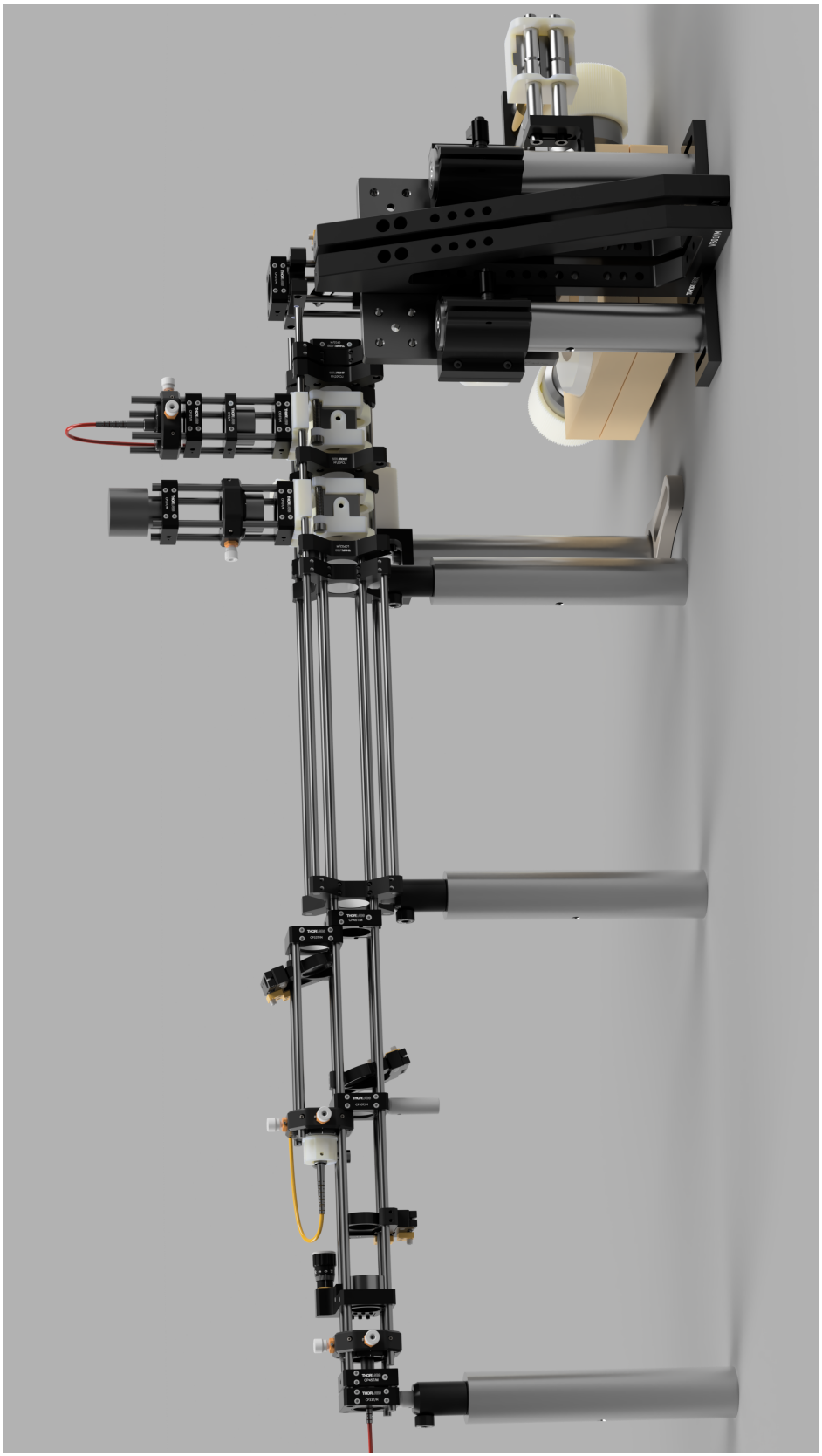

FIGURE 2.18: CAD render of the final microscope design from the back.

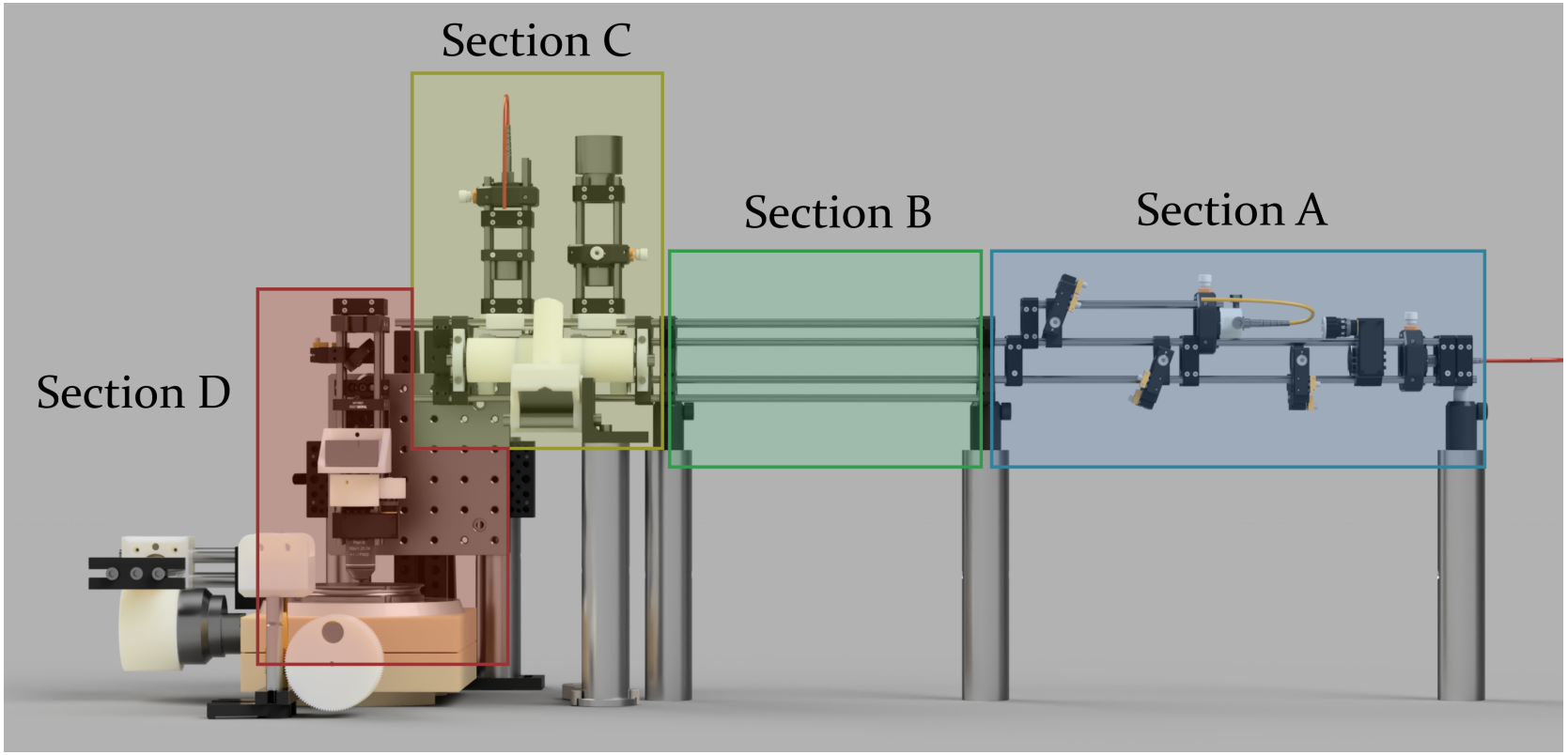

FIGURE 2.19: CAD render profile view showing the four sub-assemblies, to be discussed in the text.

What follows is a breakdown of the components of each sub-assembly, and discussion of the technical issues encountered during prototyping and the justification for the final designs.

2.3.2 Section A - Raman Optics

The first subsection shown in Figure 2.21, is the dual-cage optics system, which uses the same design as the modular setup except that instead of the dovetail adapter we use removable cage-plates from ThorLabs (see Figure 2.20). The dual-cage module is then set at a fixed width and snapped into place between the two steel posts and tightened, which provides excellent stability and reliably brings the laser/collection axis onto the optical axis of the microscope (Figure 2.21(a)/(b)).

Polarization optics can be inserted into the cage using snap-on low-profile mounting brackets with a half-inch diameter rotation mount (see Figure A.7). These then hold a half-wave plate for rotating the linear polarization of light, or a quarter-wave plate for inducing circular polarization. These optics can be dropped in and out as required, where required. For instance, the half wave plate often sits just after the laser fiber collimator to control the incident polarization angle (green shaded area in Figure 2.23), whilst a polarizing filter is placed before or after the collection VBG notch filters, to select for certain scattered photon polarizations (red shaded area in Figure 2.23).

The only other change to the dual-cage system is a 3D printed part to add tilt control to the fiber-collimator. These fixed fiber-collimators are deliberately designed to mate with the end of an optical fiber at a slight angle to help prevent dangerous back-reflections at the aspheric lens into the laser cavity. However, this causes the collimated laser to exit off-axis with respect to the collimator body, which is an issue here because the next optic in the path is one of the angle-sensitive VBG filters.

(a) (b)

FIGURE 2.20: (a)/(b) Removable cage-plates used in the dual-cage design. They clip on to the 6 mm cage-rods and tighten via screws on the side.

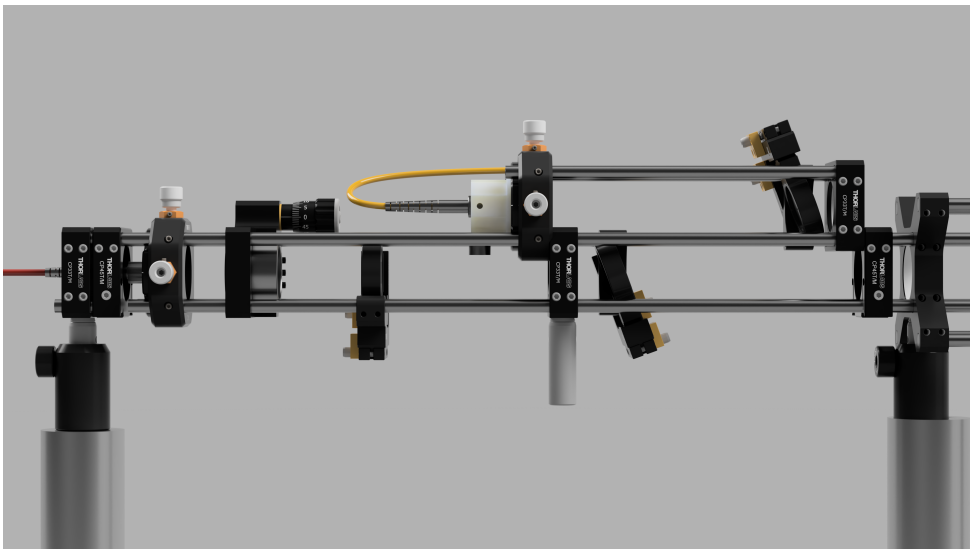

(a)

(b)

FIGURE 2.21: (a) Side view of the dual-cage optics in operation and (b) angled view of it lifted out.

Since both VBGs reflect at the same fixed angle, the final angle of the beam after two reflections will be the same as the initial incident angle. If this is not on axis with the cage, the laser will not be aligned down the microscope.

Ideally, we'd have two mirrors after the collimator to steer the beam and correct for the tilt. For instance, I could have included a third parallel cage to introduce two mirrors in gimbal mounts to bring the laser on-axis with the correct angle (see Figure 2.22). However, this adds extra complexity and bulk to the design, and at the time we had a shortage of these relatively expensive gimbal mounts.

Instead, I designed a 3D printed adapter for the fiber collimator which allows for a small amount of tilt control to make the beam co-axial. Figure 2.24 shows the

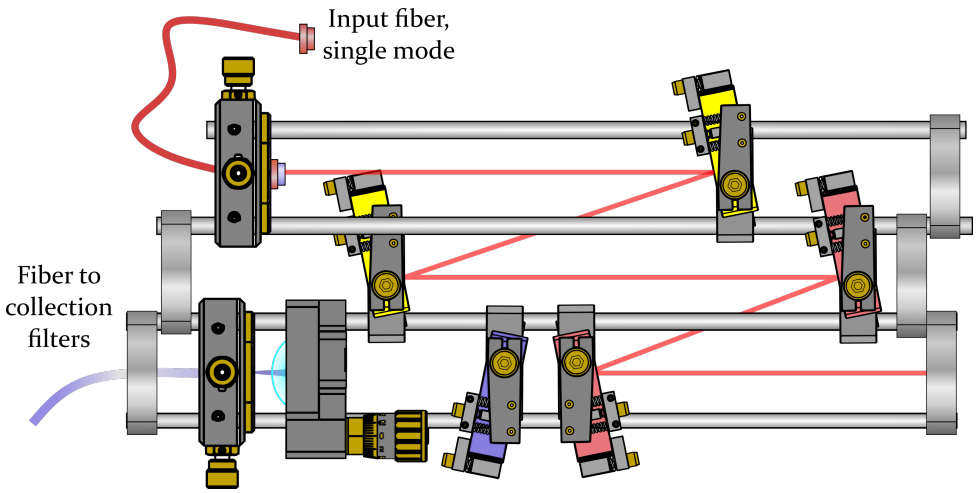

FIGURE 2.22: Schematic representation of a triple-cage design to include two standard mirrors (yellow mounts at the top) which could be used to adjust for the off-axis fiber collimator and align the beam on axis before reaching the VBGs (red red mounts).

design of this part. It has an outer body with SM1 thread for mounting to cage plates, and and inner body with an internal M11×0.5 thread which matches the fiber collimator's external threading. The inner and outer pieces are connected with a 0.2 mm thin section of plastic (marked circle in (c)), which is flexible enough to allow the internal body to pivot but does not allow translation. At the other end there are four threaded holes separated 90° apart. Two of these fit M6 screws, which

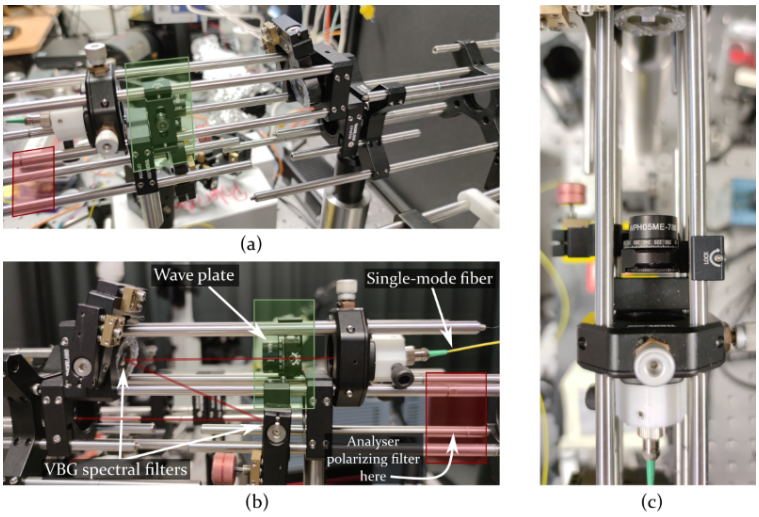

FIGURE 2.23: (a/b) Side view photos of Section A showing the positions of polarization optics with respect to other optical components. The green outline indicates positioning of optics for control over the incident polarization (half and quarter-wave plates). The red outline indicates a region where analysing polarizing filters can be placed (not currently installed in this photo). (c) Top-down view of the half-wave plate in its optic holder, with angle indicator markings visible.

are the tilt adjusters, while the other two fit M3 screws, which lock in springs that tension against the tilt adjusters. The screws and springs are in contact with a 3D printed collar which sits tightly around the fiber collimator housing to help seat the springs and prevent damage to the housing. Threading this adapter into a ThorLabs X/Y mount allows translation of the tilt-adjusted co-axial beam to bring it exactly centred on-axis. Note that ThorLabs offer multi-axis fiber collimators called FiberPorts(see Figure A.2) which offer three-axis tilt and X/Y and Z translation control to an aspheric lens - designed specifically for collimating single-mode fibers. However, the Z-translation for adjusting the lens focus is coupled to the three tilt-axes, and requires moving all three by the same amount to adjust the focus without also affecting tilt. This makes it unbelievably difficult to achieve the correct focus while maintaining the correct angle of incidence with the VBG filter. In comparison, it is trivial to use the 3D printed and X/Y translation mounts to achieve the required angle of incidence on the optical axis (with the dedicated collimator taking care of focus). Incidentally, this tilt adapter is not required when only using one VBG filter. In this case the optic in the first gimbal (VBG) mount is a standard mirror, and so the off-axis beam can corrected through a combination of translation using the X/Y mount and angle of the first mirror. This is achieved by translating the off-axis beam so that it strikes the centre of the mirror where the cage-axis intersects it, then adjusting the mirror angle to send the beam towards the centre of the VBG.

2.3.3 Section B - Optional Extras

The next section along, shown in Figure 2.25, is not actually a sub assembly, but rather a blank segment for any additional optics which might be introduced to the setup (e.g. polarization optics and filters). It also serves as a convenient length of empty space across which alignment can be done (i.e. it is easier to align optics across larger distances). This section uses 30 to 60 mm cage-plate adapters which allow more rods for stability, but also the flexibility to remove some if an additional assembly requires the space.

2.3.4 Section C - Illumination and Camera

The third section, shown in Figures 2.27 and 2.28, contains the camera and a fiber-coupled white light source, and the optics necessary for collimation, focusing, and aligning everything onto the principal axis.

Illumination Source

Sample illumination is provided by an LED source which is focused into a 100 or 200 µm fiber optic cable. Figure 2.26 shows images of the optics assembly containing the source - an XM-L2 white-light LED, collimating lens, focusing lens and fiber.

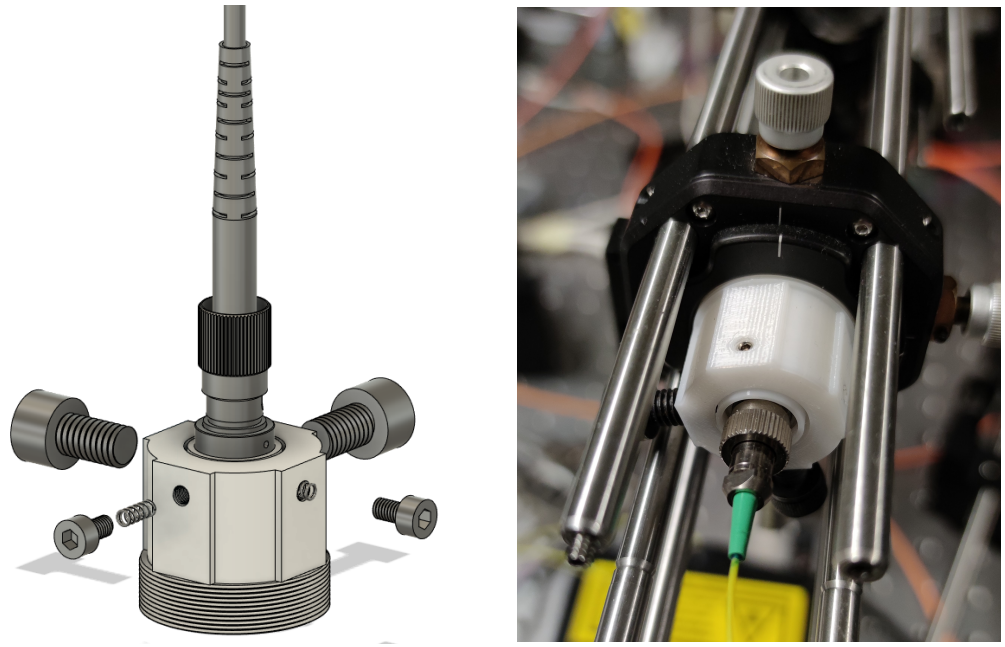

(a) (b)

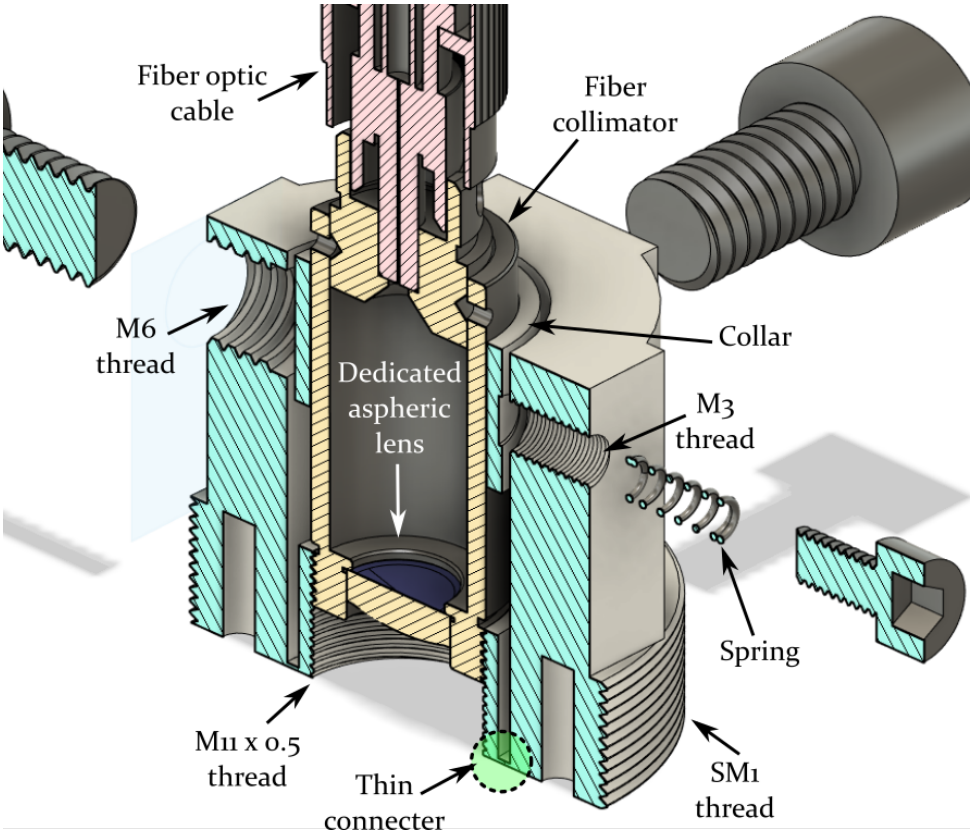

(c)

FIGURE 2.24: (a) CAD drawing, semi-exploded view of the tilt-adapter and fiber-optic cable. (b) Photo of the tilt-adapter as mounted in the 785 nm low-frequency dual-cage. (c) Cross section view of (a) showing the various features discussed in the text.

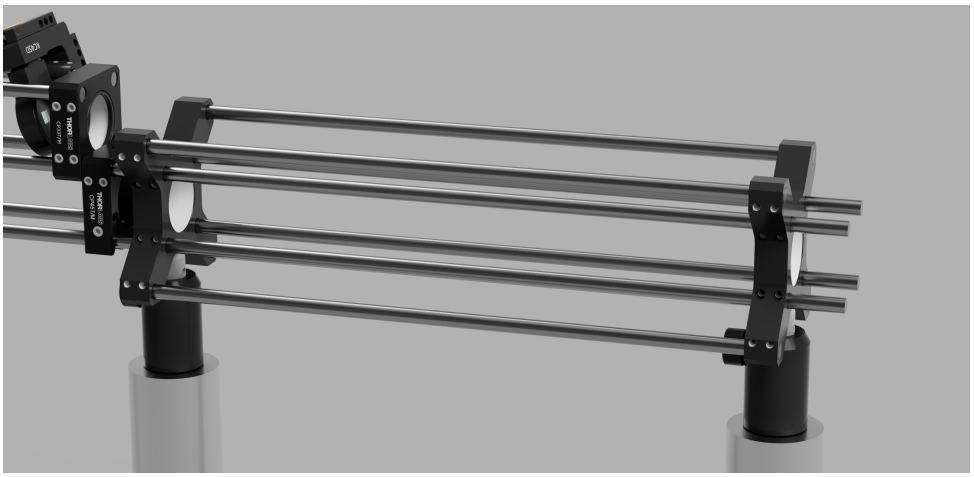

FIGURE 2.25: Section B - a blank canvas for additional optics construction and alignment aid.

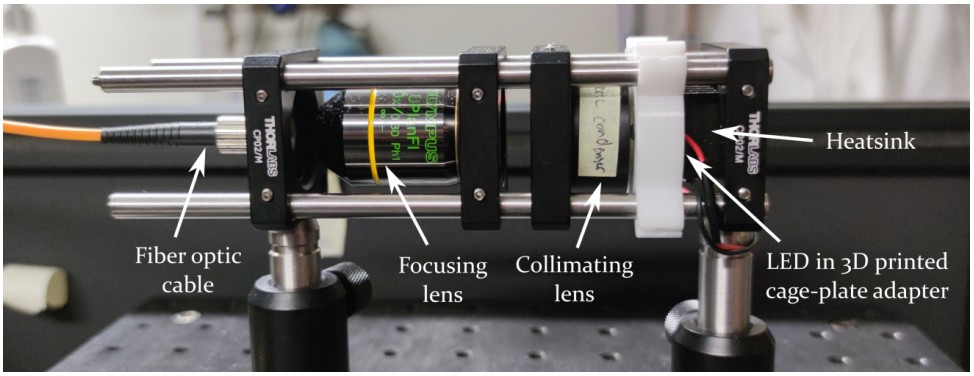

(a)

FIGURE 2.26: Side view of the optics assembly containing the white-light illumination LED source and collimating/focusing elements for fiber collection.

The LED has a heat-sink attached with thermally conductive glue, as these LEDs get quite hot during operation, and can burn out if this heat is not dissipated. This is quite a simple illumination design, as much of the light is not efficiently coupled to the fiber since it originates from a relatively large source. That being said, enough light is collected to clearly illuminate the sample, so the design is sufficient for our needs. It is also able to be run using power from the controller electronics, and can therefore be controlled through the software alongside the other microscope functions.

The collimating lens for the LED source is shown schematically in 2.16 and represented by the grey cylinder below the fiber optic cable in the CAD drawings in Figures 2.27 and 2.28. This lens is slid up and down the cage to adjust the focus, and the ideal "collimation" is actually slightly over-focused, such that the lens produces a focal point in the back focal plane of the microscope objective. This results in light

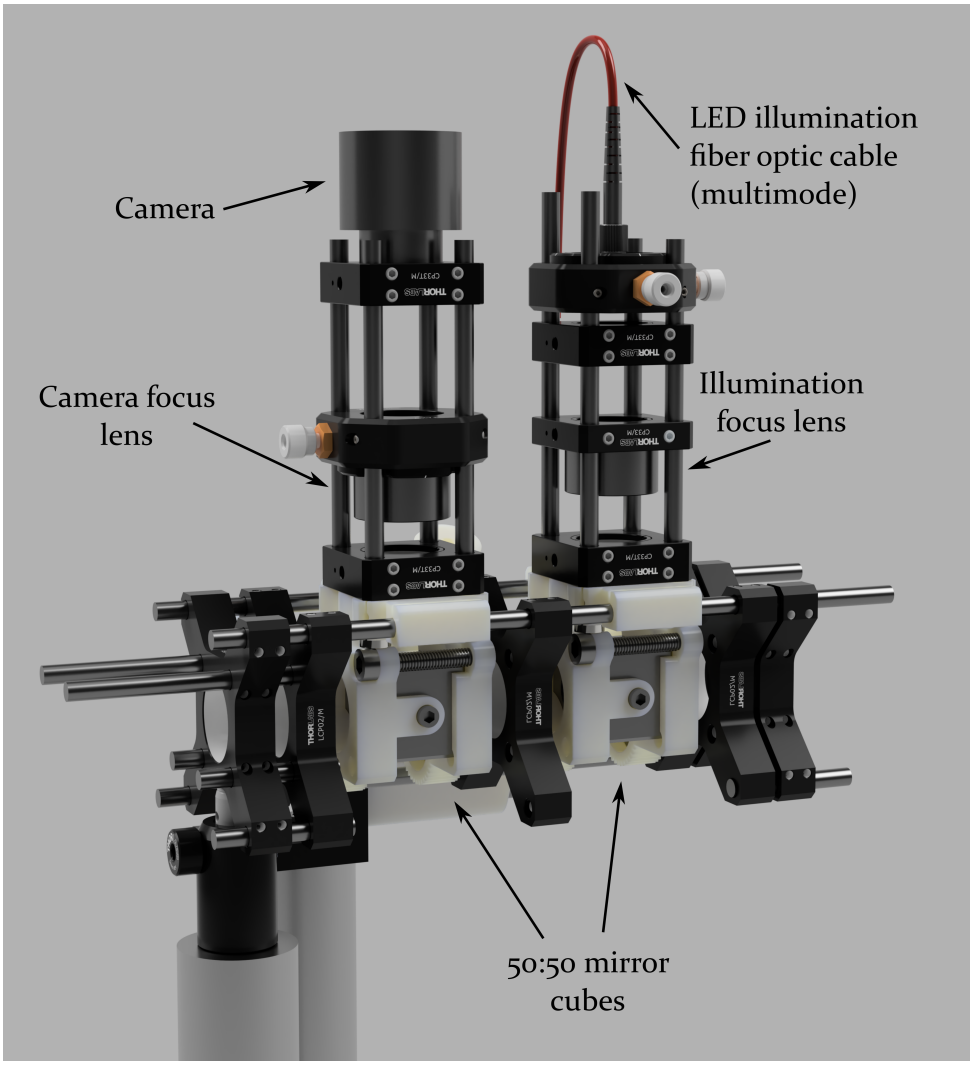

FIGURE 2.27: CAD render of the final (current) version of Section C, front view.

exiting the microscope objective front face collimated, which is known as Köhler illumination, and the even illumination produces excellent quality images with high sample contrast.

Swing Adapters

In order to view the sample, we first need our visible light source to reach it, then we need the reflected light to return on an optical path to the camera. We also want to observe the laser spot with respect to the sample, so that we can line up our map and linescans with regions of interest. This essentially means that we need three optical paths to converge at the sample - with one of them being the path to the camera. Short of having an overly-complicated microscope configuration, the easiest and most efficient way to to do this is with partially-reflective mirrors. In this setup we use two 50:50 mirror cubes which, in the correct geometry, let 50% of

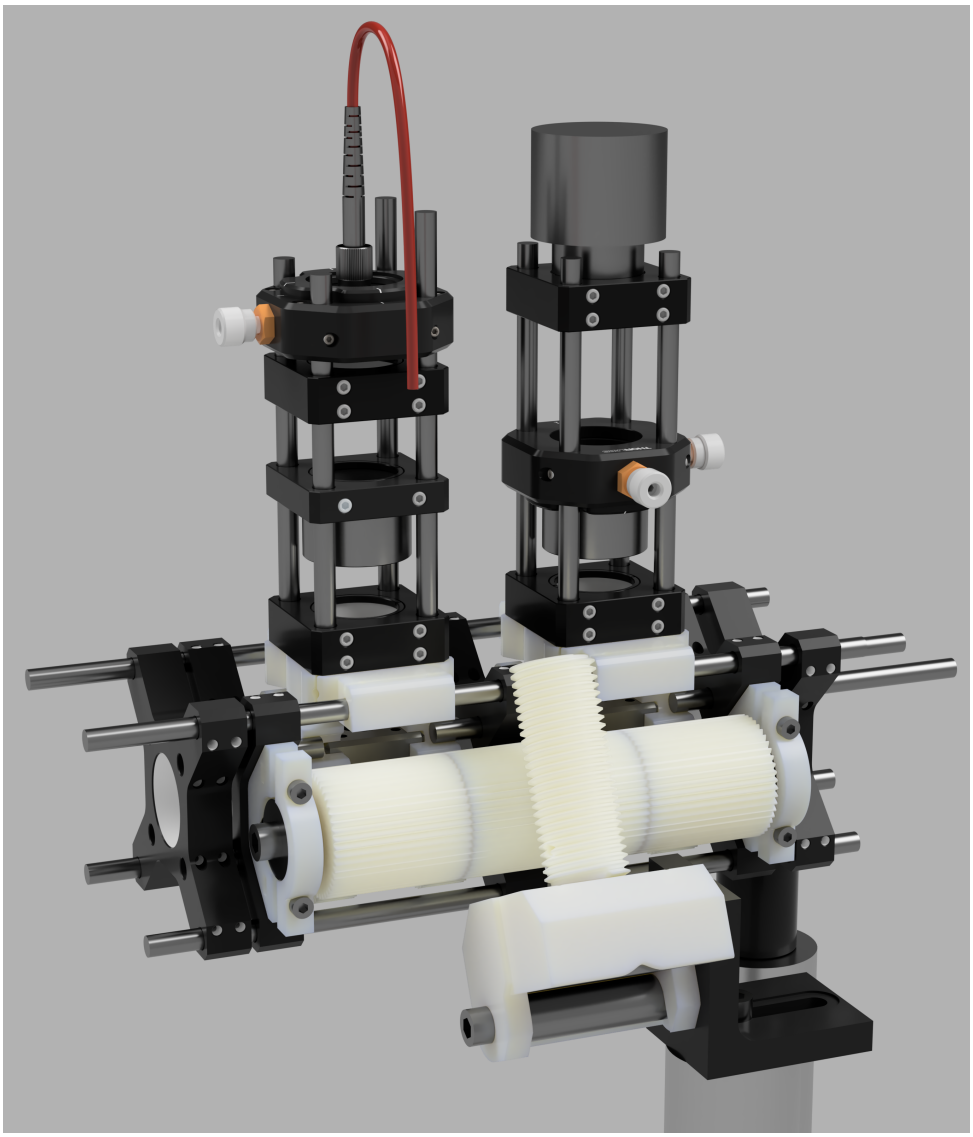

FIGURE 2.28: CAD render of the final (current) version of Section C, back view.

incident light transmit through while 50% is reflected off at a 90° angle. These are positioned at the intersection of the main microscope axis with the light source and camera axes (see Figures 2.16 and 2.31).

However, if we place two 50:50 cubes on the microscope axis and try to collect a Raman spectrum, we will lose 75 % of incident laser light to those reflections before reaching the sample, followed by a loss of 75 % of the Raman scattered light on the way back. Therefore we need some way of moving these mirrors in and out of the optical path to swap between imaging and Raman collection modes. Large microscopes often use a row of mirrors on a linear rail to cycle between different optical paths, but since we've designed the main microscope axis to be the Raman collection axis, we only need the two states - mirrors in and mirrors out.

Several designs were considered, but the most practical solution was to utilise

the cage as a pivot for a rotating mechanism. Figure 2.29 shows an early proof of concept using 3D printed adapters to hold the 50:50 cube between two removable cage-plates. These cubes are designed to be mounted rigidly in a 16 mm cage system via the threaded holes around the cube housing. In this sense they were not designed to be rotated, nor were they designed to fit completely within a 30 mm cage - as Figure 2.29(d) shows the corners of the housing protrude into the region where the cage rods are located. This was initially concerning as it meant that the cage-rods could not pass through the assembly completely, and threatened to compromise stability. However, when mounted close between two supporting cage-plates (shown in Figure 2.31), the relatively short cage rods provided a sufficiently rigid frame for clamping to.

Figure 2.30 shows improvements to this design, and the current working design in the microscope. This design is not perfect, yet so far has worked almost flawlessly and not needed further iteration, such that its place in the final design is simply a consequence of leaving "well enough" alone. Ideas for more robust and future-proofed designs will be mentioned at the end of this section.

In Figure 2.30, the removable cage-plates were replaced with a 3D printed part, which seats a standard ball bearing ($22 \times 8 \times 7$, 608 2RS M8) on the pivot axis to provide smooth motion. A small shim adapter is used to ensure the 6 mm cage rod is firmly centred in the bearing's 8 mm internal diameter. Friction provides a strong hold on the cube by the two adapters, while the mounting support arm is tightened to the cube housing through an M4 screw at the back. In addition, an M6 screw passes through one adapter and threads into the other, holding them together.

The open arch at the top of the adapters on the pivot-axis side is designed to gently snap onto the 6 mm cage rods in the "on-axis" position. When snapped on, there can be a small amount of slack leading to slight variability in the final position. To ensure the mirrors swing into the same position every time, a magnet protrudes down from the orthogonal cage-plates above, engaging with the M6 screw and pulling it into contact (see Figures 2.31(b) and 2.32).

The orthogonal cage-plates, visible in the top of Figures 2.31 and 2.36, are designed to allow cage construction at 90° angles, and are analagous to parts offered by ThorLabs (LCP30, used in next section). These are used here to mount the camera and LED source optics off the optical axis. They are not as sturdy as the ThorLabs metal plates as they cannot be firmly tightened and are not as rigid as metal. However, they are suitable here as they are only supporting weight in the vertical direction, rather than in any overhanging configurations where gravity can cause them to flex away from alignment.

Figure 2.32 shows schematics of the part, which demonstrates a convenient method for tightening 3D printed cage plates and other components to cage rods, without needing additional hardware or thick threads. The cage-rod holes are designed to be deliberately undersized, between 5.8 and 5.9 mm in diameter, so that initially the 6 mm cage rods will not fit. The oval sockets indicated in Figure 2.32(a)

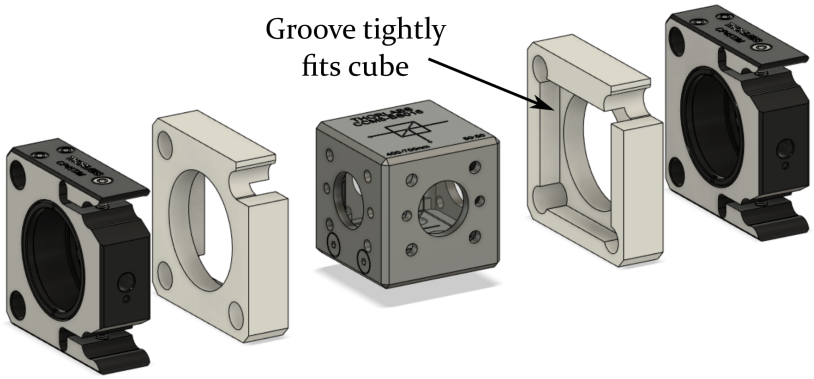

(a)

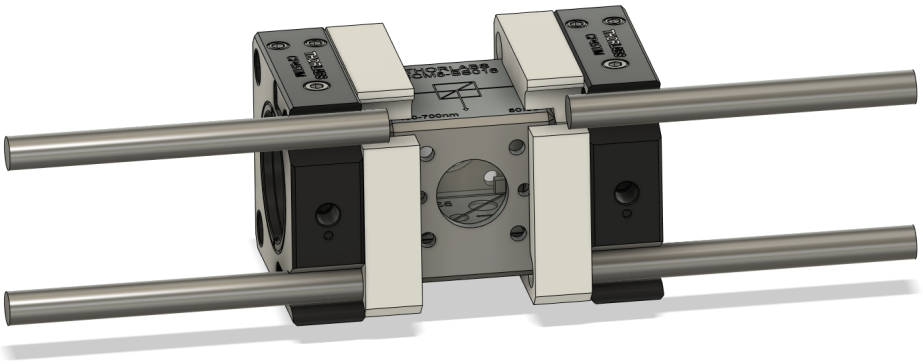

(b)

(c)

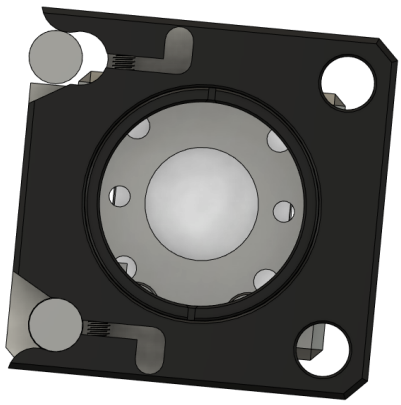

(d)

FIGURE 2.29: CAD drawings of a proof-of-concept swing adapter for the 50:50 mirror cubes: (a) exploded view, (b) attached to cage-rods, (c) render with the mirrors rotated off-axis, (d) side-view showing how the housing of the 50:50 cubes occlude the cage-rod holes.

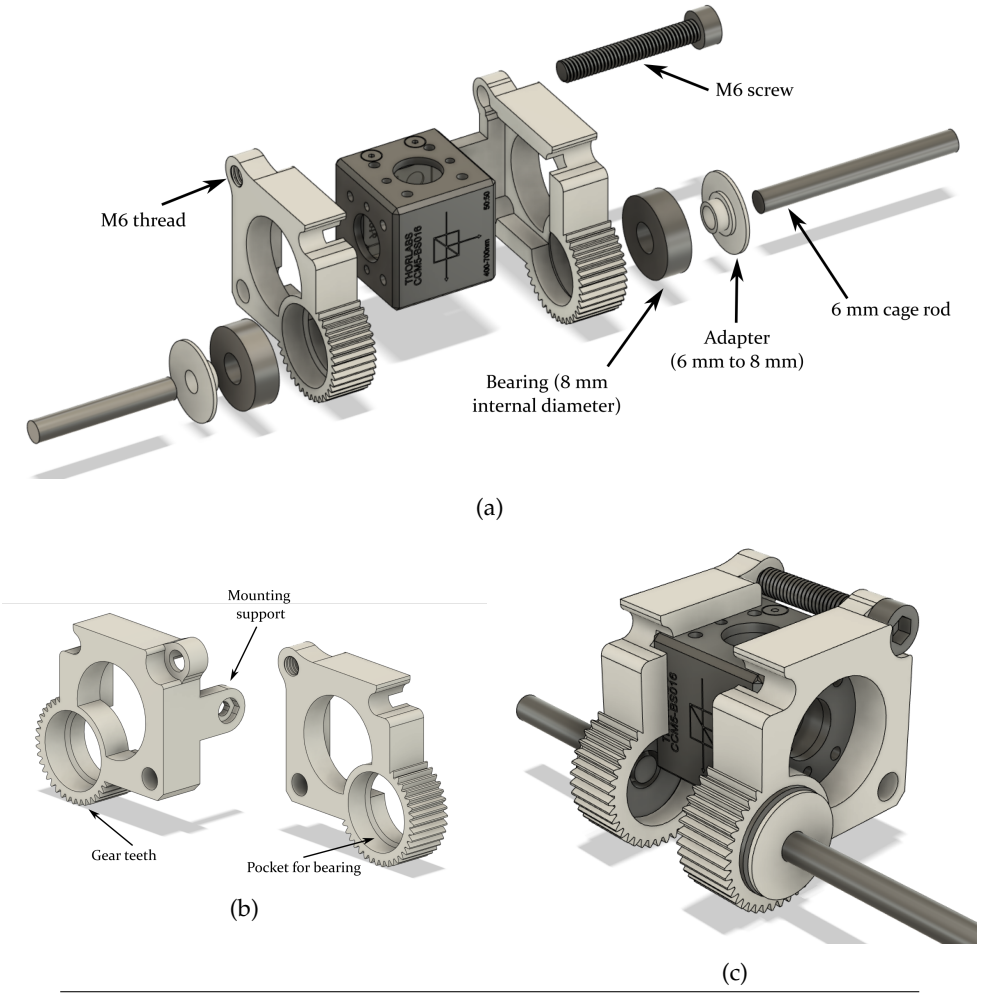

FIGURE 2.30: CAD drawings of the current swing-adapter version. (a) Exploded view and labels of each part. (b) Individual views of the two half-adapters, showing the bearing pockets. (c) Assembled view of (a).

/(c) are designed to have 2-3 mm screws (like the grub screws used for tightening ThorLabs cage plates) screwed in to the plastic in a self-threading fashion. As the screws are twisted they bite the plastic and pull themselves in towards the cage rod hole, which forces the walls of the hole apart which increases its diameter - eventually allowing cage rods to be freely inserted. Then, once the desired position is achieved, the screws can be unscrewed which causes the walls to clamp down on the rod, applying tension as a result of strain in the part. The initial hole diameter can be decreased to increase the tension on the rods, and can result in a very strong grip.

Currently, the orthogonal adapters also provide a convenient way of locating the magnet at the correct height (see Figure 2.32(b)/(c)). These adapters could be replaced by metal ThorLabs parts following a redesign of the magnet holder to be independent of the orthogonal adapter in a future design of the swing adapters.

While manual operation of the rotating mirrors works well enough, the ability

(a)

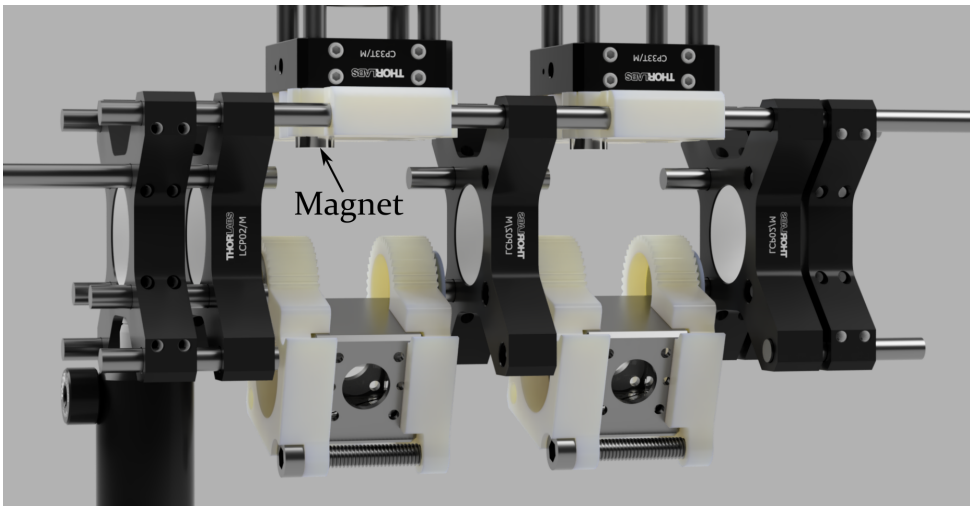

(b)

FIGURE 2.31: (a) On-axis and (b) off-axis CAD renders of the swing-adapters and 50:50 cubes, as currently installed in the microscope. The position of one of the locating magnets is marked in (b).

to automate this action improves workflow and (in combination with the stage controls) allows one to remotely operate the microscope - which is particularly useful for setting up long scans and maps. This is the purpose of the geared teeth on the cube adapters visible in Figure 2.30. Before we continue I'll briefly speak to the design motivations of these 3D printed parts.

There are certain limitations on what shapes and geometries can and cannot be 3D printed as a consequence of the layer-by-layer, bottom-up fabrication process. This is analagous to the limitations of many metal machining techniques which, for example, might struggle with sharp internal corners, or with cutting material from under and around parts. For FDM 3D printing, overhanging parts are the biggest problem, and while there are work-arounds avoiding them entirely (if possible) is the best strategy. On the other hand, 3D printing is well-suited to intricate parts

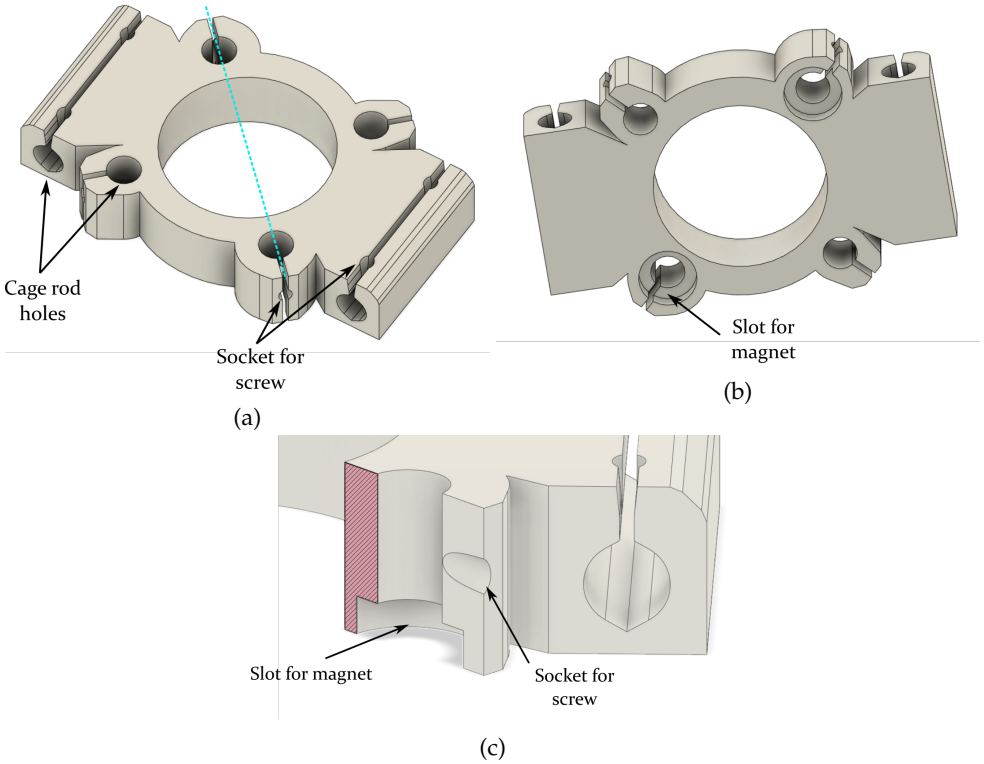

FIGURE 2.32: CAD drawings of the orthogonal cage-plate design from (a) above, (b) below, and (c) cross section through the blue dashed line in (a). Note the slot for a magnet in (b) and (c), and the design of the rod holes which allow tight clamping to the rods using strain in the parts (discussed in text).

with lots of detail and complex structures, which allows a great deal of functionality to be built into single parts. As such, minimising the overhang issues whilst maximising utility have been the driving design principles for these parts.

Rather than printing a single-piece adapter for each 50:50 cube, it was printed as two parts to avoid undesirable overhangs around features with tight tolerances. For instance, the bearing pockets need to be smooth and tightly fitting to prevent slack and wobble when rotating (which would result in alignment issues), and a single-piece design required support structures which would have compromised on this fit.

Using these adapters results in two independently rotating cubes, which in this case need to rotate together. In addition, we want each cube to have the same forces applied to each half-adapter, since applying force to only one gear on one side may apply a torque that twists the assembly slightly out of alignment. Therefore, I decided to use a long gear ("geared barrel") at the back of the assembly to link all four gears and drive them in unison. This geared barrel is then driven by a stepper motor and helical worm drive. Figures 2.33 and 2.34 shows this geared barrel in the assembly.

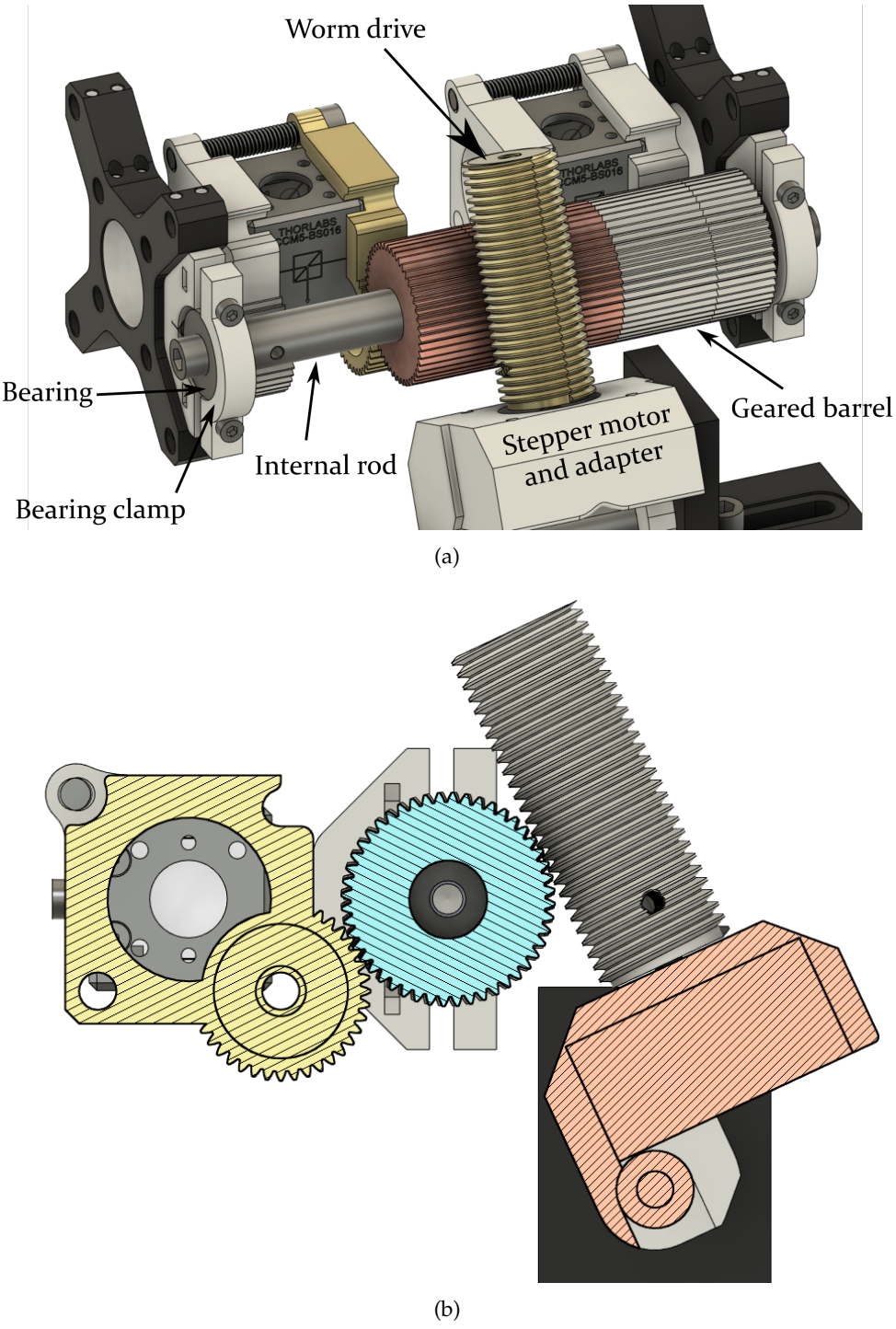

FIGURE 2.33: CAD drawings of the gear-barrel and motor assembly. Note the colours are simply to provide contrast between parts, and the section of geared-barrel on the left of (a) is hidden to show the internal rod. (b) Cross section through the swing-adapter (yellow) and geared barrel, showing gear meshing between the parts.

The geared barrel is printed as a single piece, with a helical gear section in the centre to match the worm drive on the stepper motor (see Figure 2.34(b)). The barrel sits to the side of the rotating adapters (Figure 2.33), fixed to the optical framework

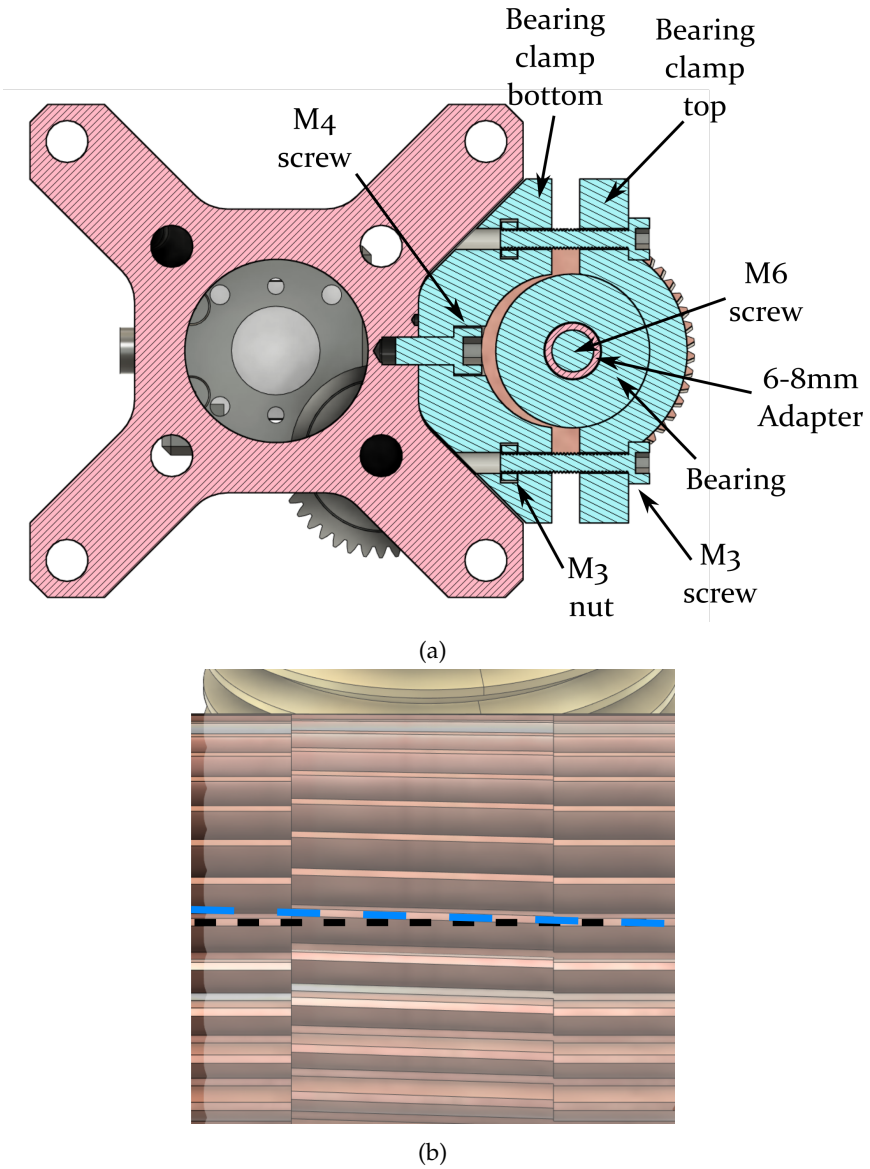

FIGURE 2.34: (a) Cross sectional view of the bearing clamp holding the geared barrel assembly to the structural 30-60 cage plate adapters of Section C. The cross section reveals the M3 nuts and screws used for tightening the clamp and adjusting the gear separation distance, and the M4 screw mounting the clamp to the cage. Also visible is the 6-8 mm 3D printed adapter or shim used to centre the M6 screw in the bearing. (b) Close-up view of the central helical gear section of the barrel - the dotted lines show the helical section is angled with respect to either side, which is matched to the angle of the thread on the worm screw.

through bearing clamps attached to cage-plates. This barrel has an internal shaft (12.8 mm diameter) which tightly fits a ThorLabs half-inch optical post. The shaft runs the full length of the barrel, fixed to the inner race of a bearing at each end by an M6 screw. Another 3D printed 6-8 mm adapter ensures the shaft and screw are centred in the bearings. A cross-section through the adapter gear and barrel in in Figure 2.33(b) shows how the teeth of each gear are aligned.

The bearing clamps are printed as two pieces, and Figure 2.34(a) shows a cross-section through them in the assembled state. The bottom clamp is mounted firmly to the cage-plate via an M4 screw, then the bearing is seated in the curved face and clamped down on with the top half. There are slots in the side of the bottom clamp to fit M3 nuts, which allows an M3 screw to be passed through the top clamp and tightened down. Note in previous parts (tilt-adapter) I have 3D printed threads into the part, which is useful when using M4 and M6 screws with deep threads and small loads. For smaller screws with shallower threads, over-tightening can strip the threading from the plastic, and therefore it is sometimes better to insert a nut (and sometimes washer), which is pulled into the plastic wall upon tightening to provides a strong hold. Note that in the schematic in Figure 2.34(a) the bottom clamp curvature is slightly undersized compared to the bearing. This allows it to act as a spring when the top clamp is tightened, which allows fine-tuning of the gear separation distance between the barrel and cube adapters by tightening or loosening the M3 screws in unison. Once again, these clamps are not perfect, but have worked well enough at this time that they have not been optimised further.

The position and angle of the stepper motor can be adjusted through the mounting L-bracket in Figure 2.35(a), while (b) and (c) show the stepper motor and 3D printed adapter. The stepper motor is fixed to the adapter through the M3 mounting holes, and an optical post is inserted into the marked channel to provide structural support and an M6 thread, which allows tightening to the L bracket in (a) at a set angle. This L-bracket is mounted to a 1.5 inch optical post, which is clamped to the laser table with a fork which allows free adjustment of its position (visible in 2.17).

Figures 2.27 and 2.28 show full CAD renders of the final section design, and Figure 2.36 shows actual photos of the setup. A final feature not shown in the CAD but visible in the photos is an optical post which attaches a cage-plate at the unsupported end of Section C to a breadboard mounted above the microscope (see Figure A.5 to see position of breadboard). The purpose of the post is to provide extra support, which cannot run vertically downward since the stage is directly below (see Figure A.4).

Future Improvements

While the current rotating cube design works well enough, it requires the geared barrel to swing both cubes simultaneously, which adds complexity and moving parts that may wear over time. In addition, only one side of the two-part adapter is currently secured by the M6 screw, meaning the other side can flex outwards if the screw is overtightened. A simple upgrade to ensure the adapters are held together well would be to fit another screw on the other side, just above the gear section.

For a more comprehensive upgrade, the 50:50 mirror can actually be removed from the housing via the four screws at the base. A new housing design shown in

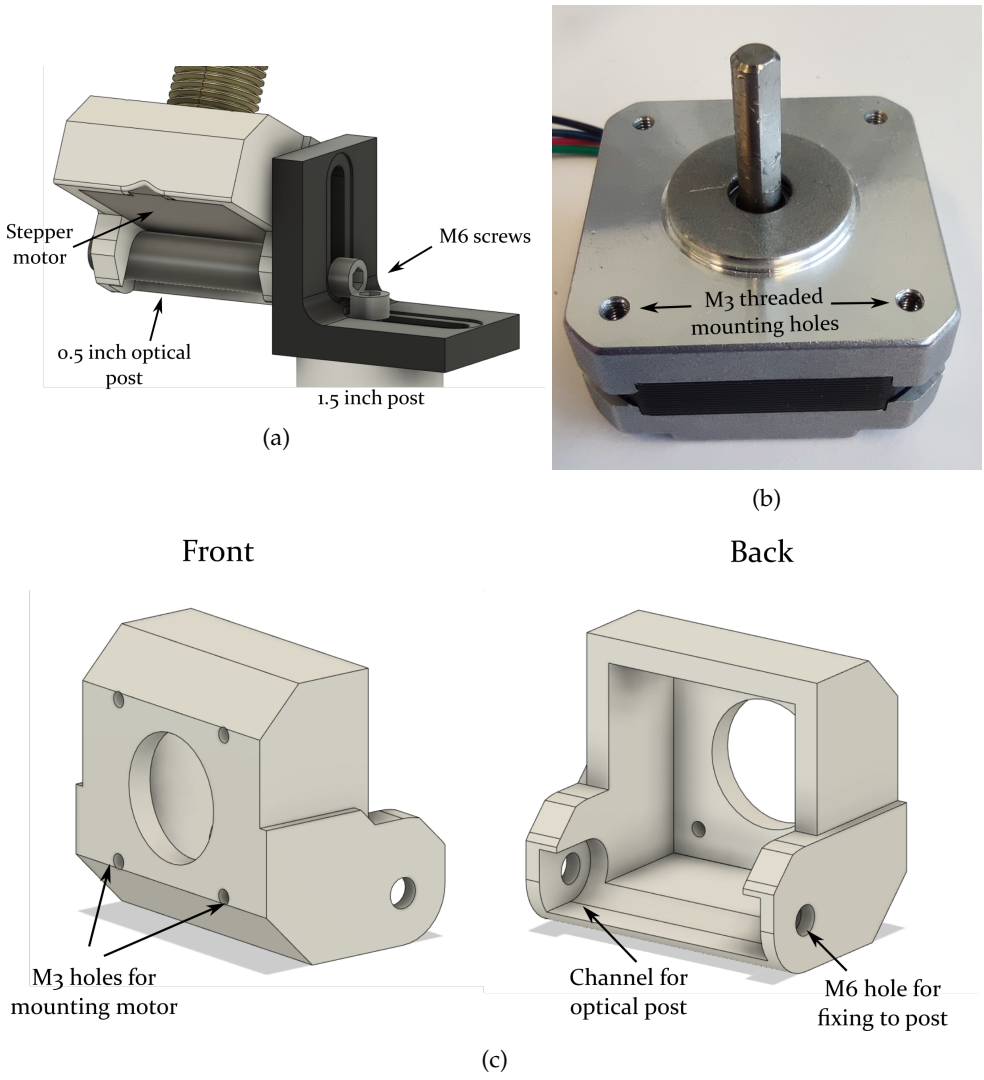

FIGURE 2.35: (a) CAD drawing of the swing-adapter stepper motor assembly, showing the mounting L-bracket and optical post supports (half-inch brace and 1.5 inch mounting post). (b) Photo of one of the stepper motors, showing the M3 threaded holes used for mounting to the 3D printed adapters. (c) Front and back views of the 3D printed stepper motor adapter in (a).

Figure 2.37, does not clip into the cage-rod section, allowing more rods to be inserted and provide more structural support to the section. We have also recently acquired a new 3D printer, which uses a UV-cured resin technology and overcomes many of the overhang and support issued faced by FDM printers. It should therefore be possible to print these adapters as a single-piece, which means the geared barrel can be removed and the part can be driven directly by the worm-screw. Even without the resin printer, it would still be possible to print the adapters in two-halves, then assemble with screws afterwards to achieve the same result.

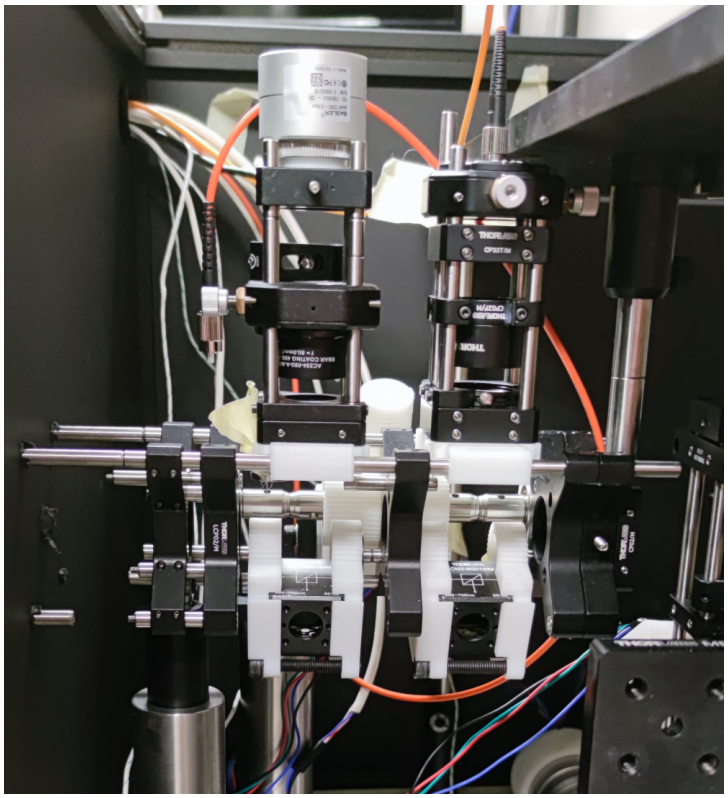

(a)

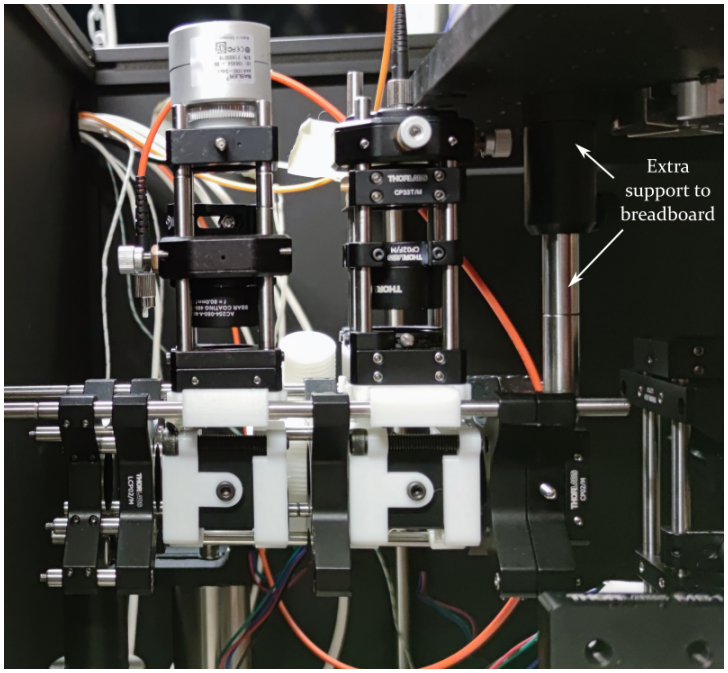

(b)

FIGURE 2.36: Photos of the final assembly in its current state on the microscope, with mirrors in the off-axis (a) and on-axis (b) positions. Note the surrounding black box is for thermal management (discussed later) and the optical post on the right connects to a raised breadboard for extra support (see Figure A.5(a) for breadboard image)

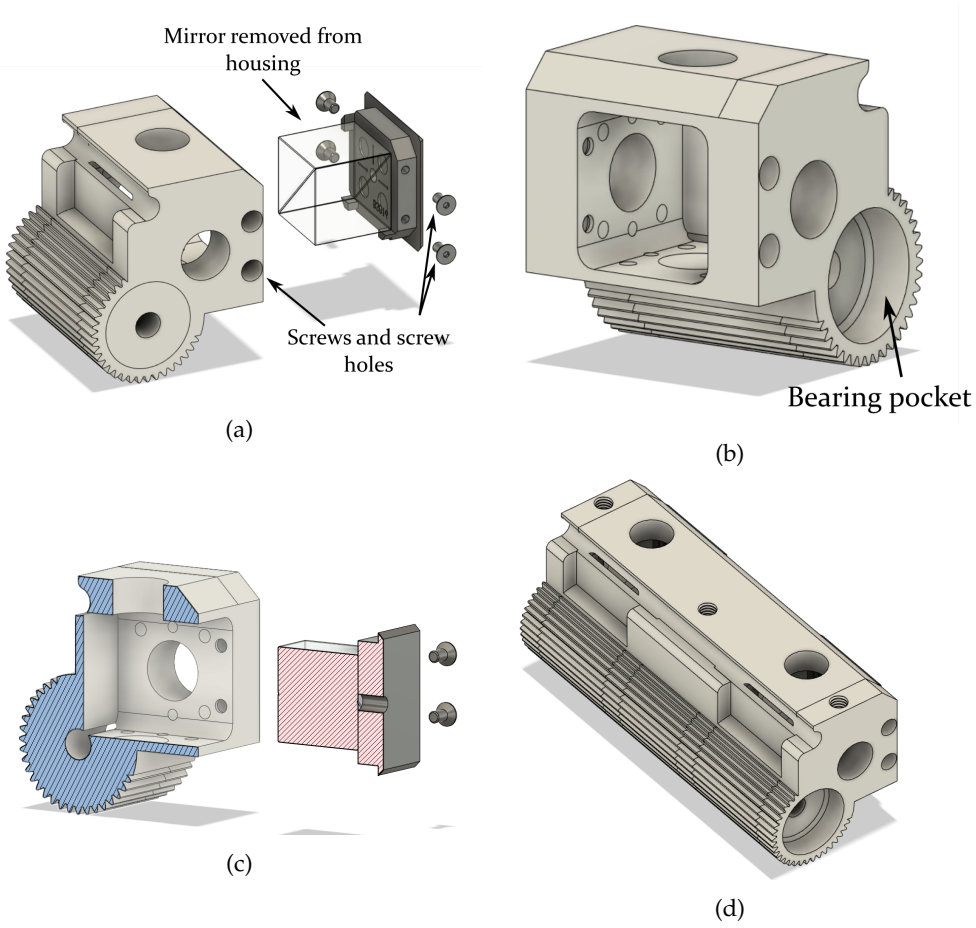

FIGURE 2.37: (a)/(b) Single-piece 50:50 mirror adapter design, for the mirror removed from its cube housing. (c) Cross section of (a) showing the internal shape of the adapter. (d) A large, two-mirror single-piece adapter. Note these designs will require printing on a resin-based 3D printer, or separation into two or more parts to mitigate overhang issues.

2.3.5 Section D - Stage and Focusing Optics

Structural Support

The final section, shown in Figure 2.38 and 2.39, contains the motorised stage and the optics and optomechanical components required to reflect the beam 90° into the upright configuration. This section had the most issues with performance, mainly due to structural instabilities.

As it turns out, our main source of error when performing long collections is due to component drift effects as a result of thermal expansion. The movement of a sample was recorded though optical imaging at 100× magnification over 12-48 hour periods, and it was found that the position of the sample would drift, stabilise, then drift again at intervals which coincided with the on and off cycling of the room's climate control unit - as monitored by strategically placed thermocouples (see Figure 2.41). The distances covered by these drifts at the sample were on the order of a

few microns - imperceptible to the naked eye but large enough to cause significant problems with sample positioning (see Figure 2.40). In general, more stable configurations resulted in drifts of smaller magnitudes, with more predictable directionality. In addition, less stable configurations tended to exhibit a degree of hysteresis, where the structure would not relax and expand back to the same positions as temperatures fluctuated, making it more difficult to identify the cause and correct for it.

With the current most stable setup, I was able to determine that the "sample" drift was mainly in the direction of the connecting support (i.e. perpendicular to the breadboard surface), which corresponds to an unbalanced thermal expansion of the optics assembly in this direction (see Figure 2.40(b)). For example, connecting this vertical Section D to the horizontal Section C using cage rods through the right-angle adapter (which can be seen at the top of Figures 2.38 and 2.43) adds an additional amount of drift in the direction of the Section C principal axis as well (perpendicular to the main drift). This is one of the reasons why Sections C and D are not physically joined in the final design. The other reason is that, when attached to Section C, the

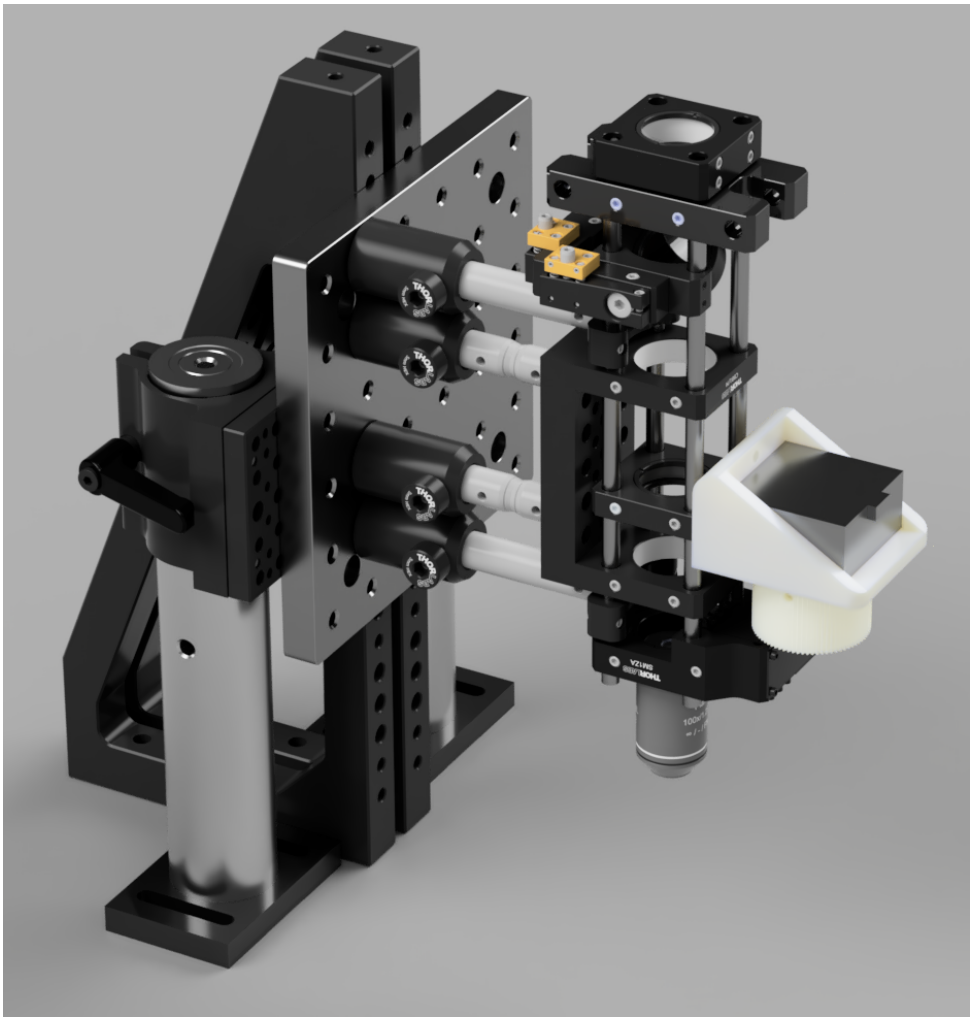

FIGURE 2.38: CAD render of Section D from the front, showing the support arm structure (left) and cage optics (right). The stage omitted.

forces applied by the motor during rotation of the 50:50 cubes in Section C flexes the cage enough to create a visible shift of the "sample" of a few microns (actually Section D relative to the sample), which makes lining up for scans at specific points on the sample difficult. The right-angle adapter is kept in place in Section D for alignment purposes - cage rods are passed through this part and joint to the 60 mm cage of Section C, then removed once Section D is fixed to the structural support.

The purpose of the black box surrounding Sections C and D in some of these images is to dampen and minimise the effects of room-temperature fluctuations. The full box can be seen in Figure A.5, and Figure 2.41 showing temperature measurements from inside and outside the box. Clearly, our lab needs to invest in better climate control.

In the design of the support structure (indicated in Figure 2.39), each large right-angle bracket has excellent stability against motion in their in-plane direction, but poor stability in the out-of-plane direction, even when placed on either side of a

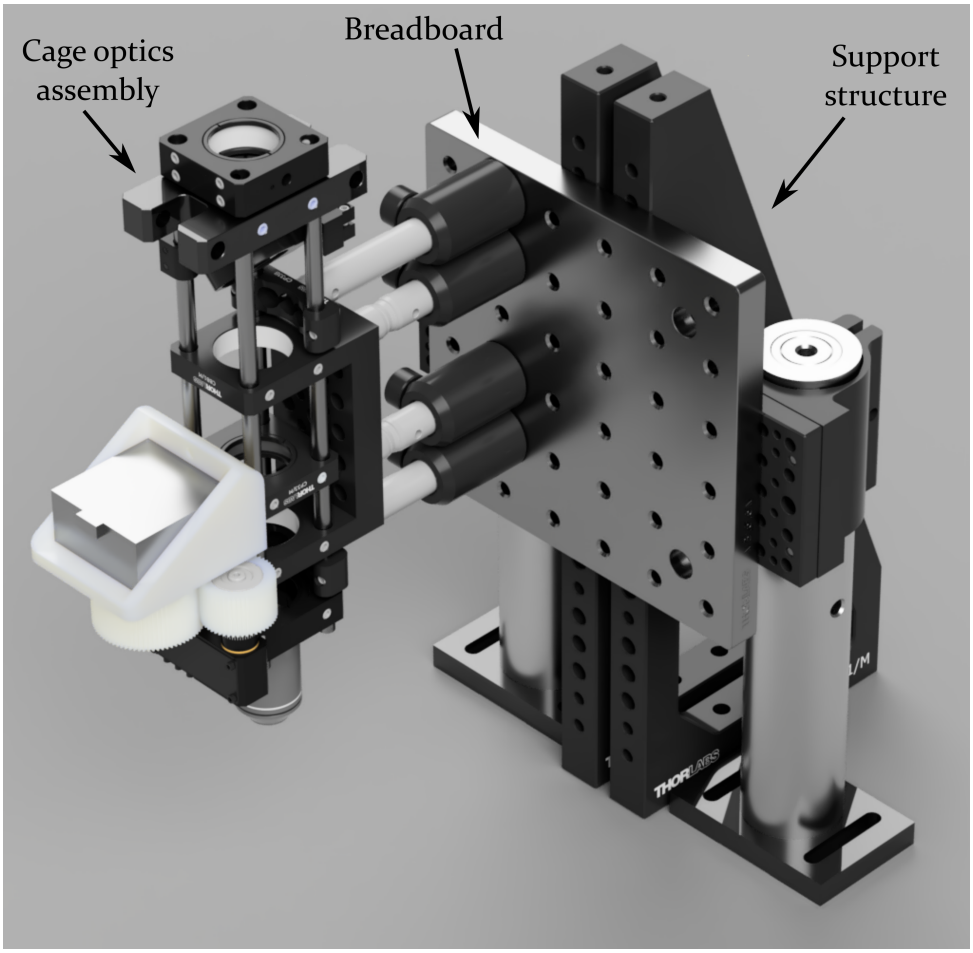

FIGURE 2.39: CAD render of Section D from the back, showing the support arm structure (right) and cage optics (left). The stage omitted for clarity.

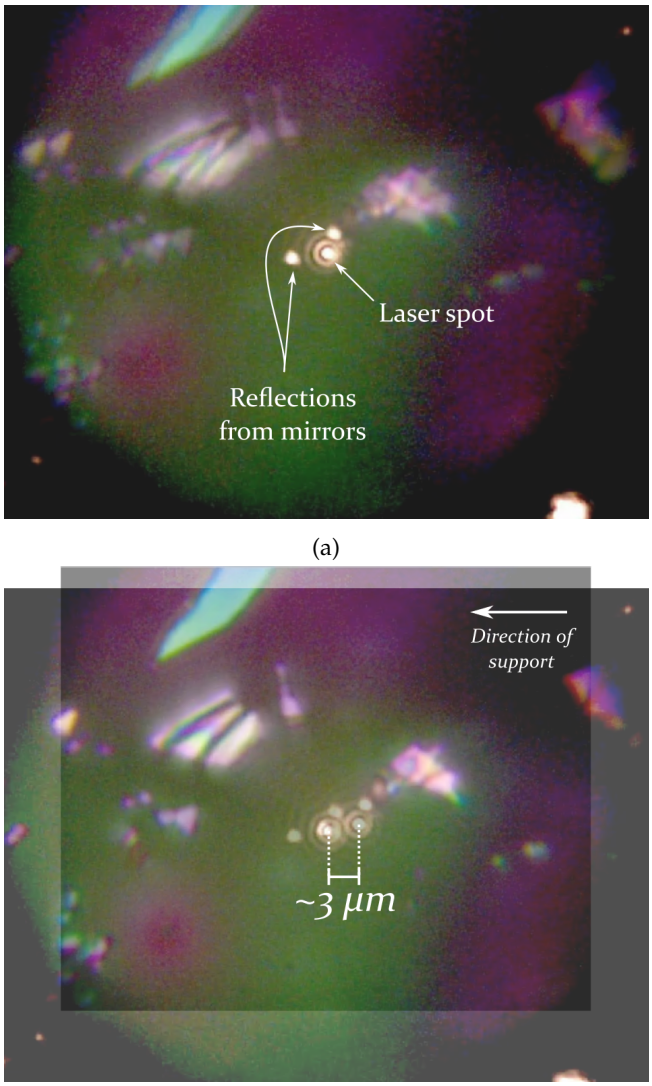

FIGURE 2.40: Examples of the "sample" drift associated with thermal fluctuations. (a) and (b) contain the same images, taken from a recording at two points of where the drift between them is the largest for any two points in the recording. These have been made semi-transparent and overlaid. (a) Shows the images with the camera as the stationary reference frame (i.e. as the camera recorded it). The doubling of all the flakes represents the different positions at drift maxima. (b) Shows the images realigned to the flakes, which makes the sample the stationary reference frame, and highlights the motion of the spot. The maximum drift in this case was approximately 3 µm.

solid breadboard as shown in Figure 2.42(a). A single post, as shown in (b), has more or less the same stability in all directions, but in general does not provide satisfactory stability for the mounted optics. Flexion in the rod (seen as movement at the sample) becomes significant due to the height at which the optics are mounted, and the relatively small base of contact to the table. In addition, the rod is susceptible to resonating with vibrations - such as those produced by the focusing motor. Two posts separated far apart provide good stability in the direction connecting them, but

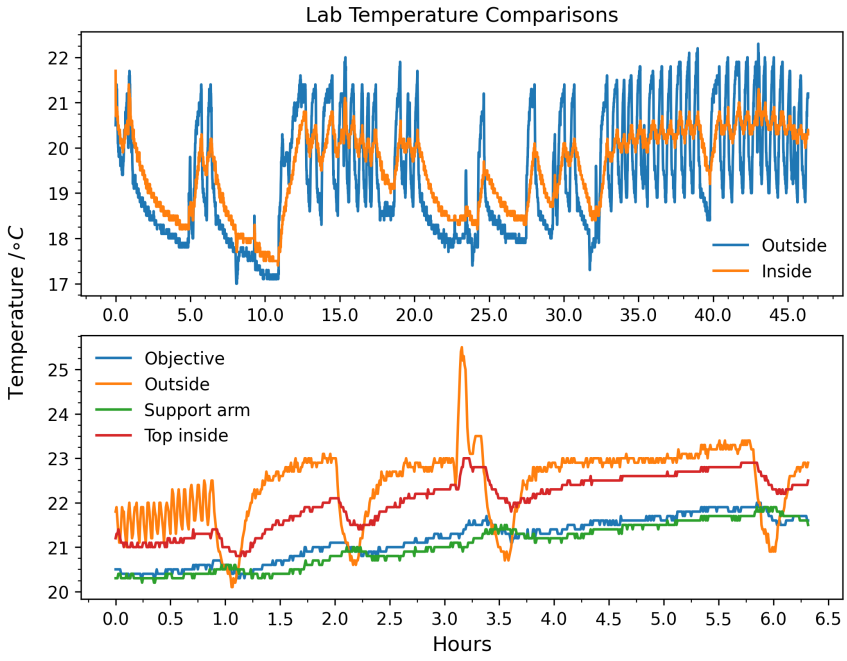

FIGURE 2.41: Thermocouple readings around the Raman microscope comparing temperature swings over time as a result of the cycling climate control system, for inside and outside the insulating box. The legend in each graph indicates the position of the thermocouple giving the reading.

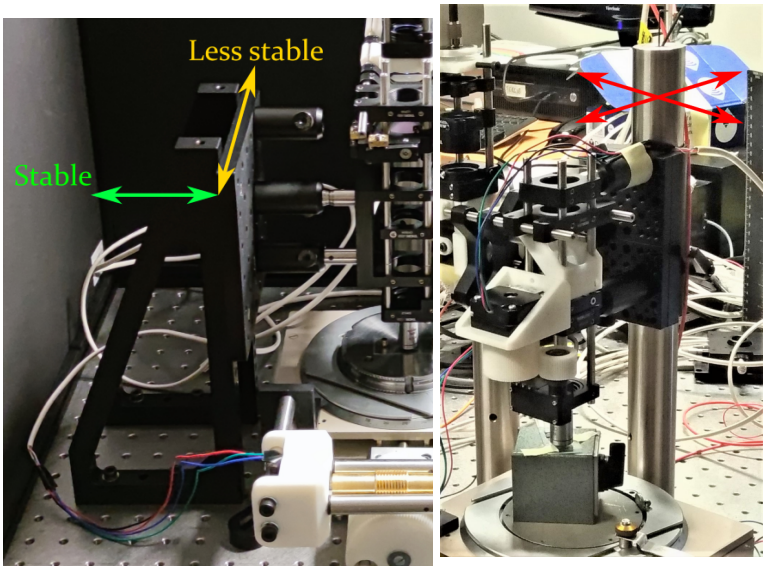

(a) (b)

FIGURE 2.42: (a) Shows a photo of a support bracket prototype, which is more stable in the left-right direction than the up-down direction (with respect to the page). (b) Shows a single-post mount, which is generally unstable (relative to the final design) in all directions.

not so much perpendicular to that direction. The combination of right-angle brackets in one direction and 1.5 inch steel posts spanning the perpendicular direction, all firmly fixed to a breadboard gave the most stable configuration from available parts. The breadboard then provides a flat base off which to mount the optics.

The cage construction for this section of vertical optics is relatively simple. Figure 2.43 shows a profile view of the parts used. Working from the top down following the numbering, we have:

1. A thick cage-plate to hold the four rods firmly in position while aligning the rest of the hardware. Possibly redundant in the final design, but is kept in place to provide extra rigidity to the top section of the cage.
2. The 30-60 mm cage-plate adapter (LCP30) from ThorLabs. During assembly, rods are inserted through this plate to Section C, in order optimise height for the Section D cage.
3. A gimbal mount holds a 1-inch protected aluminium coated mirror, tilted at 45° to turn the beam towards the stage. Aluminium mirrors give good reflective across the visible and near infrared spectral regions, but other types of mirrors can be used (such as broadband dielectrics with high reflectivities).
4. The CP338B is a compact mounting bracket, designed to fit only two cage rods. These have a counterbored hole for using an M4 screw to mount the bracket to an optical post and provide a rigid mount to the support structure.
5. The U-bracket from ThorLabs is another useful structural element. The single piece design establishes a rigid support structure for cage components between the two cage-plates. The connecting body contains a series of M6 and M4 tapped holes. The optical posts are firmly tightened to the M6 holes using M6 grub screws.
6. A stepper motor is mounted here, adapted to a standard cage plate so its height can be adjusted and locked in to the cage system. The adapter is shown in Figure 2.44 and discussed below.
7. Next is another CP338B compact bracket. The compact design prevents interference with the Z-translation mount on the other side.
8. The Z-translation mount holds the microscope objective and allows fine translation along the cage optical axis, which provides focusing control. A 3D printed gear adapter allows motorised control through the stepper motor.

The CP338B compact brackets are useful here for two reasons. Firstly, their compact design allows them to be positioned close to other cage components with minimal interference, as is the case shown in Figure 2.43(7/8), which enables them to be positioned near the ends of the cage for better support.

Secondly, the M4 hole allows them to be firmly tightened to the stainless steel optical posts. Standard cage plates are machined from aluminium, and it is possible to strip the (relatively soft) internal threading upon tightening. Therefore, these mounts can be firmly tightened to their steel supports without fear of damaging the components.

The stepper-motor adapter for the focusing motor is slightly different to the other mounts. It has a relatively low-profile shape to prevent interference with other parts. The mounting holes for the stepper motor are in fact short slots, which allows 3 mm of translational control over the final position of the motor, and is used to fine-tune

FIGURE 2.43: A side view of the cage optics assembly used in Section D. The numbers are referenced in the text for describing the function of each part.

the distance between the drive-gear on the motor and the gear adapter on the Z-translation mount. The gear adapter on the Z mount slots over the original thumb screw, and is held in place by friction. The relatively small forces applied by the motor do not require any additional fixing of the adapter to the thumbscrew.

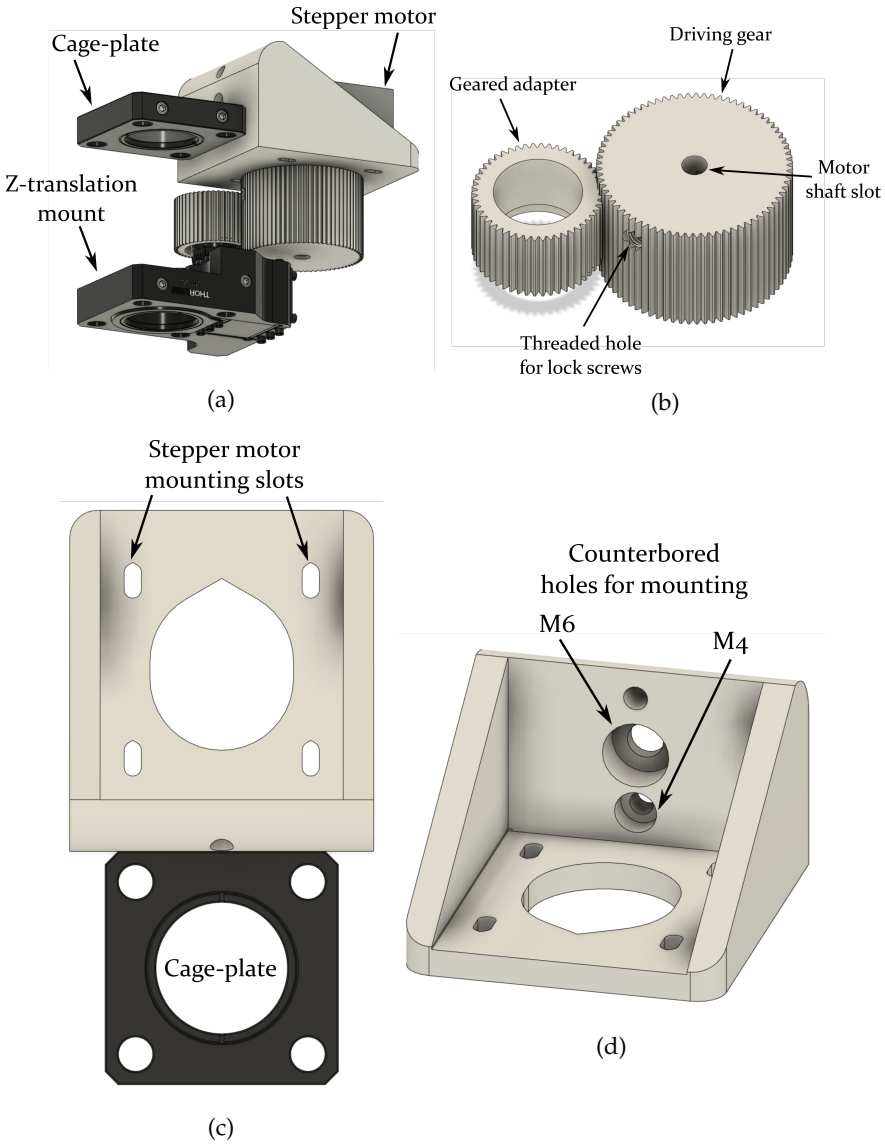

FIGURE 2.44: CAD drawings of the focus motor adapter. (a) Adapter assembly as used in the cage. (b) Adapter and mounting slots for the stepper motor. (c) Adapter and mounting holes for attaching to the cage plate. (d) The driving gear on the motor shaft, and gear adapter which slots over the Z-translation thumbscrew.

Motorised Stage

The high-precision stage (Figure 2.15) is capable of accurately positioning samples across tens of milli-meters, with measurable precision down to a single micro-meter using the vernier scales. In addition, the large diameter lead screw barrels (knobs) allow smooth motion in sub-micron steps, despite not being readable on the scales.

Given that our flake and CVD samples are tens to hundreds of microns across and the diffraction limit of light prevents spatial resolution below $\sim 350\,\text{nm}$, the range and resolution of this stage is ideal for our purposes.

Several designs were considered for mounting stepper motors to the lead screws to motorise the axes, and in the end I decided on a worm drive mechanism shown in Figures 2.45 and 2.47. The worm-screw sits just out of contact with the worm-gear, which is a 3D printed helical gear that slots over the stock lead-screw barrel, with a hole in the centre for fixing in place with a screw. The separation between the

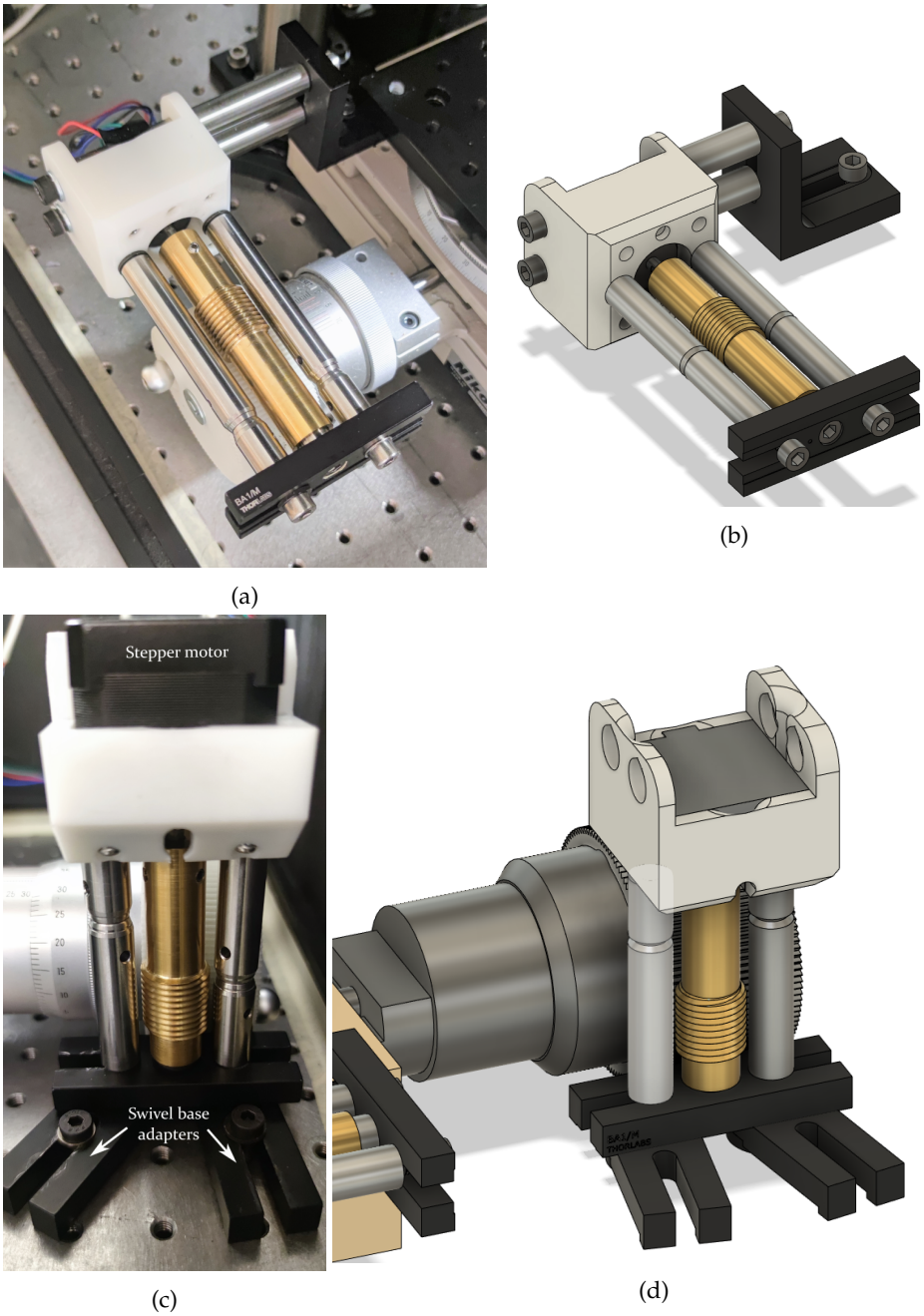

FIGURE 2.45: Photos and CAD drawings of the stepper motor assemblies for the stage Y and X control (a)/(b) and (c)/(d) respectively.

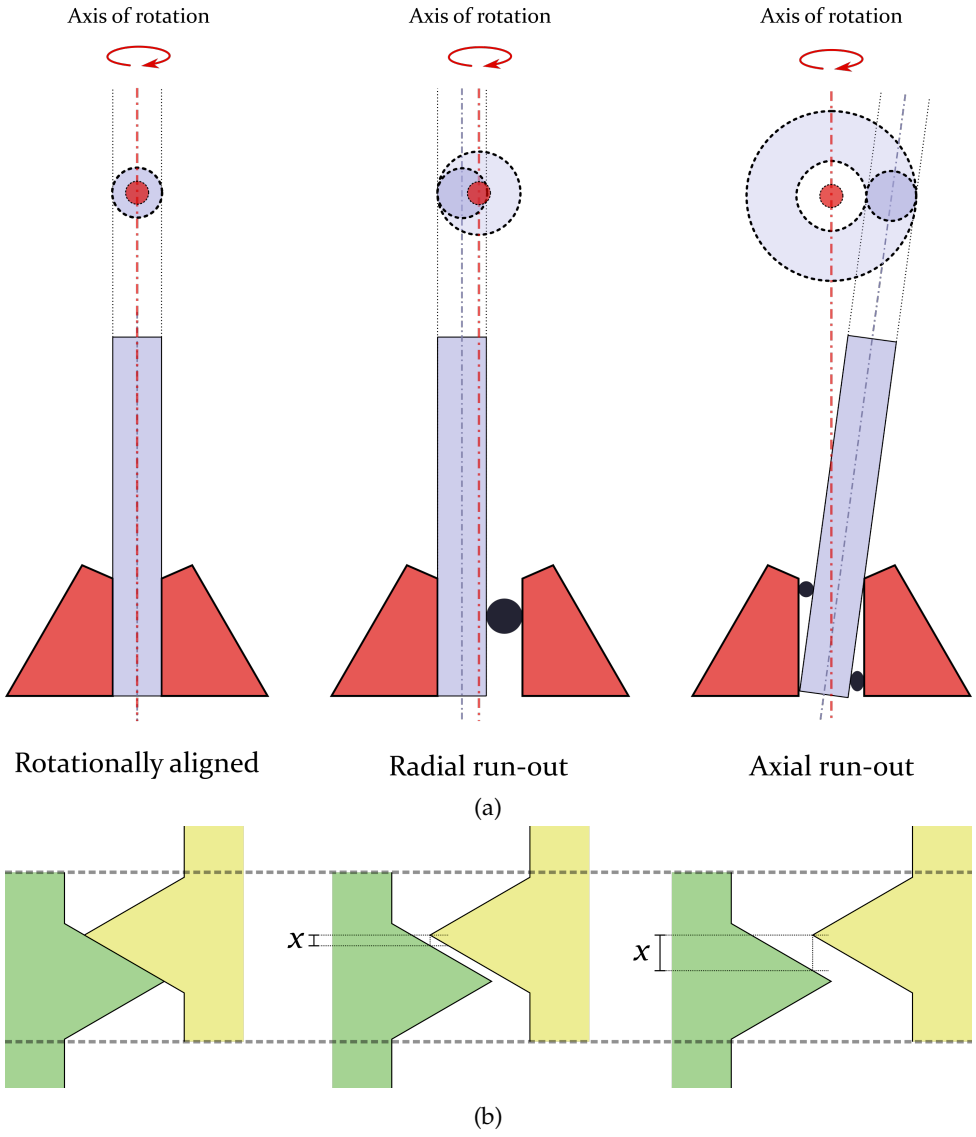

FIGURE 2.46: (a) The two kinds of run-out compared to a rotationally-aligned system (left). The rotational axis is indicated by the red dot-dash line, while the object's central axis is indicated by the blue dot-dash line. The circles above indicate the cross-sectional area that the part traces during rotation (looking down the rotational axis from the top). The black circles represent something that prevents the object from aligning correctly. (b) The effect of run-out on the position of the gear teeth. Neglecting gear motion in the vertical direction (from the screw motion), run-out causes the teeth to move apart and back together during rotation - which results in an increasing and decreasing gear-teeth separation in the vertical direction (x).

worm-screw and worm-gear creates a small amount of backlash, which is known and corrected for during the scans.

We initially considered removing the outer barrel of the lead screw knob and mounting the motor shaft directly to the lead screw shaft via flexible or inflexible couplings. While the most straight-forward approach, these designs suffer from drawbacks which affected the reliability of the system. Firstly, removing the outer barrel also removes the high-torque advantage it provides for smooth driving of the lead screw. If we were to use an inflexible coupling between the leadscrew and motor shafts, any imperfections in the alignment of the motor-shaft axis and leadscrew axis would result in resistance to rotation of the motor, due to the fact that the motor shaft is essentially creating mechanical run-out, and rotating into the body of the adapter (Figure 2.46). Run-out describes the inaccuracy of a rotating part or tool with respect to the driven rotation axis. There are two types of mechanical run-out, shown in Figure 2.46(a). Radial run-out is when the object's center axis is parallel but offset in a plane perpendicular to the rotational axis, such that when rotating, a part traces a circle larger than its own diameter, and the measured run-out is the same along the whole rotation axis. Axial run-out is when the two axes are not parallel, and the run-out varies depending on how far along the rotating axis it is measured.

The stepper motors used are relatively small, basic models, which have no feedback mechanism, and are considered "open-loop" with regards to positioning. Under loads which are too high for a stepper motor, such as the resistance created by run-out, they can exhibit skipped or missed steps, which is when a driving pulse from the stepper motor controller does not have enough power to rotate the motor shaft under load to the next step, and the controller thinks the motor has moved when it hasn't. Closed-loop systems check and correct for this, but are typically much more expensive. As such, in our open-loop design missed steps will result in positioning errors and distortions to Raman map images.

A common solution to this problem is to use flexible couplings (see in Figure A.8), which allow slight misalignment between the motor and leadscrew axes by flexing with the motion of the run-out. Unfortunately, these introduce an amount of backlash from the build-up of elastic potential energy in the spring-like coupling, which results in positioning inaccuracies.

Another possible solution could be to upgrade to either closed-loop or larger stepper motors. Larger motors can typically handle higher loads before skipping, but are also much heavier. As such, the adapter to the stage would need to be carefully designed to balance the masses involved, and make sure the stage does not tilt or bend - particularly at the extremes of their ranges.

The worm-drive mechanism overcomes these issues by providing a large driving torque from small motors without requiring strict alignment of the worm-screw and worm-gear axes. It is, however, still important to ensure good alignment of the worm-screw with the motor axis (see below). The large torque is a consequence of

the large barrel remaining in place, and the fact that worm drive systems are highly-geared. This high gearing is also convenient for improving the precision of the stage motion, since one full rotation of the motor and worm-screw gives only a fraction of a rotation at the worm-gear and lead-screw. The overall precision will ultimately be limited by the mechanical components of the stage (i.e. higher gear ratios do not indefinitely improve precision - stiction and friction and machining imperfections throughout all moving parts will determine the maximum precision). That being said, the worm mechanism seems capable of reliably stepping in increments below 200 nm, which is more than suitable for our diffraction-limited needs. The maximum precision is in fact often limited by run-out in the worm-gear on the motor shaft, which will be discussed below.

Worm-screw Mechanism

The design of the worm-screw and stepper adapter has also gone through extensive optimisation, with the final design demonstrated in Figure 2.45. Note that while not shown in the following graphics, washers and spring washers are used with screws wherever possible to spread the tightening loads and minimise the amount of vibration-induced loosening of the screws.

Although I stated above that this design is not sensitive to the alignment between the motor and leadscrew axes, it is still necessary to ensure good alignment between the motor and worm-screw axes. This is because misalignment between the motor and worm-screw axes will create run-out in the worm-screw rotation, and while this won't affect torque, run-out will cause the worm-screw to move towards and away from the worm-gear during rotation. This in turn results in a sinusoidal translation with rotation, and inaccurate step sizes. If we assume the run-out is small enough that the teeth of the worm-screw stay in contact with the teeth of the worm-gear, we can understand this in terms of the how the position of the worm-screw changes with the rotational period. Figure 2.46(b) shows that if we move the worm-screw thread and worm-gear away from each other in the direction perpendicular to the screw axis, the distance between the teeth increases, and creates backlash between the parts. This backlash would need to be taken up before the worm-screw can drive the worm-gear again. If the run-out is relatively small the worm-screw teeth move up or down the rotational axis faster than run-out pulls them away from it, meaning during rotation the worm-screw teeth are in constant contact with the worm-gear. Therefore, the backlash is taken up simultaneously while moving, and the result is that the worm-gear will not move as far as it would have without run-out. As the worm-screw rotates the run-out will pull the teeth away to a maximum distance. Rotation from this point on causes the opposite effect - the run-out now causes the worm-screw teeth to move towards the worm-gear, meaning the "backlash" from before is now adding to the worm-gear motion, and the stage moves further than it would have otherwise.

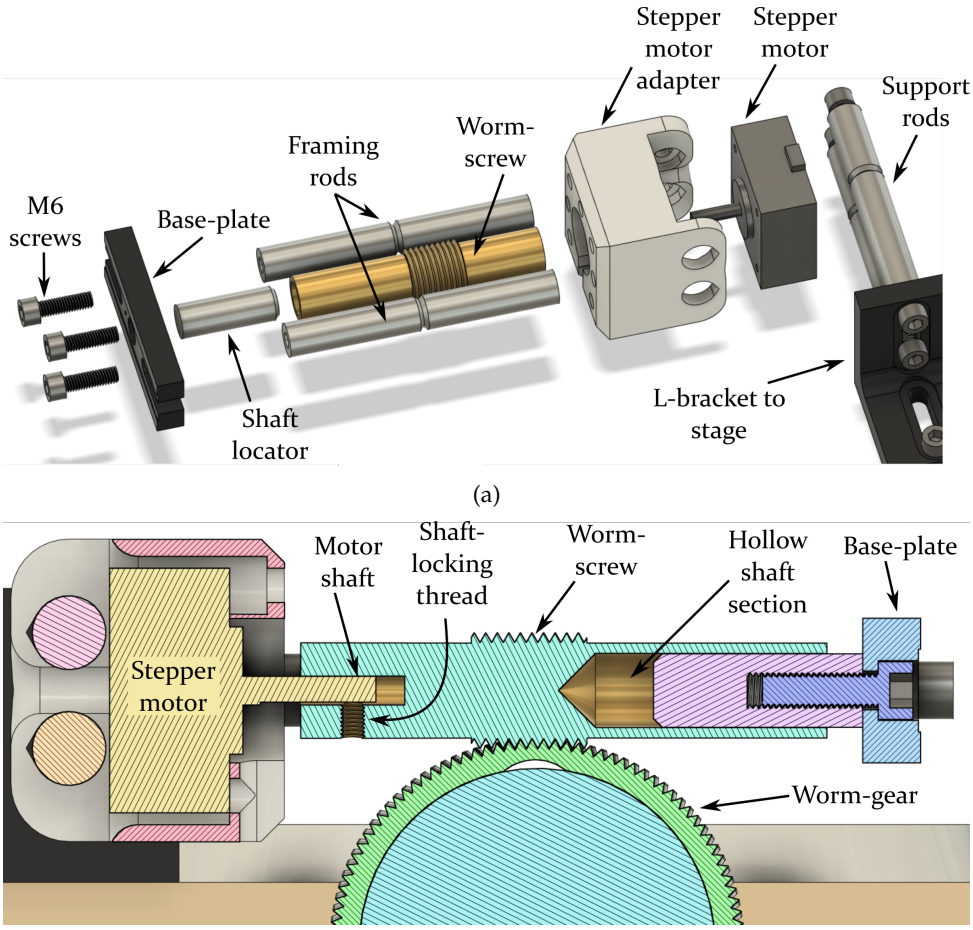

FIGURE 2.47: CAD drawings of the Y-axis assembly. (a) Exploded view of the motor assembly. (b) Cross section view of the motor assembly, through the centre of the worm-screw and bisecting the worm-gear.

Therefore the net result is a sinusoidal translational motion of the stage with rotation of the motor, which is observed as an acceleration and deceleration of the stage motion. This reduces the positioning accuracy of the stage and distorts the resulting Raman maps and linescans. In addition, if the worm-screw is allowed to press fully into the worm gear (i.e. such that there is no backlash in the gear-teeth when changing direction), the pressure applied by the motor creates a visible movement of the stage on the order of a few microns, meaning that run-out can also cause positional inaccuracies by flexing the stage.

Consequently, the design of the motor adapters shown in Figure 2.47 is aimed at minimising run-out. Firstly, the worm-screws are machined from brass on a lathe, with a particular focus on ensuring the motor shaft is a snug but smooth fit, and axially aligned with the outer body.

3D printed worm-screws can be used, and were extensively used for rapid prototyping, but the relatively soft material is not ideal for strict axial alignment, as locking to the motor shaft with a grub screw can push the worm-screw off-axis. This is exacerbated by the shape of the internal surface of the 3D printed shaft. Since FDM 3D printing is a layer-by-layer deposition, the surfaces of the finished product exhibit bumpy ridges, which can deform easier than a flat surface under applied pressure. While the shaft can be reamed to size after printing, it is difficult to ensure the final shaft is co-axial and on-axis. Furthermore, heat generated by the stepper motors softens the plastic parts even further and typically causes alignment problems over time. Consequently, machining out of metal on a lathe provides a much more reliable end-use part.

Secondly, the design uses a locator shaft to help keep the worm-screw on-axis (see Figures 2.47 and 2.49). A shaft is bored out of the worm-screw at the opposite end to the motor, and reamed to just over 12.7 mm in diameter, which allows a ThorLabs optical post (which are already precision ground to 12.7 mm in diameter) to be slotted into the worm-screw end. The optical post is fixed to a bracket (base-plate), allowing it to act as a rotation guide for the worm-screw at the opposite end to the motor. This bracket is kept in the correct location by two lengths of optical post (framing rods), which are tightly screwed to the face of a stepper motor adapter. The brass worm-screw already has low run-out when attached to the motor shaft, but the the locator acts to minimise any run-out created by slack in the motor-shaft fit.

The core design of the X and Y-axes are the same, but differ in the way they are mounted to the stage. The lower axis (X-axis) only moves in one direction, meaning the motor can be mounted directly to the table. However, the upper axis (Y-axis) sits on top of the X-axis and moves with it, so the motor assembly must move with it as well. To achieve this, the Y-axis adapter is mounted directly to the stage via a ThorLabs slotted L-bracket (see Figure 2.48).

To ensure that the weight of the motor and worm-screw assembly does not cause

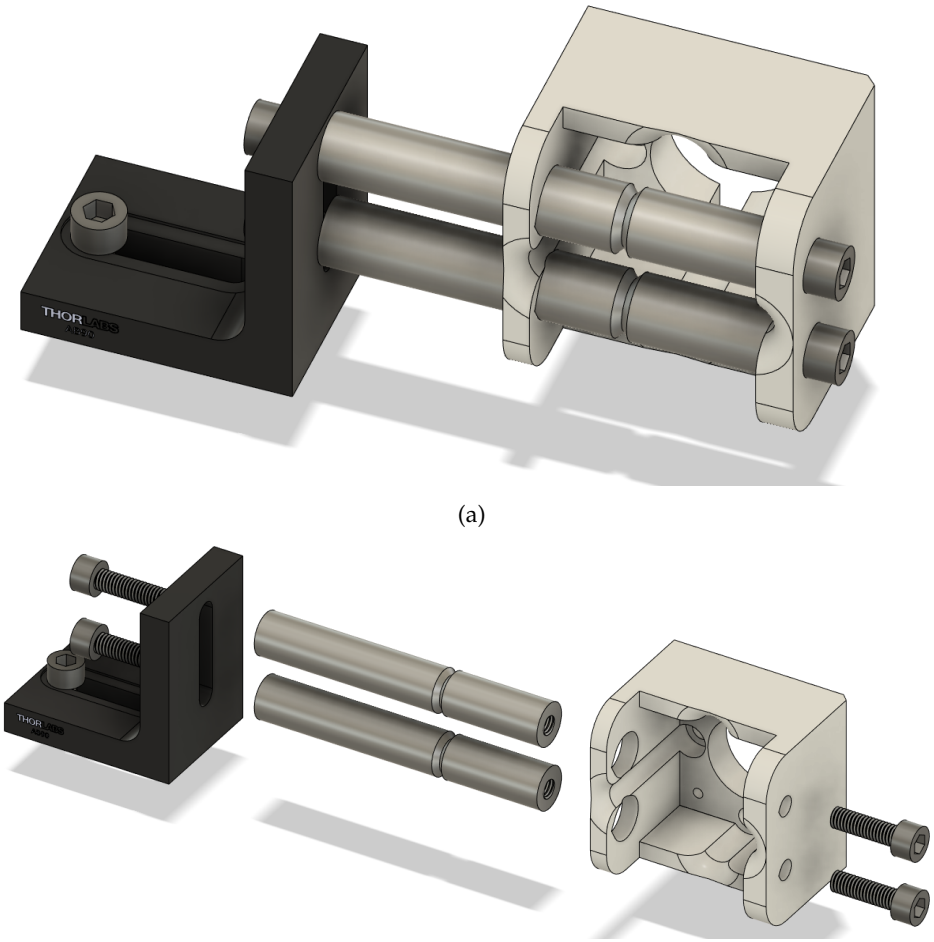

(a)

(b)

FIGURE 2.48: CAD drawings of the support arm holding the motor assembly to the L-bracket on the stage. (a) Standard and (b) exploded view.

it to sag or twist away from the mount, two half-inch optical posts support it horizontally, and are in line vertically to maximise rigidity against gravity. These posts are passed through holes of the same diameter in the 3D printed motor adapter, before being tightened hard against the adapter wall by two M6 screws (see Figure 2.49).

A small amount of positional control is available by moving the assembly up and down within the slot of the L-bracket, and can be used to bring the worm-screw teeth into alignment with the worm-gear. Note that the worm-screw is not pressed up against the worm-gear, but sits just above it to ensure any run-out does not flex the stage.

The X-axis motor assembly is shown in Figures 2.45(c)/(d) and 2.50. M6 screws are passed through two ThorLabs swivel base adapters before passing through the base plate and tightening to the frame rods (see Figure 2.50(b)), which clamps the swivel adapters in place. This allows the assembly to be mounted vertically on the

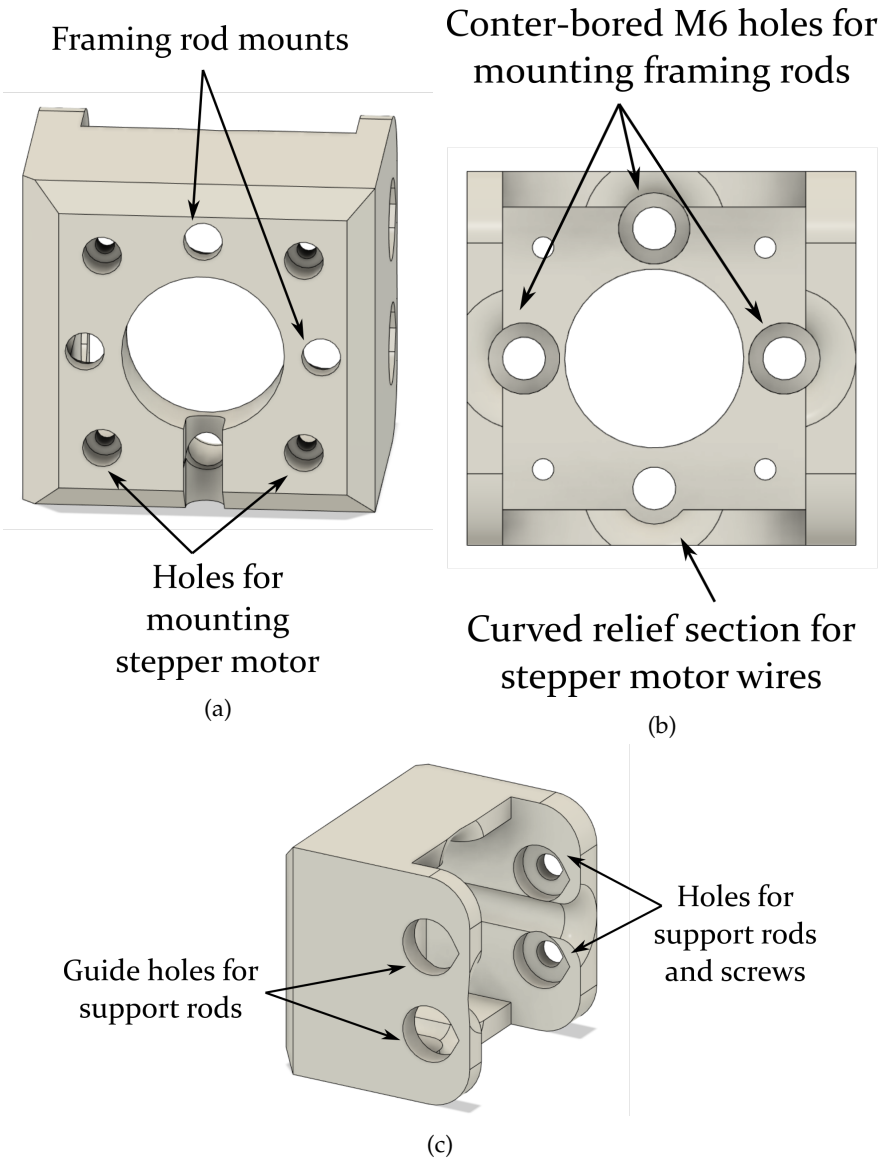

FIGURE 2.49: CAD drawings of the stepper motor adapter. (a) Front face showing M3 mounting holes for the stepper motor, and M6 holes for fixing the framing rods to the face of the adapter. (b) back view showing the counter-bored M6 holes for the framing rods. (c) Side view showing the guide holes and end-stop holes for mounting the support rods with M6 screws.

table, which provides good support for the motor weight through the frame rods.

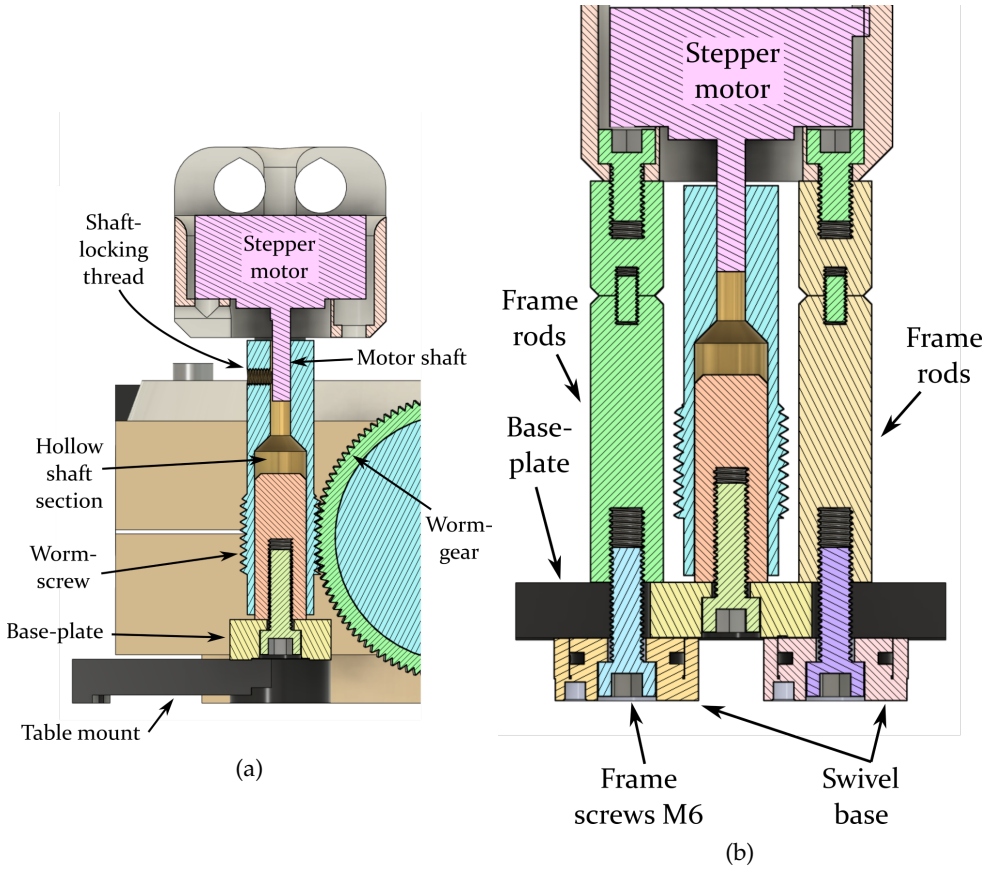

FIGURE 2.50: Cross section views of the X-axis motor assembly in two different planes: (a) through the worm-screw and bisecting the worm-gear axis, and (b) through the worm-screw, framing rods, and swivel base adapters.

The swivel base adapters can rotate their forks freely about the base component (which is fixed by the frame screws), which facilitates positioning on the table. Upon tightening to the table through M6 screws, the forks clamp down on the base component, which locks the orientation of the swivel base adapter and keeps the assembly rigid. It is important to ensure both adapters are tightened with approximately equal torque, as tightening one more than the other twists the assembly ever so slightly, but it's enough to cause an audible oscillatory squeak as run-out pulls the worm-screw into the shaft locator. This can cause the motor to miss steps, and can be seen in the stage movement (at 100× magnification). Like the Y-axis, the worm-screw teeth of the X-axis are brought into mesh with the worm-gear, but not pressed into it, and the backlash is managed in the software.

Once the motor-assemblies are in place the axes cannot be moved manually. However, the X-axis motor assembly can be quickly unscrewed from the table to manually adjust the stage for initial sample positioning.

A key advantage of the worm-gear system demonstrated here is that the 3D printed parts are fully customisable. The worm-gear caps used here over-top the

stage's stock micrometer knobs can be printed to fit any size or shape of micrometer or stage control knob. Therefore, this system of stepper motor controlled stage motion should be applicable to a variety of stage designs on many microscope systems.

2.3.6 Low-Temperature

We have the use of a Linkam THMS600 temperature controlled stage, shown in Figure 2.51, covering a range of −195 °C (liquid nitrogen) to 600 °C, which is primarily used to reach low-temperatures with a manual controller. In order to accommodate the stage, our mechanical engineers machined a disc of steel with a rim which seats the THMS600 mounting clamps (see Figure 2.51(c)). The disc has holes for mounting to the motorised stage with screws, allowing linescans and Raman maps to be performed with the temperature stage attached. When the THMS600 is not attached, the steel disc doubles as the standard sample mount, and procedures for mounting samples can be found in the methods section.

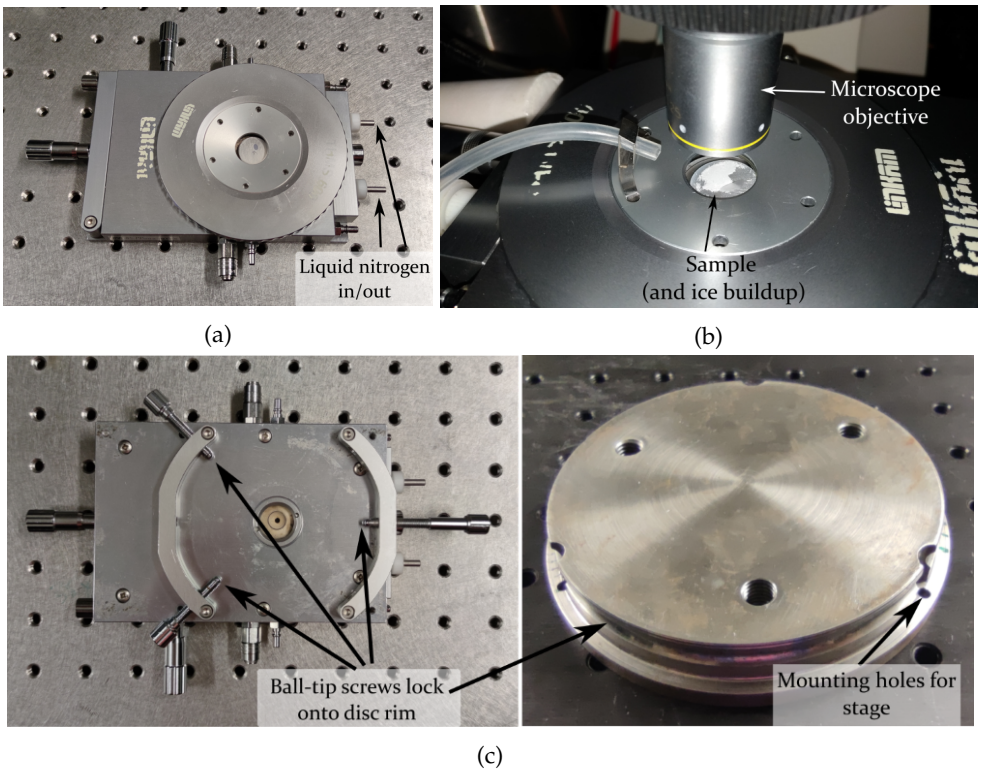

FIGURE 2.51: (a) Linkam THMS600 temperature controlled stage. (b) Linkam stage running at liquid nitrogen temperatures under a microscope. The sample sits inside the stage in an inert atmosphere to prevent ice build-up on the sample, with a viewing window for the microscope to focus through. After sufficient time slow leaks result in ice build-up. (c) The underside of the stage, showing the clamping mechanism: ball-tip screws tighten down on the recessed lip of a steel disc, which itself is designed to screw into the stage via the mounting hole indicated and two others 120° apart.

2.3.7 Electronics and Software

Controller

In order for the stepper motors to control stage motion, they need to be connected to and driven by a stepper motor controller. This controller needs to in turn receive commands from a computer, which has software a user can control.

Fortunately, the recent surge in hobbyist 3D printing has made stepper motor controllers readily available and relatively cheap. The ones driven by G-code (also known as machine-code) commands can be easily interfaced with motion control software - or in this case, hard coded in programming languages.

Here, I have utilised a top-of-the-line 3D printer controller - a Duet 2 Ethernet by Duet3D, shown in Figure 2.52. These control boards are designed for highly-customisable, often home-built 3D printers - which is ideal given that we're going to have it run a microscope, not a printer. The controller has slots for five independent stepper motors, and each one is driven by Trinamic Motion Control stepper motor drivers, which are considered industry-leading chips that are specifically designed to optimise microstepping performances - improving torque and precision, and minimising vibrations and noise. Minimising vibration is particularly important for the Y-axis motor, since it is mounted directly to the stage, and the vibrations induced by low-quality drivers can be seen vibrating the stage in optical images. Minimising vibrations in general is a priority, as they can cause samples to vibrate out of position, and over time may loosen screws used in various assemblies.

The Duet controllers use a firmware known as RepRap, which is again designed to be highly customisable. There is extensive documentation available online (reprap.org) for understanding how to use the firmware, how to set up a configuration, and what commands can be used to control the electronic components. The current configuration, which tells the controller how to behave like a microscope rather than a 3D printer, can be found in our research group's Git repository (https://github.com/Mark-Waterland-Research-Group/Scanning-Microscope.git).

Software

The actual sequence of operations for a scanning microscope is fairly straight-forward - it's basically a loop of move and wait and collect commands until the sequence (line or map) is complete. There are a few extra steps involved, but in general the main program only needs to be concerned with a handful of commands, which can be hard-coded using a programming language. Our Raman collection system uses the software "LightField" - by Teledyne Princeton Instruments, which has the architecture to interface with MATLAB, LabVIEW, and Python code. Given

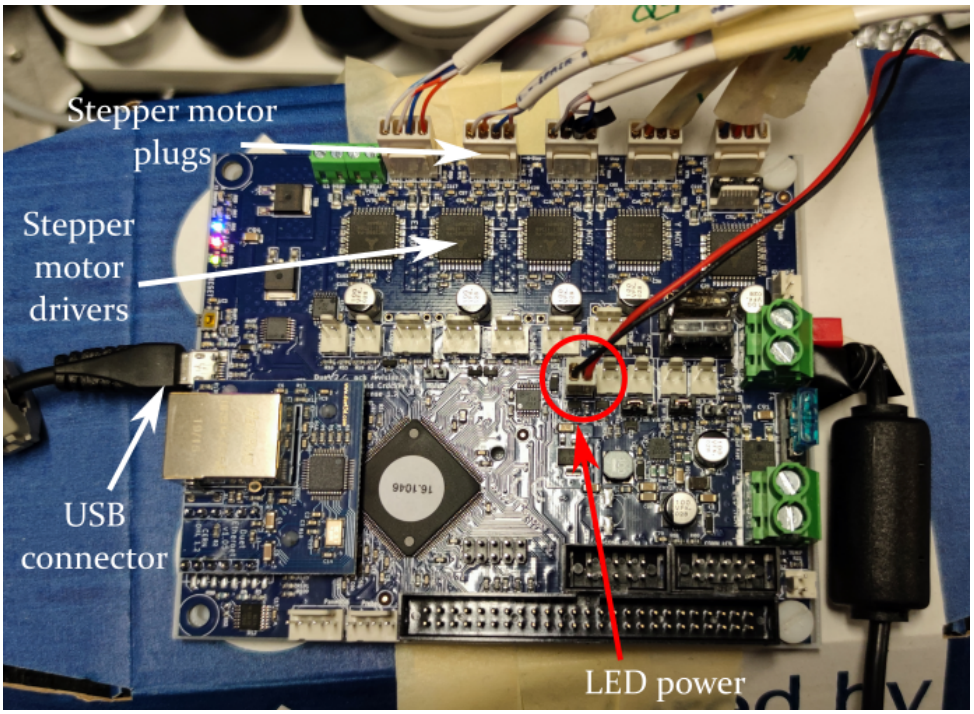

FIGURE 2.52: The Duet 2, 3D printer controller used to drive the stepper motors and control the LED source using G-code commands sent via USB cable.

our experience with Python coding, and the abundance of useful code in the community, I chose to write a custom Python program to handle the microscope operation. The code can also be found in the aforementioned Waterland Research Group Git repository, and here I will briefly explain the processes it performs.

The Python script is designed to use the "pySerial" module to send individual G-code commands as binary across a USB serial communications (COM) port on Windows computers. Interface with LightField for spectrograph and detector control is achieved with Python modules provided by Teledyne Princeton Instruments, and instructions for installing and using these can be found with the LightField electronic user manuals.

The Python script has various functions which send a set of G-codes required to perform an action. These include:

- **Move** - takes X and/or Y values and moves that distance in microns.
- **Adjust power** - A stepper motor controls the power of the 785 nm diode laser by rotating the manual power knob.
- **Focus** - controls the focus stepper motor to focus and defocus the sample image and laser spot.
- **Lights** - controls the power sent to the LED from the controller to adjust the amount of illumination light sent into the microscope (0 to 100%).

- **Raman mode** - prepares to collect a Raman spectrum. Instructs the swing mirror assembly motor in Section C to rotate the mirrors out of the optical axis, turns laser power to maximum and turns off the LED illumination.
- **Image mode** - prepares to observe the sample with the camera. Instructs the swing mirror assembly motor in Section C to rotate the mirrors into the optical axis, lowers the laser power and turns on the LED illumination.
- **Linescan** - sets up and runs a Raman linescan, taking in a start position, finish position, and number of steps to acquire at between the two.
- **Raman map** - sets up and runs a Raman map, taking a start position, finish position, and scan resolution. The script generates a grid of points to collect at from the input values.

During the "Linescan" and "Raman map" setup, variables for file/series name, start position, finish position, scan resolution or number of steps, acquisition time, and laser power are entered as inputs, returning basic information like the grid size and estimated scan time. Once initiated, the script will loop over a sequence of points, collecting at each for the set acquisition time and exporting the data to a save directory. During this process, scan directions are established and backlash is taken up automatically whenever direction is changed (typically only needed for maps) by having the microscope move past the new point, then approaching it from the initial scan direction. Data is saved with information needed to reconstruct the 1D or 2D scan in the spectra file names, and upon completion the microscope returns to the start position, with the software ready to receive new commands.

Note that each spectrum is exported as a ".csv" file as it is generated, but the script has no ability to restart a scan if it crashes or closes (though crashes are rare in the current version). That being said, it wouldn't be difficult to establish a protocol to check for incomplete runs and restart them, it would just take some time. While simple, the program in its current state works well and is capable of generating excellent Raman maps and linescans (see Figure 2.53).

2.4 Results and Scans

The resulting data collected by the system mostly speaks for itself. Figure 2.53 shows a 2D scan resulting in a 3D heatmap of spectral intensities across the sample, and when comparing with the optical image, the accuracy of the representative Raman map is excellent. The map was collected over approximately 25 hours, with 15 second acquisitions at a 500 nm step resolution. While this is a best-case scenario with no obvious aberrations in the scan image, it should be noted that over this collection time period there would have been many thermal fluctuations, meaning that the insulating box was doing sufficiently well to mitigate these issues.

Figure 2.54 shows another Raman map of a CVD sample of MoS_2 with the box walls open, and the distortions from the expected shape shown in the optical image are obvious. It is worth noting that the motors produce a significant amount of heat during operation, which causes the internal box temperature to rise slightly above ambient over the course of several hours following closing of the box. This undoubtedly creates an additional buffer against temperature changes in the room, and for the best scans it is advisable to wait a few hours following closing of the box to ensure it has had time to equilibrate.

An additional advantage of writing the software in user-friendly Python is that custom scanning and mapping protocols can be written and implemented. For instance, many samples can be loaded on a well-plate or sample holder and the sample positions can be entered to perform high-throughput screening and data collection over hours or days of automated operation.

2.4.1 Optical Resolution

The optical resolution of our microscope can be determined by analysing the linescan and map data it generates. As will be discussed in Chapter 3, bulk MoS_2 at 785 nm excitation exhibits an edge-localised enhancement effect, which has an effective radius significantly smaller than the spot size and essentially appears as a 1D feature which we can use for calibration. Figure 2.55(a) shows a linescan across the edge of a flake as indicated by the arrow in (b), with the left hand graph showing the raw data with the spike in intensity at key modes, and the right hand graph showing peakfits of these intensities as a function of sample position. It is not necessary to know the meaning of the frequency labels in the legends of (a) at this time, just that these peaks increase in intensity at edges (see Chapter 3 for details).

From the peakfits we can extract average values for $1/e^2$ and full width at half maximum (FWHM) of 1.72 µm and 0.67 µm respectively. The objective used in this scan was a basic 100× oil immersion objective with an NA of 1.25, focal length of ∼1.66 mm and clear aperture of ∼5 mm (see Figure A.6). We can use equation G.6 to calculate the ideal diffraction-limited spot size for the Airy disc as 0.766 µm. However, Figure 2.56 shows the actual laser beam profile, as measured by a gentec-eo BEAMAGE-3.0 beam profiler, and we can see that not only is it only half the clear aperture diameter at 2.5 mm, but it is also not an ideal Gaussian - it has patches of higher intensity, and a noisy wavefront. Recalculating for only half the effective NA gives an ideal beam diameter of 1.53 µm, which is not far off our calculation from the linescan, with imperfections in the shape of the beam and the basic quality optics in the objective likely making up the difference.

When thin samples on sapphire or silicon are prepared for Raman measurements, they are done so using the methods outlined in section 5.3.2, whereby a thin

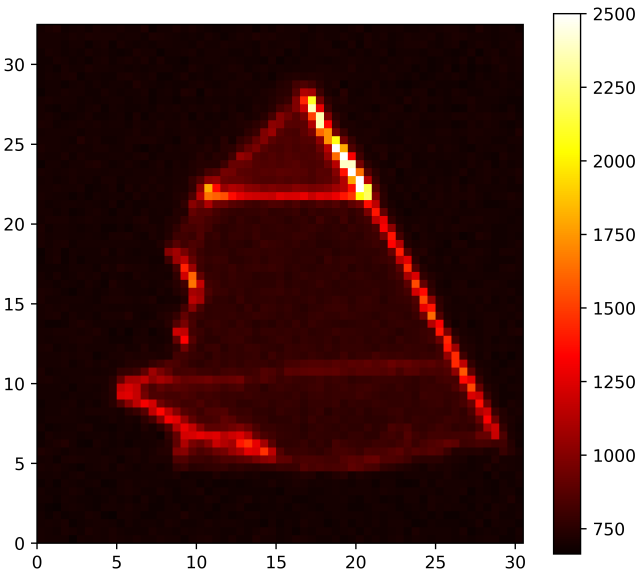

(a)

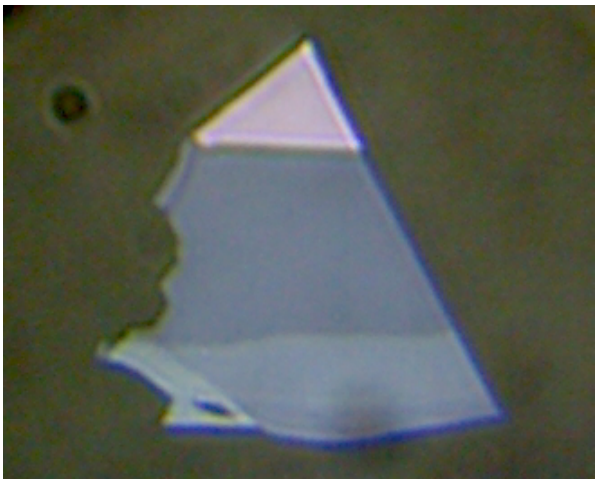

(b)

FIGURE 2.53: (a) A Raman map of a flake shown in (b), demonstrating the capabilities of the scanning microscope. The scales in (a) are in microns, and the colour-bar values indicate intensity of an edge signal.

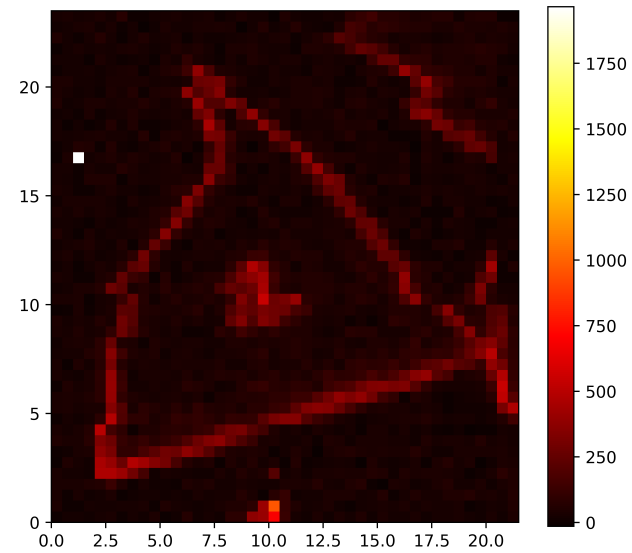

(a)

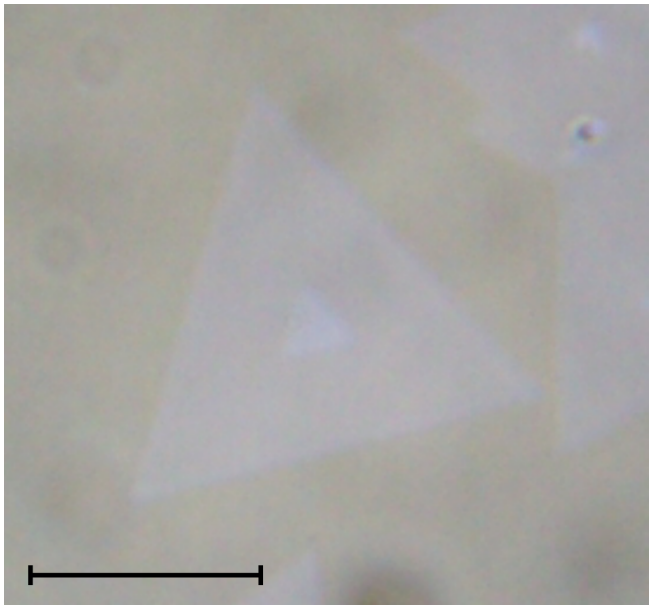

(b)

FIGURE 2.54: (a) A Raman map of a CVD flake of MoS_2 shown in (b), demonstrating the warping effects temperature fluctuations have on the sample with the temperature-box lids off. The colour-bar values for (a) indicate intensity of an edge signal. The scales in (a) are in microns, and the scale bar in (b) is 10 µm.

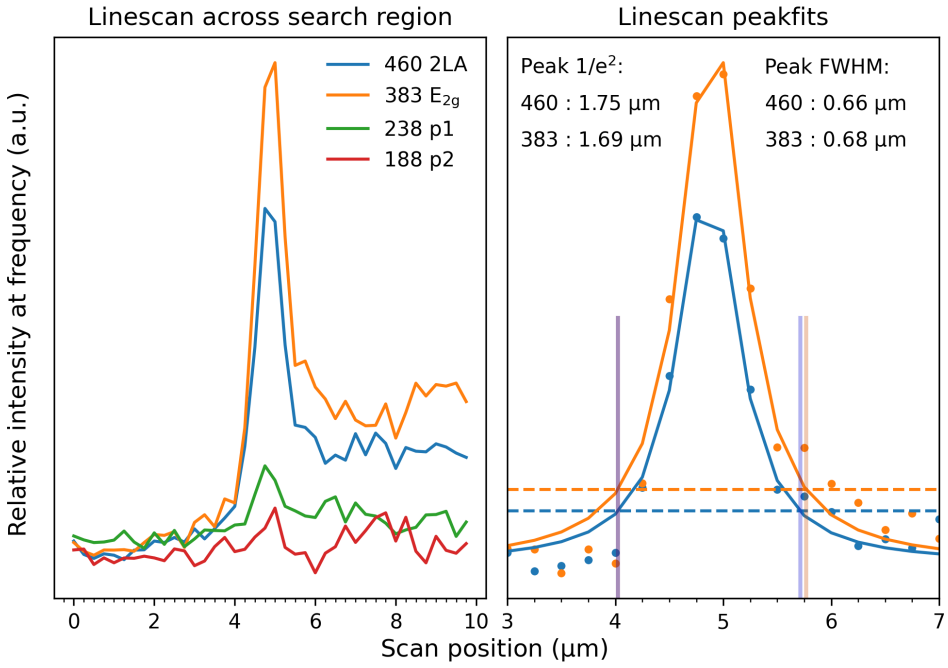

(a)

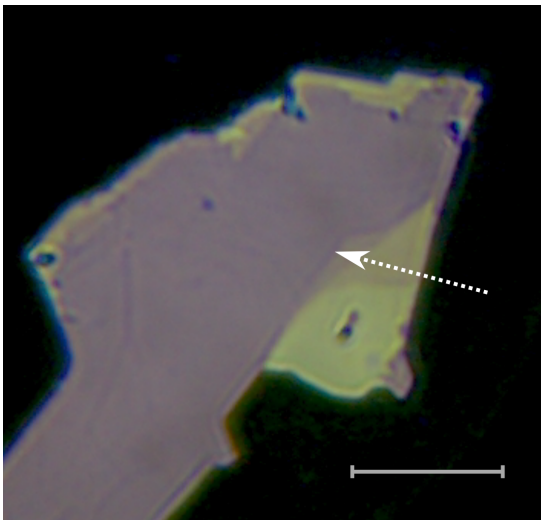

(b)

FIGURE 2.55: (a) Linescan test across an edge of MoS_2, which has an edge-specific resonance enhancement which can be used like a 1D line for calibration of spot size. Left graph shows the linescan raw data, and the right hand graph shows the peakfits of the line graph intensities and their FWHM. The dotted blue and orange horizontal lines indicate the $1/e^2$ intensity, with the vertical lines marking the distance between those points. The left legend indicates the peak frequencies from which the data is extracted, which are not important to know here other than that they spike at edges, but are discussed in Chapter 3.

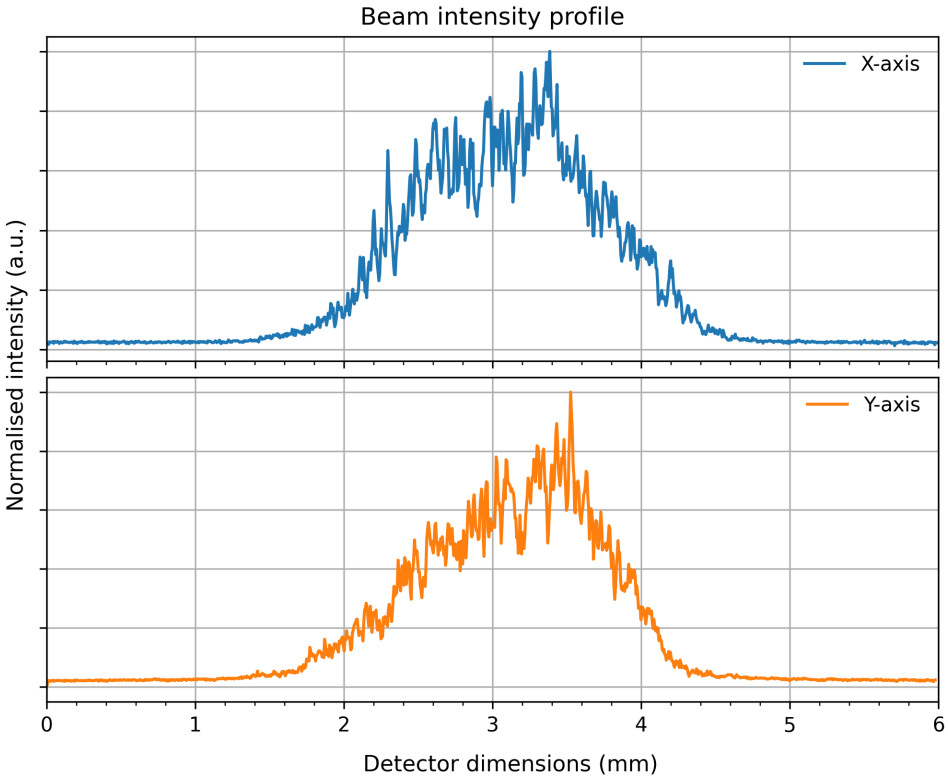

(a)

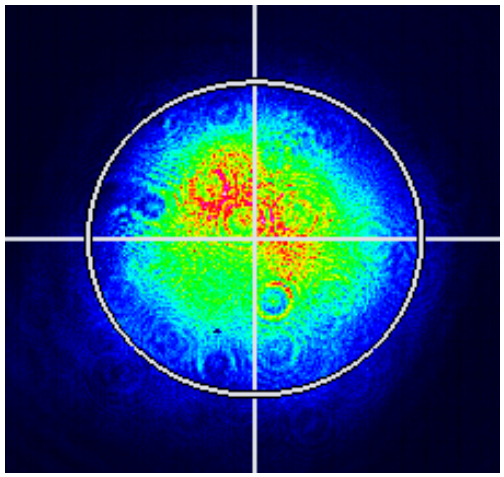

(b)

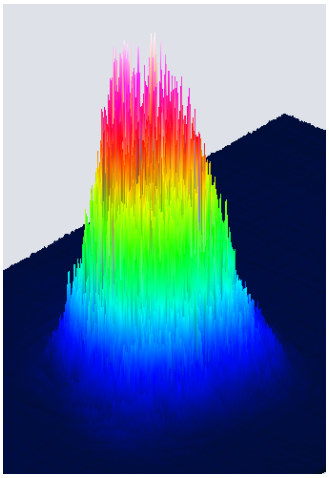

(c)

FIGURE 2.56: (a) The profile of the laser beam, measured in the X and Y directions of the beam profiler. (b) A 2D and (c) a 3D visualisation of the intensity and shape of the beam. The colour and height in (b) and (c) represents intensity at that point on the detector.

glass cover slip is placed directly over the sample to prevent the immersion oil from contaminating it. This typically creates a slight air gap between the sample and cover slip, which results in a decrease in the NA due to air having a lower refractive index than glass or water, and thereby gives a slightly larger spot size. While the cover slip is held as close to the sample as possible, imperfections in the machined surface of the steel disc result in a slightly uneven surface, meaning some parts of the sample are raised and have larger air gaps than others. This can occasionally be observed near the edges of chip substrates, as either warping of the cover slip at points of contact, or a thin-film interference effect from a decreasing air gap, resulting in dispersion of the white light source in a rainbow pattern.

For the purposes of collecting this linescan, however, the sample underneath the cover slip was deliberately coated with a thin layer of oil to mimic the normal operating conditions for the objective and minimise aberrations from the cover slip (i.e. normally imaging into water). During collection conditions in air, the point-resolution is not quite as good.

There are several improvements that can be made to the system to reach diffraction-limited performance. First, the laser beam needs to be expanded up to the objective clear aperture and reshaped and have the noise removed. The poor quality beam is likely a consequence of a damaged fiber end, and fixing this would require either cleaving the fiber to reveal a new end, or installing a new diode since the fiber is directly mounted to the cavity output. Alternatively, the output from the laser can be focused into a pinhole, and diffraction at the pinhole allows re-collimation into a cleaner beam - albeit with a loss of power. Whatever the case, it would be useful to match the optic focal lengths to ensure the collimated beam diameter matches the clear aperture of the objective - which, while we're speaking upgrades, should be replaced for a high-quality immersion lens with the highest possible NA. Lastly, the sample holder should be precision ground to a flat, smooth finish, so that the sample is kept level and the air gap is kept minimised and even across the sample.

2.5 Conclusions

This chapter demonstrates an optical design for a high-performance low-frequency Raman microscope, with low-temperature capability and a customisable design. The dual-cage optical assembly which houses the low-frequency optics is designed to be modular, and quickly changed to another laser excitation energy for rapid, scanning-capable, resonance Raman analysis. Addition of a dovetail adapter also enables the rapid changing between upright and inverted microscope configurations to accommodate various sample orientations and preparation methods.

The parts and assemblies demonstrated here enable the conversion of a standard Raman microscope setup into a scanning Raman microscope using basic stepper motors, standard mechanical components, and 3D printed components. These days, motorised stages can be purchased to retrofit a microscope for scanning capabilities. These presumably do a good job, but it should be noted that not every microscope will have the structural stability to perform scanning experiments well at high-magnifications. The novelty of this work is that the design is is constructed from readily available ThorLabs structural and optomechanical components, and the use of 3D printed parts enables adaptation of the design to other microscope systems. The use of readily available relatively inexpensive ThorLabs components, and fully customisable 3D printed components enables construction of a scanning microscope for a fraction of the cost of commercial systems (see table 5.1 for parts list). Furthermore, the use of self-written Python code as the driving software enables complete control of the scanning routines for custom experiments.

The 3D printed parts demonstrated here have a precision and accuracy that could not have been achieved with 3D printing technology ten years ago, and the results here and in Chapter 3 provide a strong use case demonstrating the potential of 3D printed parts in the optics lab. The technology is still rapidly improving, with recent advances including new materials with different physical and mechanical properties, and new printing methods becoming readily available such as UV-cured resin technologies that offer even better accuracy and precision. It will be interesting to see how 3D printing technologies can be utilised in the optics lab in years to come.

Chapter 3

MoS_2 Defect Modes - Indirect Double Resonance Raman

3.1 Introduction

3.1.1 Phonons in Crystals

It is useful to have a basic understanding of how vibrational modes occur in solid-state systems. If you're familiar with the vibrational properties of solid-state systems you can skip this section. While in molecular systems we may consider a vibrational mode as the motion of a discrete number of atoms in a molecule, vibrational modes in crystals behave as a collective oscillation of atoms across the many unit cells under irradiation. We use the term "phonon" to describe a quanta of vibrational energy, in analogy to the photon, and it's typically used in the context of crystal systems where instead of discrete vibrational modes we have a quasi-continuum of modes.

We can understand how the vibrational continuum arises by building up a chain of atoms and finding the normal vibrational modes (following that normal modes must maintain their centre of mass throughout their motion). If we imagine a two-atom system, such as a molecule of nitrogen gas N_2 pinned in space so it cannot rotate or translate, we find that there is only one normal mode - the symmetric stretch, where both atoms move together and away from each other simultaneously (see Figure 3.1).

In a 3 atom system, such as CO_2, we find that there are now two stretches (symmetric and asymmetric) and also two bending modes in the plane of the page and out of the page (see Figure 3.1). With four atoms there are more stretches, and we can see that they start to involve "bunches" of atoms moving in a similar direction (see Figure 3.1). If we keep adding atoms we see that their displacements follow a sinusoidal pattern, and we can represent the magnitude of this displacement with a sine wave in space and time propagating along the chain.

Figure 3.2 shows these displacements and this representative wave for the first 6 vibrational energy states for the longitudinal and transverse waves (LA and TA respectively) for a string of atoms in 1D. For a longitudinal wave the displacement of the atoms occurs in the direction of wave propagation, while for transverse waves the direction of displacement is orthogonal to the direction of propagation. Note

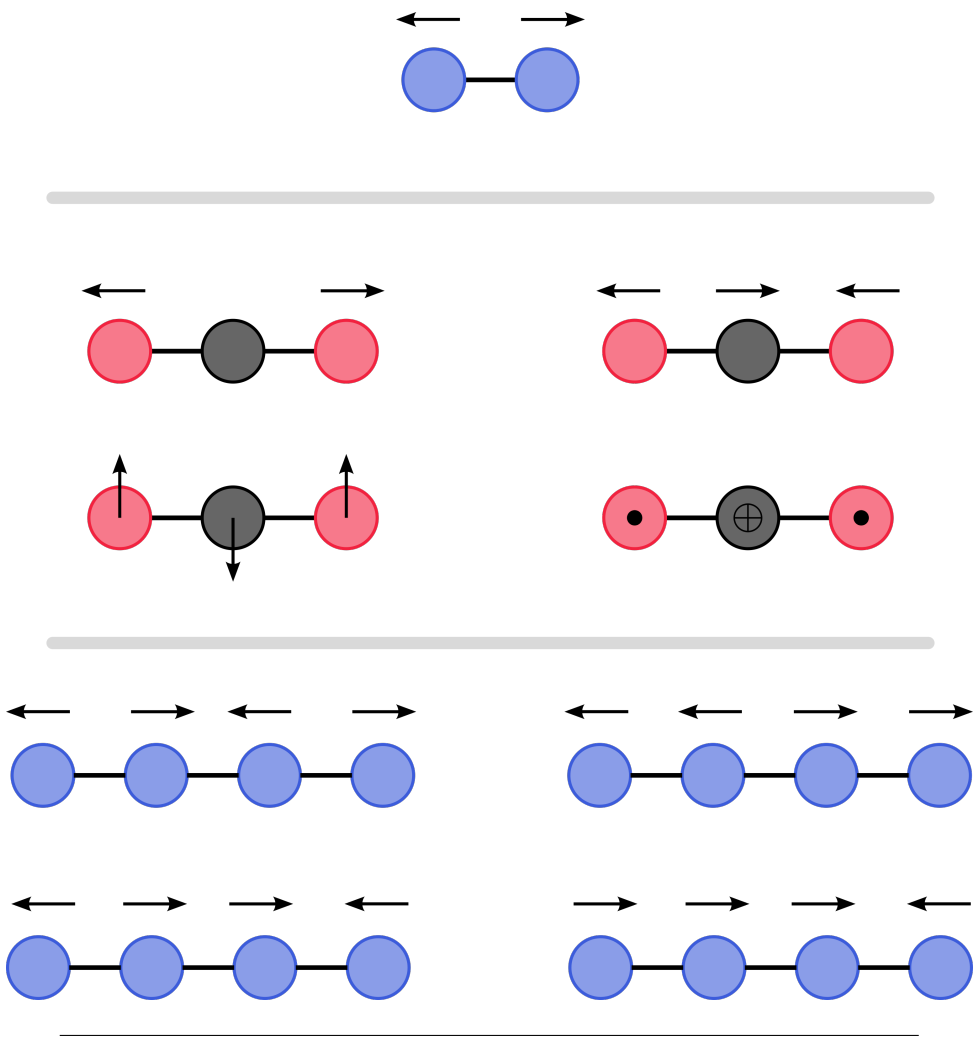

FIGURE 3.1: Schematic representation of vibrational motion of atoms on a string. The $\oplus$ and $\bullet$ indicate bending motion into and out of the page respectively. Note for the 4-atom set, bending motions are not shown.

that there is a maximum relative displacement of neighbouring atoms when the sine waves have a maximum positive amplitude on one atom, and a maximum negative amplitude on the neighbouring atom ($\lambda = 2a$, $n = 6$ in Figure 3.2).

We consider this to be the highest energy mode, as the total atomic displacement is maximised. Increasing the frequency of the wave does not increase the relative displacement further, but instead reproduces the atomic displacements one of the previous modes (see Figure 3.3). Conversely, the minimum energy state could be considered a motion described by a very long wavelength, such that if it were any smaller it would actually result in a translation of the string of atoms rather than a vibration, and places a lower limit on the vibrational modes. Each of these modes have a discrete energy, but extrapolating out to an appreciably large crystal means more and more states fill the range between the highest and lowest energy, and after a while we consider the densely packed vibrational energy states to be a continuum. Each continuum is labelled with an irreducible representation (irrep.) and represents

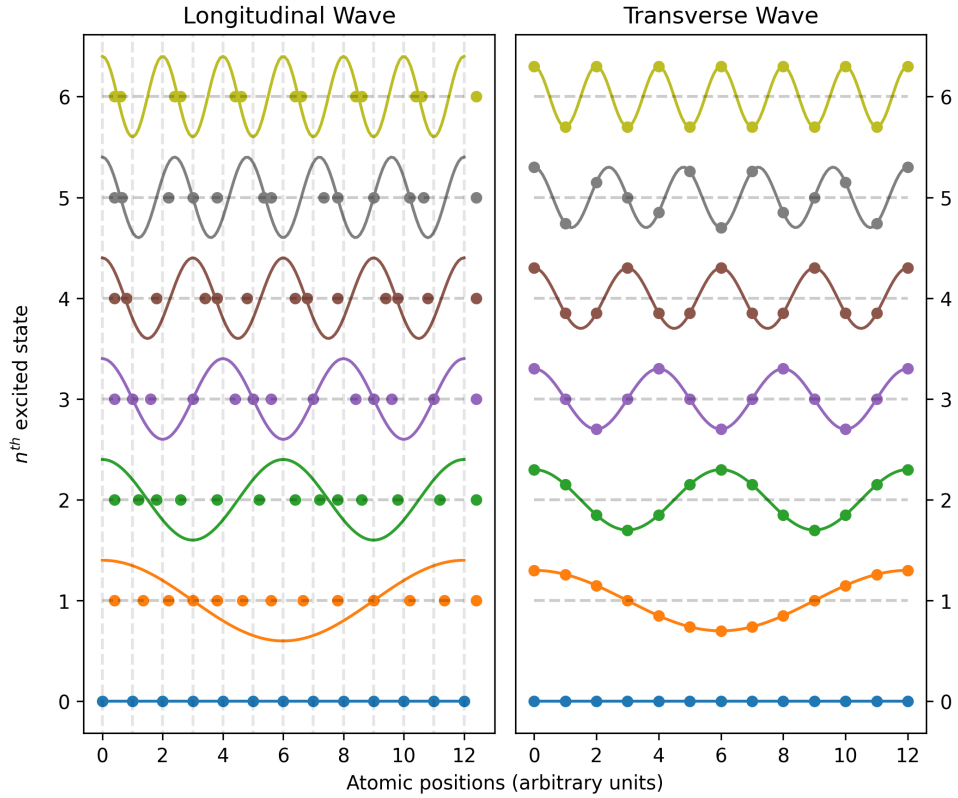

FIGURE 3.2: Acoustic and transverse motion for the first 6 modes of a hypothetical 1D set of atoms on a string. The dots indicate atomic positions, the dashed lines indicate atomic equilibrium positions, and the solid sine trace represents the motion of the atoms, where the magnitude of displacement from equilibrium positions is indicated by the magnitude of the wave at that point.

a "branch" of the total "phonon density of states" (pDOS), analogous to the "bands" which contribute to the "electronic density of states" (DOS).

If there are two or more atoms (N) in the primitive unit cell, there are $3N$ branches in the dispersion relation: 3 acoustic branches (1 longitudinal acoustic (LA) and 2 transverse acoustic (TA)) and $3N - 3$ optical branches.[165]

Optical phonons involve atoms or points with opposite charge, where their opposing oscillation creates an electric polarization which can couple to the alternating electromagnetic field of photons. Acoustic phonons are collective oscillations regardless of charge which mimic the way sound propagates (hence "acoustic"), and therefore cannot be directly excited by photons. However, both these phonons can interact with intermediate excited state charge carriers to appear in the Raman spectrum, and will be discussed further below.

Wavevectors are useful descriptors of all kinds of waves in solid state physics, and carry with them direction and magnitude components. The magnitude (k) of the wavevector $\boldsymbol{k}$ is the angular frequency, or wavenumber, related to wavelength

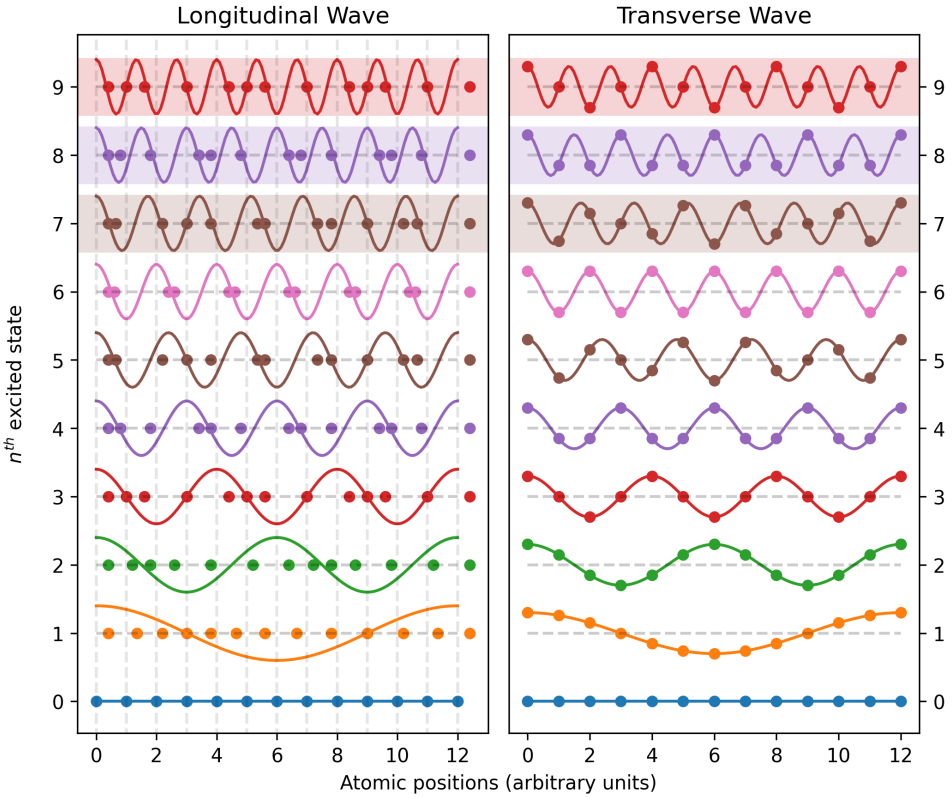

FIGURE 3.3: The first 10 modes of the 1D system in Figure 3.2. Notice how increasing the frequency of the wave past the 6^{th} state (highlighted, colour coded) does not increase vibrational amplitude or frequency, but rather reproduces one of the lower-energy modes with the same atomic displacements.

by $k = 2\pi/\lambda$. The direction can specify directions in real space (i.e. wave propagation) and in reciprocal space in the Brillouin Zone. Phonons and electrons in a crystal have an associated crystal momentum, given by $\boldsymbol{p}_{cry} = \hbar\boldsymbol{k}$, which must be conserved throughout interactions. Note that crystal momentum can be conserved within integer multiples of the lattice wavevector $\boldsymbol{K}$, such that $\boldsymbol{k} = \boldsymbol{k} \pm n\boldsymbol{K}$ where n is any integer. The crystal momentum ($\boldsymbol{p} = \hbar\boldsymbol{k}$) and energy of a phonon ($E = \hbar\omega$) are related by the dispersion relation ($\boldsymbol{k}$ vs ω), shown schematically in Figure 3.5(b). The pDOS is then a sum of the number of vibrational states approximately at some energy, and whilst usually calculated can be inferred by the gradient of the phonon dispersion (large gradient = small number of states in that energy range).

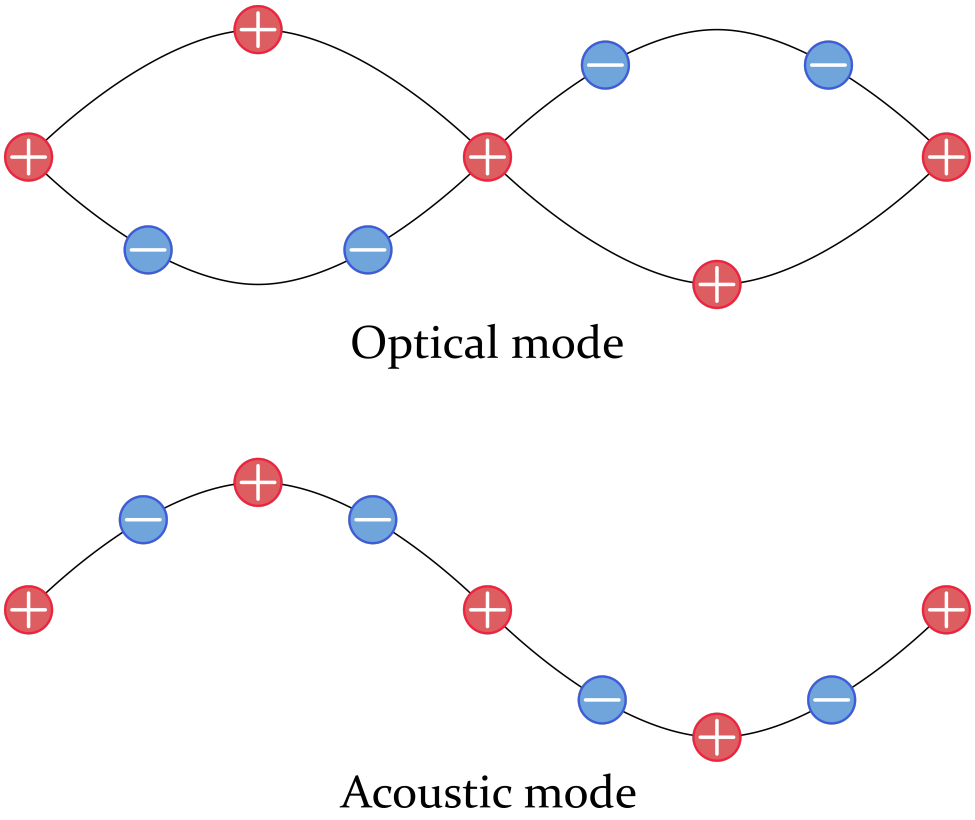

FIGURE 3.4: Representations of optical and acoustic vibrational modes for a 1D string of atoms. ⊕ indicates positively charged atoms and ⊖ indicates negatively charged atoms. Figure adapted from Kittel[165]

3.1.2 Raman Spectroscopy

Raman spectroscopy is a versatile vibrational spectroscopy technique which has become a standard practice in molecular and materials characterisation. While many consider Raman spectroscopy as simply analogous to infrared spectroscopies for basic characterisation, in reality the use of visible light sources means Raman measurements can be coupled to complex optical and electronic phenomena. As such, resonance Raman spectroscopy, which uses excitation energies near optical transitions, provides a powerful probe of light-matter interactions that extend well beyond simple analysis of vibrational motion.

This section serves to outline the basic concepts of Raman spectroscopy in solid-state systems, while the following section builds upon this to describe how the technique is applied in TMD systems to probe these complex physical phenomena. This extends into Double Resonance Raman (DRR) - the concepts of which form a foundation for understanding the results of the research presented in this thesis. For a detailed introduction to Raman spectroscopy the reader is referred to Long[166] and Yu and Cardona.[167]

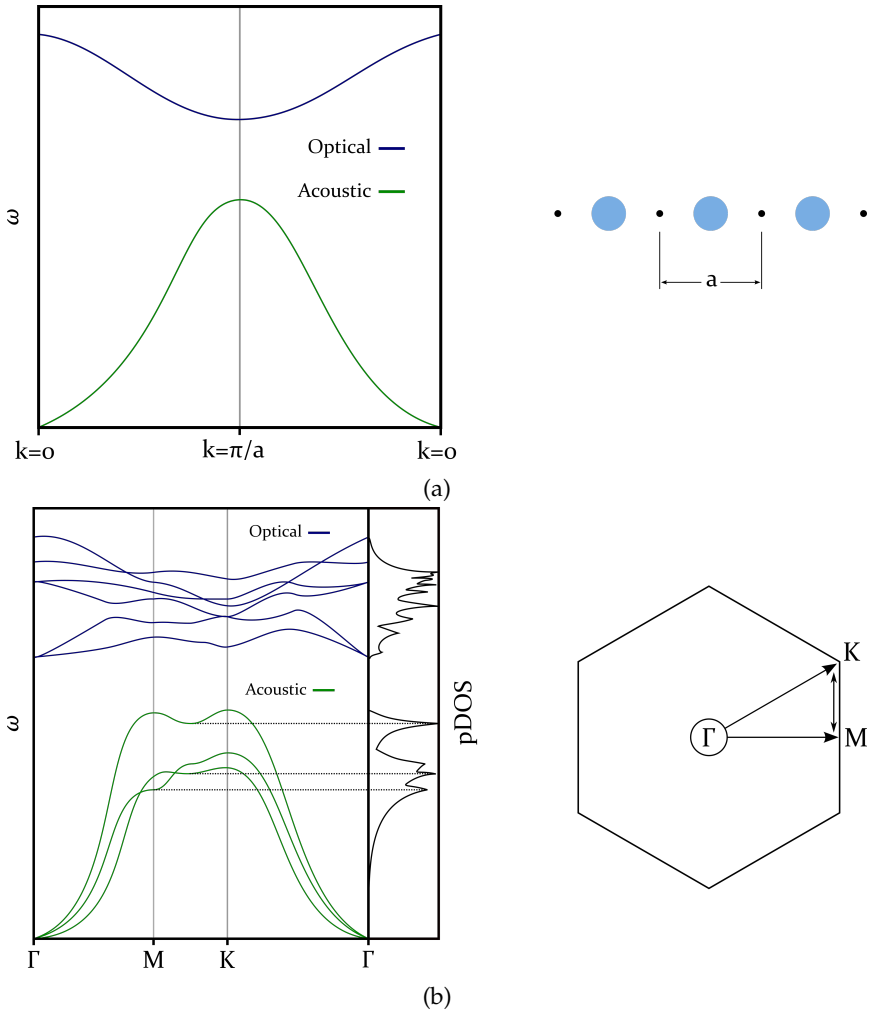

FIGURE 3.5: Schematic representations of phonon continuum and dispersion relations. (a) shows a hypothetical phonon dispersion for a 1D periodic system with lattice spacing of "a", indicated to the right. The BZ is in units of wavevector $\boldsymbol{k} = \pi/a$. Note in this a one-atom per unit cell system, there would be no optical modes. (b) Schematic representation of the phonon dispersion and phonon density of states (pDOS) for a crystal with two atoms in the 2D primitive cell with hexagonal symmetry. The dotted lines indicate areas where the gradient is shallow, which creates a large density of states (spikes in pDOS). The hexagon on the right shows which parts of the BZ are represented by the phonon dispersion, and the wavevectors of the phonon dispersion also contain components from the second crystallographic axis.

Basic Principles

Unlike infrared spectroscopy where the primary interaction is absorption of a low-energy photon, exciting a system to some higher vibrational state, the primary interaction in Raman spectroscopy is inelastic scattering of visible light. Incident photons are scattered via interaction with inhomogeneities in a medium, in this case, fluctuations in density brought about by vibrational motion.[168] This interaction involves an exchange of energy to/from the vibrational modes, which we measure as a subtle shift in the frequency of the scattered photon. We typically consider three main

scattering events in Raman spectroscopy: Rayleigh scattering, Stokes scattering, and anti-Stokes scattering. Figure 3.6 shows these processes schematically. In all cases, the process involves a brief excitation to some virtual state, which is considered to be a superposition of all the quantum states (vibrational and electronic) in the system, followed by relaxation down to some vibrational energy level by emitting a photon. This scattering process is rather weak, with typical probabilities giving one Raman scattered photon for every one million photons incident, and as such high quality filters and sensitive detectors are typically used.[169] That being said, modern instruments are remarkably efficient and well engineered, meaning most commercial Raman systems do not require painfully long acquisition times or low-light environments (see section 2.1 for instrument design details).

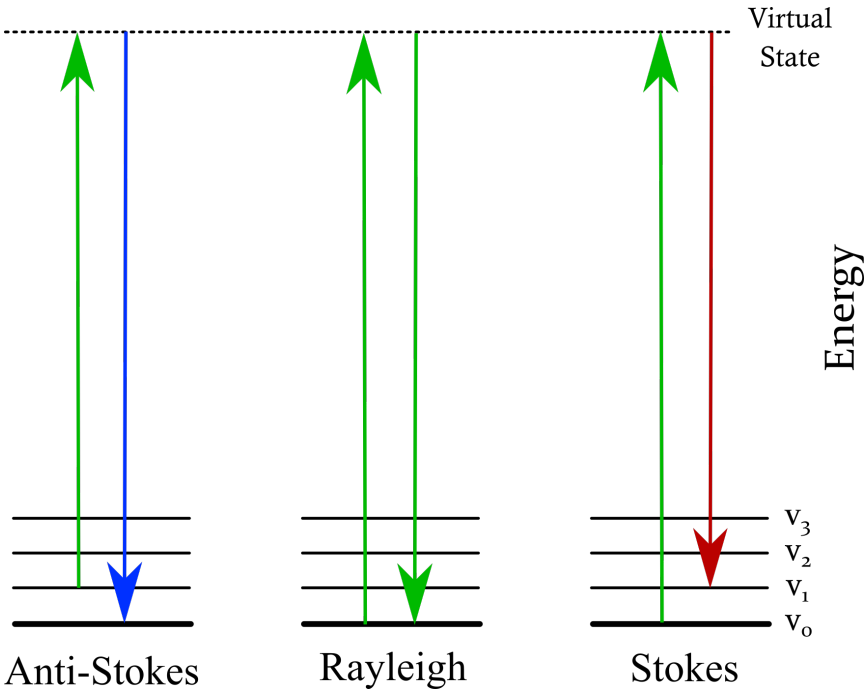

FIGURE 3.6: Schematic representation of the classical Raman process. v_0 indicates the ground vibrational state, while $v_{1\rightarrow3}$ indicate excited vibrational states. The virtual state is much higher in energy than the highest vibrational state.

In the Rayleigh process, the initial and final states are identical, and therefore no energy is exchanged and the process is considered elastic scattering. In the Stokes process, the final state is some higher energy vibrational state than the initial. Energy is imparted on the system from the photon in the form of creation or excitation of a phonon, and the resulting scattered photon energy is less than the incident photon. In the anti-Stokes process, the initial state is some already excited vibrational state, and the final state is lower in energy, such that the scattered photon has gained some energy from the system (by absorbing a phonon). The final change in energy of the photon is typically given as a "Raman shift" measured in inverse centimetres from

the excitation frequency (cm^{-1})(wavenumbers).

In order for a vibrational mode to be Raman-active, the vibration must induce a change in the polarizability of the atoms involved, which is essentially a measure of how easily the atoms in a molecule or material are polarized by an electric field. This is the primary selection rule for Raman scattering. In molecules, where an oscillating electric field induces a localised molecular dipole, this is known as the molecular polarizability α, and the induced dipole moment $\boldsymbol{p}$ by an electric field $\boldsymbol{E}$ is expressed as

$$\boldsymbol{p} = \alpha \boldsymbol{E} \tag{3.1}$$

For extended systems such as crystalline MoS_2, instead of a discrete dipole (at a specific point in space) the oscillating electric field induces a polarization density $\boldsymbol{P}$ throughout the material. As such we consider the polarizability per unit cell described by the average electric susceptibility χ, whereby

$$\boldsymbol{P} = \epsilon_0 \chi \boldsymbol{E} \tag{3.2}$$

where ϵ_0 is the electric constant (vacuum permittivity) and χ is related to the dielectric constant of the material ϵ_r by $\chi = \epsilon_r - 1$. In the case of a simple molecular crystal α and χ are essentially equivalent, as the unit cell will contain a single molecule. In other systems we may relate χ and α by the Clausius-Mossotti relation:

$$\frac{\chi}{\chi + 3} = \frac{N\alpha}{3\epsilon_0} \tag{3.3}$$

where N is the density of atoms/molecules per unit volume.

Given that the electric field of linearly polarized light is an oscillating sine wave in space and time, we can write the electric field experienced by the crystal under irradiation as

$$\boldsymbol{E}(\boldsymbol{r}, t) = \boldsymbol{E_i}(\boldsymbol{k_i} \cdot \omega_i) \cos(\boldsymbol{k_i} \cdot \boldsymbol{r} - \omega_i t) \tag{3.4}$$

with a wavevector $\boldsymbol{k_i}$ and angular frequency ω_i, and where $\boldsymbol{r}$ is the spatial position vector, $\boldsymbol{E}_i$ is the wave amplitude/magnitude of the electric field, t is time. The subscript i indicates the incident photon.

The induced polarization of a crystal $\boldsymbol{P}$ by $\boldsymbol{E}(\boldsymbol{r}, t)$ is then,

$$\boldsymbol{P}(\boldsymbol{r}, t) = \boldsymbol{P}(\boldsymbol{k_i}, \omega_i) \cos(\boldsymbol{k_i} \cdot \boldsymbol{r} - \omega_i t) \tag{3.5}$$

where

$$\boldsymbol{P}(\boldsymbol{k_i}, \omega_i) = \chi(\boldsymbol{k_i}, \omega_i) \boldsymbol{E_i}(\boldsymbol{k_i} \omega_i) \tag{3.6}$$

An important note from this is that the induced polarization has a characteristic wavevector and frequency, which it inherits from the incident electric field, and the magnitude of the induced polarization is determined by the magnitude of χ.

The atomic displacements $\boldsymbol{Q}(\boldsymbol{r},t)$ brought about by a phonon can also be represented as wave equations, where

$$\boldsymbol{Q}(\boldsymbol{r},t) = \boldsymbol{Q}(\boldsymbol{q},\omega_0)\cos(\boldsymbol{q}\cdot\boldsymbol{r}-\omega_0 t) \tag{3.7}$$

with wavevector $\boldsymbol{q}$ and frequency ω_0, and these atomic displacements modify χ.

Yu and Cardona[168] show that a combination of induced polarization from the incident radiation and the oscillating χ induced by the atomic vibrations leads to the expression

$$\begin{aligned}\boldsymbol{P_{ind}}(\boldsymbol{r},t,\boldsymbol{Q}) =&(\partial\chi/\partial\boldsymbol{Q})_0\boldsymbol{Q}(\boldsymbol{q},\omega_0)\ \cos(\boldsymbol{q}\cdot\boldsymbol{r}-\omega_0 t)\ \boldsymbol{E}_i(\boldsymbol{k}_i,\omega_i)cos(\boldsymbol{k}_i\cdot\boldsymbol{r}-\omega_i t)\\ =&\frac{1}{2}(\partial\chi/\partial\boldsymbol{Q})_0\boldsymbol{Q}(\boldsymbol{q},\omega_0)\ \boldsymbol{E}_i(\boldsymbol{k}_i,\omega_i t)\times\\ &\{cos[(\boldsymbol{k_i}+\boldsymbol{q})\cdot\boldsymbol{r}-(\omega_i+\omega_0)t]\\ +&\ \ cos[(\boldsymbol{k_i}-\boldsymbol{q})\cdot\boldsymbol{r}-(\omega_i-\omega_0)t]\}\end{aligned} \tag{3.8}$$

where the last two terms contain the Stokes and and anti-Stokes scattered radiation. Frequency and wavevector are both conserved in the above equations, and we can write $\omega_i = (\omega_s \pm \omega_q)$, and $\boldsymbol{k}_i = \boldsymbol{k}_s \pm \boldsymbol{q}$ (where the subscripts i and s denote incident and scattered radiation, and $\boldsymbol{q}$ is the phonon wavevector). Frequency conservation accounts for the Stokes and anti-Stokes scattered light, and wavevector conservation leads to an important consequence for Raman spectroscopy in crystals. Figure 3.7 shows that for wavevector conservation to hold, the magnitude of the phonon wavevector, $\boldsymbol{q}$ must be less than twice the photon wavevector.

The photon wavevector can be given by $\boldsymbol{k}_i = 2\pi/\lambda$, and that of the phonon is dependent on its location in the BZ. This means zone-edge phonons can reach as far as π/a, where a is the lattice spacing. If we choose a standard visible laser wavelength of 532 nm, and use the lattice spacing for MoS_2 as 3.16 Å, we find

$$\frac{\pi}{3.16\,\text{Å}} = 0.9943\,\text{Å}^{-1} \gg 2\left(\frac{2\pi}{5320\,\text{Å}}\right) = 2.36\times10^{-3}\,\text{Å}^{-1} \tag{3.9}$$

which shows the photon wavevector is approximately 200 times smaller than the width of the BZ, and so we define the section rule in crystals that *for one-phonon (first-order) processes only phonons near the zone-center* Γ *can be observed.* The allowed values of $\boldsymbol{q}$ are small enough that $\boldsymbol{q}$ is typically considered to be zero, and is commonly referred to as the $q \approx 0$ selection rule.

The intensity of Raman scattering is often given as

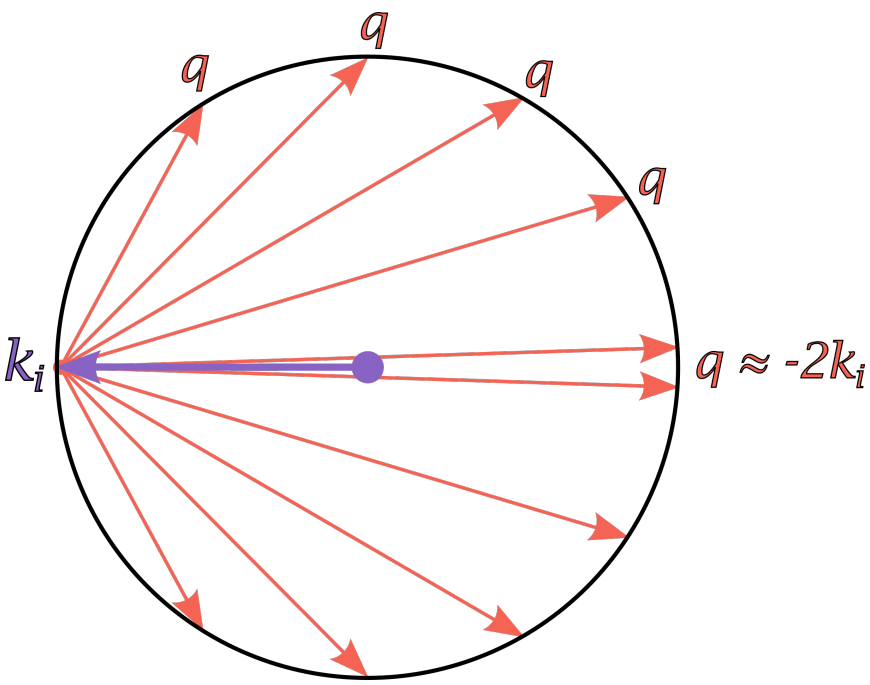

FIGURE 3.7: Schematic demonstrating wavevector conservation. For wavevector conservation to hold, only those wavevectors with the tail on $\boldsymbol{k}_i$ and head somewhere on the black circle will allow a photon of the same magnitude as the incident photon wavevector $\boldsymbol{k}_i$ to be emitted. Assuming a continuum of phonons exists, this will contain any vector from 0 to $|2\boldsymbol{k}|$.

$$I_s \propto |\boldsymbol{e}_i \cdot \mathcal{R} \cdot \boldsymbol{e}_s|^2 \tag{3.10}$$

where $\boldsymbol{e}_i$ and $\boldsymbol{e}_s$ are the (linear) polarizations of the incident and scattered radiation respectively, and $\mathcal{R}$ is a second rank tensor known as the Raman tensor. The Raman tensor relates the incident and scattered photon polarizations, and the non-zero elements of its 3×3 matrix (its "shape") depend on the symmetry of the vibrational mode, and for certain polarizations the Raman scattering intensity will be zero. In addition, measuring the polarization dependencies allows one to determine the phonon symmetries of Raman-active modes in a spectrum.

The formulation in equation 3.8 provides a macroscopic or classical theory. In order to describe the resonant Raman process, where the intermediate state is a real excited electronic state and the Raman intensity is dependent on the excitation energy, we need to use a microscopic/quantum mechanical theory. This can be established by breaking down the Raman process into three steps: photon absorption, phonon interaction, and photon emission. The probability of Raman scattering can be expressed using Fermi's Golden Rule as

$$P(\omega_s) = \left(\frac{2\pi}{\hbar}\right) \left| \sum_{a,b} \frac{\langle f| \mathcal{H}_{eR}(\omega_s) |b\rangle \ \langle b| \mathcal{H}_{e-ion} |a\rangle \ \langle a| \mathcal{H}_{eR}(\omega_i) |i\rangle}{[\hbar\omega_i - E_x - i\Gamma]\,[\hbar\omega_i - \hbar\omega_0 - E_x - i\Gamma]} \right|^2 \times \delta\left[\hbar\omega_i - \hbar\omega_0 - \hbar\omega_s\right] \tag{3.11}$$

where i, a, b, and f are the initial, photo-excited intermediate, scattered excited intermediate, and final states respectively. $\hbar\omega_i$ is the incident photon energy, $\hbar\omega_0$ is the phonon energy, $\hbar\omega_s$ is the scattered photon energy, and E_x is the energy of the $\langle a| |i\rangle$ transition.[168] Γ is a damping constant inversely proportional to the process lifetime. Note the resonance can be termed "incoming" or "outgoing" based on whether the resonance matches the first or second of the denominator terms respectively.

The Hamiltonians $\mathcal{H}_{eR}$ and $\mathcal{H}_{e-ion}$ are that of the electron-radiation (electric dipole) and electron-phonon interactions respectively. The electron-radiation Hamiltonian describes the photon absorption process and can be given by

$$\mathcal{H}_{eR} = \frac{e}{mc} \boldsymbol{A} \cdot \boldsymbol{p} \tag{3.12}$$

which contains a vector potential $\boldsymbol{A}$ generated by the electric field, and a momentum operator $\boldsymbol{p}$ for the electron. The electron-phonon interaction describes the change in energy of the electrons as the atoms are displaced by vibrations, and can take many forms depending on the type of phonon involved. These are described in detail by Yu and Cardona,[170] but have the general form

$$\mathcal{H}_{e-ion}(\boldsymbol{r}_i, \delta\boldsymbol{R}_j) = \left(\frac{\partial \mathcal{H}_e}{\partial \boldsymbol{R}_j}\right)\Bigg|_{\boldsymbol{R}_j} \cdot \delta\boldsymbol{R}_j \tag{3.13}$$

where $\boldsymbol{r}_i$ denotes the position of an electron (in the electronic Hamiltonian $\mathcal{H}_e$) and $\boldsymbol{R}_j$ denotes the position of the atoms, while $\delta\boldsymbol{R}_j$ is a function describing their vibrational motion. Note that this is the first-order term of a Taylor series expansion of the electronic Hamiltonian $\mathcal{H}_e(\boldsymbol{r}_i, \boldsymbol{R}_j)$ using the Born-Oppenheimer approximation.

In general, the electron-phonon interactions can be described using deformation potentials and strain tensors, which arise as a consequence of perturbations to the lattice from thermal fluctuations, incident electromagnetic radiation, and electrostatic potentials from propagating excited-state charge carriers. The magnitude of the evaluated electron-phonon interaction matrix elements is known as the electron-phonon coupling (EPC) strength, and a strong EPC can be thought of as involving processes where the phonon geometry helps translate the electron from some initial to some final electronic state.

Raman Spectroscopy of MoS_2

Raman spectroscopy is prevalent in semiconductor research due to the ability for excited state charge carriers to generate additional scattering interactions. These effects are particularly evident in MoS_2, as the layered structure results in a reduced coulombic screening of charge carriers, which allows tightly bound excitons to form with energies on the order of 200 meV - observable at room temperatures. As such, excitonic effects dominate the on-resonance Raman spectrum, and Livneh and Spanier[171] show that up to 80 individual Raman peaks can be observed and assigned under excitation resonant with the direct band gap at the K point of the BZ. These resonant-enhanced features are a result of multiple exciton-phonon interactions throughout the BZ, not just limited to the zone-centre Γ. Therefore it is useful to have a basic understanding of semiconductor physics, and the reader is referred to Yu and Cardona[168] for detailed descriptions of the multitude of scattering processes, and Kitajima[132] for a good background on defect scattering in Raman spectroscopy.

The first order Raman-active modes of MoS_2 can be identified by applying the Raman selection rules and symmetry constraints, and are shown for off-resonance conditions in table 3.1.

The E_{1g} mode is rarely observed as it is forbidden in the backscattering geometry used in most microscopy setups,[173] and the E^2_{2g} mode is below the wavelength cutoff of most Raman systems, typically requiring a low-frequency system (like ours) to observe. As such, literature typically focuses on two main modes for MoS_2: E_{2g} and A_{1g}. Incidentally, it has been shown that the difference in wavenumber between the E_{2g} and A_{1g} is proportional to layer number - thereby making it a convenient metric for quantifying layer number in materials publications. However, the peak shift is insignificant above 4-5 layers, and small enough in few layers that peak fitting is typically required for accurate measurement. Care must be taken to minimise contributions to the peak positions from other factors including dopants, strain, and inhomogeneous broadening effects.

If one aims to quantify layer number with Raman spectroscopy alone, the best approach is to observe the evolution of the interlayer shear modes and breathing modes (B^2_{2g} and E^2_{2g} respectively), which shift dramatically as layer number decreases.[148,174] These modes arise from synchronous motion of the entire layer, where the shear mode corresponds to an in-plane layer sliding motion, and the breathing mode is an out-of-plane expansion and contraction of the interlayer distance. Since the entire layer is involved, the frequencies of these modes are very low, and requires high quality lasers and specialised low-frequency optics to filter out the laser line only. Although it is now possible to purchase low-frequency Raman microscopes, such instrumentation is not common. Even in our low-frequency setup we struggle to observe the breathing mode in MoS_2, as our spectrograph resolution is relatively low and stray light from the Rayleigh line often obscures this region. Therefore, where it is pertinent to identify layer number in this work, atomic force microscopy

(AFM) is used which, for appropriately prepared samples is capable of quantifying layer number.

TABLE 3.1: The Raman-active fundamental modes of MoS_2, as reported by Livneh and Spanier[171] and Kim *et al.*[172]

Irreducible Representation	Frequency (cm^{-1})
B^2_{2g}	15
E^2_{2g}	35
E_{1g}	286
E^1_{2g}	383
A_{1g}	408

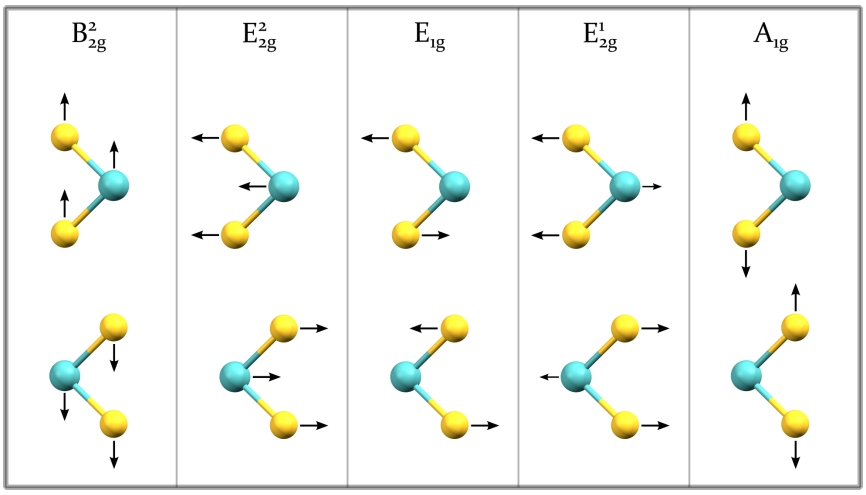

FIGURE 3.8: The relative motion of each atom in the unit cell of 2H-MoS_2 for each of the Raman-active irreducible representations (at Γ), as indicated by the arrows.

3.1.3 Double Resonance Raman

Under appropriate resonance conditions MoS_2 displays a rich, multi-phonon higher-order spectrum due to strong electron phonon coupling to tightly bound excitons (exciton-phonon coupling). Higher-order features are a consequence of scattering via multiple phonons before relaxation - with second-order features involving two phonons, third-order involving three and so on. A key feature of higher-order Raman processes in solid-state is that because more than one phonon is involved, the allowed phonons are not limited to those near the Γ point, as momentum can still be conserved when $\boldsymbol{q}_1 \gg 0$ so long as the total combination of phonon wavevectors upon relaxation is near 0. For a second-order process, this means $\boldsymbol{q}_2 = -\boldsymbol{q}_1$, and an

n^{th} order processes $\sum_{i=1}^{n} \boldsymbol{q}_i = 0$. The $\boldsymbol{q}_2 = -\boldsymbol{q}_1$ condition is known as a backscattering condition (in reciprocal space), as the phonon wavevectors are rotated 180° from each other.

These higher-order processes can be observed at low-temperatures and under resonant conditions.[175–177] It should be noted that these higher-order processes are not limited to optical phonons, and that acoustic phonons and their combinations can be observed by the interaction with the excited electron.

There is a distinction to be made between a standard off or on-resonant second-order feature, and a double resonance feature. The scattering probability of a higher-order processes will be significantly enhanced if the electron is scattered into another real state (also in/near resonance), rather than to or from a virtual state (see Figure 3.9).[178] This process is described as double resonance Raman (DRR) and triple resonance Raman (TRR) for processes with any two or three real excited states respectively, and has been used extensively to explain the multi-phonon spectrum of graphene and TMDs. A unique feature of DRR and TRR bands is that because scattering occurs to real states the wavevector responsible is bound by energy conservation, and as different excitation energies are used different wavevectors are required to connect the initial and scattered states (see Figure 3.10). This results in bands whose frequency disperse with excitation energy.

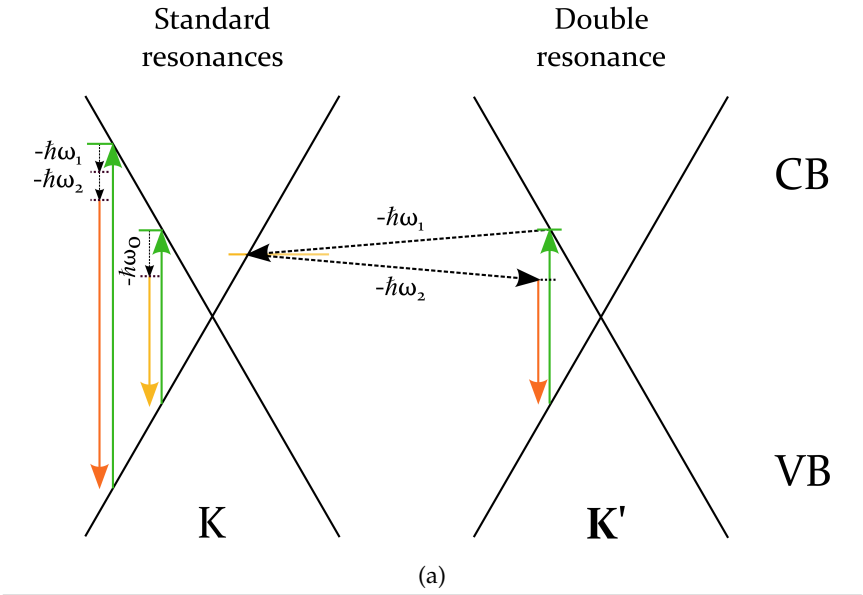

FIGURE 3.9: Representation of the DRR process in a 2D slice of the BZ around K-K′. Dotted lines ($\hbar\omega$) indicate phonons (their energy). Horizontal dotted lines at the arrowheads indicate virtual states, and anywhere an arrow lands on the solid lines of the band structure are real states. Processes from left to right are: standard resonant second-order mode, standard resonant first-order mode, and double resonant intervalley scattering. Note if $\omega_1 = \omega_2$, it is the first overtone of ω, if $\omega_1 \neq \omega_2$ and both have the same sign, it is a combination mode, and if $\omega_1 \neq \omega_2$ with different signs, it is a difference band.

Graphene

Graphene serves as an ideal introduction to DRR due to its unique band structure, and conveniently shares the same hexagonal symmetry as MoS_2. It is a semi-metal (or zero band-gap semiconductor) where the valence and conduction bands meet near the Fermi level in Dirac cones at the K and K′ points of the BZ - known as the Dirac points (see Figure 3.9/3.10). This means that direct (vertical) transitions near the K point are possible at a continuous range of wavelengths spanning the near infrared and visible. Therefore, resonance can be achieved with almost any visible laser, and the dispersion of phonon modes can be followed accordingly.

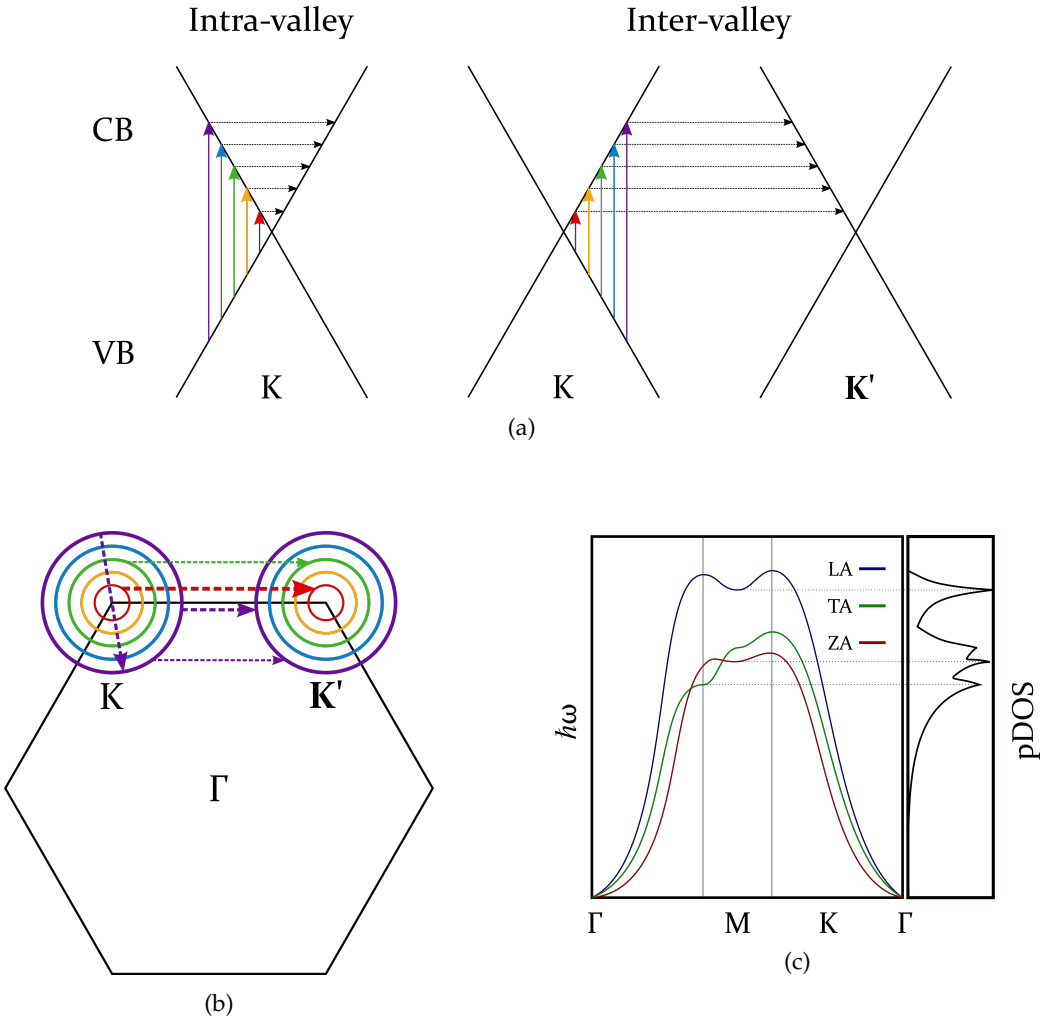

FIGURE 3.10: (a) Depiction of Dirac cones at K points of BZ for graphene, showing how different excitation energies result in different wavevectors/phonons (dotted lines) connecting two real states. (b) Schematic of a hexagonal BZ, with circles around the K points indicating in 2D the relationship between excitation energy and phonon wavevector in (a). The arrows are an arbitrary selection of wavevectors showing various possible scattering processes. The size of the arrow (also arbitrary) represents a probability of interaction, which depends on a number of factors. (c) Representation of the acoustic phonons in a hexagonal BZ phonon dispersion.

Figure 3.10(a) shows how for different laser wavelengths, direct transitions occur at different distances (actually different radii in 3D BZ) away from the K points. K' indicates an adjacent K point in the BZ. Upon excitation to the CB, intra-valley and inter-valley scattering can occur via phonons with appropriate wavevectors (dotted lines). For the intra-valley process, these wavevectors increase in magnitude as excitation energy increases, while for the inter-valley process the wavevector magnitudes decrease with increasing energy. These trends are a consequence of the shape of the electronic band structure. In graphene, the trends are approximately linear near the K points, but in most materials (including MoS_2) these bands are parabolic in shape. Figure 3.10(b) shows an arbitrary selection of wavevectors in the 2D BZ which represent some intra-valley and and inter-valley scattering processes. The thicknesses of the arrows suggest different probabilities of scattering (also arbitrary), which are a result of several factors, including whether the phonon can even connect the states by symmetry (allowed/not), the magnitude of the EPC, and the number (density) of phonon states around this wavevector (c). Note that for any wavevector there are several branches in the phonon dispersion which may be capable of scattering the charge carrier - which can be an electron, hole, or other quasi-particle (e.g. exciton).

The intensity of the DRR modes can be defined by adding a term for the second intermediate state to eqation 3.11

$$P(\omega_s) = \left(\frac{2\pi}{\hbar}\right) \times \left| \sum_{a,b,c} \frac{\langle i|\,\mathcal{H}_{eR}(\omega_s)\,|c\rangle\ \langle c|\,\mathcal{H}_{e-ion'}(\omega_2)\,|b\rangle\ \langle b|\,\mathcal{H}_{e-ion}(\omega_1)\,|a\rangle\ \langle a|\,\mathcal{H}_{eR}(\omega_i)\,|i\rangle}{[\hbar\omega_i - E_x + i\Gamma]\,[\hbar\omega_i - \hbar\omega_a - E_x + i\Gamma]\,[\hbar\omega_i - \hbar\omega_a - \hbar\omega_b - E_x + i\Gamma]} \right|^2 \times \delta\left[\hbar\omega_i - \hbar\omega_1 - \hbar\omega_2 - \hbar\omega_s\right] \tag{3.14}$$

where a, b, and c, are the intermediate states and $\hbar\omega_1$ and $\hbar\omega_2$ are the phonons scattering a to b and b to c respectively.

The above situations describe DRR processes for phonon emission, and the same principals apply to phonon absorption (anti-Stokes) and difference bands, provided there is a sufficient density of phonons in an excited state. We can use the Bose-Einstein distribution to estimate the ratio of phonons of energy $\hbar\omega$ in the excited and ground states as

$$\frac{N_0}{N_i} = \left\{ e^{\hbar\omega/k_B T} - 1 \right\}^{-1} \tag{3.15}$$

where k_B is the Boltzmann constant and T is temperature. Equation 3.15 shows

that the ratio of phonons in the excited state drops off rapidly as temperature is lowered, and as such we would not expect much signal from anti-Stokes or difference bands in the Raman spectrum at low-temperatures, even if the resonance conditions are met.

In addition to scattering by phonons, crystal defects of all kinds can scatter excited state charge carriers, changing their momentum and providing an additional avenue for momentum conservation. The scattering of charge carriers by defects is considered elastic in an energy sense, such that if we were to consider the above DRR processes in the presence of a defect (see Figure 3.11), momentum conservation can be satisfied when one phonon is involved, and the resulting spectral signature is that of a first-order phonon.

Most crystal defects are either point defects or larger but generally disordered features, meaning that the scattering direction by these is somewhat random. This random scattering in crystals means that phonons from all across the BZ are able to satisfy momentum conservation, and the net result averaged over time is that features which approximate the density of states appear in the Raman spectrum.[132] We can also introduce the concept of a "phonon correlation length", which is essentially a measure of the distance over the crystal that a phonon can propagate, and is limited by anything that breaks the translational symmetry, such as defects.[132] The phonon line width in the Raman spectrum is inversely proportional to its phonon correlation length.

For line defects such as grain boundaries and edges an angle dependence

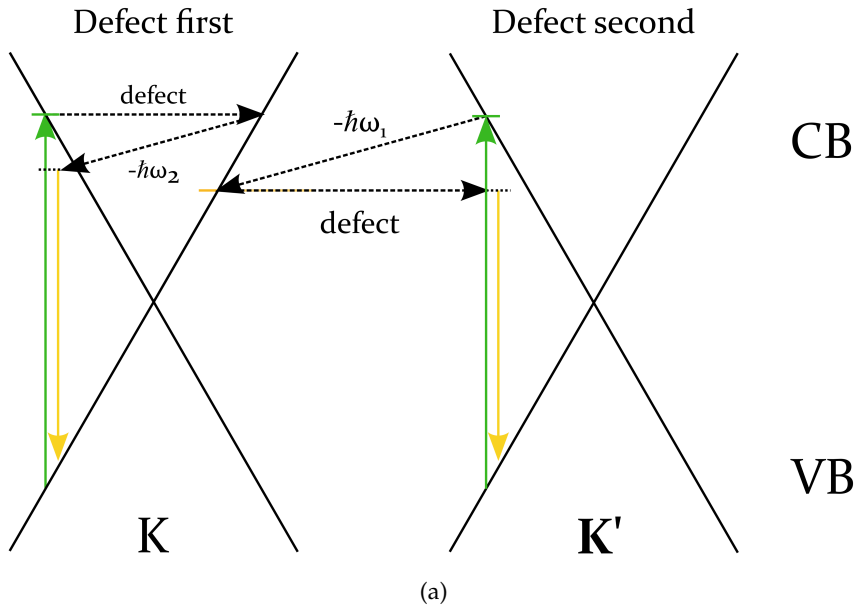

FIGURE 3.11: Representation of defect scattering DRR processes. Note the phonon exchanges energy with the excited state charge carrier, and therefore the arrow is pointed slightly lower down the bands to indicate a loss of energy. The defect scattering is elastic - no energy is exchanged so the arrow is horizontal.

emerges for collisions to satisfy momentum conservation. For an electron propagating through the crystal, scattering by one of these line defects is analogous to reflection of a photon off a mirror, in that the reflected angle with respect to the surface normal equals the incident angle (see Figure 3.12). This can be understood by treating the moving electron as a propagating wave in the medium, and that at the edge is a sharp change in refractive index between the crystal (which is typically high for solid-state media) and air, such that the electron is reflected back upon collision with an edge. Alternatively we can give a quantum mechanical explanation, where the electron's Bloch function is well defined in the crystal, and not at all in the vacuum, and so the edge acts as a large potential barrier and diffraction at the barrier results in reflection-like motion of the electron. Since the charge carriers are travelling in a direction consistent with their crystal momentum, their momentum is expected to change in a predictable manner.

We find that for an edge defect and a single phonon interaction, crystal momentum is only satisfied if the angle of incidence is normal to the edge direction. That is, only at normal incidence does a reflection produce $\boldsymbol{k}_r + \boldsymbol{K} = -\boldsymbol{k}_i - \boldsymbol{K}$ where $\boldsymbol{k}_i$ and $\boldsymbol{k}_r$ are the incident and reflected electron momenta, and $\boldsymbol{K}$ is a unit vector of the reciprocal lattice. This requirement is described as a real-space backscatter condition at the edge.

A consequence of this backscatter condition is that it is highly specific to a single direction in k-space, and results in a selection rule for those phonons. In graphene, optical absorption in the visible wavelengths occurs near the K-point of the BZ creating an electron-hole pair.[179] One of these charge carriers subsequently interacts with a TO phonon around the K point, which imparts the charge carrier with crystal momentum $\boldsymbol{q}_{phonon}$ and causes an intervalley scattering to the K' point. An edge-defect

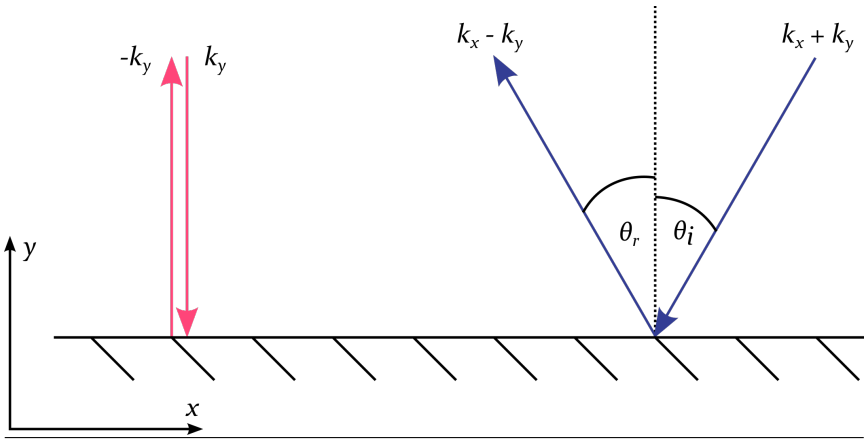

FIGURE 3.12: Representation of the elastic scattering at an edge. Any particle travelling towards the edge not at normal incidence (right, blue) has both x and y components in its wavevector. Upon reflection, only the y component is flipped, while the x component remains the same. This kind of reflection does not conserve crystal momentum. The reflection on the left is at normal incidence, and so only has a y component, and therefore does conserve crystal momentum.

can then mediate another inter-valley scatter with equal and opposite momentum $\boldsymbol{q}_{defect} = -\boldsymbol{q}_{phonon}$, thereby satisfying momentum conservation and allowing recombination to occur. This process results in the observation of the defect or D mode in graphene.[130,131]

Given the backscattering requirements above and that only the TO(K) and none of the M phonons are involved in the D mode, only the arm-chair edges have the correct orientation to satisfy the backscattering constraints in reciprocal space, as the zigzag edge is perpendicular to the M point (see Figure 3.13). As such, the D mode in graphene can be used to determine crystallographic orientation and the structure at the edge,[131] which can strongly influence the electronic properties, particularly for nanomaterials such as 1D nanoribbons.[115,116]

This backscatter condition also applies in real space for free charge carriers, as for recombination to occur after scattering, the electron and hole must be reunited in approximately the same region of space (Figure 3.14).[130]

During excitation, an incident photon with polarization $\boldsymbol{e}_{in}$ creates an electron and a hole with momenta $\boldsymbol{k}$ and $-\boldsymbol{k}$. Inspection of the matrix element for the creation/annihilation of an electron-hole pair shows that the direction of $\boldsymbol{k}$ and $-\boldsymbol{k}$ is proportional to $\boldsymbol{e}_{in} \times \boldsymbol{k}$, and that the probablility of generating an electron and hole in a specific direction is maximum when $\boldsymbol{e}_{in} \perp \boldsymbol{k}$.[130] Casiraghi *et al.* show that this results in a strong polarization dependence due to the backscattering requirements in both reciprocal and real-space.[131] From another perspective, Gruneis *et al.* show that an inhomogeneous absorption around the K point in graphite selectively enhances absorption of photons with polarization parallel to the armchair edge, thereby contributing to the observed polarization dependence.[180] Casiraghi *et al.* shows this dependence can be modelled with a $\cos^2\theta$ fit and through geometric and trigonometric analysis show that the intensity of the D mode can be given as

$$I(D)(\theta_{in}) = I(D)_{min} + [I(D)_{max} - I(D)_{min}]\cos^2(\theta_{in} - \theta_{max}) \tag{3.16}$$

where $I(D)_{min}$ and $I(D)_{max}$ are the minimum and maximum values for D mode intensity across all polarization angles, and θ_{in} and θ_{max} are the angles which correspond to some input polarization angle, and the angle which gives the maximum $I(D)$, respectively. They also show that for long armchair edges, $I(D)_{min}/I(D)_{max}$ tends towards 0 and for long zigzag edges $I(D)_{min}/I(D)_{max}$ tends towards 1, and values in between indicate a mixture of the two. There is also an identical relationship for the scattered polarization dependence, such that accounting for both incident and scattered radiation gives

$$\begin{aligned} I(D) =& [I(D)_{min} + [I(D)_{max} - I(D)_{min}]\cos^2(\theta_{in} - \theta_{max})] \times \\ & [I(D)_{min} + [I(D)_{max} - I(D)_{min}]\cos^2(\theta_{out} - \theta_{max})] \end{aligned} \tag{3.17}$$

where the analyser polarization angle θ_{out} replaces θ_{in}. It is not necessary to

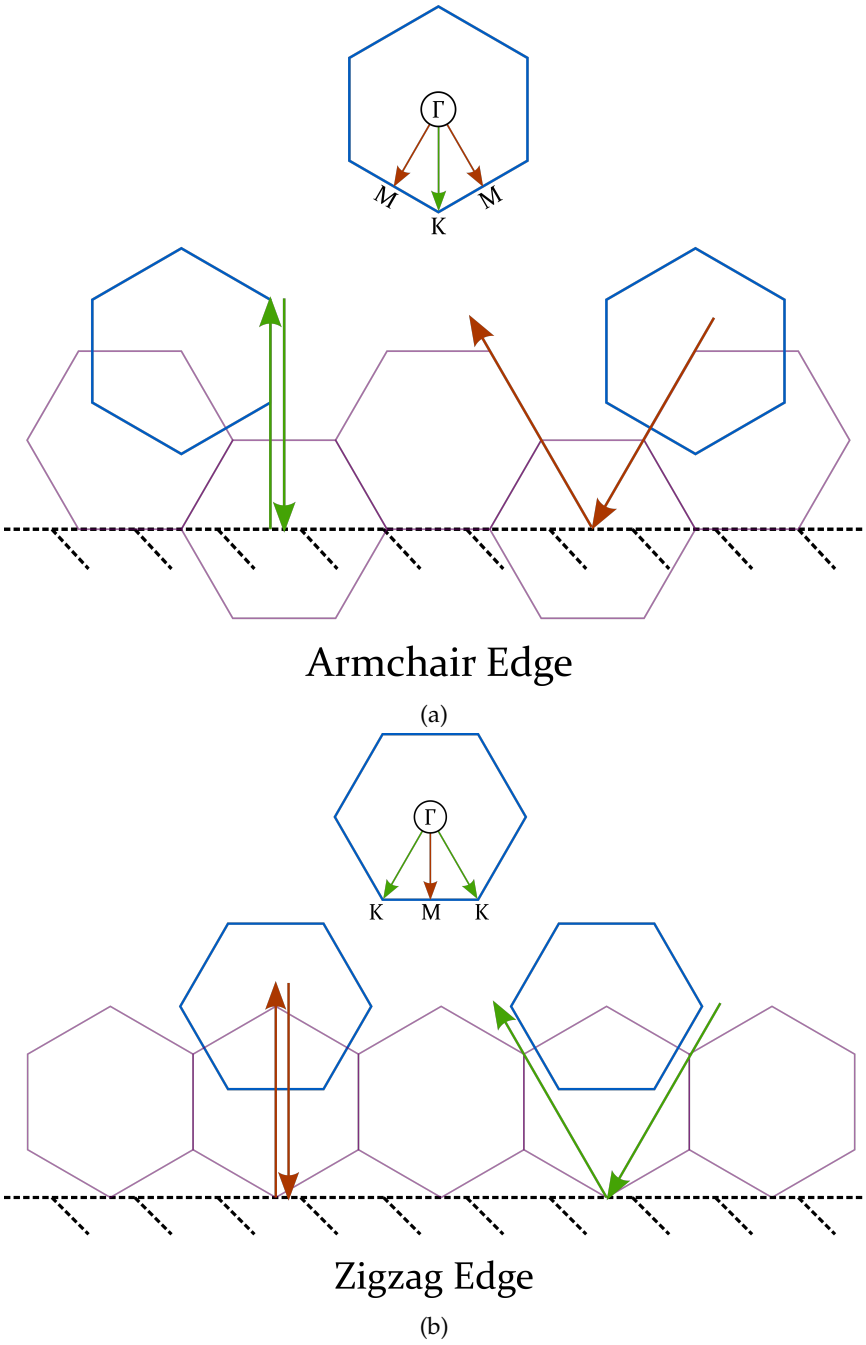

FIGURE 3.13: Representations of scattering at a hexagonal edge for (a) armchair and (b) zigzag edges. The blue hexagons represent the orientation in reciprocal space, and therefore an armchair edge is perpendicular to the ΓK (and KK') direction, while zigzag is perpendicular to the ΓM (and MM) direction.

measure the polarization state of the scattered radiation for most experiments, so equation 3.16 is sufficient for determining edge ratios. When performing Raman crystallography on these modes, the analysed polarization is fixed at exactly parallel or perpendicular polarization configurations, and therefore $I(D)_{||} \propto \cos^4\theta$ and $I(D)_{\perp} \propto \sin^2\theta\cos^2\theta$.[181]

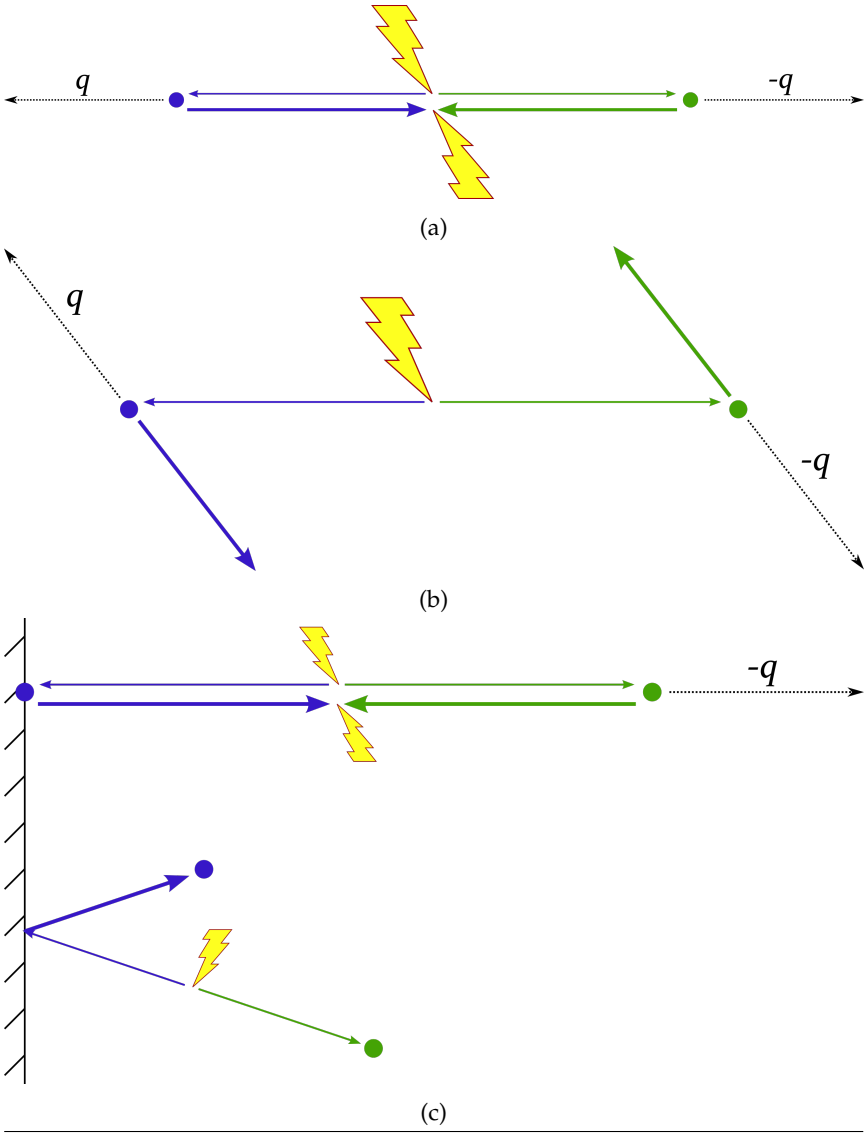

FIGURE 3.14: Various backscatter conditions in free space for single particles (adapted from Basko).[130] The lightning bolt indicates a photon absorption/emission, the blue circle is an electron, and the green circle is a hole. Solid arrows represent the direction of travel in real space and the dotted arrows indicate phonon interactions. (a) A two-phonon backscattering event conserves momentum and brings the particles back for recombination. (b) The phonon interactions send the charged particles away from each other, so recombination does not occur. (c) Edge scattering at normal (upper) and oblique incidence. Only the normal incidence returns charge carriers to the same point in space for recombination to occur.

MoS_2

The DRR experience in MoS_2 and the other layered TMDs is slightly different from graphene. Firstly, owing to the presence of a band gap, there is a lower limit to the energies capable of exciting electrons from the valence band to the conduction band. For MoS_2, the band gap is indirect for all but single layer thickness, which ranges from $\sim$1.3 eV in bulk to $\sim$1.5 eV in two-layers (2L).[54] For single-layer MoS_2 (1L),

a crossover occurs in the band structure which makes the lowest energy transition direct at the K point.[58] In addition, the bands around K are not linear but parabolic in shape.

Secondly, instead of single-particle charge carriers, excitations in MoS_2 and TMDs produce tightly bound excitons, where the electron and hole are correlated in space. While quantitative analysis of excitonic DRR phenomena requires consideration of effective masses and exciton band structures, the exciton-phonon scattering processes in DRR can largely be described qualitatively using a single-particle model, simplifying the interpretation.[103]

In MoS_2, spin orbit splitting of the VB near K results in the formation of two excitons - labelled A and B,[58] which are both involved in DRR phenomena.[182] As the lowest-energy direct inter-band transitions in MoS_2, these excitonic processes are responsible for most of the photo-physical properties of interest, and as such are the typical focus of DRR in literature. Higher energy excitations can provide additional insights into material properties, and are reviewed below.

The main DRR features in MoS_2 at these energies are a convolution of second-order combination and overtones between 380 and 500 cm^{-1}.[179] Accurate assignment of these features has been a topic of debate in literature due to the multitude of excitonic effects that can contribute to scattering processes.[168,183,184]

The ideal test for DRR features in a spectrum is to sweep laser excitation in small increments across the transitions of interest, and follow the evolution of phonon shifts with the dispersion relation. Each branch in the pDOS disperses uniquely, so computational analysis is invaluable for mapping experimental shifts to the calculated dispersion relations. Raman modes at Γ and normal second-order features do not shift with excitation energy.[178,179] To sweep excitation over relatively small energy ranges typically requires a tunable laser source such as a dye-laser (or titanium-sapphire for near IR) and triple spectrograph, which are not necessarily standard tools in the modern spectroscopy lab. The availability of high quality single mode lasers, blazed grating spectrographs, and high-performance Raman and laser-line filters has seen a shift away from these tunable setups in favour of more efficient designs. For instance, our setup uses a series of different lasers, each with dedicated optical filters and single stage spectrograph. Nevertheless, there are additional methods for testing DRR modes such as controlling temperature, pressure, and layer number, as these all shift the energy of bands in TMDs, moving different features in and out of resonance with a single excitation wavelength.

Recent studies by Carvalho *et al.*,[103] Gontijo *et al.*,,[182,185] and Fan *et al.*[186] using tunable lasers, temperature, pressure, and computational methods have made significant strides in understanding and assigning DRR contributions the second-order spectrum. For instance, Carvalho *et al.* has shown that the broad and intense feature around 460 cm^{-1} referred to previously as the 2LA band contains three DRR features assigned $\mathrm{LA}(\sim \mathrm{K}) + \mathrm{TA}(\sim \mathrm{K})$ (also known as the *b* mode)($\sim$ meaning

near), 2LA($\sim$ M), 2LA($\sim$ K), and one dispersionless second-order feature originating from the van Hove singularity half-way between K and M.[103] In this notation, the letter in the brackets identifies the high-symmetry point from which the phonon originates. The near degeneracy of the LA phonons at the M and K points complicates analysis, but their contributions become assignable when comparing layer number, as the scattering pathway responsible for the 2LA($\sim$ M) mode ($K_{CB}Q_{CB}$) is lost in single layers. In addition to these relatively well defined features, Livneh and Spanier propose a handful of additional weaker second-order features which are likely present across this band, contributing to the convolution.[171]

As it turns out, the 2LA(M) intervalley scattering is responsible for valley-depolarization,[187] and so understanding how these processes occur and how to work around them may facilitate the development of valley-polarized information storage applications.[98,99]

The nature of the DRR process means that the available scattering pathways depend on the energy landscape of the band structure. For instance, the aforementioned loss of M phonon resonances in 1L-MoS_2 is a result of the Q point shifting higher than the K point and no longer being within accessible energy of the LA(M) phonons. One can therefore imagine that photon energy selects a slice of the band structure about which scattering can occur - the width of this slice being dependent on the energy of the phonons available to access those states.

In this vein, higher-energy excitation probes deeper into the band structure, accessing not only new CB states but also new VB states - through which holes can scatter in DRR and TRR processes.

Fan *et al.*[186] use multiple excitation wavelengths across the visible (400-700 nm), noting that away from A and B excitons near 633 nm any DRR bands are weak or non-existent. This suggests that these regions of the band structure do not support DRR, either for energy or symmetry reasons.

However, in addition to the A and B excitons, the so named "C" exciton has garnered interest in literature, which forms under deep UV excitation from an absorption near the Q point in 1L-MoS_2. Liu *et al.*[176] and Sun *et al.*[188] have shown that this exciton also supports strong DRR bands. Liu *et al.*[176] show that excitation at 354 nm results in a dramatic enhancement of DRR features from 500-900 cm^{-1}. They attribute part of the enhancement mechanism in the UV to a large increase in absorption coefficient due to band nesting (VB and CB bands which temporarily run parallel) allowing more states to be accessed by a single excitation energy (i.e. larger joint-density of states (jDOS) at this wavelength). In addition, they indicate that these locations in the BZ match with regions of high phonon density in the pDOS. They use this argument to justify the interesting absence of DRR features in higher energy UV excitations, which absorb around Γ and Q in the BZ and correlate with relatively low pDOS. While this is accurate, they neglect to consider the electron-phonon coupling in these processes, and it is likely that the symmetries of the states

and phonons play a key role in determining which DRR modes are active at each excitation wavelength, and may explain the absence of K point phonons and M point difference bands in their DRR spectra.

For instance, Qiu *et al.*[60] show that several excitons contribute to the UV region of the MoS_2 absorption spectrum, which have fundamentally different orbital contributions than the A and B excitonic states. Carvalho *et al.*[189] then shows that the symmetry of the C excitonic states results in fundamentally different electron-phonon (exciton-phonon) coupling, leading to preferential enhancement of the E_{2g} mode over the A_{1g}, while the opposite relationship is observed for the A and B excitons.

Sun *et al.*[188] show that a similar set of modes become active at 325 nm excitation as a result of a TRR process involving hole scattering at the K point, which is particularly dependent on the magnitude of the spin-orbit splitting, providing a sensitive mechanism for the quantification of spin-orbit splitting in MoS_2.

It's worth pointing out that DRR and TRR bands have been minimally explored in other layered TMDs, including $MoSe_2$, WS_2, and WSe_2.[177,179,190–192] Each material has a similar but unique band structure - for instance in MoS_2 the Q_{CB} point is aligned with K_{CB} point in single layer and misaligned in bulk, while the opposite trend is observed for WS_2.[64,193] In addition, the size of the band gaps of these materials is significantly different, meaning the resonance onset for each material is at different energies/wavelengths. Given the relative infancy and complexity of this field, there remains significant scope for DRR research in TMDs.

Defects can also be probed with DRR in MoS_2, but not as effectively as in graphene. Instead of a sharp and clear "D mode", the effect of defects in MoS_2 creates broad, weak features in the 100-250 cm^{-1} region, while broadening the fundamental modes from a loss of long phonon correlation lengths.[132] The general consensus in literature is that defects in MoS_2 manifest as a simple non-specific breakdown of the $q \approx 0$ selection rule, resulting in features which resemble the pDOS.[133,179,185,194] However, as this work will show, resonant defect modes can be observed by utilising low-energy excitation to excite via the indirect band gap.

While the eventual fate of the A, B, and C excitons is to radiatively recombine, making them easily observable, it is possible to form excitons, trions, polaritons and other exotic quasiparticles throughout the BZ,[61] with many being non-radiative, or decaying from their initial states and appearing as A or B excitons. These "dark" excitonic processes can participate in phonon scattering and result in DRR features in Raman spectra.[63] Their contributions can be identified in the fine structure of absorption and pump-probe ultrafast spectroscopies.[62,195,196] It may be possible to encourage such dark excitons to radiatively decay sooner via interaction with defects, leading to the observation of exotic excited states via their unique spectral features.

3.2 Results

3.2.1 Initial Investigations in Nanomaterials - Direct Resonance and off-Resonance

The primary motivations for this work were to identify defect-related vibrational modes as a means of quantifying defects and pursuing the rational development of highly-efficient catalysts and photoluminescent materials. Although it is surprising that no resonant analogue of the graphene D mode has yet been reported for MoS_2, the exotic light-matter interactions provided by excitons (trions, charged, neutral, momentum indirect, spatially-indirect, dark/non-radiative etc.),[168] polaritons, and other quasiparticles may interact with defects and edges in unique ways to act as spectroscopic reporters.[197,198] In addition, it has been shown that defect trapped excitonic states can provide giant oscillator strengths for resonant-enhanced coupling to defect vibrational modes in semiconductors,[67,110,111,199,200] suggesting the same could be possible in MoS_2 to enhance local vibrational modes.

One of the challenges faced by early work was the onset of fluorescence in synthesised nanomaterials. As particle size decreases we expect more edges, and therefore expect to have a better chance of identifying edge vibrational modes from resonant techniques. However, as particle size decreases quantum confinement and exfoliated layer effects alter the energies of the band structure. One consequence of this is that in nanomaterials we observe significant fluorescence signal flooding the detector at 633 nm and 532 nm excitations, drowning out the relatively weak Raman signal. A second complication arose in the form of inhomogeneous broadening. For samples which were prepared using the somewhat crude "top down" methods such as ultrasonication, one can expect from the resulting nanoparticles a relatively random mixture edge structures and defect bonding arrangements, depending on the relative stabilities of such structures. The presence of contaminants such as oxygen, metallic ad atoms or organic molecules could diversify the possible structures further.[50] Consequently, it was not unusual for a sample to exhibit a broad (sometimes intense) baseline as a result of inhomogeneous broadening and fluorescent effects. These effects could dissipate and resolve into weak Raman bands upon laser-induced annealing at higher powers, indicating their initial relatively random nature.

In attempts to minimise fluorescent effects I moved to a lower energy excitation - 785 nm. There are several reasons why this is not an ideal option. Firstly, if we do not account for resonance contributions, Raman scattering intensity is proportional to the inverse 4_{th} power of the excitation wavelength, i.e. $I \propto \lambda_i^{-4}$, such that we stand to suffer a significant drop off in Raman scattered intensity by moving to 785 nm excitation. Secondly, it brings us below the direct band gap of MoS_2 which means we are no longer in resonance with the A and B excitons. While this helps minimise fluorescence, it means we may lose valuable excitonic effects. Excitation across the band-gap is still possible in the bulk through an indirect transition, but this requires

the interaction of a phonon to conserve crystal momentum, and lowers the rate of transitions considerably.[168]

These points considered, there are some advantages. In addition to lowering fluorescence signals, at lower energies we have better chances at exciting from/to mid-gap states induced by defects and edges,[66] whereas with 633 nm and 532 nm excitation the photon has enough energy to skip over any mid-gap states entirely. In addition, while the 633 nm and higher excitations have been explored thoroughly in literature, the lower energy excitations have not, presenting greater opportunity for novel discoveries.

3.2.2 Indirect Resonance

The sample type and characterisation methods used in Raman spectroscopy of MoS_2 typically depend on the motivations of the research. In many cases, such as when synthesising powders for catalysis or solutions of dispersed material, there is no need for orientation or polarization specific measurements as samples are typically randomly oriented. Conversely when electronic applications are in mind, such as in semiconductor and photovoltaic devices, samples are typically large crystals grown or mechanically exfoliated onto flat substrates. Most literature examining the properties of few and single-layer MoS_2 do so via chemical vapour deposition (CVD) or mechanically exfoliated samples on silicon, gold or sapphire substrates. These samples are 2D in nature with specific crystalline orientations, and therefore benefit from analysis with polarization and orientation specific techniques.

In order to observe how edges and defects affect the Raman spectrum, I utilise both 2D and powdered samples using a number of synthetic techniques. This section will initially focus on the former due to the well-defined edge and basal plane regions found in exfoliated flakes. Here, samples were prepared by mechanically exfoliating (scotch tape method) MoS_2 onto polished sapphire substrates (see section 5). I have also utilised CVD techniques to grow high-quality triangular crystals of MoS_2 on sapphire.

In order to effectively measure the spectral changes between specific regions of a sample (edge, basal plane, grain boundary etc.) we need fine positional control on the order of - and ideally smaller than - the diffraction limited spot size of our Raman microscope. The modification of our Raman microscope to enable high-resolution scanning experiments with low-frequency and low-temperature capabilities forms a significant component of this thesis, and is presented in Chapter 2. Here, I focus on the results generated by this instrument.

MoS_2 Flake Scans

Figure 3.15 shows the resonant and non-resonant Raman spectra of a flake of bulk mechanically exfoliated MoS2 at three excitation energies – 532 nm, 633 nm and

785 nm. For each excitation wavelength, spectra were taken from the linescans in Figure 3.16 at the marked points, corresponding to the edge and basal plane regions indicated on the optical image in Figure 3.15(b). A linescan as described here is a graph of the intensity of key Raman shift frequencies, plotted as a function of position across a sample.

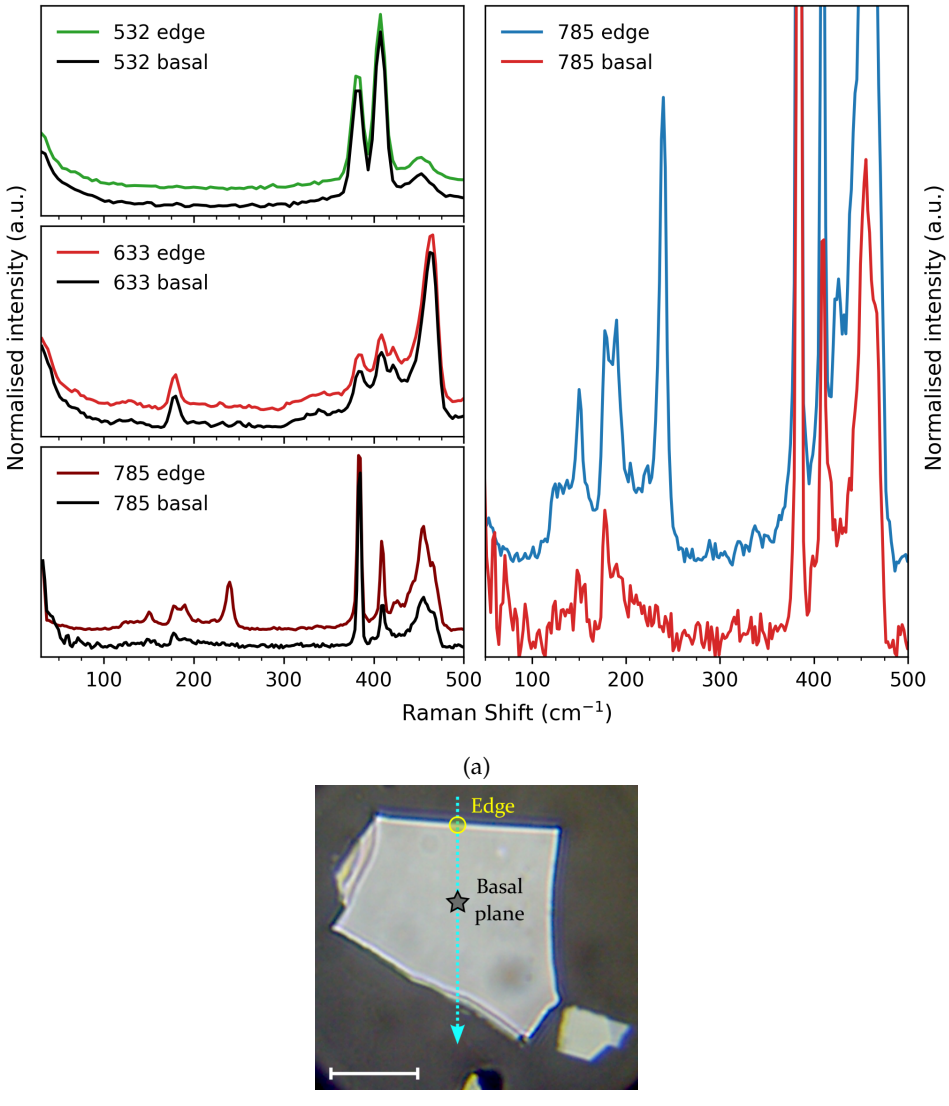

FIGURE 3.15: Raman spectra of linescan data over the flake in (b). (a) Left shows comparison of spectra for edge and basal plane regions (marked with yellow circle and black star respectively in (b)) for three excitation energies. Spectra are offset for clarity. (a) Right shows the 785 nm excitation spectra normalised to the 200-250 cm^{-1} region. Scale bar in (b) is 10 µm.

The spectra in 3.15(a) are normalised to the most intense band with the edge spectrum offset above the basal plane spectrum for clarity. At each excitation wavelength, the fundamental first order E_{2g} and A_{1g} modes are clearly visible near 383 cm^{-1} and 408 cm^{-1} respectively. It should be immediately clear that at 532 nm and

633 nm excitation (top and middle graph) there is little, if any difference between the edge and basal plane spectra. These correspond to the off-resonant and direct-resonant energies for 532 and 633 nm respectively. However, for 785 nm excitation (bottom graph) a set of features become prominent in the $100 - 250$ cm^{-1} region.

Figure 3.15(b) shows the 785 nm spectra normalised to this region with four sharp features at 238, 188, 177, and 149 cm^{-1}. It is clear from the linescan in Figure 3.16(a) that these modes are localised at the edges, with little to no intensity in the basal plane region. The exception to this is the mode at 177 cm^{-1} which, as will be shown later in the low-temperature measurements, is the the second-order A_{1g}(M)-LA(M) difference band observed under standard resonant conditions.[171]

At slightly higher frequency around 450 cm^{-1} is the signature of the double resonance Raman processes typically addressed in literature. Commonly referred to as the 2LA mode, this set of features results from the convolution of specifically enhanced two-phonon scattering events (e.g. the 2LA(M) and 2LA(K)), and a non-specific imprint of the 2pDOS from interactions across the BZ. Accurate assignment of this region is a topic of intense discussion in literature. Recent publications by

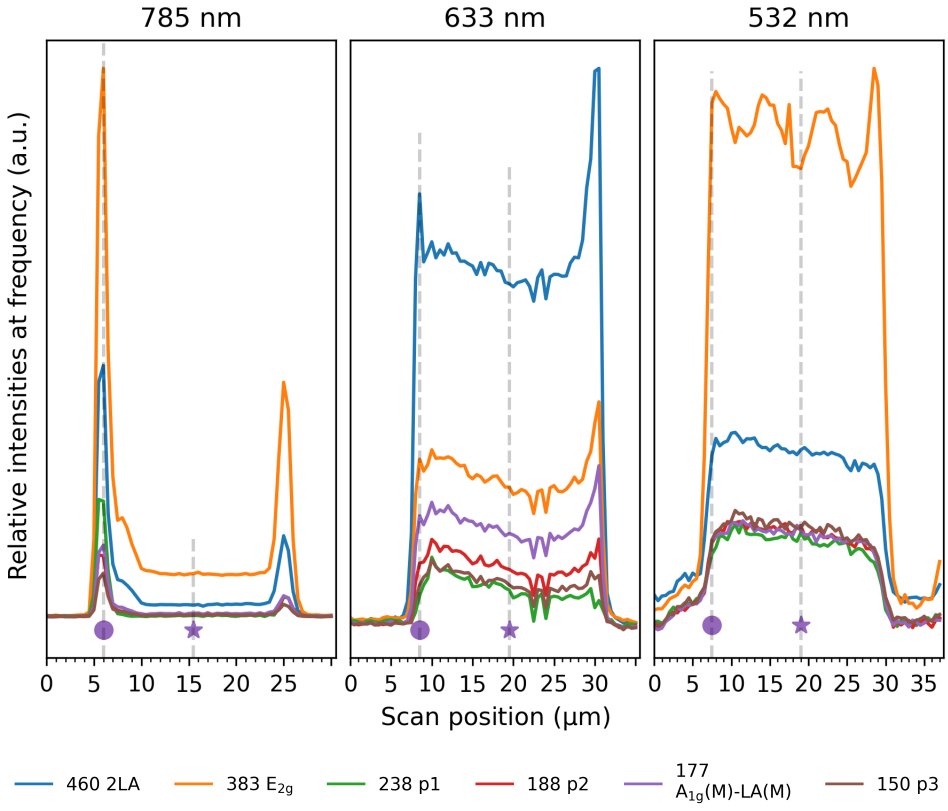

(a)

FIGURE 3.16: Linescans along the flake in Figure 3.15(c) for 785 nm (left), 633 nm (middle), 532 nm (right) excitation. The circles and stars represent the points at which the edge and basal plane spectra are taken.

Carvalho *et al.*[103] and Gonjito *et al.*[182] take advantage of tunable lasers and temperature control near 633 nm (∼1.96 eV) and show that distinct double resonance features contribute to the relatively broad shape, including the two-phonon LA processes from K and M points of the BZ. These features are useful for analysis, and we will return to them during the discussion of DRR features later.

Placidi *et al.*[201] have previously reported similar features in this low-frequency region using 785 nm and 1064 nm excitation lasers, assigning them to forbidden first-order acoustic phonons (including ZA(M), TA(M), LA(M) and LA(K)) and second order processes enabled by a defect-mediated indirect transition.

In their discussions, since they are observing in the basal plane and expect relatively defect-free material, they assume the defects involved are non-covalent interlayer stacking faults as opposed to covalent defects such as vacancies, grain boundaries and edges. However, I will show later that these defects must in fact be within the plane of each layer (covalent), and they were likely observing grain boundaries or small cracks in the crystal.

Defect induced bands in MoS_2 in the $150 - 230$ cm^{-1} region have been well reported in literature,[133,185] and the general consensus is that they are the sum of many acoustic phonons across the BZ. Whilst normally Raman-inactive, these modes appear as a result of elastic scattering by defects and a breakdown of the wave vector q≈0 selection rule crystalline materials, resulting in pDOS-like features in the spectrum.

The LA branches of the phonon dispersion reach inflection points near the M and K points around 220 cm^{-1}, resulting in a high pDOS around this frequency.[202–204] These LA features are therefore usually the first identifiable "defect bands" in this region, and are generally regarded as an indication of poor crystalline quality.[133] This effect can be seen in Figure 3.17(a), which shows the Raman spectra of a sonication series. In this series, MoS_2 powder is aggressively sonicated at high power to deliberately cleave the flakes into smaller pieces, while simultaneously exfoliating to few layers. After sonication, the samples are purified into size distributions via differential centrifugation, creating a series of decreasing average particle sizes. (a) shows the Raman spectra of these samples at 633 nm excitation, normalised to either the E_{2g} or A_{1g} fundamental modes. The inset shows the low-frequency region of interest, and we can see a clear trend for broad features emerging around 230 cm^{-1}, which is the commonly observed defect feature in literature. Figure 3.17(b) and (c) shows the same series under 785 nm excitation, and the contrast is striking. Three intense features grow as the series progresses, with distinct changes to features around the fundamental modes as well.

We therefore suggest that these features at 785 nm excitation are in fact defect modes, arising from single-phonon defect-mediated scattering, similar to what was reported by Placidi *et al.*[201] However, the sharpness and intensity of these features suggests that additional resonant mechanisms are involved. Also, the frequency of the most intense of these modes at 238 cm^{-1} is near the upper limit for an acoustic

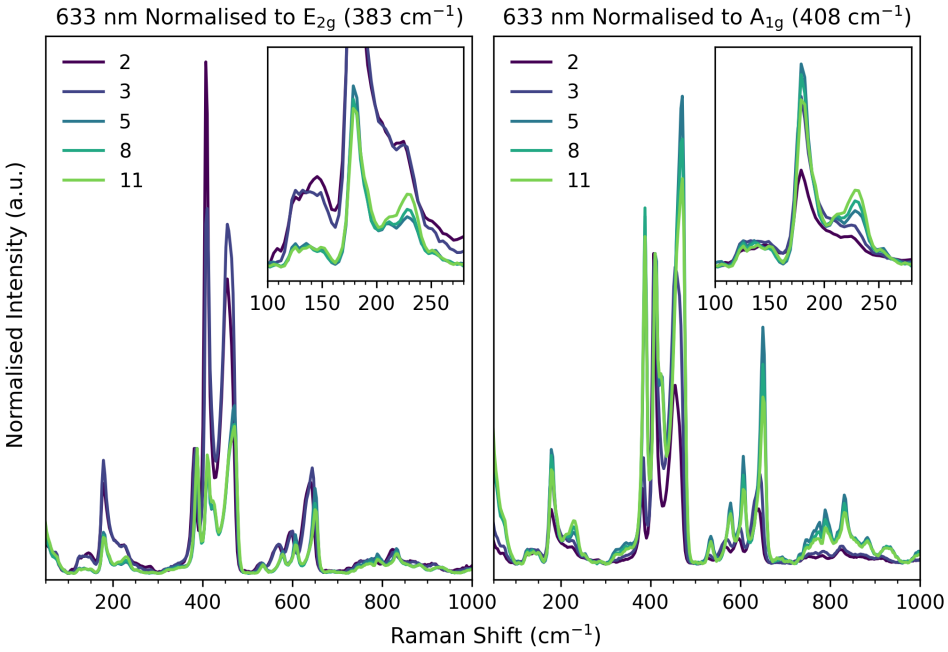

(a)

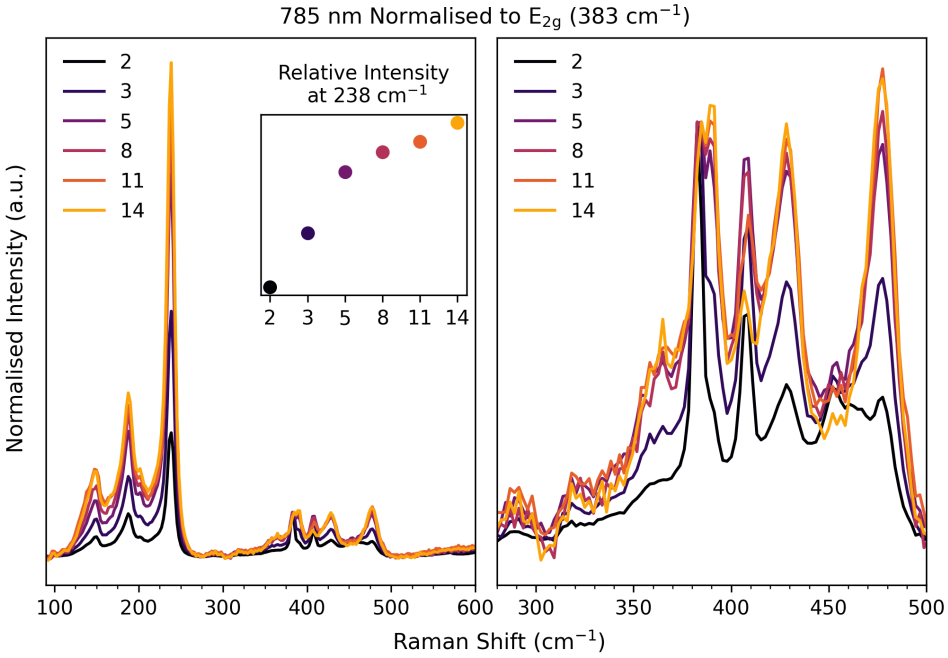

(b)

FIGURE 3.17: Series of sonicated MoS_2 particles at (a) 633 nm and (b) 785 nm excitation. The labels of each spectra are numbers based on the centrifugation speed used to purify the fraction ($\times$1000 rpm). Therefore a high number indicates a small average particle size. Note sample 14 is absent in 633 nm due to excessive fluorescence. The inset in (b) shows the relative intensity of the peak at 238 cm^{-1} normalised to the E_{2g} fundamental mode.

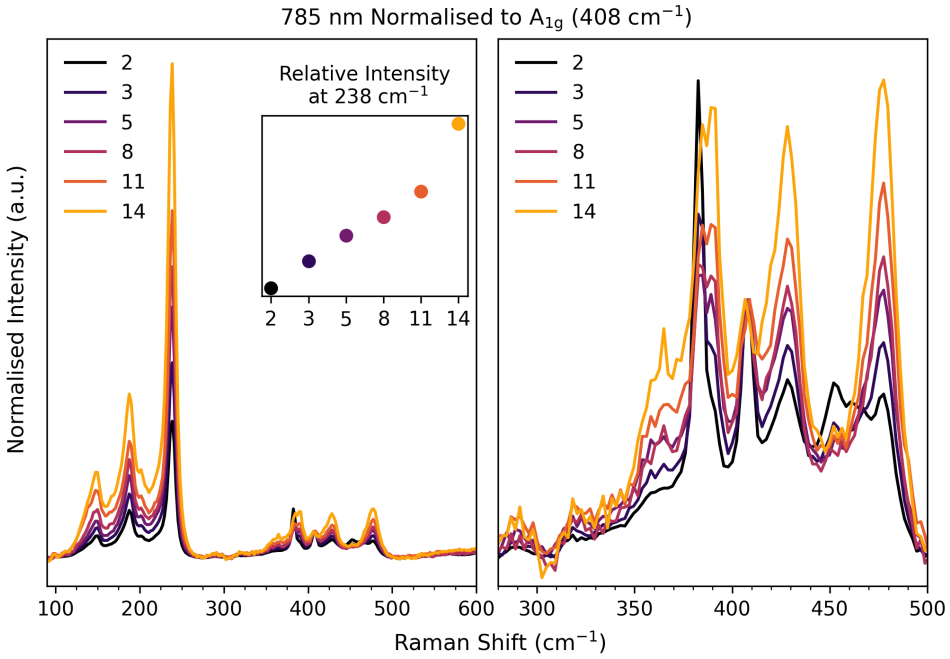

FIGURE 3.18: The same sonication data at 785 nm excitation as in Figure 3.17(b), normalised to the A_{1g} fundamental mode.

phonon,[202] but there are actually very few states at this energy, which means they are not simply reflecting the pDOS but rather some specific enhancement mechanism is selecting for phonons at this energy.

3.2.3 Mode Assignments

From this point onward, the set of features in the 100-250 cm^{-1} region are referred to collectively as the "defect modes", and are temporarily assigned the labels $p1$, $p2$, and $p3$ to the 238 cm^{-1}, 188 cm^{-1}, and 149 cm^{-1} peaks respectively. The mode at 177 cm^{-1} does not appear to be an edge-mode strictly speaking, as it is also observed in the basal plane and does not seem present in the spectra of the sonicated series (Figure 3.17).

Livneh and Spanier[171] show that under direct resonant conditions (~633 nm) a particular group of phonons significantly contribute to the second-order spectrum in this region, and that they are mostly difference bands. The strongest of these near 177 cm^{-1} is assigned to A_{1g}(M)-LA(M). Difference bands are a result of one Stokes scattering event, and one anti-Stokes scattering, meaning that there needs to be an appreciable population of excited state phonons for scattering to occur. The Bose-Einstein distribution shows that at lower temperatures (e.g. liquid nitrogen, 70 K) there is a very low probability of finding phonons above 100 cm^{-1} in excited states (see equation 3.15), so we can use low-temperature measurements to filter out difference bands from the spectrum. Initial experiments at 70 K in Figure 3.19 show this mode and the surrounding features disappear, indicating they most likely belong to

these second-order difference modes. Therefore, we can tentatively assign the mode at 177 cm^{-1} as the A_{1g}(M)-LA(M) difference mode. The right hand graph of Figure 3.19 shows $p1$, $p2$, and $p3$ are unaffected at low-temperature, and given that there are no suitable combinations of other modes at these frequencies, suggests they belong to first-order acoustic phonons.

To determine assignments for these modes, we can reference the phonon dispersion to see which phonons have matching frequencies. However, there are multiple phonon branches with phonons at these frequencies,[202] so we also need to consider which scattering pathways are accessible with 785 nm (1.58 eV) excitation. This involves comparing the band structure energies and symmetries of the states.

In bulk MoS_2, the lowest energy direct transition between the valence and conduction bands is at the K point around 1.85 eV, which is significantly higher than our 1.58 eV excitation. As such, we do not expect to observe a direct transition with this energy, and any excitation must occur near or at the Γ point. From inspection of band structures in literature[54,57,58,205] and our calculations (shown in Figure 1.2), it appears that the M, K, and Q or "Λ" points are all accessible, where Q or Λ is the point half-way between Γ and K.

Experimental electron energy loss spectroscopy (EELS) and angle-resolved photoemission spectroscopy (ARPES) literature find momentum-indirect excitonic

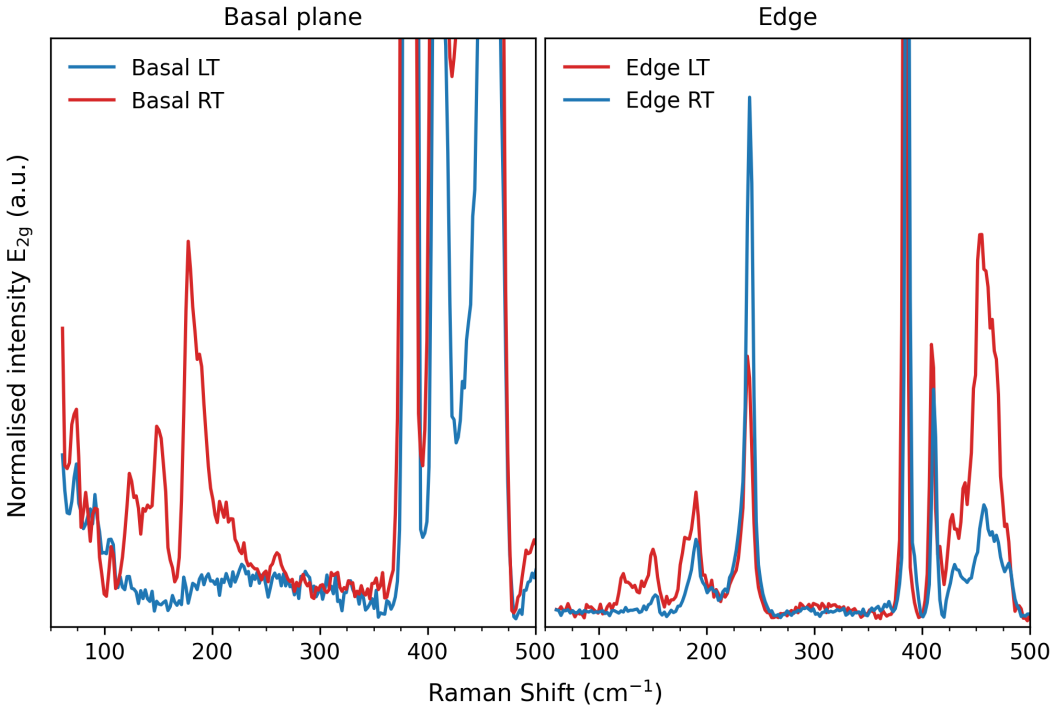

FIGURE 3.19: Room-temp and low-temperature (∼70 K) comparisons of basal plane (left) and edge spectra (right) at 785 nm excitation.

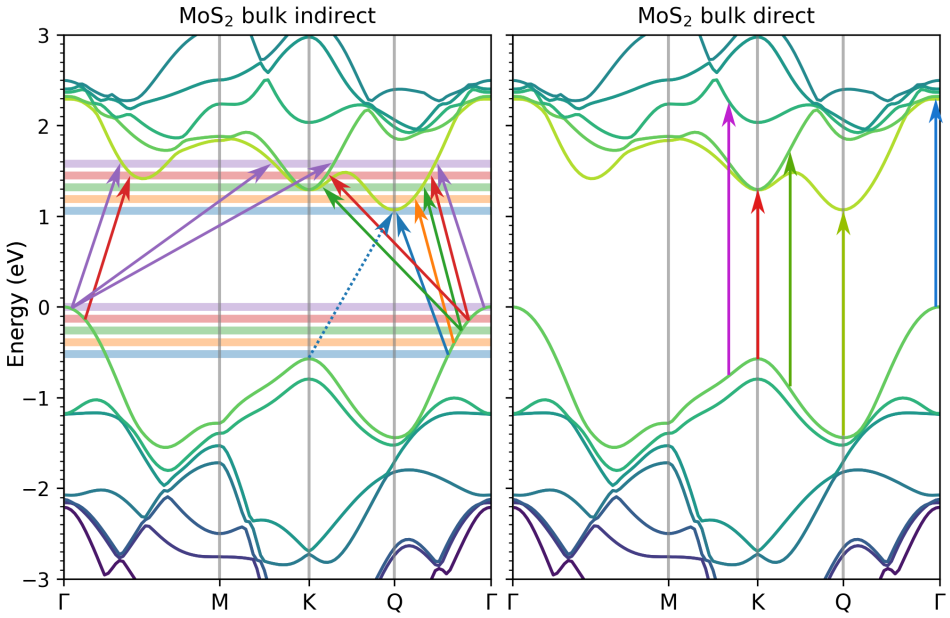

FIGURE 3.20: Diagrams illustrating indirect transitions at 1.58 eV (left) and direct (right) transitions of arbitrary energy. Indirect transitions can occur from/to zones of the same shaded colour, provided the phonon providing the momentum difference (indicated by the horizontal magnitude of the arrows) are allowed by symmetry with the initial and final states. Conversely, direct transitions are fixed within a narrow region of the BZ where the transition energy matches the photon energy.

states below 1.58 eV, with momentum matching that of the M, K, Q points, suggesting viable pathways for all of the above transitions.[206,207]

It is known in literature that Q point phonons have relatively poor electron phonon coupling with other high-symmetry points and a low pDOS,[103,208] so we do not expect much contribution but will keep them in mind for later discussion.

Instead, the observed defect modes can be reasonably assigned as either M or K point phonons or a mixture of contributions from both, as the energies of phonon dispersions at K and M are very similar. In particular, the frequency of $p1$ is too high to be anything but an LA phonon near M or K - but the frequency difference between the M and K points is typically 3 cm^{-1}, making them difficult to differentiate.

Livneh and Spanier[171] also give a thorough analysis of the various phonons and their irreps. at each high-symmetry point of the BZ, with a summary of relevant information presented in table B.1.

In order for one of the above points to be allowed in the indirect transition, the symmetry of the phonon must translate the initial state into the final state symmetry. In other words, the product of the initial state, phonon, and final state must produce the irreducible representation A_1.

However, given the number of states accessible at and around the high symmetry

points using 1.58 eV excitation, without more information restricting our choices we can find possible combinations of initial and final states allowing every acoustic phonon from both M and K points (see tables B.3 and B.4). In direct-resonance DRR, for a given photon energy the states that can be excited from/to are fixed in a narrow momentum range of the BZ - defined by the negligibly small photon momentum. However, if indirect processes can access any momentum value in the BZ, then we need to consider all of the possible combinations of initial and final states separated by the incident photon energy - regardless of their momentum values (see Figure 3.20).

Initially the defect modes appeared to be dispersionless - in that they seemed to have a fixed frequency near 238 cm^{-1} regardless of temperature and layer number. However, careful analysis of a terraced flake shown in Figure 3.21 reveals that $p1$ does indeed show dispersion in thinner layers (see Figure 3.22 and table 3.2 for layer height indications via AFM).

The top left graph of Figure 3.21(a) shows the linescan indicated by the arrow in (b), and the other three graphs are plots of the peakfitted frequencies of key modes $p1$, E_{2g}, and A_{1g} as a function of scan position, matched with the linescan axis and indicated by the vertical shaded lines. The plots here demonstrate that as layer number becomes appreciably thinner, the $p1$ mode increases in frequency by approximately 1.5 cm^{-1}, which is subtle but well within the combined capabilities of our detector and peakfitting algorithms to differentiate. Furthermore, the decrease in layer number is evident in the shifts of both E_{2g} and A_{1g} modes.[209]

The consequence of this dispersion is that while we could identify possible excited states in the CB using the measured phonon frequencies and calculated phonon dispersion, without an accurate quantitative measure of the band gap at each of these points we cannot be certain about where the initial states are in the VB. For instance, if we don't accurately know the definitive energy of the band gap at these layer numbers (which may be altered by the sapphire substrate and scotch-tape residue visible in the AFM image of 3.22 as brighter dots), we cannot say for sure which states in the VB are involved - only that each layer excites to a different point or set of points near K_{CB}. In a best case scenario, we might assume the transitions

TABLE 3.2: Layer heights calculated from each of the lines in 3.22.

Steps	Step height (nm)
1-2	2.472
2-3	0.446
3-4	0.889
4-5	0.536
5-6	0.793

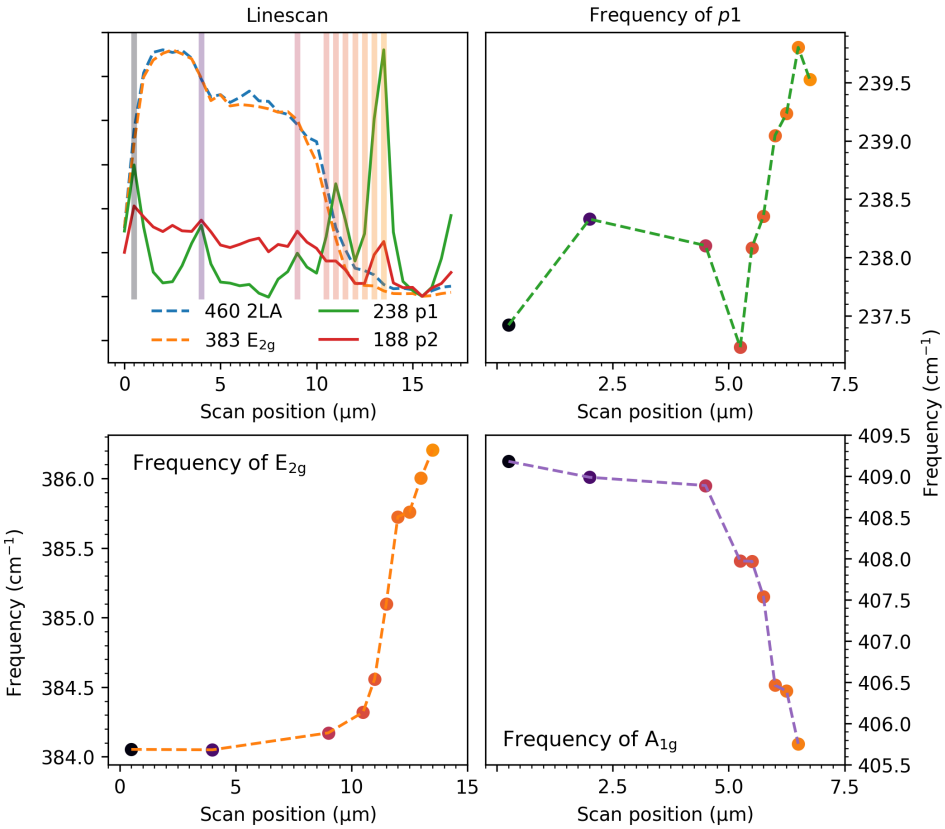

(a)

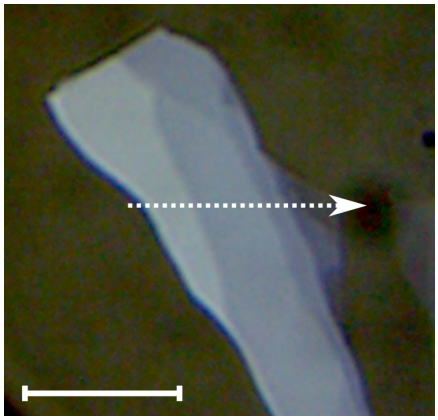

(b)

FIGURE 3.21: (a) Linescan of the flake in (b) and plots of the peakfitted values for shifts in key mode frequencies at positions in the linescan. Scale bar in (b) is 10 µm.

excite from exactly from Γ_{VB}, in which case we have an initial state to perform symmetry analysis on. However, there are still multiple states near K_{CB} which may be involved, including two separate bands (see band structure in Figure (3.20 and Figure C.3). Between these two bands are enough states either side of K to allow every phonon by symmetry, so none can be excluded at this point. We therefore need more information to assign these phonons, and turn to temperature and polarization measurements.

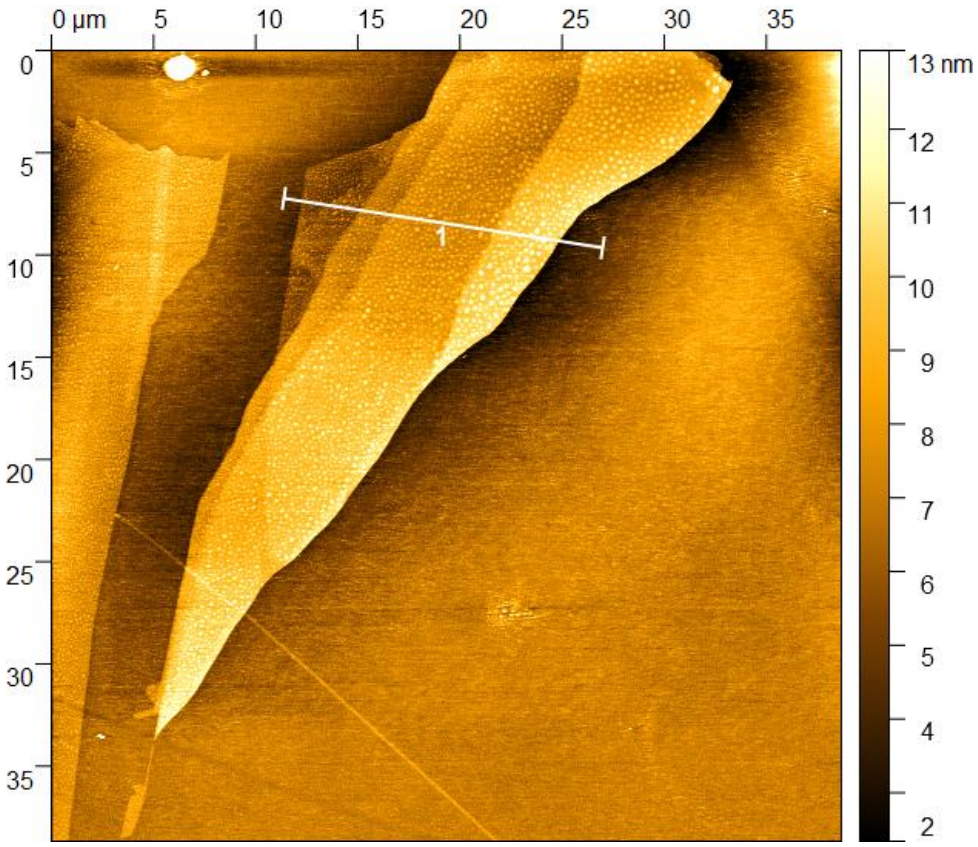

(a)

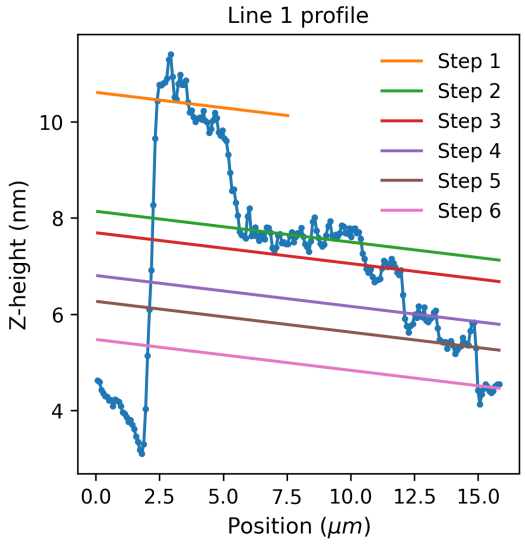

(b)

FIGURE 3.22: (a) AFM image and (b) height profile across the flake shown in Figure 3.21. The step lines in (b) are the layer step heights fitted in Gwyddion. The calculated heights from these lines can be found in table 3.2.

Polarization measurements

Similar to the D mode in graphene, we also observe an incident polarization dependence in these defect modes.

TABLE 3.3: Optimised parameters for the $\cos^2\theta$ fits in Figure 3.23. A low I_{min}/I_{max} indicates the edge has high uniformity, and is not disordered.

Frequency (cm^{-1})	I_{min}	I_{max}	I_{min}/I_{max}
238	0.0833	0.9632	0.0865
188	0.1310	0.9834	0.2227
149	0.1298	0.9698	0.4701
383	1926.5852	2112.5771	0.912
409	313.1725	327.5279	0.9562

Whilst in graphene the charge carriers are treated with a single particle model (unbound electrons and holes), the reduced dielectric screening in MoS_2 requires consideration of an excitonic scattering model. A key difference from the single particle model is that excitons correlate the electron and hole in space, travelling through the crystal as a bound pair. Upon initial consideration, this suggests that the real-space backscattering condition demonstrated by Casiraghi *et al.*[131] does not apply, as the particles will not drift apart and will always be close enough for recombination (outlined in section 3.1). However, the reciprocal backscattering condition still holds as crystal momentum must be conserved, so for a single-phonon interaction involving an edge-defect scattering, this must still be a backscatter event (i.e. collision with edge at normal incidence) to provide the necessary equal and opposite momentum.

Figure 3.23(a) shows the incident polarization dependence on the angle of plane-polarized 785 nm light for $p1$, $p2$, and $p3$. The point from which data was collected is marked by the circle in (c), and the thickness of this flake is ~5 layers (see Figure C.1). We start with this flake rather than the one in Figure 3.15 as the bulk analysis is more complex, and will be discussed later.

For each angle, the spectra are baselined and the peak intensities extracted from peak fitting with Lorentzian and pseudo-Voigt functions. The resulting data is then fit with

$$I = I_{max} - I_{min}\cos^2\theta_{in} \tag{3.18}$$

for each of peak of interest, where I_{max} and I_{min} are the maximum and minimum intensities across all polarizations, $\theta_{in} = 0$ is the parallel to the edge configuration, and $\theta_{in} = 90$ is perpendicular.

Each fit was optimised using a non-linear least-squares algorithm using Python's SciPy module. Details of the various data processing steps can be found in the Methods section (5). For $p1$ the fitted intensity essentially goes to zero at perpendicular angles (within our detection limits), which suggests the edge structure is predominantly one type (armchair or zigzag, not both) and relatively well ordered. Note that

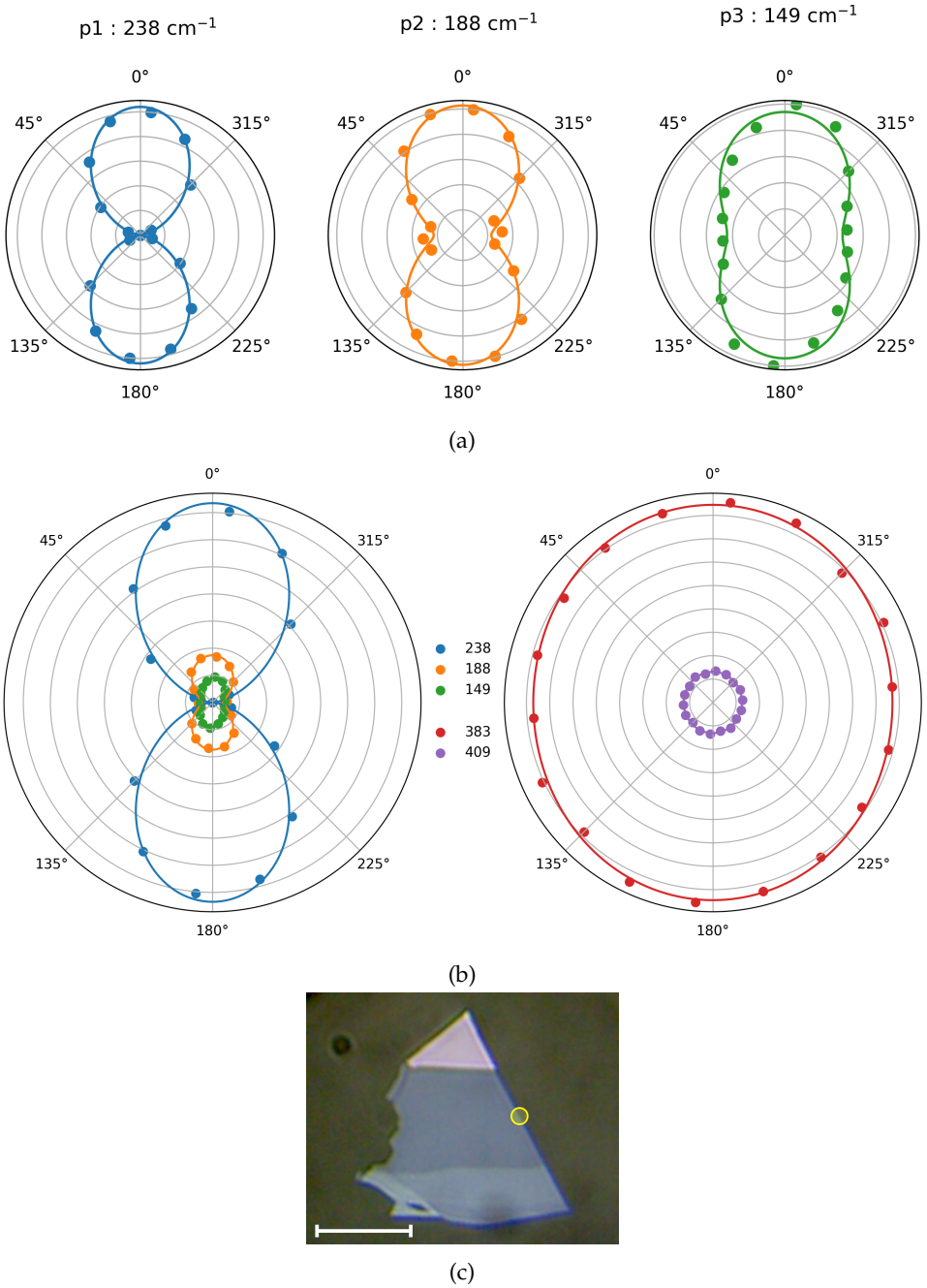

FIGURE 3.23: (a) Incident polarization dependence of the three defect modes, normalised for each mode. (b) Plots in (a) stacked and normalised to *p1* (left) and polarization dependence of fundamental E_{2g} and A_{1g} modes (right). The numbers in the legend between the plots is frequency in wavenumbers. (c) Flake and edge (yellow circle) from which the spectra were taken. Scale bar is 10 µm

p2 and *p3* show different I_{min}/I_{max} values, which is due to a number of factors, including: the presence of second-order difference bands from the basal plane in this region; possible contributions from non-resonant defect scattering (i.e. the pDOS signature); and a consequence of the relatively low signal to noise for these peaks,

where the peak-fitting algorithm tends to "fit the noise" above the baseline (see Figure 3.27). However, because *p1* sits right on the upper limit of the pDOS acoustic phonon frequencies and is the most intense of the three modes, there is very little background and shows a textbook polarization dependence.

In the graphene model the polarization dependence can be explained by the real-space backscattering of unbound charge carriers and the inhomogeneous absorption. For MoS_2, the bound exciton precludes explanation via a quasi-classical real-space scattering argument, which suggests there must be a quantum mechanical explanation, similar to the inhomogeneous absorption in graphene.

We can understand the polarization dependence by noting that the photon absorption process is coupled to the phonon interaction through the intermediate step.

Upon excitation to the intermediate state (in this case a virtual state), an electron of wavevector $\boldsymbol{k}$ will begin propagating through the lattice which will induce a deformation of the lattice ions as they experience the time-averaged electronic potential.

This deformation will be along some vector consistent with the motion of the electron, applying some directional deformation potential and will therefore favour interaction with phonons in particular directions (particular wavevectors). As such, we can expect that the probability of indirect absorption via phonons of wavevector $\boldsymbol{q}$ will be enhanced for particular polarizations. This should therefore present itself as a $\boldsymbol{q} \cdot \boldsymbol{k}_e$ dependence in the electron-phonon interaction Hamiltonian, with $\boldsymbol{k}_e \perp \boldsymbol{e}_{in}$.[130,131,210] Given the backscattering condition is required to observe these modes, we find that only wavevectors perpendicular to the edge give rise to the modes and so we observe a strong polarization dependence.

Noffsinger *et al.*[211] and Ridley[212] show that the indirect absorption processes can be modelled using an extension of Fermi's Golden Rule, and that the polarization dependence can be shown in the expression for the absorption coefficient, α_{ind}, as

$$\alpha_{ind} \propto |\boldsymbol{\lambda} \cdot (\boldsymbol{S_1} + \boldsymbol{S_2})|^2 \tag{3.19}$$

where $\boldsymbol{\lambda}$ is the photon polarization vector, and $\boldsymbol{S_1}$ and $\boldsymbol{S_2}$ are generalised matrix elements for the two main contributing pathways shown in Figure 3.24. $\boldsymbol{S_1}$ and $\boldsymbol{S_2}$ can be written as

$$\begin{aligned} \boldsymbol{S_1}(\boldsymbol{k},\boldsymbol{q}) &= \sum_{mv} \frac{\boldsymbol{v}_{im}(\boldsymbol{k}) g_{mf,v}(\boldsymbol{k},\boldsymbol{q})}{E_m - E_i - \hbar\omega + i\Gamma} \\ \boldsymbol{S_2}(\boldsymbol{k},\boldsymbol{q}) &= \sum_{mv} \frac{g_{im,v}(\boldsymbol{k},\boldsymbol{q}) \boldsymbol{v}_{mf}(\boldsymbol{k}+\boldsymbol{q})}{E_m - E_i \pm \hbar\omega_{v\boldsymbol{q}} + i\Gamma} \end{aligned} \tag{3.20}$$

where $\boldsymbol{v}$ is the velocity matrix element, which describes the interaction between

the incident radiation, the electron, and the lattice without any atomic motion.[211] g is the EPC matrix element, which describes how the time-averaged electronic perturbation on the lattice affects the ion positions, and thereby couples to associated phonons.[210] i, m, and f represent the initial, intermediate and final states; ν is the phonon mode; and $\boldsymbol{k}$ and $\boldsymbol{q}$ are the wavevectors of the initial state and phonon. The denominator describes the resonance terms for the intermediate and final states, depending on when in the sequence of events the photon absorption occurs ($\boldsymbol{S_1}/\boldsymbol{S_2}$). E_m and E_i are the energies of the intermediate and initial states; $\hbar\omega$ and $\hbar\omega_{\nu\boldsymbol{q}}$ are the incident photon and phonon energies; and Γ is a damping factor. Note the sum over m and ν is to account for the fact that there are multiple phonon branches for a given wavevector which have their own frequencies and intermediate states to evaluate with.

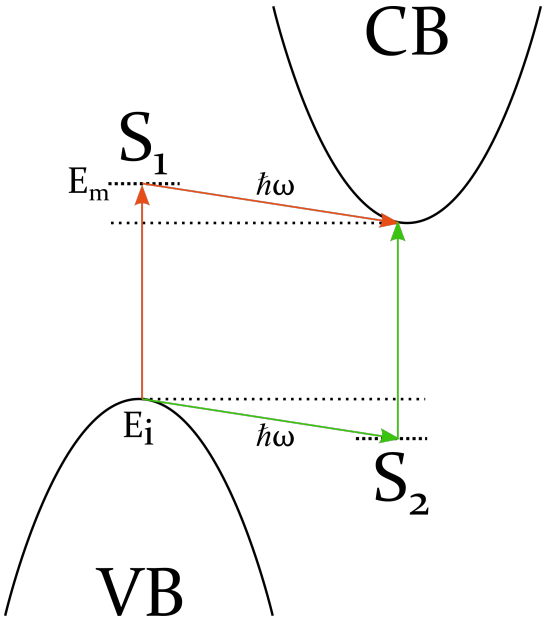

FIGURE 3.24: Representation of the two (main) pathways for an indirect transition. $\boldsymbol{S_1}$ indicates a photon absorption first to a virtual state, followed by phonon emission (or absorption) to a real final state, and $\boldsymbol{S_2}$ indicates a phonon emission (or absorption) first to a virtual state, then photon absorption to the real final state. E_m and E_i are the intermediate and initial state energies respectively.

It is worth noting that the backscatter conditions from these polarization measurements imply that the scattered photon also exhibits the same polarization dependence, and this is indeed what we observe - the defect modes are most intense when an analysing polarizing filter is parallel to the edge, regardless of the incident polarization angle.

In contrast to the edge polarization dependence, we do not expect a polarization dependence for two-phonon interactions in the basal plane, as there is no edge-mediated backscatter to select for one of six equivalent phonons. The symmetry of

the BZ means that under normal circumstances, when coupling to a phonon from some high symmetry point - say the LA(K) phonon, the probability of interaction is proportional to $\cos^2\theta$ for every 60°, and we see that the sum of these dependencies at any given angle is the same (Figure 3.25). Thus we see no polarization dependence in the basal plane.

Establishing a polarization dependence for these modes is hugely beneficial, as this means the first-order defect phonons originate from one specific direction in k-space, and that different edge structures will select for phonons from different high symmetry points (see Figure 3.13). That is to say armchair edges should activate the K point phonons, and the zigzag edge should activate the M point phonons.

If we assume we have a single crystal of MoS_2, then from geometric analysis we can say that for corners with angles which are multiples of 60°, the two edges are expected to have the same orientation, but for multiples of 30° or 90°, we expect to find a different orientation on each edge (see Figure 3.26(f)). We now return to the flake in 3.15, reproduced in Figure 3.26(f) for convenience, to compare spectra at two different edge orientations.

Figure 3.26 shows the RT and LT spectra of two edges in the top right of the flake in (f), oriented 90° from each other. (a)/(b) show the edges marked "X" and "Y" in the optical image in (f). While (a) is similar to what we've seen in Figure 3.19, with the

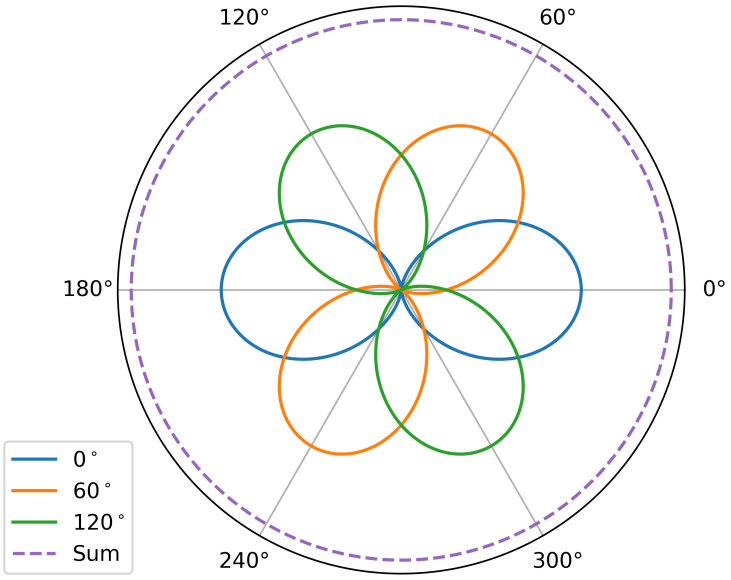

FIGURE 3.25: Simulated polarization dependencies for the bulk. The probability of interaction with a particular high symmetry point has a $\cos_2\theta$ dependence, and because of the 6-fold symmetry of the BZ there is a separate $\cos^2\theta$ dependence for every 60° interval. The edge backscatter selects for one of these, but in the basal plane there is no such condition, meaning for two-phonon DRR modes the probability of interaction with a certain phonon is proportional to the sum of the probability at every angle - shown here to be invariant for all angles.

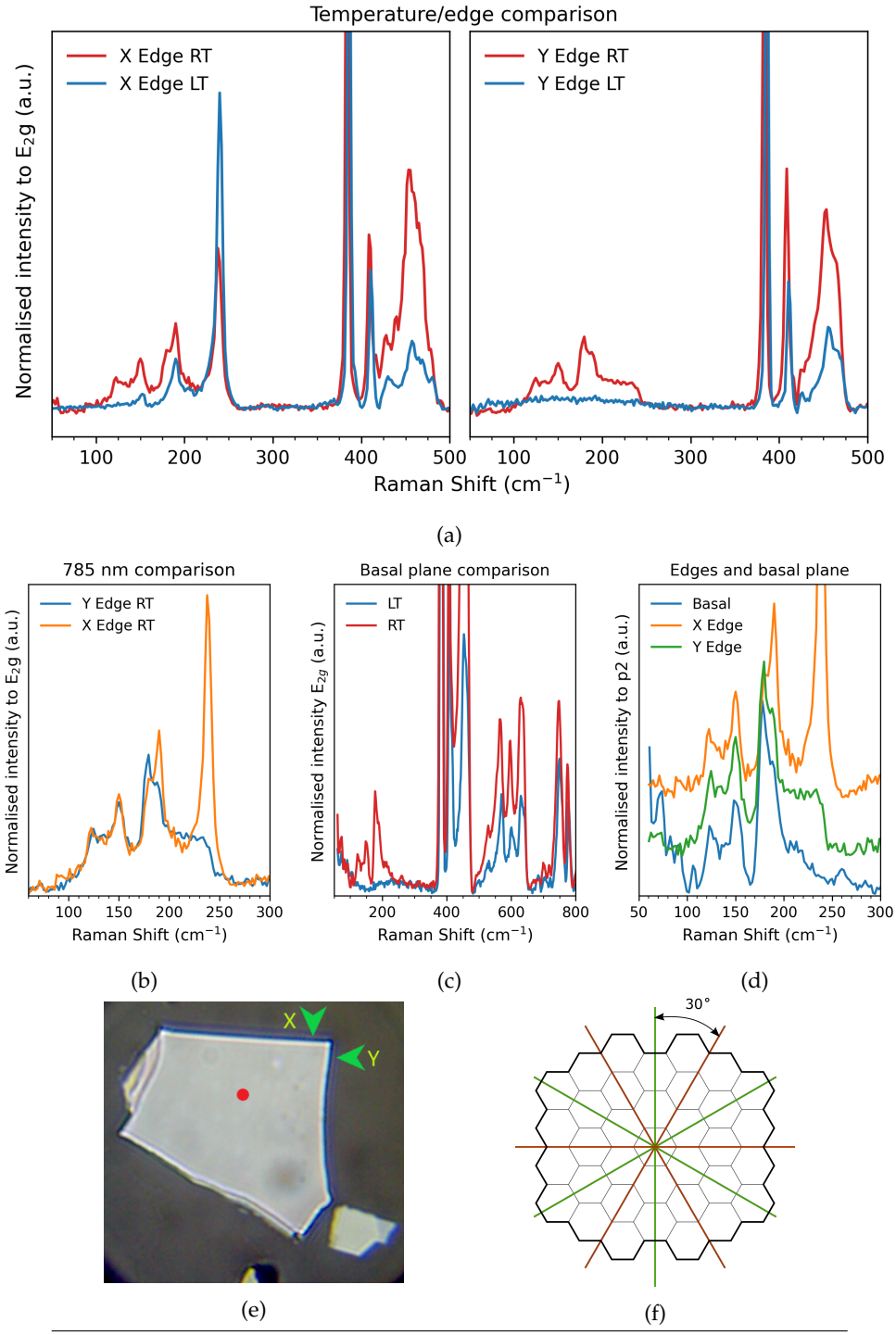

FIGURE 3.26: (a) Comparison of Raman spectra of two edges at 90°, as indicated in (e), at room temperature (RT) and low-temperature (LT)(∼ 70 K). (b) shows the defect-mode comparison between the two edges. (c) shows this region at RT and LT in the basal plane area marked by the red circle in (e). (d) a comparison of the defect modes from the three regions (basal plane, X edge, Y edge). (f) shows how edge structure is expected to vary with edge angle for a single crystal. Red lines indicate armchair edges while blue lines indicate zigzag edges (figure adapted from Casiraghi *et al.* [131]).

difference bands falling away and revealing the first order modes, the same region in (b) seems entirely composed of difference bands, leaving a featureless defect mode region at LT. (c) shows an overlay of this region from both edges, and we can see that all the features observed in (b) are seen in (a) as well, to varying degrees but with remarkable resemblance. (d) and (e) then show that the modes observed in the Y-edge in (b) are almost identical to the difference bands previously observed in the basal plane (at the red dot in (f)), where no backscatter mechanism is present. It seems that the modes in (b) occur under all conditions (and both edge orientations) and disappear at LT, suggesting they are in fact second-order difference modes.

Another explanation for their disappearance could be a loss of resonance condition due to the slightly larger band gap at LT, however we can see in (c) that the 2LA and second-order features above $500\,\mathrm{cm}^{-1}$ are still present, which indicates that a resonance condition is still being achieved. Note the diminished intensity of these modes is likely the effect of the bands shifting away from resonance.

The second order difference bands, consisting of two phonon interactions, do not need an edge to be observed, as unlike a single acoustic phonon, they can conserve crystal momentum as phonons of wavevector $\boldsymbol{q}$ and $-\boldsymbol{q}$. It is therefore not surprising to find them in the basal plane. It should be noted that these modes are more intense at the edge than in the basal plane, suggesting they still benefit from a real-space backscatter mechanism, and we will return to this in the discussions below.

The difference band features in Figure 3.26(b)/(d) show strong resemblance to the group of modes which result from the "resonant group" of M-point phonons described by Livneh and Spanier,[171] which indicates this may be the M edge. It is advantageous that layered TMDs show such significant band gap modulation with layer number, as we can use the widening gap to test for an M point resonance. As layer number decreases, the Γ point states in the VB decrease in energy (and Q point states in CB increase in energy) while the K and the M point states in the CB remain relatively unchanged. Therefore we would expect a bulk $\overrightarrow{\Gamma M}$ resonance around 1.5 eV to be lost before a $\overrightarrow{\Gamma K}$ resonance around 1.3 eV. In fact, the $\overrightarrow{\Gamma K}$ resonance should remain all the way down to 2L-MoS_2 which is expected to have an indirect gap of ~ 1.5 eV (and lost in 1L-MoS_2).

Figure 3.27(b) shows a Raman map of the flake in Figure 3.23. The map is a 2D array of spectra taken in a grid at 0.5 µm resolution, where the value (colour) of the heat-map represents the *p1* intensity of the spectrum at each point. We can identify regions of varying thickness by the optical contrast of the flake in (c) - confirmed by atomic force microscopy to quantify the layer numbers (see Figure C.1). The purple/pink triangle at the top of the image is a thicker section ($>$ 20 layers) approximating the bulk, while the middle blue section is much thinner (5 layers), approximating few layers. The strip at the bottom is slightly thicker than the middle section. We can see from the Raman map that *p1* is most intense at the edges, which varies depending on the relative incident polarization angle (parallel to the

right-hand edge).

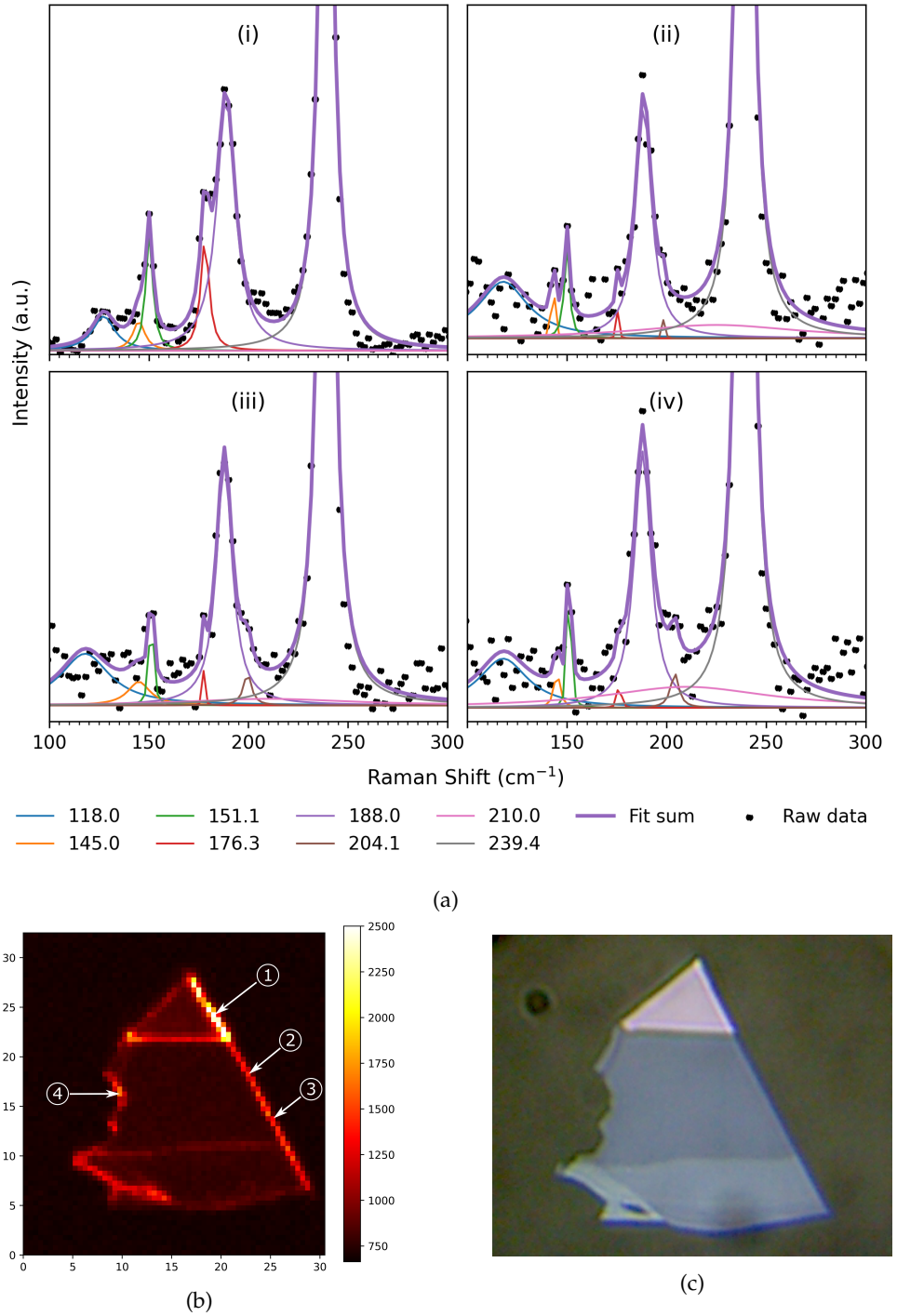

FIGURE 3.27: (a) Peak fits i → iv correspond to spectra taken from the points 1-4 in the Raman map in (b). (b) Raman map of the flake in (c), where the colour bar represents intensity of the *p1* mode. The axis scales in (b) are in micro meters.

Figure 3.27(a) shows four peak-fitted spectra, labelled i → iv which correspond to the spectra at points 1 → 4 respectively in (b). (i) shows a "thick" edge of the top triangle section, while (ii)→(iv) show various edges of the thin section. It can be

seen that at the thick edge there is a not-insignificant contribution from the A_{1g}(M)-LA(M) difference mode at $\sim 177\,\mathrm{cm}^{-1}$. For the other three points, there is little to no contribution from the M point modes. Contributions to these spectra result from measurement in the basal plane due to the finite spot size, or from the algorithm peak-fitting noise in the spectrum.

In fact, if we apply the peak-fitting algorithm to the entire map we can see that, although weak, the contributions from A_{1g}(M)-LA(M) are focused around the edges of the thick section and throughout the basal plane, but not necessarily at any of the thin edges (Figure 3.28(a)). It is, however, difficult to identify the contributions in the basal plane and thin edges due to the low signal-to-noise in these areas.

Figure 3.29 shows a longer acquisition linescan of the flake in Figure 3.27 running

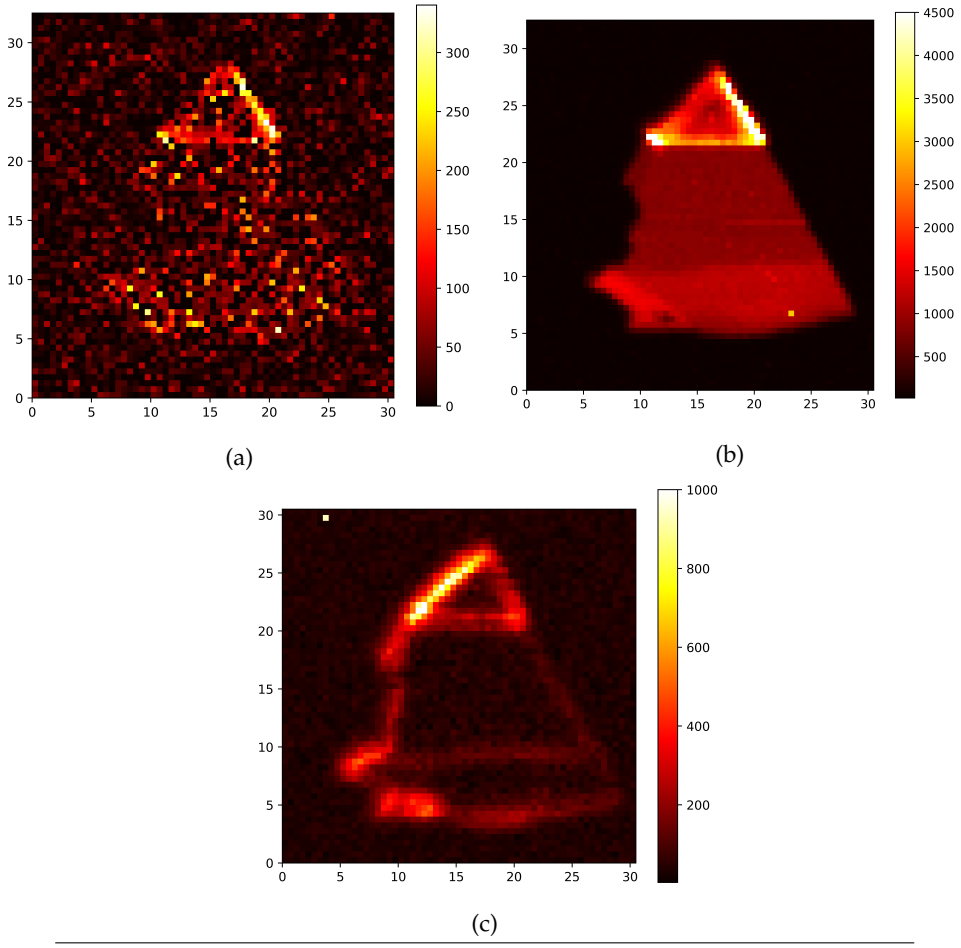

FIGURE 3.28: More Raman maps of the flake in Figure 3.27. From the same map data in Figure 3.27, (a) and (b) show intensities at $177\,\mathrm{cm}^{-1}$ and $383\,\mathrm{cm}^{-1}$ respectively. (c) shows a different map of the flake, where the incident polarization angle is rotated by 90°, such that it is perpendicular to the right edge but parallel with the edge in the top left. The colour bar represents intensity of *p1*. Comparing (c) with Figure 3.27(b) shows clearly the incident polarization dependence across the flake. The axis scales in these images are in micro meters.

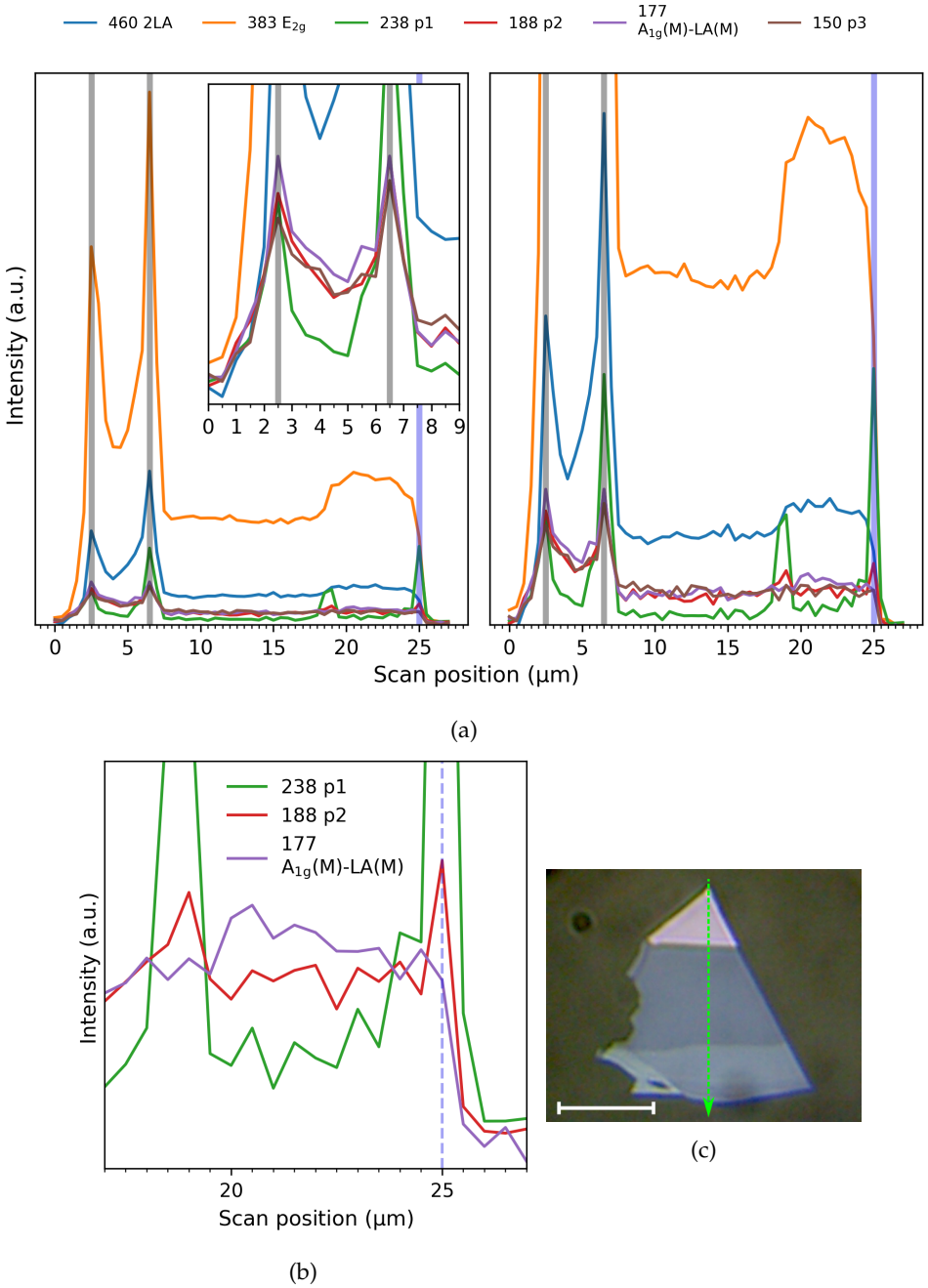

FIGURE 3.29: Linescan data of the flake in (c) running vertically down as indicated by the arrow. The top edge near the start of the scan shows clear contributions from the general resonance enhancement (inset of (a) left), while the bottom edge shows contributions from a more specific enhancement. The distinction between these enhancements is shown by the shaded regions in (a): the general enhancement enhances all modes while the specific enhancement only enhances the defect modes. The scale bar in (c) is 10 μm.

vertically from top to bottom as indicated by the dotted line in (c). The evolution of peaks moving across the edges is markedly different for the thick and thin edges. In the initial points of the linescan crossing the thick edges (0-10 μm) the defect modes reach their maxima at the same point as the fundamental mode E_{2g}, as indicated

by the grey dashed lines in (a)/(b). At these points, the A_{1g}(M)-LA(M) mode has significant intensity in this region (inset of (a)). In the final points of the linescan crossing the thinner edges (20-27 µm), the defect modes reach a maxima while the E_{2g} mode is approximately half-way to its maxima. This is exactly the relationship we should expect from an edge-specific signal and bulk signal under a circular laser spot (see Figure 3.30).

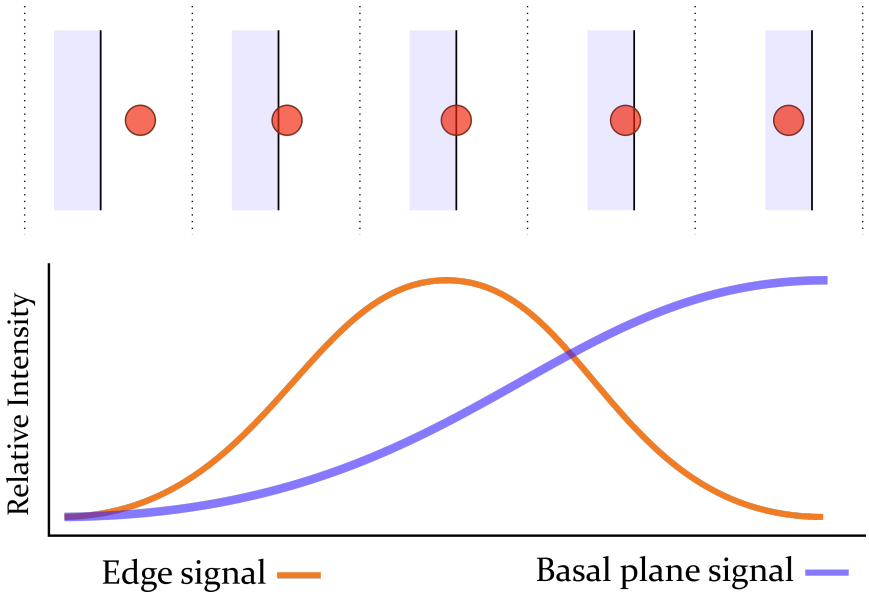

FIGURE 3.30: Representation of the expected evolution of mode intensities at the edge (yellow trace) and basal plane (blue trace) as the laser spot (red dots in top section) moves from off the flake (left side), over the edge (middle) then completely into the basal plane (right).

Importantly, the A_{1g}(M)-LA(M) mode does not have a peak on this edge, but instead it plateaus in the basal plane, indicating it is not activated by the thin edge. The fact that it does not necessarily reach a maximum at the same time as the E_{2g} mode is likely a result of poor signal to noise. The relationship is more clear in Figure 3.31, which shows another linescan in the horizontal direction of this flake, running over only thin material. Here we can see clearly that A_{1g}(M)-LA(M) reaches a maxima at approximately the same position as the E_{2g} mode, thereby suggesting its contribution to the spectrum of thin flakes is primarily from the basal plane.

It is interesting to note that, while weak, there are still some second-order features such as the A_{1g}(M)-LA(M) in the basal plane of 2L MoS_2 (see Figure 3.32), which are likely the result of non-resonant (non-DRR) second-order processes.

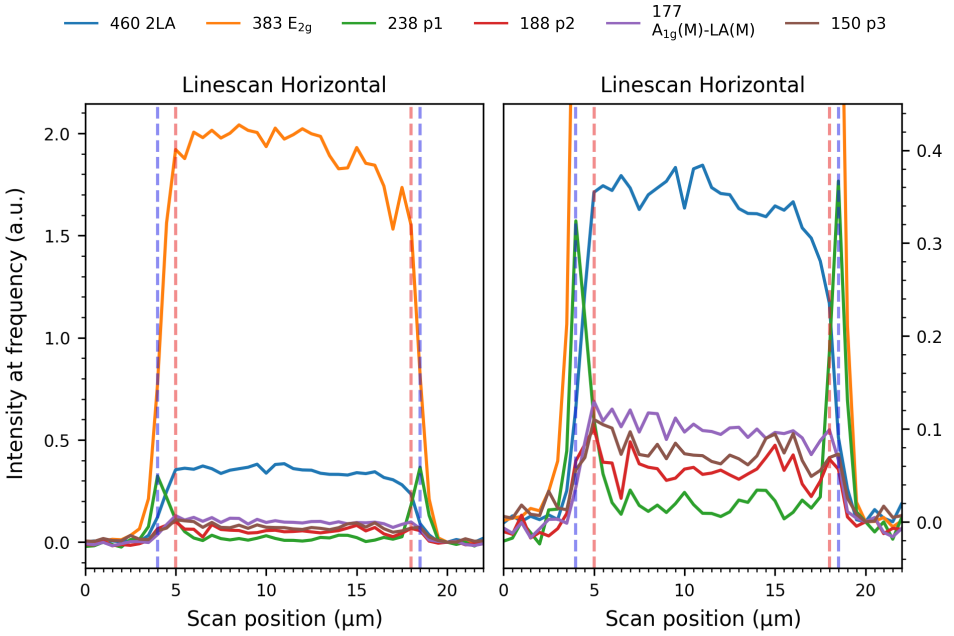

(a)

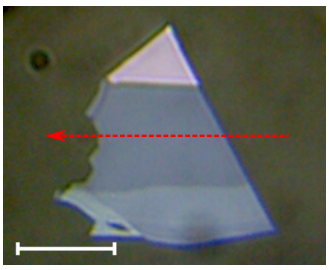

(b)

FIGURE 3.31: (a/b) Linescan data of the flake in (c) running horizontal from right to left. This thin section shows only the specific enhancement of defect modes and no contributions from the general enhancement. Scale bar in (c) is 10 µm.

To summarise, we find that:

- The A_{1g}(M)-LA(M) mode and associated Y-edge difference modes in Figure 3.26(b) are enhanced by thick edges, regardless of orientation, due to their second-order nature.
- The Y-edge modes bear remarkable resemblance to the M point "resonant group" difference bands reported by Livneh and Spanier,[171] suggesting an M point origin.
- While observed at the edges of thick samples, these modes are not observed at the edges of thin samples, where the band-gap is larger. The X-edge defect modes remain visible down to and including 2L-MoS_2.
- We expect the K point (and not the M point) to be in resonance in 2L-MoS_2.

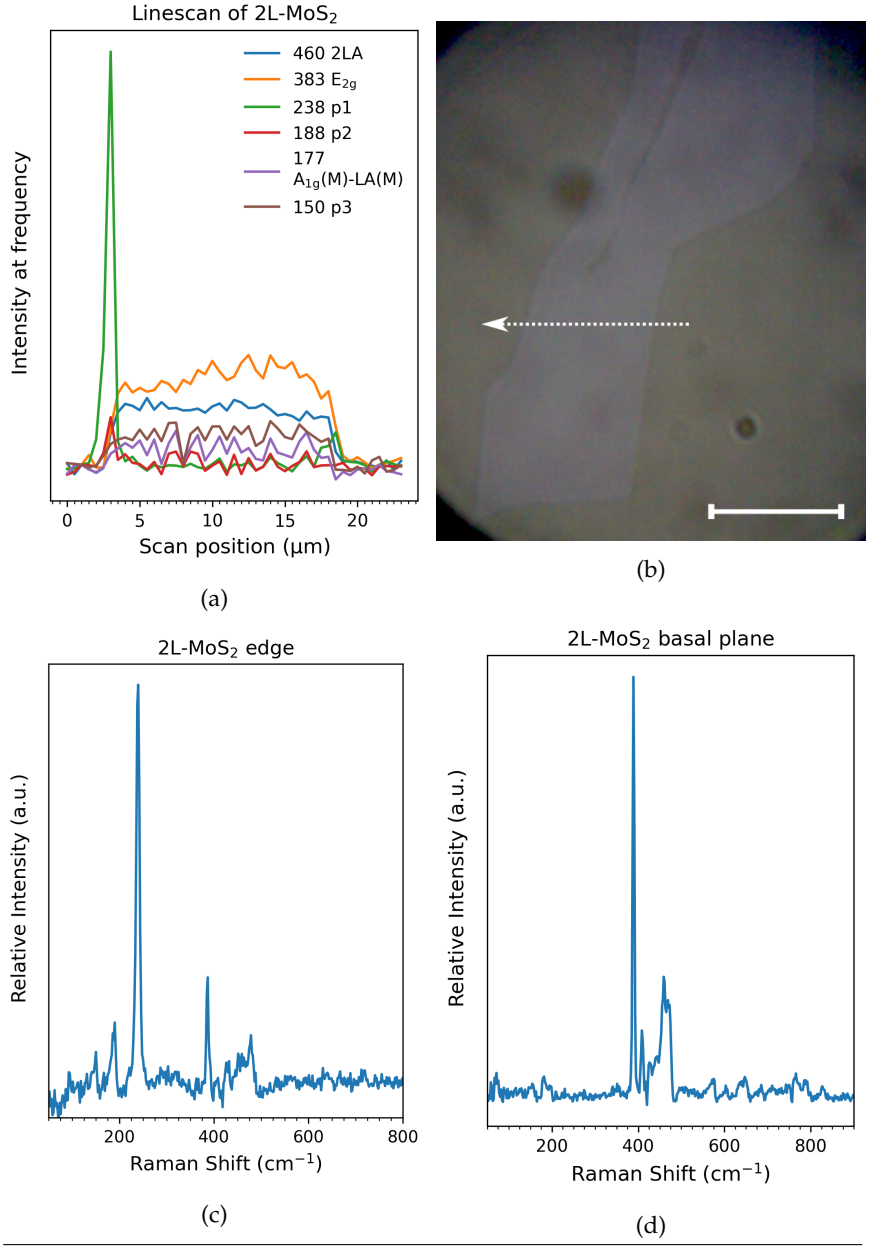

FIGURE 3.32: (a) Linescan of a 2L flake of MoS_2 (b) in the direction of the arrow (right to left). (c) and (d) show sample spectra from the edge and basal plane regions respectively. Scale bar in (b) is 10 µm.

Therefore I conclude that the Y-edge second-order phonons are originating from the M point, and the X-edge first-order phonons originate from the K point. I assign the Y-edge modes to various second-order difference modes including A_{1g}(M)-LA(M), and *p1* and *p2* to the first-order acoustic phonons LA(K) and TA(K) respectively. A list of the assignments is given in table 3.4.

LA(K) and TA(K) are assigned based on their frequencies in the phonon dispersion near K, and given the asymmetric shape of *p2* on the low-energy side we may also be observing a ZA(K) phonon at $\sim 180\,\mathrm{cm}^{-1}$. The frequency of *p3* is too low

TABLE 3.4: Assignments of defect modes based on discussion. The ZA(K)* indicates a mode that I expect is present but is weak and convoluted beneath other features in the region.

Label	Phonon	Frequency (cm^{-1})
p1	LA(K)	238 cm^{-1}
p2	TA(K)	188 cm^{-1}
	ZA(K)*	180 cm^{-1}
p3	TA(Q)	149 cm^{-1}
	A_{1g}(M)-LA(M)	177 cm^{-1}

to be a K or M phonon, and its presence at LT indicates it is a single phonon rather that a difference band. It is therefore likely a phonon from the Q point, as these phonon wavevectors lie along the same $\overrightarrow{\Gamma K}$ direction in the BZ, and their frequencies are in the right range. Based on frequency, *p3* is likely the TA(Q) phonon, while the ZA(Q) phonon is disallowed by symmetry (see table B.6 and table B.7). The only other phonons with a lower frequency are the shear modes, and *p3* could be a higher-order combination of these. However, the shear modes are known to vary in frequency significantly with layer number, and *p3* shows little to no dispersion with layer number, even in the extreme case of 2L-MoS_2 flakes (see Figure 3.32), so this assignment is unlikely. Assignment to a Q phonon indicates that the $\overrightarrow{\Gamma Q}$ resonance pathway is also active at armchair edges, and therefore LA(Q) phonons may also be contributing to the spectrum near 188 cm^{-1},[202] further broadening the *p2*/TA(K) feature.

3.2.4 M-point General Resonance at Bulk Edges

As I mentioned before, the bulk resonance is slightly more complicated, as the M point resonance is active at both edge structures in the bulk, and displays different enhancement effects than the K point resonance. However, now that we have assignments for the phonons we can explain these effects. Figure 3.33 and Figure 3.34 show linescans of the X-edge and Y-edge from the above discussion (Figure 3.26) with the incident polarization parallel to each edge. The previous linescans at 785 nm have shown that at the bulk edges there is a strong enhancement of not just the defect modes, but all the modes in the spectrum. This effect is what we would expect for a pre-resonance rather that an actual resonance, which is when the energy terms in the denominator become close enough to start providing a general enhancement to the spectrum, but not so close that a single mode (or group of modes) is strongly enhanced. This fits well with our assessment that the M point resonance fades first as the band gap increases, as this pre-resonance will be very sensitive to band-gap shifts.

The fact that this pre-resonance appears at both edges suggests it is not bound by the backscatter constraint, which is supported by the fact that all of the defect modes appearing on this Y-edge are second order modes, meaning they provide their own momentum conservation. So if the edge is not required for momentum conservation, then what causes the pre-resonance to be so strongly localised at the edges? I suggest two possible explanations for this.

The first explanation is that, although not required for observation, the backscatter at an edge may enable additional wavevector combinations to conserve momentum. Figure 3.35 shows a schematic of some two-phonon interactions that become allowed in the presence of an edge. Essentially, since an edge backscatter results in momentum conservation for phonon wavevectors perpendicular to the edge (wavevectors in reciprocal space, edge in real space), then any phonon wavevectors (yellow arrows) whose sum is a new wavevector perpendicular to the edge (blue arrows) will be allowed by momentum conservation. Without the edge, only the $\boldsymbol{q}$, $-\boldsymbol{q}$ combinations are active. The increased number of allowed combinations at an edge leads to an increased probability that a scattering process will occur to bring the system to the pre-resonant state, leading to higher intensities at the edges.

The second explanation is that there will be some defect-induced gap-states at the edges of the crystal which may provide a higher energy state from which to excite, thereby reducing the effective gap energy (see Figure 3.36).[111,112] A similar effect may alter the states already present through doping interactions from the under-coordinated or oxidised edges.[213,214] Such states would also likely exhibit some kind of polarized absorption along a length of ordered edge.

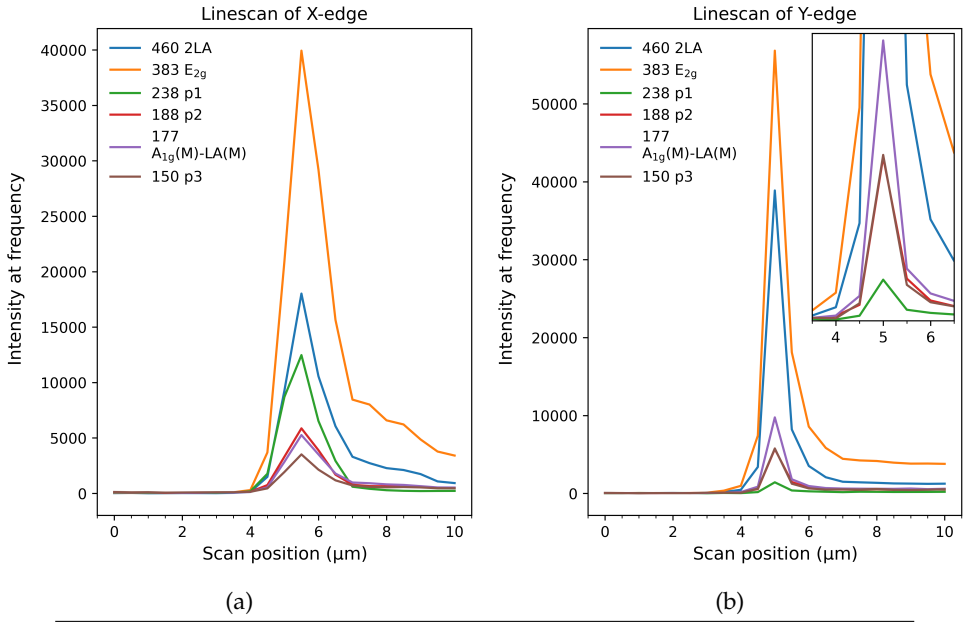

FIGURE 3.33: Linescans of (a) the X-edge and (b) the Y-edge in 3.26. In each case, the incident polarization is parallel to the edge. In both cases, there is a large enhancement of all the modes, not just the defect modes.

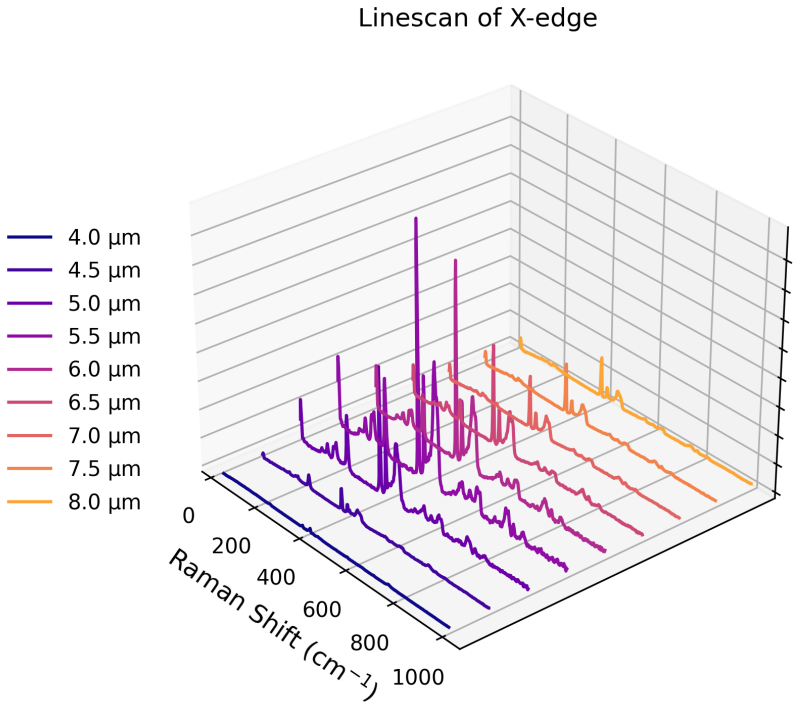

(a)

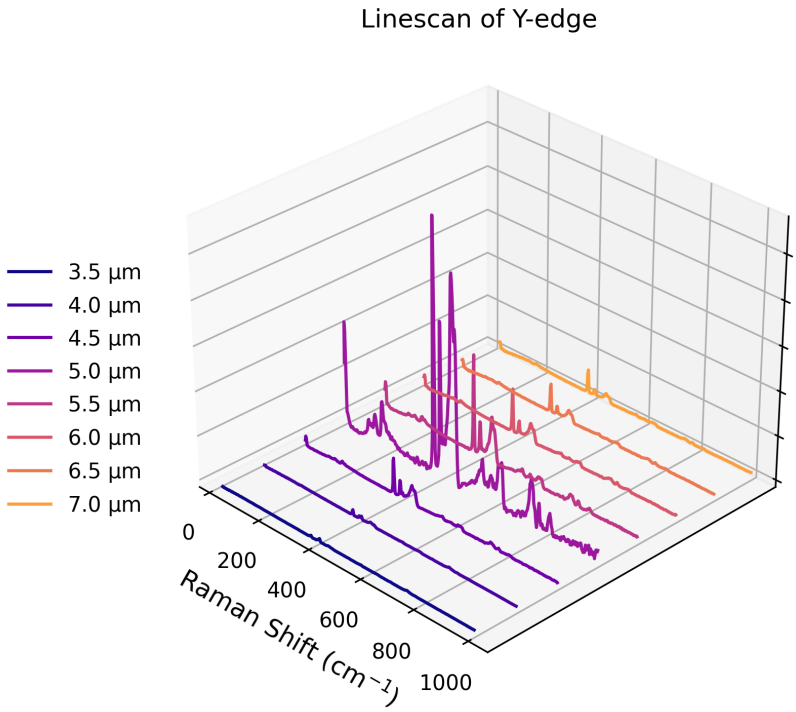

(b)

FIGURE 3.34: Spectra from a selection of points in the linescans of Figure 3.33, showing the full spectral enhancement at the edges. The legend indicates the absolute positions of spectra in the linescans of Figure 3.33.

Figure 3.37 shows the polarization dependence for the X-edge and Y-edge for the flake in Figure 3.26. This time, in the thick flake samples, we see a polarization

dependence on all the modes, including E_{2g} and A_{1g}. Interestingly, the A_{1g} shows the opposite polarization dependence to every other peak, and the reason for this is unclear at this time. Figure 3.38 shows the same data normalised to the E_{2g} mode at each polarization angle. We can see that while a slight polarization dependence remains for the X-edge modes, the Y-edge difference bands all lose their polarization dependence, suggesting that they share the same polarization dependence mechanism as the E_{2g} mode. This trend is clearer in the overlaid plots at all angles in (c) and (d).

Note that even when the incident polarization is perpendicular to the edge ($\theta_{in} = 90°$) there is still a significant amount of enhancement via the M point resonance (i.e. the enhanced intensity does not go to zero, see Figure 3.41). We can understand this

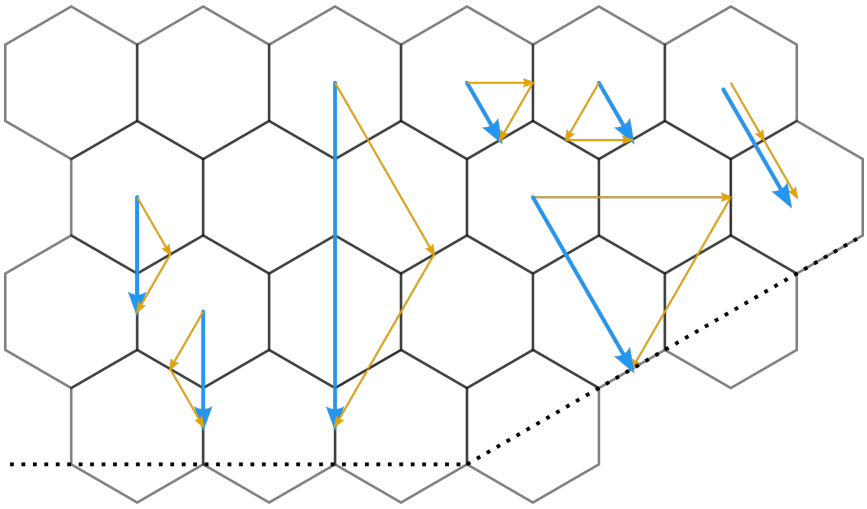

FIGURE 3.35: Schematic diagram of the type of two-phonon modes that become allowed near an edge. Yellow arrows are phonon wavevectors, and blue arrows are the sum of those wavevectors.

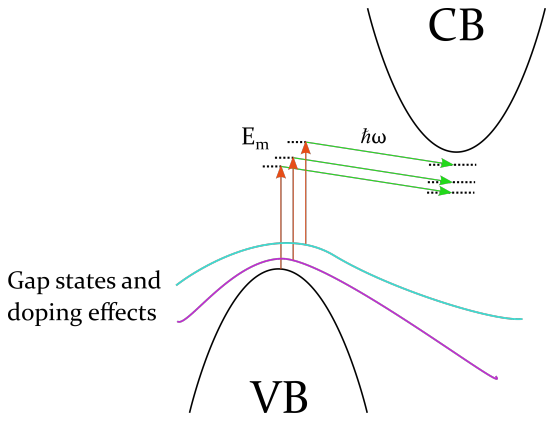

FIGURE 3.36: Representation of the effect of gap-states (blue and purple traces) induced by defects and dopants may have on the resonance condition. Gap states may allow lower energy transitions to occur, bringing them into resonance. The black parabolas represent the band structure of the defect-free crystal.

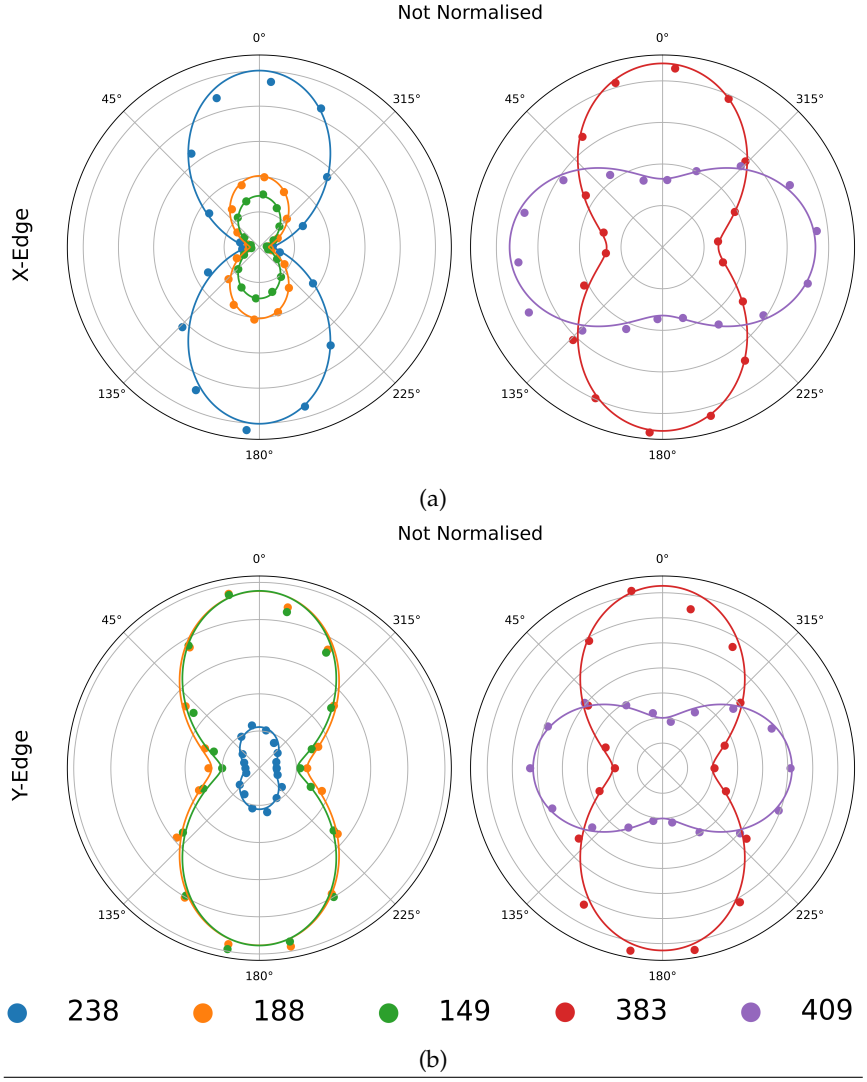

FIGURE 3.37: Incident polarization dependencies for the (a) X-edge and (b) Y-edge in Figure 3.26. Note that for these thicker edges the fundamental modes (E_{2g} and A_{1g}) also experience a polarization dependency. We do not yet understand the cause of the opposite dependence in A_{1g}.

as a result of having two-phonons in the process, as there is a non-zero probability that phonons at 30 and 60° to the edge normal can interact with the charge carrier - then another phonon scattering can result in the wavevector sum being perpendicular to the edge.

Following this logic, there are several factors that may lead to the polarization dependence of the bulk resonance.

Casiraghi *et al.* discuss an additional polarization dependence which arises from the lifetime of the excited-states and associated charge carriers.[131] A limited lifetime means there is a limit to how far the charge carriers can travel before decaying, and since charge carriers travelling at some angle to the edge (not perpendicular) have to cross a larger distance to get there, they originate from a smaller volume than charge carriers travelling directly towards the edge (see Figure 3.39). This essentially

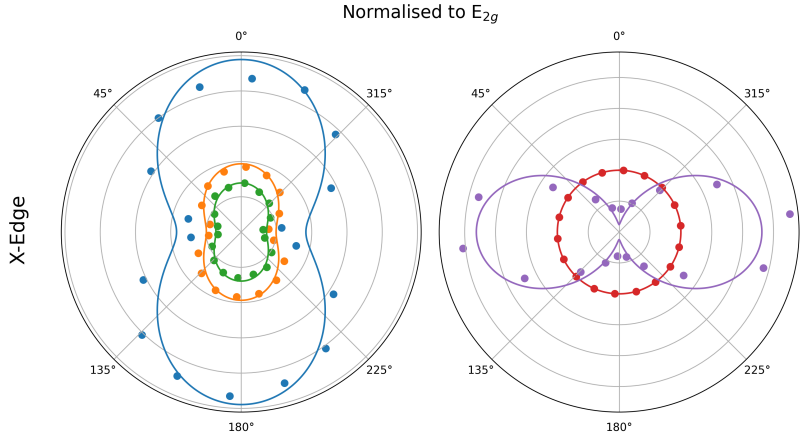

(a)

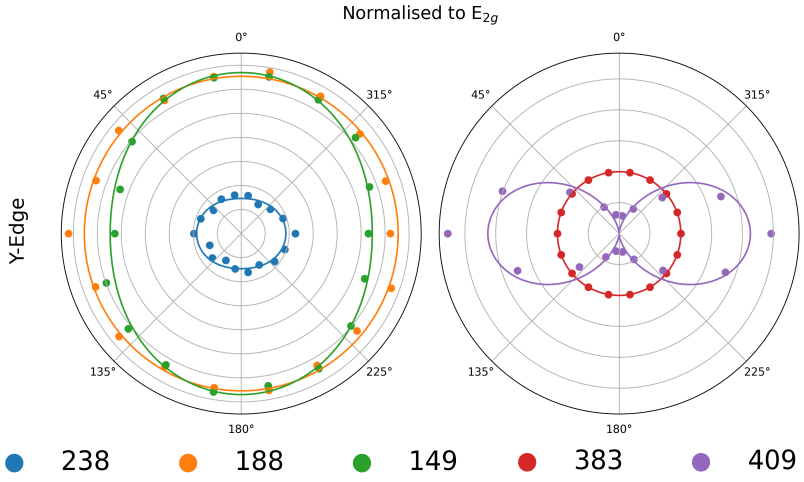

(b)

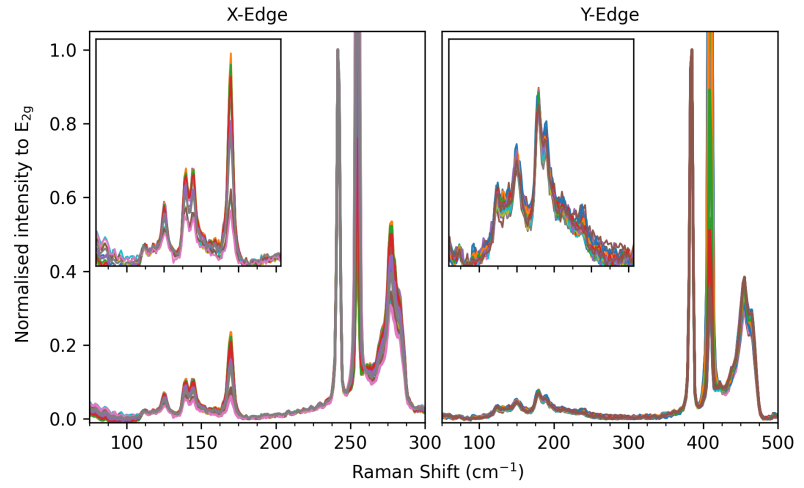

(c)

FIGURE 3.38: The polar plots in 3.37 normalised to the E_{2g} mode. Note some polarization dependence remains in the X-edge defect modes, while that of the Y-edge is lost in the defect modes. The trend may be clearer in (c) which overlays all the spectra in (a) and (b), with insets showing the defect modes region.

amounts to a smaller scattering (interaction) volume, and therefore we expect to see the most intensity when the polarization is perpendicular to the edge.

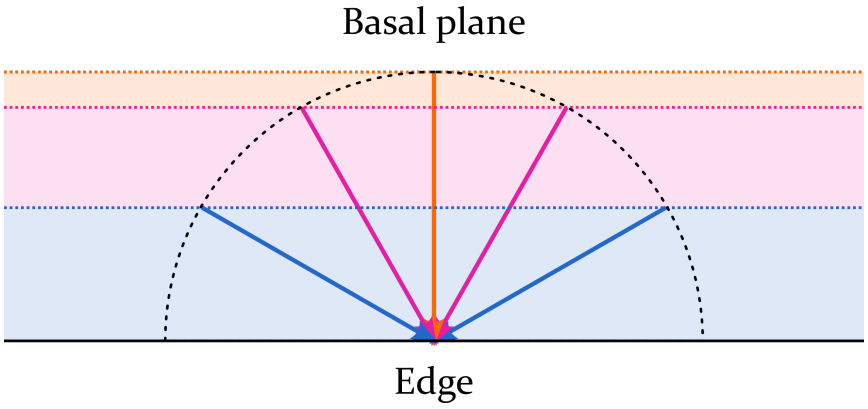

FIGURE 3.39: For some maximum distance a charge carrier can travel in a finite lifetime (length of the arrow), carriers impacting the edge at an angle cannot originate as far into the basal plane as those travelling straight towards the edge. The depth is indicated by the shaded areas. This results in fewer scattering events at oblique angles for a given laser spot size. If we make the diameter of the semi-circle the laser spot, we find that the intensity of the modes will be proportional to the cross-section of the shaded area in the semi-circle.

In addition, in order for the two phonon wavevectors to sum with a wavevector perpendicular to the edge, the wavevector of the second phonon must be a mirror of the first wavevector in a plane running perpendicular to the edge and the basal plane. As the angle between the wavevector of the first phonon and edge approaches 90°, so to does the second phonon, and the angle between the two wavevectors approaches 180°. If we consider the process to be sequential, in that one phonon interaction occurs before the other (rather than both happening simultaneously) as equation 3.11 depicts it, the wavevector of the first phonon $\boldsymbol{q}_a$ will impart its wavevector to the electron, and thereby influence the selection of the second phonon wavevector $\boldsymbol{q}_b$ through the electron-phonon interaction Hamiltonian. As such, the probability of the two-phonon process will be proportional to the wavevector product $\boldsymbol{q}_a \cdot \boldsymbol{q}_b$, and this will be maximum when the incident polarization is parallel to the edge.

This argument may also explain the observation of the 2LA(K) shown in Figure 3.40. Careful examination of the 2pDOS region in the thin flake edge reveals a peak which shares the same polarization dependence as the LA(K) and twice the frequency at 480 cm^{-1}. Note that this peak sits at a frequency higher than the 2pDOS region, much like the LA(K) sits higher than the pDOS region, suggesting a specific resonant enhancement is responsible for its appearance. In this case, because it is a two-phonon process, we should expect to also see the 2LA(K) in the zigzag edge of thin MoS_2 - except for the specific case where the two wavevectors are identical ($\boldsymbol{q}_a + \boldsymbol{q}_b = 2\boldsymbol{q}_a = 2\boldsymbol{q}_b$), as this requires the $\overrightarrow{\Gamma K}$ direction to be perpendicular to the

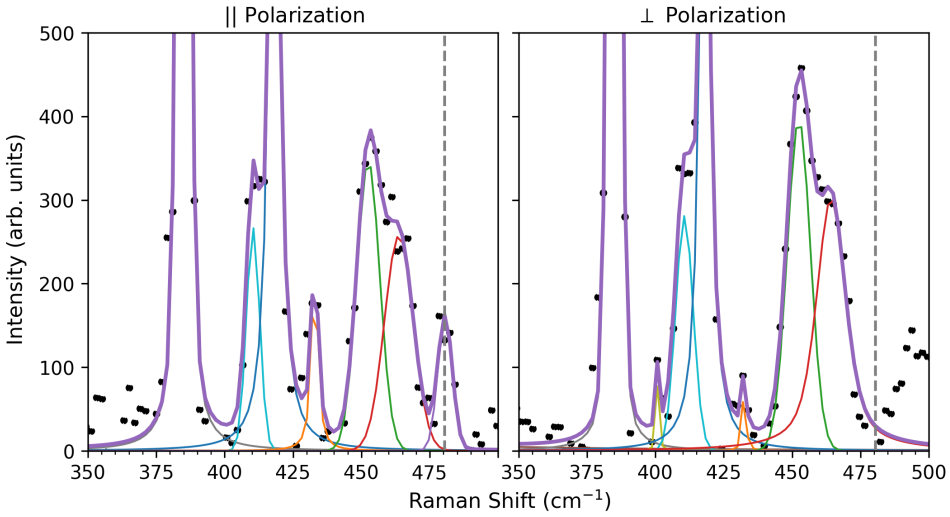

FIGURE 3.40: Peakfitted spectra taken from an edge region showing the 2LA region with (left) a clear peak around 480 cm^{-1} at parallel incident polarization with the edge, and (right) showing no peak under perpendicular incident polarization.

edge (i.e. an armchair edge). Unfortunately, it can be difficult to find thin zigzag only edges, as in general zigzag edges are (from overall observations of edge modes and flake geometries) not as common as armchair. In addition, thin flakes tend to have disordered edges, in which case we are unable to differentiate from which edge structure the signal is originating. At bulk zigzag edges the only features we observe in this region are the 2pDOS, which is likely a consequence of the M point enhancement overshadowing any specific modes. It should be noted that it is not appropriate to quantitatively fit the 2LA/2pDOS without detailed experimental or computational data, since these features are convolutions of an unknown number of higher order scattering events throughout the BZ. Here, it is only fit with two peaks to help constrain the peak optimising algorithm.

3.2.5 Symmetry Analysis

Now that we have ascertained that the scattering pathways involve $\overrightarrow{\Gamma M^*}$ and $\overrightarrow{\Gamma K}$ we can draw some more definitive conclusions from the symmetry of the transitions (M^* indicates the virtual states below M point).

M Point

For the pre-resonant scenario we can assume that the virtual state is a superposition of states dominated by contributions from the lowest energy bands at the M point. In this situation, we expect the denominator terms in the resonant Raman equation

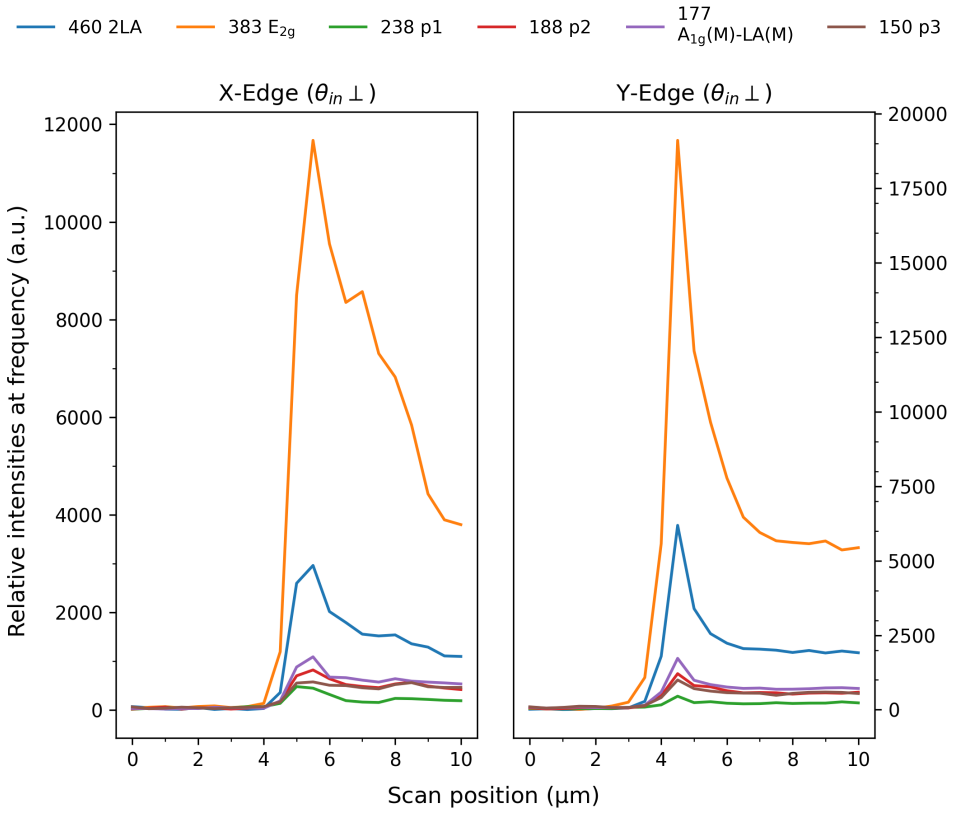

(a)

FIGURE 3.41: Linescans of the X-edge and Y-edge in Figure 3.26 with incident polarization perpendicular (⊥) to each edge direction. Note while the specific resonance at the X-edge is (mostly) gone, the general resonance remains, though slightly diminished, for both edges.

(equation 3.14) to favour a transition which gets as close to the M point states as possible. These will originate from the highest VB state, meaning unlike the K point resonance we can be confident that the M point resonance initial states are exactly on Γ. In reality there will be some distribution of initial states near Γ with sufficiently close energy to also be considered, but these all share A_1 symmetry so the analysis is the same. Symmetry decomposition from DFT calculations using QE (see section B.2) provides us with the irreducible representations of the CB states at the M point. We can therefore condense table B.5 in Appendix B and reduce the symmetry of the states at Γ to the D_{2h} point group to get table 3.6.

Thus we can see that the only individual phonon from the M point capable of mediating the transition is the LA', and that the irreps. of the phonons contributing to the higher-order modes will multiply to give A_g or A_{2u}. Phonons which meet this condition for the difference bands with matching frequencies are listed in table 3.7, and are the most intense features. Weaker features in these regions may be the result of contributions from off-M and of off-Γ states with different symmetry, and therefore different (but less intense) allowed combinations.

TABLE 3.5: Phonon symmetries from the M and K points of the BZ published by Linveh and Spanier. Phonon frequencies (ν) are gathered from various computational reports in literature (cited in Livneh and Spanier[171]), and correspond to the frequencies at 0 K.

Mode	M point (D_{2h})	ν (cm^{-1})	Mode	K point (D_{3h})	ν (cm^{-1})
ZA′	B_{3g}	174	ZA′	A_2'	184
TA′	B_{1g}	160	TA′	A_2''	188
LA′	A_g	233	LA′	A_1'	237
ZA	B_{1u}	182	ZA	A_2'	185
TA	B_{3u}	156	TA	A_2''	190
LA	B_{2u}	235	LA	A_1'	234

TABLE 3.6: Irreducible representations of the states at Γ_{VB} reduced to D_{2h} symmetry, and at the M point, as determined by DFT calculations. The phonon column identifies M phonons capable (or not) of mediating the transitions by symmetry.

Γ Band	Symm (in D_{2h})	Phonon	Symm	M
26	B_{3u}	A_g (LA′)	B_{2u}	27
26	B_{3u}	A_{2u} (None)	B_{1g}	28

Some of the bulk zigzag edges show a weak peak around 236 cm^{-1} which might be mistaken as the LA(K) due to some contribution from disordered features in the edge, or hidden armchair segments in some of the layers (see Figure 3.42). However, comparison with actual armchair edges shows that this peak is approximately 3 cm^{-1} lower, which is a significant difference and clearly observable in Figure 3.42, even with our relatively low detector resolution. Given that for all our observations the LA(K) phonon disperses at most 1.5 cm^{-1} higher in few-layers than the bulk, and seems essentially dispersionless around 238 cm^{-1} until this point, a shift of this magnitude and direction seems unreasonable. Instead, if we adjust the frequencies in table 3.5 to account for the temperature difference between the calculated (0 K) and measured (293 K) spectra using the thermal coefficients reported in Livneh and Steerer,[215] we see that this is the exact frequency for the LA′(M) mode. Therefore, it seems that under the right conditions, the first-order defect-mediated LA′(M) phonon can be observed in zigzag edges. It may be that a slightly higher energy excitation source can achieve a real resonance with the M point and give a more intense LA′(M) phonon.

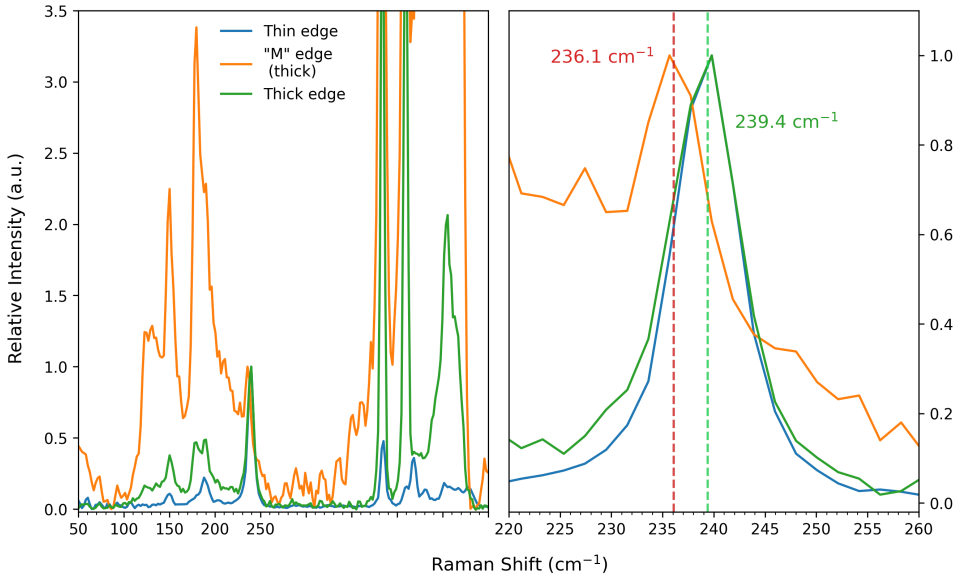

FIGURE 3.42: Comparison of an "M" edge with two "K" edges, both thick and thin samples. Right hand graph shows a zoom on the LA region. The peak in the M edge sample near the LA mode is significantly shifted from the other two, indicating it is in fact a weakly allowed single LA(M) phonon.

TABLE 3.7: Assignments and irreducible representations of M point phonon difference modes in the defect mode region.

Phonon ω (cm^{-1})	Difference mode	Difference ω (cm^{-1})	Symm
124	E_{2g}(M)-LA(M)	362-235	$B_{2u} \times B_{2u}$
149	$E_{1g}(M_2)$-ZA(M)	330-182	$B_{3g} \times B_{1u}$
179	A_{1g}(M)-LA'(M)	412-233	$A_g \times A_g$
189	unknown		

K Point

The dispersion of the LA(K) mode (shown in Figure 3.21) and the ambiguous assortment of final states means there is little extra information to be gleaned from symmetry analysis. Whether excitation occurs from exactly at Γ or near Γ, all the acoustic phonons have symmetry capable of mediating a transition to one of the states near K.

Implications of Phonon Assignments

It has been shown that the defect modes appearing at the edges of bulk and few-layer MoS_2 are a consequence of indirect resonances with the M and K points. Each pathway exhibits distinct resonance effects, and while the M-phonons are observed in both edges (of bulk) due to their second-order nature, the K-phonons are only

observed at arm-chair edges as a result of the backscatter mechanisms. These K point phonons, in particular LA(K), can be used to quantify the number of defects in MoS_2 materials, which has significant application in the characterisation of MoS_2 based catalysts. This is particularly relevant at the time of writing for the development of hydrogen evolution catalysts for the production of environmentally friendly hydrogen fuels. Defect quantification in literature has been primarily performed using ultra-sensitive techniques such as tip-enhanced Raman spectroscopy,[128] atomic-resolution imaging techniques,[124,125] or magnetic Raman techniques,[127] which are not simple techniques and are not easily amenable to large scales. This indirect resonance Resonance mechanism provides a simple, accessible technique which can be used to quantify defects and edges in a sample.

Additionally, the ability to determine edge structure is incredibly useful for nanomaterials characterisation, as armchair and zigzag edges manifest different electronic properties.[115,117] Therefore understanding the structure of MoS_2 edges is critical for fabricating ordered nanoribbons and other nanomaterials with the desired properties. This research demonstrates for the first time the application of polarized Raman spectroscopy to the determination of edge structures in MoS_2.

Considering implications further afield, there has been growing interest in the last decade in 2D van der Waals heterostructures,[216] where the layering of different 2D nanomaterials is exploited to control the electronic and optoelectronic properties of the materials. Such structures can be generated from a wide range of available stable 2D materials, and since the modulation of their electronic properties is dependent on the relative translational and rotational mismatch between the layers, a vast range of possible systems with tunable properties could be generated.[217] These changes often result in band gap rearrangements and the appearance of new excitonic transitions, independent from the original materials, including momentum indirect excitons.[218] The ability to access such transitions using this indirect DRR technique, coupled with polarization experiments and temperature control may be a powerful tool for understanding the intricate electronic structure of these materials, and provide additional insights through analysis of symmetry and the observed phonon modes and their frequencies.

Since this process involves the same phonons responsible for valley depolarization in spin-valley coupled systems, this indirect resonance mechanism may also find applications in the characterisation and design of spin-valley polarized devices for storage information.[187]

In addition, it may be possible to exploit the indirect transition or defect-mediated scattering to induce valley polarization with an additional degree of freedom - non-zero centre of momentum mass excitons. This may in turn provide an additional constraint on depolarization, similar to the coupling between layers in Zhu *et al.*,[102] and could help stabilise the system against depolarization and result in better performing devices.

Beyond the tangible applications of this technique, is also makes us consider the theory of DRR mechanisms in a different way, as most, if not all DRR literature is focused on the scattering pathways accessible following direct transitions. Strictly speaking, this indirect scattering mechanism is not considered doubly resonant, since the only one real excited state is involved. Nevertheless, the resulting processes are analagous to the DRR defect scattering in graphene, and are well described by the DRR theory. Perhaps the indirect excitations also play a role in producing the D mode in graphene. It is also likely that similar defect modes can be found in other TMD materials (see Chapter 4), and perhaps also other semiconductor crystals with appropriate band structures and symmetry constraints. Further exploration of these materials with tunable laser sources may reveal a wealth of exploitable electronic and excitonic properties.

3.2.6 Discussion of Mechanism

For a while we had considered a gap-state excitation model to explain the appearance of the defect modes. In this model, we assumed that a direct excitation was occurring from a ground state to a mid-gap state, such as the states involved in defect photoluminescence in literature.[72,112] In this case, we assumed the excitons formed were not bound, but able to propagate through the lattice. Then, upon excitation, the defect could immediately scatter the exciton away, and a subsequent phonon interaction to conserve momentum would allow radiative recombination to occur, giving rise to the Raman defect modes. The polarization dependence could be explained as a polarization dependence in the transition-dipole operator (equation 3.12), which could result from an overlap of states at the edge in a single direction. However, this model does not explain the differential activation of phonons by zigzag and armchair edges, as an initial defect scattering should be capable of scattering in any direction from the edge, thereby selecting for any BZ phonons. It also does not explain the resonance enhancement of specific zone-edge phonons.

In addition, for this direct absorption process to occur, there should be a corresponding absorption peak in the near-infrared. Figure 3.43 shows the UV-vis spectra of the sonication series in Figure 3.17, and the A, B and C excitons near 675, 615, and 450 nm respectively are clearly visible, but there are no such features in the near-infrared (right graph) where we would expect this gap-state to occur. The sloping baseline in the near-infrared is an indication of the indirect absorptions occurring. It is likely that the signal from a gap-state absorption would be very weak and may be difficult to see in the standard absorption spectra. However, there is no sign of any features in this region across all sample sizes - including the smallest sonicated particles which are fully dispersed in the solvent, and should have an abundance of edges and gap-states. It therefore seems unlikely that a direct absorption is occurring at these gap states to give rise to the defect modes.

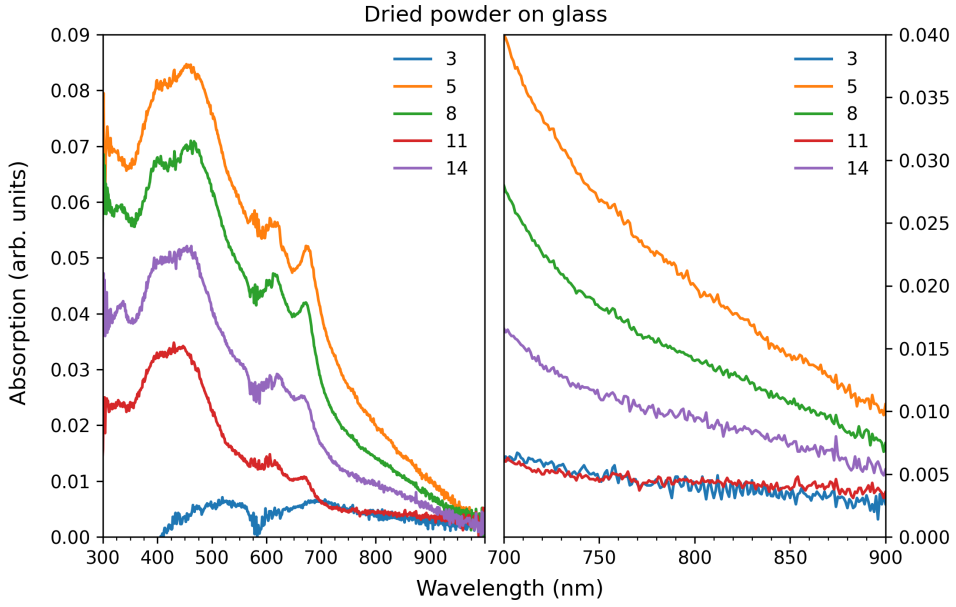

(a)

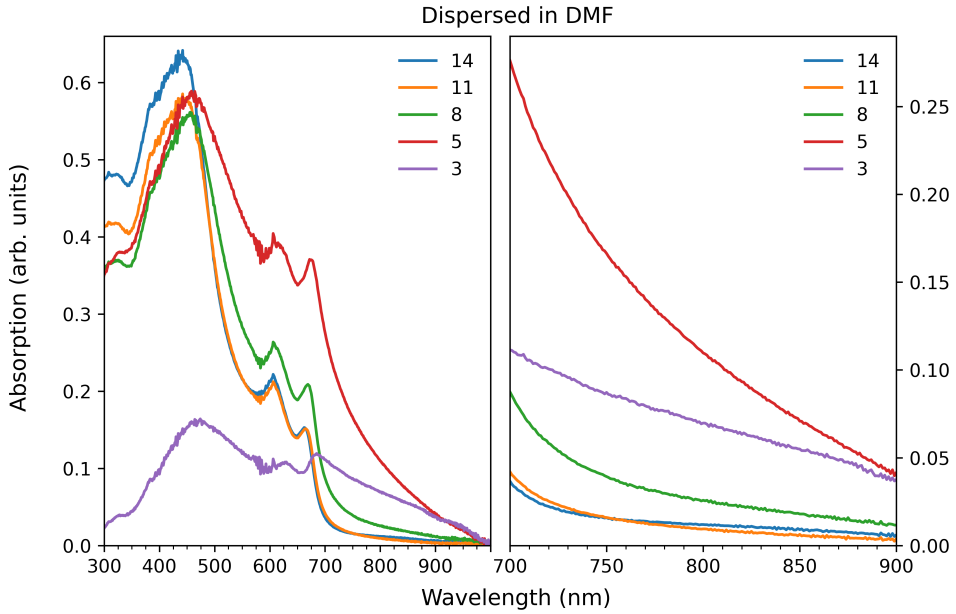

(b)

FIGURE 3.43: UV-vis absorption spectra for the MoS_2 sonication series used in Figure 3.17, measured as (a) dried powder dispersed onto glass, and (b) as a dispersion in dimethylformamide (DMF) solvent. The legend indicates centrifugation speed $\times 1000$ rpm. The left graphs show the main exciton peaks near 675, 615 and 450 nm (A, B, C respectively), while the right graphs show the near-infrared region, which has no clear peaks, only a sloping baseline from the indirect absorptions.

While it is possible that chemical contaminants may be contributing to the defect modes, their presence in samples prepared from multiple methods suggests this is not the case. So far I have shown the spectra of mechanically exfoliated "pristine"

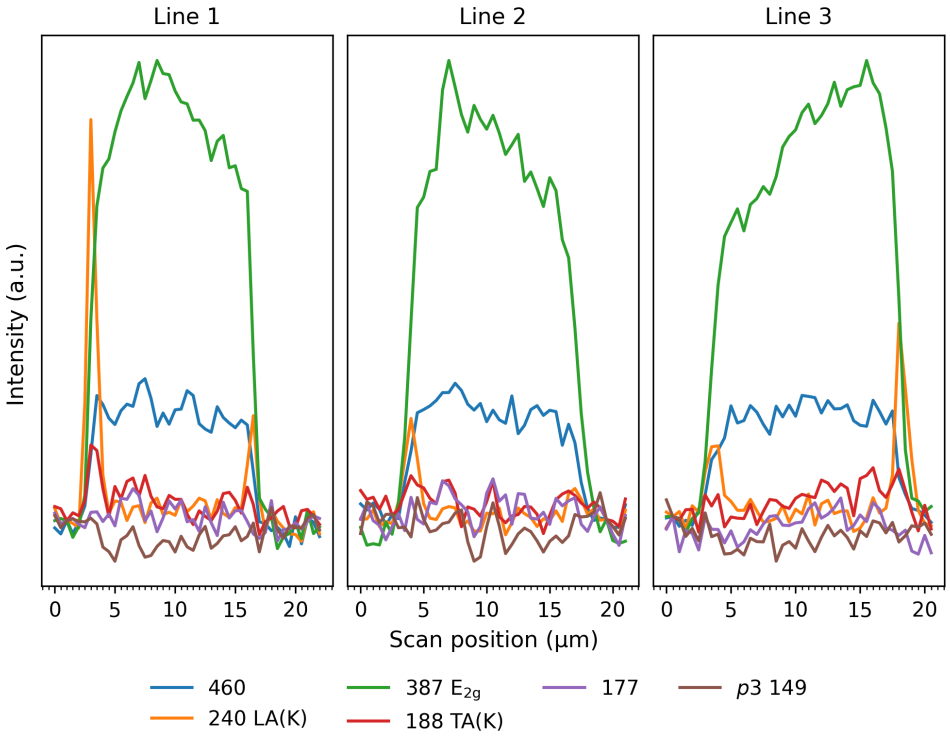

(a)

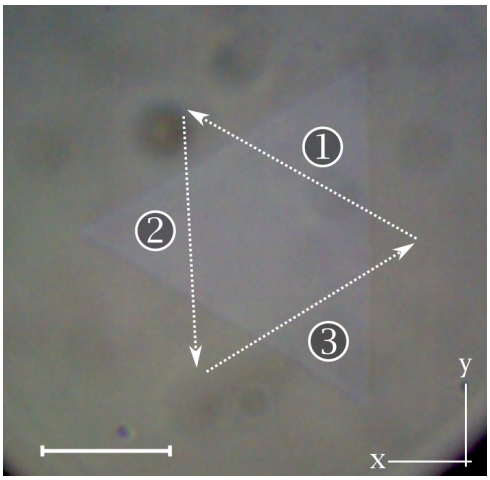

(b)

FIGURE 3.44: (a) Linescans of CVD-grown MoS_2 for three lines marked in (b), with incident polarization kept parallel for each scan - parallel with the right hand edge along the y-axis (i.e. the up and down the page). Scale bar in (c) is 10 μm.

flakes and sonicated nanoparticles. We can also synthesise single-crystals of few-layer MoS_2 using CVD growth in a tube furnace (see Methods section 5). Figure 3.44 shows the linescans on one of these crystals, and we see the same evolution of defect modes as we cross the edges. In fact, since the crystal is such a clean triangle, we can even observe the polarization dependence as the linescans cross edges at different angles (incident polarization angle kept the same for all scans). The trailing edge of line 3 does not produce as intense an LA(K) peak as line 1, which may be a result of

imperfections along the edge, since these linescans do not necessarily cross the same points twice. Crystal quality can vary from sample to sample, and within samples, depending on growth conditions. AFM images in Figure C.2 suggests the edges appear to be straight on sub-micron scales, but are likely somewhat disordered on the atomic scale.[219]

The sonicated nanoparticles can be synthesised in a variety of solvents (see section 5.2.2) - some performing better than others, but each time the defect modes are reproduced. If anything, it is possible that oxygen residues could be contaminating the edges by coordinating to molybdenum atoms, since all these samples are exposed to atmosphere. Additionally, a small amount of water in the sonication mixture seems to result in much higher yields of the small nanoparticles, suggesting water is facilitating the cleavage process, and may in fact be coordinating or reacting in the process.

In addition, I have performed annealing experiments, where the sonicated samples are placed under high vacuum and heated up to 350 °C. Under these conditions, most organic contaminants will vaporise or decompose - any hotter under this vacuum causes sulfur vacancies to form and the MoS_2 to begin evaporating. However, the defect modes only decrease in intensity slightly (see Figure C.4), which is consistent with a subtle reorganisation of edge structures and suggests chemical contamination from organic species or solvent (either covalent or non-covalently interacting) is not responsible for inducing the defect modes.

3.3 Conclusions

This chapter has demonstrated and discussed a novel defect-mediated DRR mechanism in MoS_2 which results in the observation of normally forbidden acoustic phonons and DRR combination and difference bands. These features arise as a consequence of a phonon mediated indirect absorption process, followed by a defect scattering at an edge to provide the necessary momentum conservation for radiative relaxation. This momentum conservation also demands a strict backscattering event, both in reciprocal space, and in real space, which results in unique phonon interactions for armchair and zigzag edges. Through a combination of polarization and temperature dependent studies, I have shown that the features at $\sim$238 cm^{-1} and 188 cm^{-1} are assigned to the LA(K) and TA(K)/LA(Q) phonons respectively, and are only observed in armchair edges. A general enhancement of the entire spectrum irrespective of edge orientation is attributed to a pre-resonance from Γ_{VB} to the M_{CB} point, which is lost as layer number decreases and the band gap increases.

The contribution from single acoustic phonons to zigzag edges from the pre-resonance is weak and rarely observed, but may become stronger if the excitation

energy is increased to reach a full resonance. The feature $p3$ at 149 cm^{-1} is also exclusive to the armchair edge, but has too low a frequency for the M or K phonons. Instead, $p3$ is likely a TA(Q) phonon mediating a $\overrightarrow{\Gamma Q}$ transition, which lies in the same direction of the BZ as the $\overrightarrow{\Gamma K}$ transition, and by energy and symmetry requirements should be active as well.

While analagous DRR defect modes appear in graphitic materials, no such features have yet been observed in MoS_2, except for the general pDOS features resulting from the breakdown of the $q \approx 0$ selection rule in crystals. Therefore, this research presents the first account of DRR defect modes in MoS_2, and will likely become a valuable tool for the characterisation and development of MoS_2 in a number of applications. Since the edges of MoS_2 are known to be the active sites for hydrogen evolution and other catalytic processes, this technique provides a means of quantifying the catalytic potential of synthesised MoS_2 materials, and also may provide insights into the mechanisms which cause active site passivation and performance degradation. In addition, this technique presents a novel method for determining edge structure in MoS_2 nanomaterials such as nanoribbons, in which edges of armchair and zigzag orientations present differing unique properties, and contribute strongly to the overall material properties. Therefore, this technique provides a method to differentiate between these edge structures without requiring atomic-resolution characterisation techniques, and can be performed on as-assembled electronic devices. The applications of this technique may also extend out to the characterisation of van der Waals heterostructures as a means of probing the intricate excitonic landscape of these diverse hybrid materials, and spin-valley coupled systems which may benefit from the additional degrees of freedom provided by momentum-indirect excitons.

Lastly, the indirect mechanism in this work represents a different way of thinking about DRR in 2D materials, and it may provide inspiration for a deeper understanding of the mechanisms involved and further development of the theory.

Chapter 4

Resonance Tuning

4.1 Grain Boundaries

The indirect resonance model outlined in Chapter 3 predicts that other types of defects should also activate the defect modes, not just at the edges. For instance, point defects will scatter charge-carriers somewhat randomly, but that will also include the backscatter necessary to conserve momentum and observe the single phonons. Perhaps more interesting is a grain boundary, which is a section of covalently bonded structure joining two crystals like a seam. These crystals are rotationally or translationally offset from one another, such that their two crystal lattices do not match. During growth, a grain boundary forms at the point where they come into contact to compensate for the crystalline mismatch. The grain boundary assumes the most stable structure for joining a particular mismatch, and these have been predicted to have interesting 1D magnetic properties.[104,123,220] Such boundaries should present a 1D barrier for scattering, much like an edge, but it is expected to have a vastly different electronic environment since it sits in the middle of two crystals. This may have interesting consequences for scattering, since the angle of each crystal with respect to the boundary will be unique, and may not favour a backscatter condition for either set of phonons. Conversely, the boundary may not be sufficiently ordered to matter - and it may scatter in relatively random directions.

Identifying a grain boundary in mechanically exfoliated flakes is quite difficult without using atomic-resolution or phase-dependent electron microscopy methods.[219] Fortunately, it can be much easier to identify regions with grain boundaries in CVD-grown MoS_2, since pristine crystals grow outward in ordered triangular shapes, creating a grain boundary whenever two mismatched crystals grow into each other. Figure 4.1 shows optical microscope images of our CVD grown MoS_2, with dotted lines indicating probable areas for grain-boundary formation. However, the actual location of the grain boundary at any given point becomes less certain for larger borders, as the boundary can change direction if the crystal mismatch no longer favours boundary propagation in that direction (see Figure 4.2). Nevertheless, a linescan or map is sufficient to search the general area.

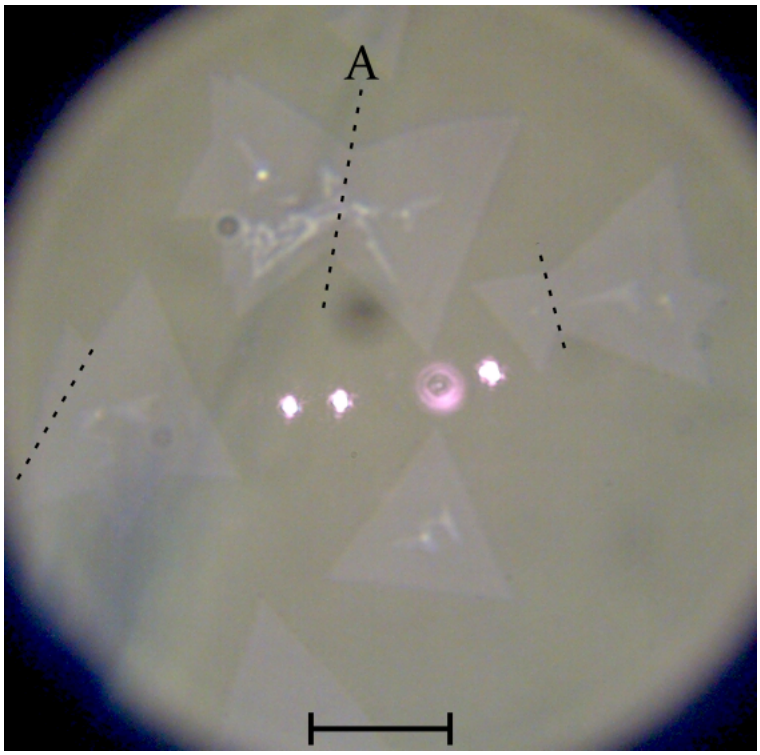

(a)

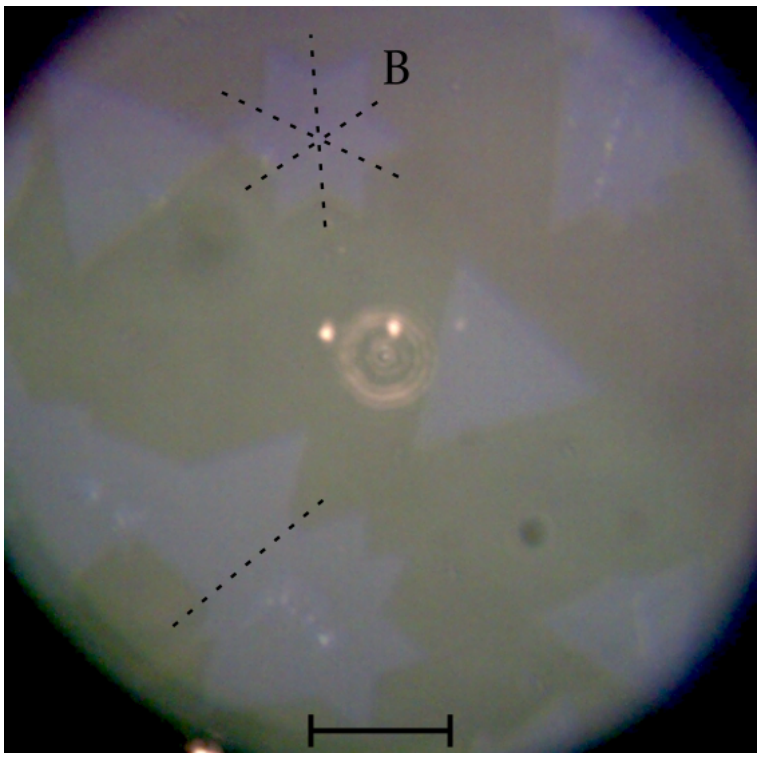

(b)

FIGURE 4.1: Optical microscope images at 100× magnification of CVD-grown MoS_2 on sapphire substrates. The dotted lines indicate the area between two mismatched crystals where a grain boundary is likely to be found. Scale bar at the bottom is 10 µm.

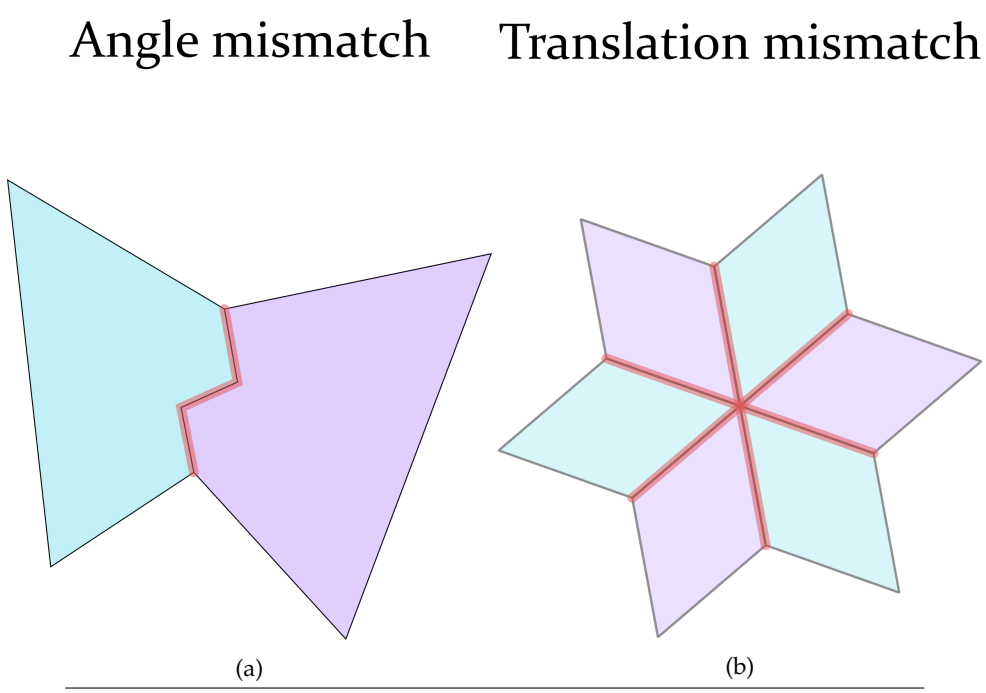

FIGURE 4.2: Examples of crystal mismatch and the kind of shapes the grain boundary can form. (a) Crystal outline traced from the flakes and boundary marked "A" in 4.1(a) and (b) crystal outline traced from the star-shaped cluster in 4.1(b) marked "B". Note the boundaries may not necessarily have these shapes, and the magnitude of the zig-zagging in (a) may be smaller or larger.

Figure 4.3(a) shows a linescan across the boundary between two crystals, through the area marked by the dotted line in (b). The polarization direction was perpendicular to the direction of travel. The scan data has the sapphire background subtracted, and shows a weak but clear peak in the LA mode (green trace) at the centre of the scan around 5.5 µm (marked by dotted line). The spectrum on the right is extracted from the linescan at this point, and although weak, clearly shows the presence of the defect mode LA(K), with a broad feature around TA(K) and perhaps just a hint of $p3$ at 149 cm^{-1}.

Figure 4.4 shows linescans of another grain boundary with the incident polarizations set perpendicular to the direction of scan travel, parallel, and half-way between the two (90°, 0°, and 45°). The intensities do vary with incident polarization angle, but trend is not necessarily obvious, nor is the actual orientation and direction/shape of the boundary at this point. This suggests the boundary is behaving like a disordered edge, either because multiple boundary orientations are under the laser spot, or as mentioned above there may be a relaxed backscatter constraint since the boundary bridges two crystals of different orientation, and K point scattering may be possible into one of the crystals at any given angle.

Additional incident polarization measurements at finer angles, different positions, and/or different crystals may provide more insights, but it should be noted

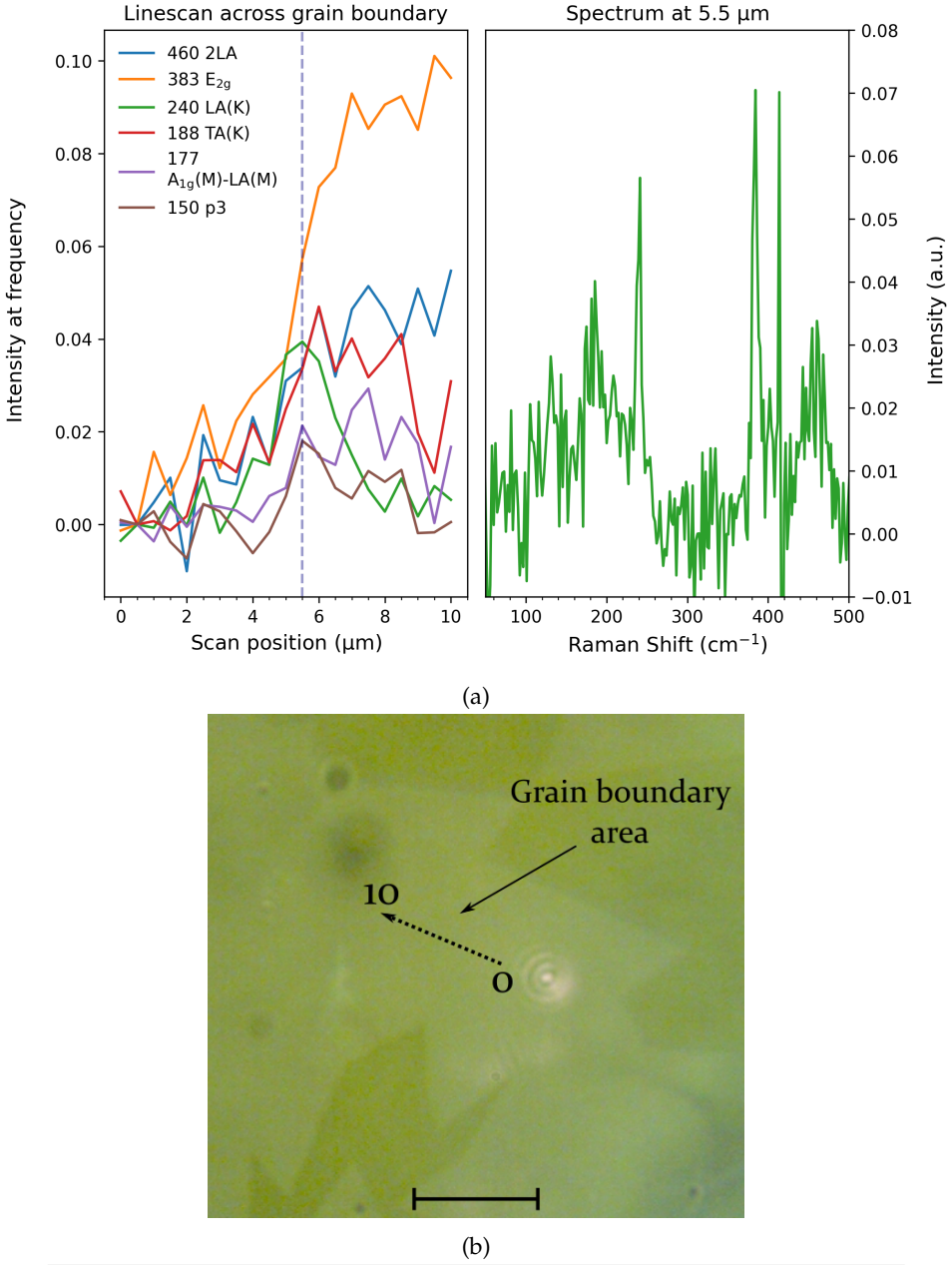

FIGURE 4.3: (a) Linescan across a grain boundary, indicated by the dotted arrow in (b), spanning 10 µm from 0 to 10. The spectrum on the right of (a) is the taken from the scan position at 5.5 µm, where the linescan data indicates a spike in the LA(K) phonon (238 cm^{-1}, green trace) and indicates scattering at a grain boundary. Scale bar at the bottom of (b) is 10 µm.

that each point in the linescan in Figure 4.4 was collected for five minutes at approximately 5 mW, and the signal from the grain boundary is still quite weak. This could be a consequence of the grain boundary appearing as a lower energy barrier to propagation than an edge, and scattering probabilities for charge carriers may be lower. To observe a clear trend with polarization, longer acquisition times would be required to resolve differences in intensity for each of the polarization angles.

For thicker samples it is often enough (and in fact better) to hold the laser at one

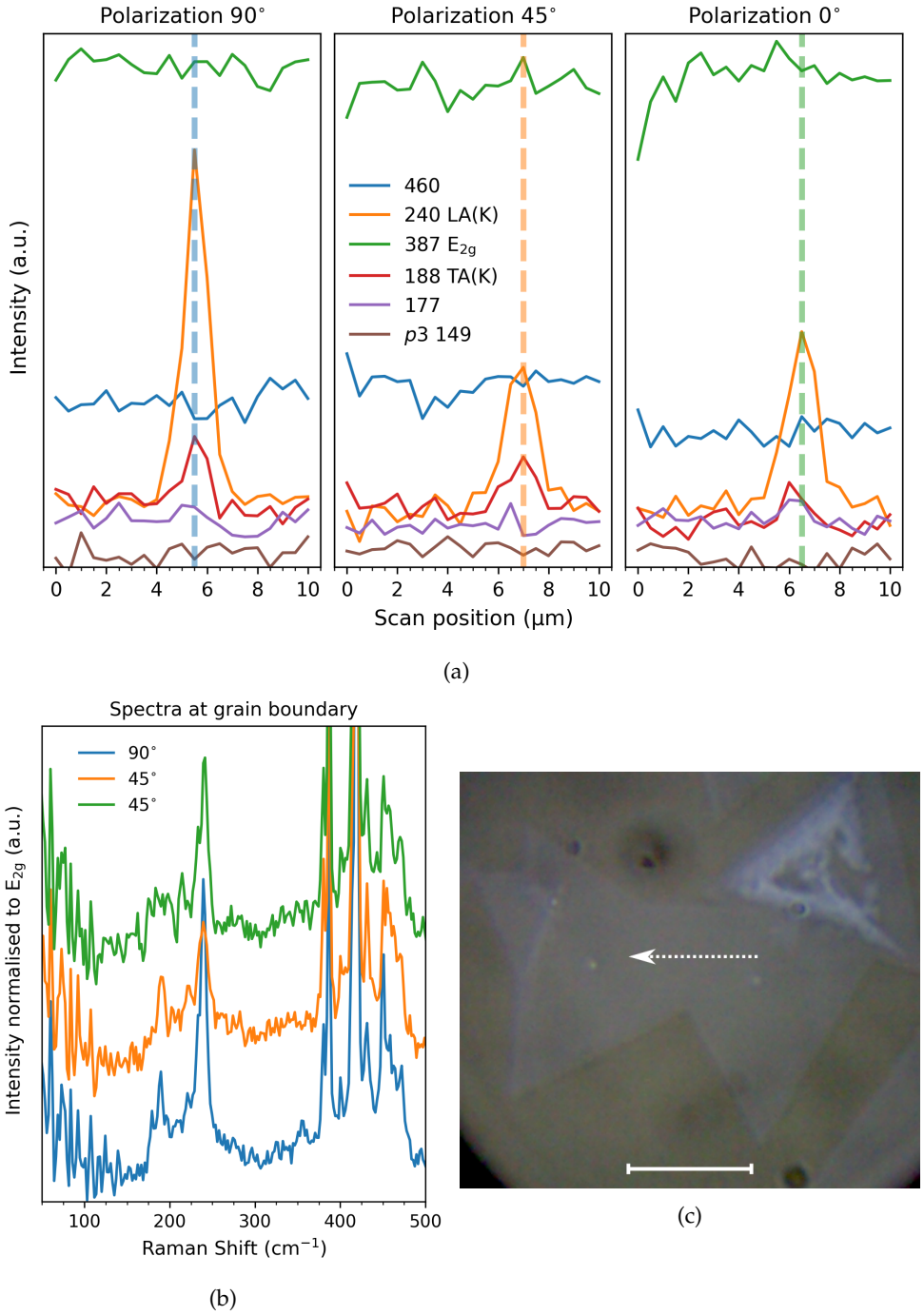

FIGURE 4.4: (a) Linescans of another grain boundary as indicated by the arrow in (c), performed with incident polarization oriented perpendicular do the direction of scan travel (90°), parallel to the direction of travel (0°), and at an angle half way between the two (45°). (b) shows the spectra at each point where the defect modes spike in the linescan, indicating the position of the boundary. Scale bar in (c) is 10 μm.

point and collect each polarization angle as individual spectra. However, in this current setup thermal drift away from the grain boundary over such a long period is a likely outcome (i.e. must remain at the same spot while collecting all angles),

and would almost certainly perturb the data set giving misleading or inconclusive results (see section 2.3.5 for thermal drift explanation). Fine-resolution linescans and averaging over a range of points could help mitigate this issue, but would of course take much longer to collect the full data set. A stronger resonance enhancement may be possible with a laser precisely tuned to the indirect gap energy, which may shorten collection times enough for accurate analysis. Regardless, it would be wise to improve the temperature control before attempting such a study, and should be an interesting avenue for future research.

The ability to detect grain boundaries using basic Raman techniques is a novel development, and allows the detection of polycrystallinity in micro-scale flakes of MoS_2 without atomic-resolution techniques. Since grain boundaries are expected to have magnetic properties, their detection using Raman spectroscopy may provide useful insights in the development of magnetic and spin-valley electronic devices. In addition, Raman spectroscopy can be used for characterisation of these materials in fabricated assemblies/devices, which is not currently possible with alternative high-resolution TEM characterisation techniques.

4.2 Resonance Tuning

4.2.1 Temperature

The LA(K) mode and 2LA features show an interesting reciprocal relationship with temperature. Figure 4.5 shows that as the sample is heated above room temperature, the intensity of the LA(K) mode disappears while the 2LA features are enhanced dramatically. Note that the temperature control in these samples is achieved through induced heating at the sample by varying laser power, and calibrated using the methods reported in Livneh and Steerer[215] (see Appendix D.1 for details.) We can also observe the same reciprocal relationship for the TA(K) and A_{1g}-LA(M) modes (see Figure D.7), suggesting the defect K phonons are being lost at high temperatures. The trend is also consistent with observations shown in Chapter 3 (Figure 3.19), which is that at low temperatures the 2LA features have reduced intensity, while the K point defect modes are enhanced. The 2LA features do not contain the 2LA(K) mode near 480 cm^{-1} (see Figure 3.40), but rather they are the general 2pDOS features observed under most resonant conditions, consisting of generally random scatterings throughout the BZ. The fact that the LA(K) mode disappears as the 2LA features are simultaneously enhanced suggests they belong to different scattering pathways throughout the BZ, and one of these pathways is in resonance for low-temperatures, and the other for high-temperatures.

This hypothesis is supported by the observation that in some cases, the anti-Stokes LA(K) can be seen disappearing before the Stokes LA(K) (see Figure 4.6),

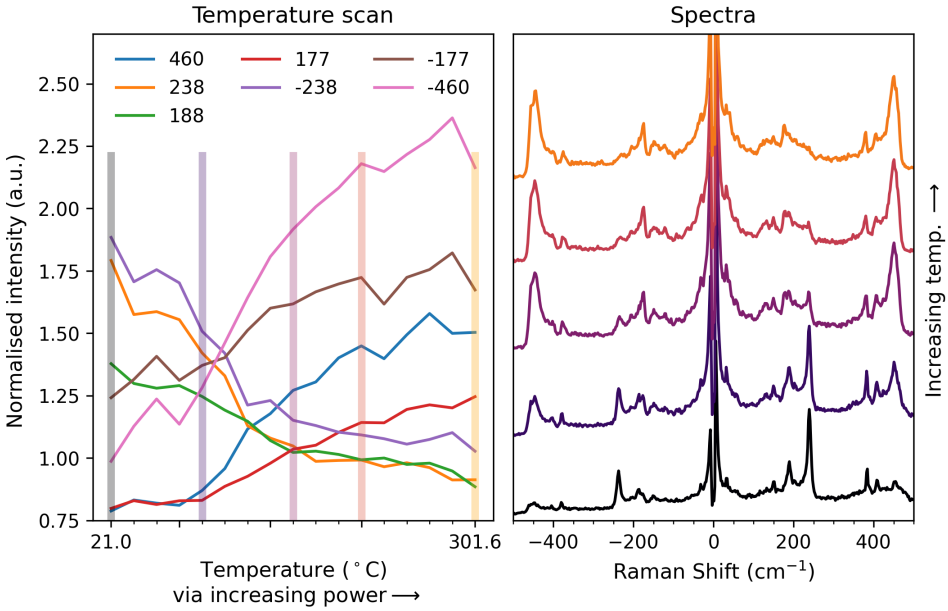

FIGURE 4.5: Temperature dependence of the defect and and second-order modes. The line plots on the left are the intensities of each labelled frequency, normalised to the E_{2g}. Anti-Stokes peaks are labelled with a "-" before the frequency, and are normalised by the anti-Stokes E_{2g}. The temperature change was achieved by proxy of laser power, and has been calculated from the shift in the fundamental modes, as demonstrated by Livneh and Sterer[215] (see Figure D.6).

which suggests the high-temperature resonance is a consequence of a shrinking band gap somewhere, rather than an increasing band gap. Figure 4.7 illustrates how only a shrinking band gap will cause the anti-Stokes phonons to reach or lose resonance before the Stokes phonons.

There are two key effects of increasing temperature on the band structure which may bring about a new resonance condition. Firstly, since thermal fluctuations disrupt the weak interlayer interactions, the indirect band gap increases - similar to the effects of reducing layer number.[57] Secondly, the direct band gap decreases due to the effects of thermal expansion within the crystal lattice.[221]

Given the complex electronic structure, the new resonance could be forming in a number of ways, such as through different momentum-indirect excitons or charged trions, and possibly enabled by defect-induced gap-states which may have been inaccessible at room and low-temperatures.[221,222] If we assume that the Γ point doesn't change energy much in this temperature range, it is possible that the new resonance is one with the M point, whereupon the pre-resonance moves into a full resonance, since the M point second-order modes seem unaffected (or enhanced) by the resonance shift.

It's difficult to quantify the change in energy from the room-temperature resonance to the onset of this high-temperature resonance, as it could involve changes

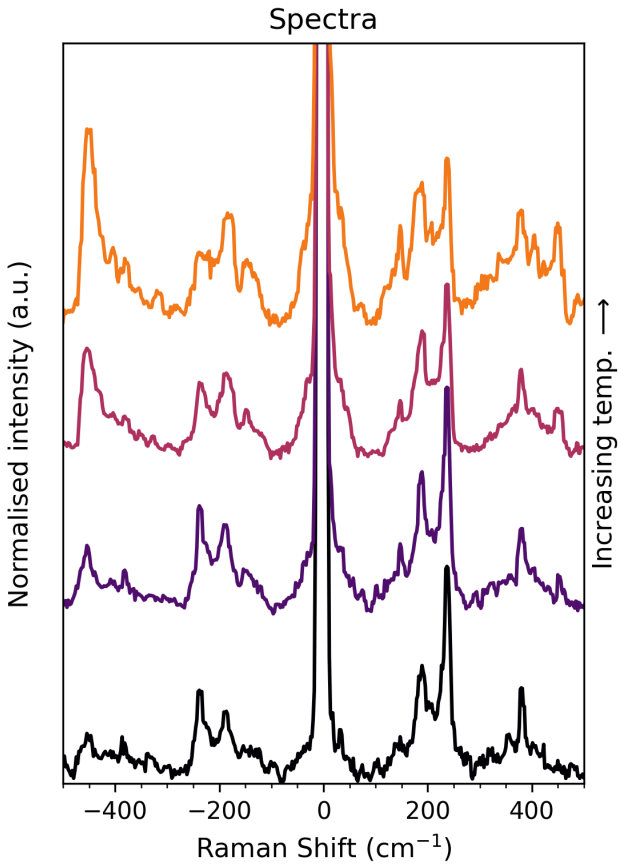

FIGURE 4.6: Spectral changes with temparature in a sample similar to the one used in Figure 4.5. In this case, the anti-Stokes phonons can be seen reacting to the resonance change before the Stokes phonons, suggesting a shrinking band-gap is responsible for bringing this high-temperature pathway into resonance.

to the band structure at multiple points, and potentially exciton binding energies. However, a ballpark estimate based on the sum of the shifts of the indirect and direct photoluminescence signals across a 300 K temperature window reported by Zhao *et al.*[57] gives around 100-200 meV shift in resonance energy. Of course, directly tuning the excitation energy would provide this number clearly, and future work accurately controlling temperature and excitation energy may help assign this scattering pathway.

4.2.2 Chemical Modification

MoS_2 can be modified or functionalised to tailor its physical and electronic properties to specific applications.[77,78,80] One method is to form covalent bonds between molybdenum atoms at sulfur vacancies and thiol groups on organic molecules (ligands), which essentially "plugs the hole" in the lattice or edge structure.[223] Since this method has been reported to modify the photoluminescent energies through band

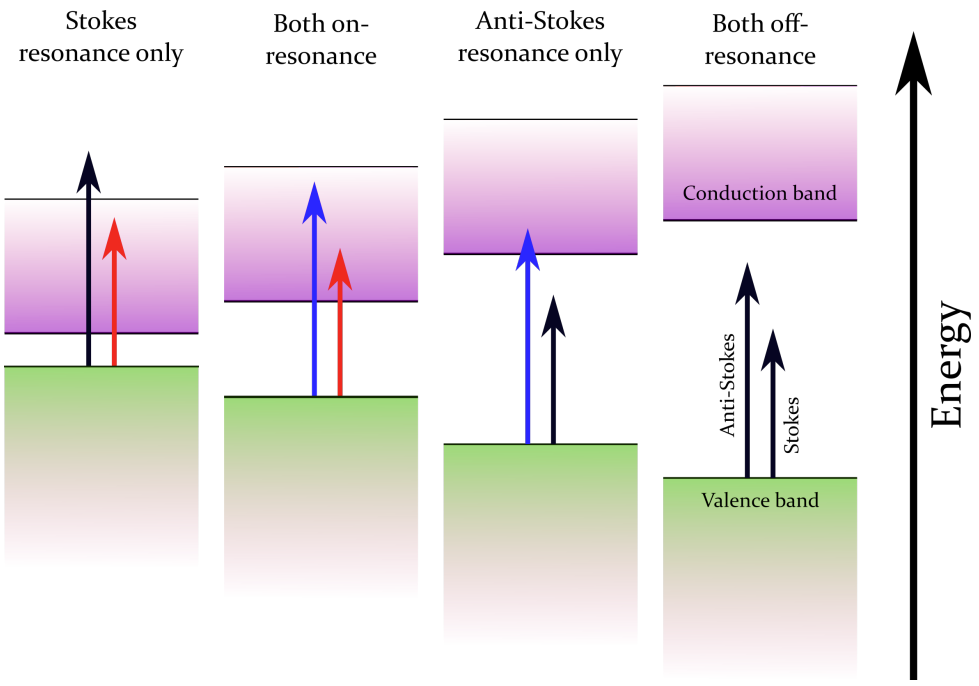

FIGURE 4.7: Schematic showing the order of onset/loss of resonance with shifting band gap. On-resonance processes occur for arrows which land in the conduction band (purple shaded area), and are represented by coloured arrows. Off-resonance processes are indicated by the black arrows. For increasing band gaps, the Stokes photons (shorter arrow) have less energy, so they fall out of resonance first. Conversely, a decreasing band gap will affect the anit-Stokes processes first, since these photons have more energy.

structure doping affects,[79] we were curious to see if the indirect resonance condition and defect modes are affected. Figure 4.8 shows some preliminary results of Raman spectra of sonicated samples which were functionalised with a variety of thiol-containing ligands following the procedures outlined in the methods section (Chapter 5). Interestingly, the modifications all seem to quench the K point phonons to some degree, causing the remaining modes to resemble the zigzag (M) edges in Figure 3.26.

In addition, the shape of the remaining modes are largely unchanged, suggesting that indirect transitions can still occur, just not to the K point, or via the defect mediated processes. We consider two explanations for this. Firstly, the functionalisations may dope the states at the K_{CB} point more heavily than the M_{CB} point, resulting in a loss of the $\overrightarrow{\Gamma K}$ resonance pathway. It would be interesting to test for this by trying to reclaim this resonance pathway with a tunable laser source. Secondly, modifications at the edges may blur the potential difference experienced by a charge carrier at an edge, such that the edge no longer presents as sharp a boundary. Canado *et al.* suggest that the sharpness of the boundary is important for satisfying the backscatter condition, stating that a pristine edge is well defined in the direction perpendicular to the edge (real space), meaning it will be completely delocalised in this direction in

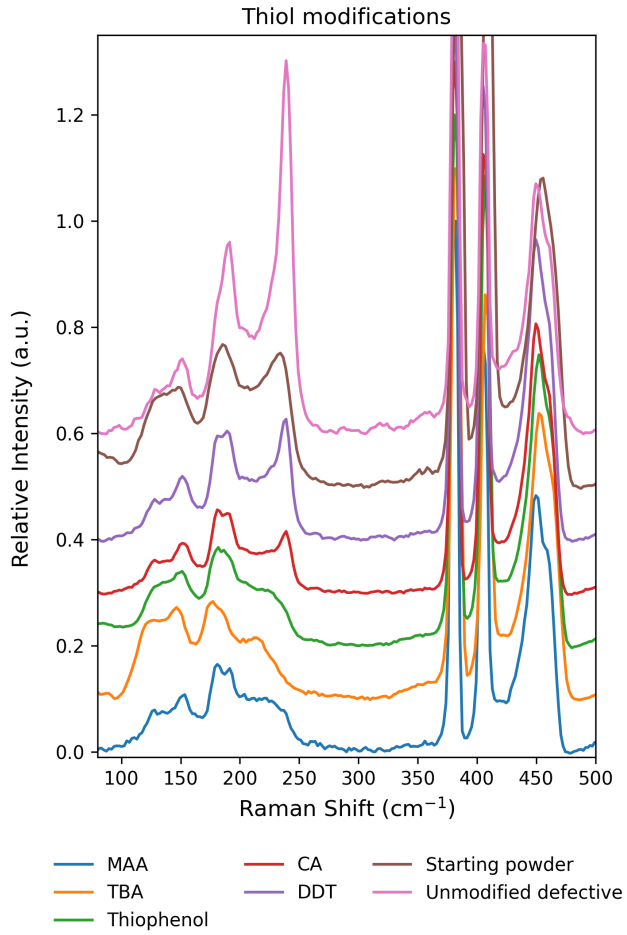

FIGURE 4.8: Raman spectra of sonicated MoS_2 with various chemical modifications at 785 nm excitation. Some of the modifications seem to remove all traces of the K phonons, while in others they remain. The legend acronyms are: mercaptoethanoic acid (MEA), cysteamine (CA), thiobarbituric acid (TBA), dodecanethiol (DDT).

reciprocal space, and a scattering wavevector can take on any value perpendicular to the edge.[181] Therefore organic molecules attached at an edge may act to delocalise (localise) that edge in real space (reciprocal space), and therefore limit the wavevectors the edge can scatter with, resulting in lower defect mode intensities.

The infrared absorption (IR) data (which measures infra-red active vibrational modes) suggests that there are some organic molecules in the sample, but the peaks are broad and are not necessarily a good indicator of functionalisation (see Figure D.5). This is because it is not clear if the molecules are covalently attached, or physisorbed on the surface or caught between layers. Typically X-ray photoelectron spectroscopy (XPS) is required/used to draw more informed conclusions, based on how the oxidation states of the molybdenum atoms and sulfur atoms (and any of the ligand atoms close to the thiol group) change before and after exposure to the ligand.[223]

In addition, for the ligands which no not quench the K phonons as well, it is not clear whether this is a consequence of the ligand's particular effect on the band structure, or whether they were not as efficient at functionalising the material. For instance, both MoS_2 and the ligand need to be well-dispersed in the solvent to ensure the ligand can actually come into contact with the edges. In some cases (cysteamine for example) the MoS_2 material did not disperse well and aggregated quickly, suggesting the ligand may not have been able to access enough of the material to fully quench the K phonon signals in the spectrum.

Nevertheless, it appears that significant changes to the defect spectrum can be induced by chemical modification under the right circumstances, and additional work in this area - with a particular focus on electron donating and electron withdrawing ligands - may yield interesting results.

4.3 Exploration of other TMDs

Using this indirect-excitation approach, we fully expect to find similar defect-mediated modes in the other TMDs. We are not sure why these modes require the indirect transition in MoS_2, as opposed to the graphene defect modes which are observable in direct resonances at energies spanning the visible spectrum. It may be that the excitonic nature of charge carriers in MoS_2 is an important factor, or perhaps the exciton-phonon coupling at the K point is not sufficient to be considered a resonant phenomenon in MoS_2.

It is also possible that this technique of indirect resonance defect detection may be applicable to other semiconductors with appropriate scattering channels in their band structures, not just TMDs.

For now, we will focus our attention on the TMDs, since they are the most likely materials to yield similar results. Unfortunately, we lack adequate tools for a complete analysis, so the investigations at this stage are cursory. This is because we need more laser wavelengths spanning the near-infrared, since the other TMDs tend to have low-energy indirect band-gaps.[224] Ideally, this study can be continued in conjunction with lower-energy lasers (i.e. 1064 nm) or a tunable near-infrared laser and triple-grating spectrometer, for complete control over excitation and detection conditions. This would allow pinpointing of the resonant energies within the band structure and accurate assignment of the $q > 0$ phonons.

Table 4.1 lists the range of band gap energies for the four most common TMDs: MoS_2, WS_2, $MoSe_2$ and WSe_2. While there are many more combinations of TMDs,[3] these ones can be purchased or synthesised relatively easily, and have indirect band gaps accessible by our laser wavelengths (except $MoSe_2$). The more exotic TMDs with niobium, tantalum, and tellurium typically have direct band gaps below 785 nm.

TABLE 4.1: Table of band gap estimates for some common TMDs, as reported in literature.

TMD	Min indirect gap (eV)	Max indirect gap (eV)	Max direct gap (eV)	References
MoS_2	1.2	1.52	1.9	54,57,58
$MoSe_2$	1.1	1.3	1.5	54,225,226
WS_2	1.4	1.7	2.1	54,57,225,227
WSe_2	1.2	1.55	1.7	54,57,226

4.3.1 Molbydenum Diselenide ($MoSe_2$)

$MoSe_2$ possesses a similar band structure to MoS_2, with the most notable difference being a lower direct band gap. In fact, it is the only member of the above table with a measured direct band gap below 1.58 eV (785 nm), which suggests our Raman spectrum will be in direct resonance, and we may not be able to observe any indirect resonance modes. Regardless, we can test our model by seeing if this is the case, and there may be additional direct resonance scattering pathways at this energy worth investigating.

The fundamental Raman active modes (at Γ) of $MoSe_2$, as reported in literature, are presented in table 4.2.

TABLE 4.2: The fundamental Raman active modes of $MoSe_2$, as reported in literature.[228,229]

Mode	Frequency (cm^-1)
A_{1g}	243
E_{1g}	168
E^1_{2g}	27
E^2_{2g}	283

Figures 4.9 and 4.10 show linescans of flakes of $MoSe_2$. The graph on the right shows spectra from selected points of the linescan, indicated by the dotted lines. The fundamental modes are labelled on the spectra. Anti-Stokes scattering did not show any additional details, so is omitted from these spectra for clarity - the full spectra and linescans of additional flakes can be found in Appendix D.

Figure 4.9 shows that while the spectrum is decorated with second-order modes, there appears to be no edge-specific response from any of the key modes. This suggests we are observing DRR modes associated with the direct resonance. Based on the contrast in the optical microscope image, this flake is considered bulk, so it would be useful to compare this to the spectra of thinner flakes with larger band

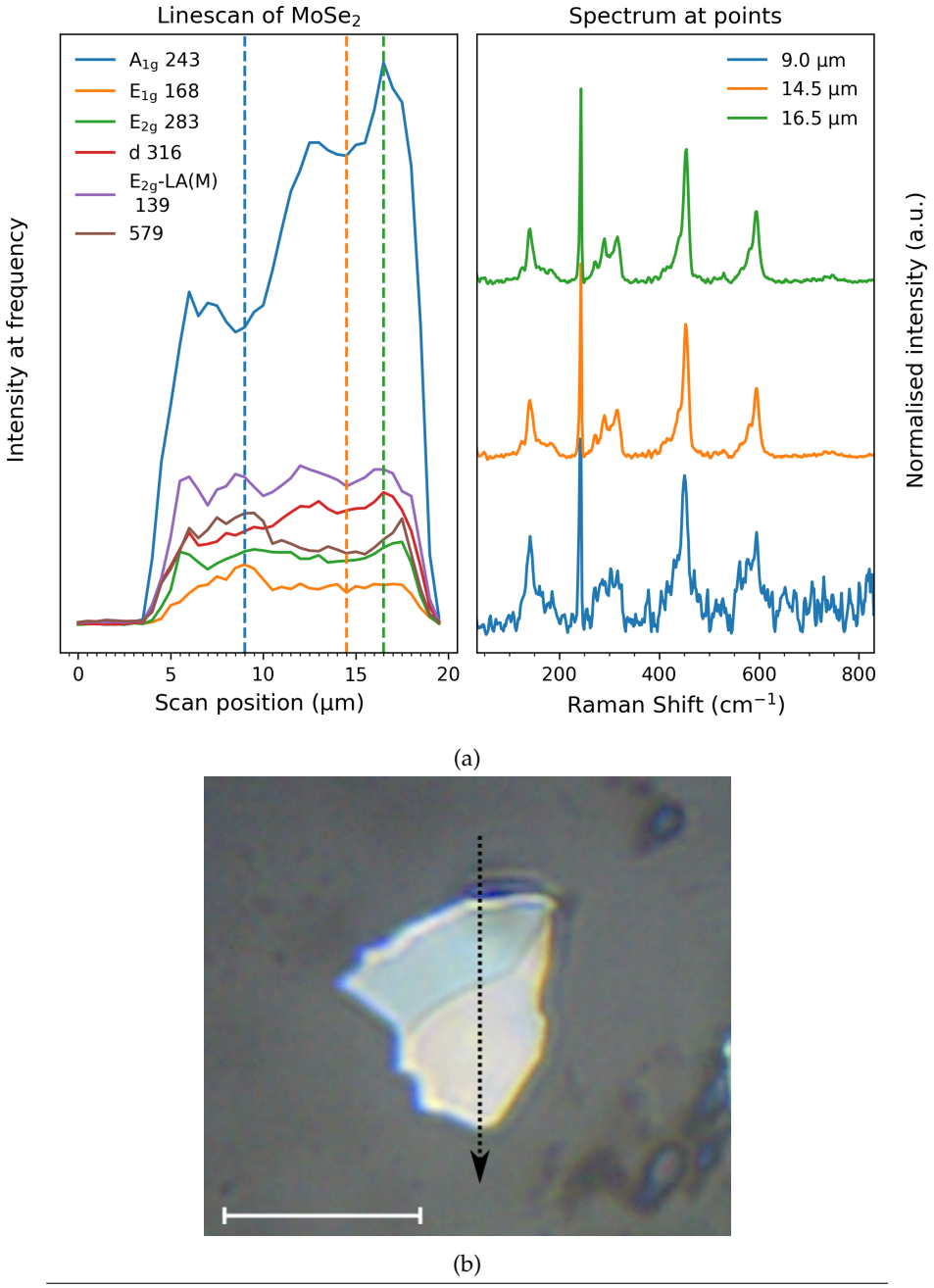

FIGURE 4.9: (a) Linescan of a flake of $MoSe_2$ as indicated by the line in the optical image in (b). The dotted lines in the linescan plot on the left represent the points from which spectra on the right are taken. Scale bar in (b) is 10 µm.

gaps. However, it can be quite difficult to find relatively large few-layer flakes. Figure 4.10 shows instead the linescan across a group of small flakes, which have relatively low contrast and appear to have few-layer thicknesses. However, as is the case for the bulk sample, there does not appear to be any edge-specific features in these flakes. As such, it appears that excitation at 1.58 eV does indeed result in a direct resonance, and a lower-energy excitation will be needed to assess possible defect modes. Note the peak near 420 cm^{-1} in the green trace (19.5 µm) is from the

sapphire substrate.

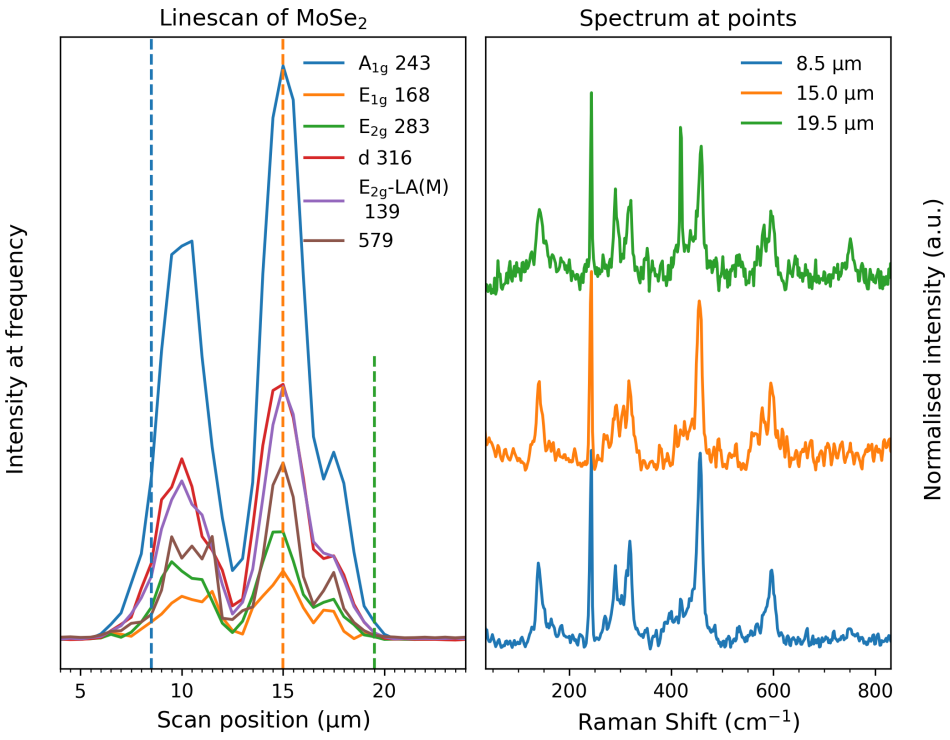

(a)

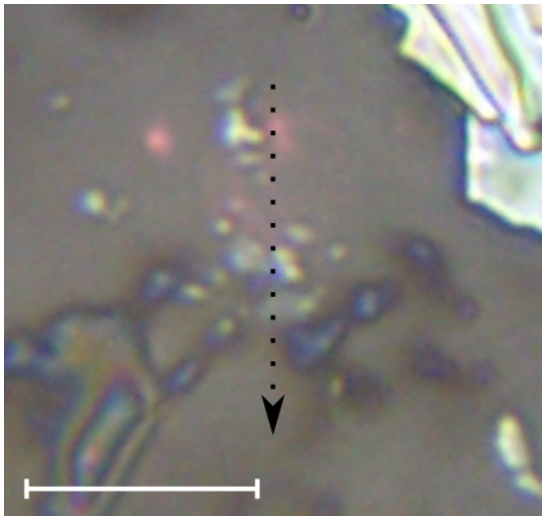

(b)

FIGURE 4.10: (a) Linescan of a a cluster of few-layer $MoSe_2$ flakes, shown in (b). The scan region and direction are indicated by the line in the optical image in (b). The dotted lines in the linescan plot on the left of (a) represent the points from which spectra on the right are taken. Scale bar in (b) is 10 µm.

4.3.2 Tungsten Disulfide (WS_2)

WS_2 also exhibits two indirect transition pathways from Γ to K and Γ to Q and has the highest band gaps of the series, with a minimum indirect gap for the bulk around

1.4 eV, and a maximum direct band gap for single layers around 2.1 eV.[227] Bilayer WS_2 has an indirect band gap around 1.7 eV,[57] which means we may not observe the indirect transition for few-layer systems, until layer number and the electronic properties begin to approach bulk.

We haven't yet acquired a sample of WS_2 with which we can prepare mechanically exfoliated flakes, but we can synthesise it quite well on sapphire substrates using CVD techniques, with pristine few-layer and larger bulk-like terraced clusters on the same sample.

Figure 4.11(b) shows a thin, few-layered crystal with an additional thicker set of layers in the center, with the linescan in (a) running directly through both. There is also a small cluster of a seed crystal at the start of the scan (arrow has been broken to show this), which results in the spike seen on the left-hand side of the linescan. The graph on the right of (a) shows the spectra corresponding to the points in the linescan indicated with the shaded vertical bars.

The spectra on the right also have shaded regions: purple (80-210 cm^{-1}) shows the region where we might expect single acoustic phonons to appear based on frequencies reported in the pDOS;[202] green shows the E_{2g} fundamental mode at 357 cm^{-1} (which happens to be very close to the 2LA mode at 350 cm^{-1}); and red shows the sapphire substrate peak which is not easily baselined out as it overlaps with A_{1g} mode around 419 cm^{-1}. The purple region here is mostly empty - but it does seem like there could be some weak broad features in the edge spectra, which could be non-resonant defect scattering throughout the BZ.

Despite this region being mostly empty, there are indications from the E_{2g} mode that that a defect-mediated resonance may be occurring. The linescan on the right-hand side shows the edge of the thinner section, whereupon the E_{2g} rises up and plateaus along the basal plane. This is the classic behaviour seen in Chapter 3 for MoS_2 when the M point resonance was lost in few-layer samples, suggesting here there is no resonance at this edge. However, the edge of the central layers causes a large spike in E_{2g} intensity, which returns down to a midpoint before rising again at the edge on the other side - indicating a resonant or pre-resonant enhancement may be occurring at the thicker section's edges. This enhancement is distinct from the MoS_2 pre-resonant analogue however, as only the E_{2g} appears to be enhanced, while in MoS_2 every mode in the spectrum was affected. Apart from this enhanced E_{2g}, there appears to be no significant difference between the spectra at the edge of this central layer and its center (compare 7.5 µm and 9.0 µm).

Now we consider the spike caused by the seed cluster at 2.5 µm. Here the linescan does pick up an increase in intensity from the acoustic phonon region, although the spectrum itself is still appears relatively featureless upon inspection. Since the

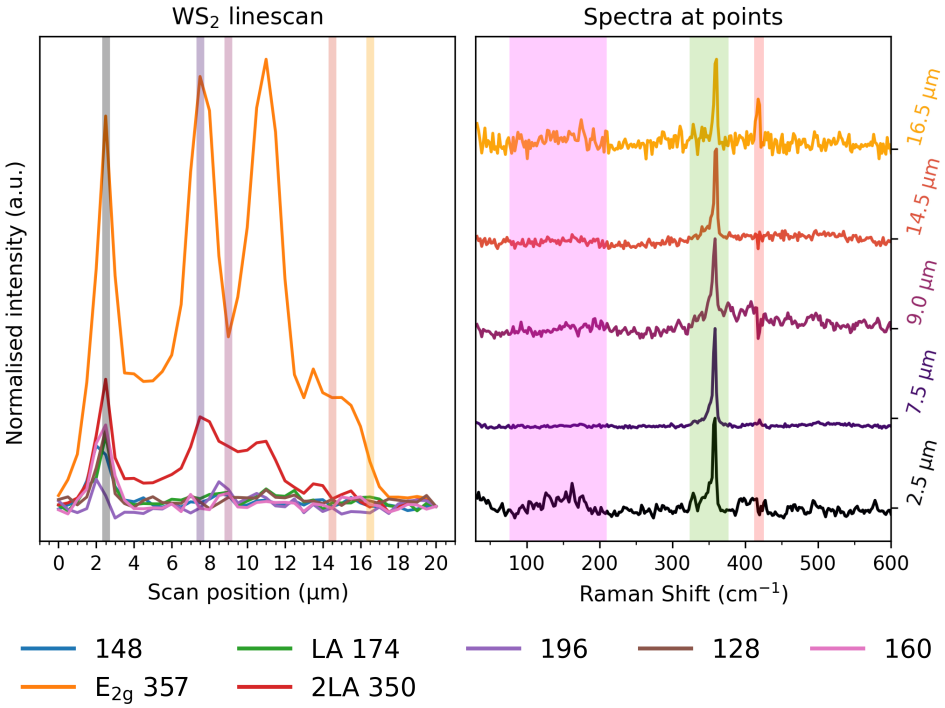

(a)

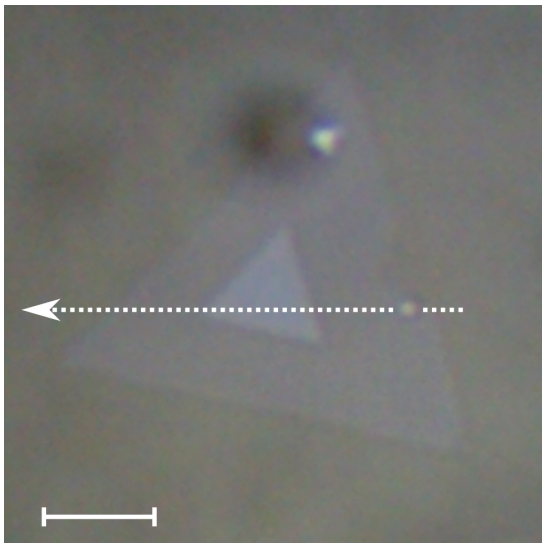

(b)

FIGURE 4.11: (a) Linescan and selected spectra at 785 nm excitation across a crystal of CVD WS_2, as shown by the arrow in (b). Scale bar in (b) is 5 µm.

cluster is spherical in nature, we cannot tell whether the observed modes are a consequence of edge scattering or simply basal plane DRR features. While this is fairly obvious in MoS_2 since the LA(K) was not convoluted by bulk DRR modes, in WS_2 there appears to be an LA mode present under resonant conditions, regardless of crystallinity.[177,227,230] This may turn out to be a separate DRR mode, which would require careful analysis to deconvolute from any LA features.

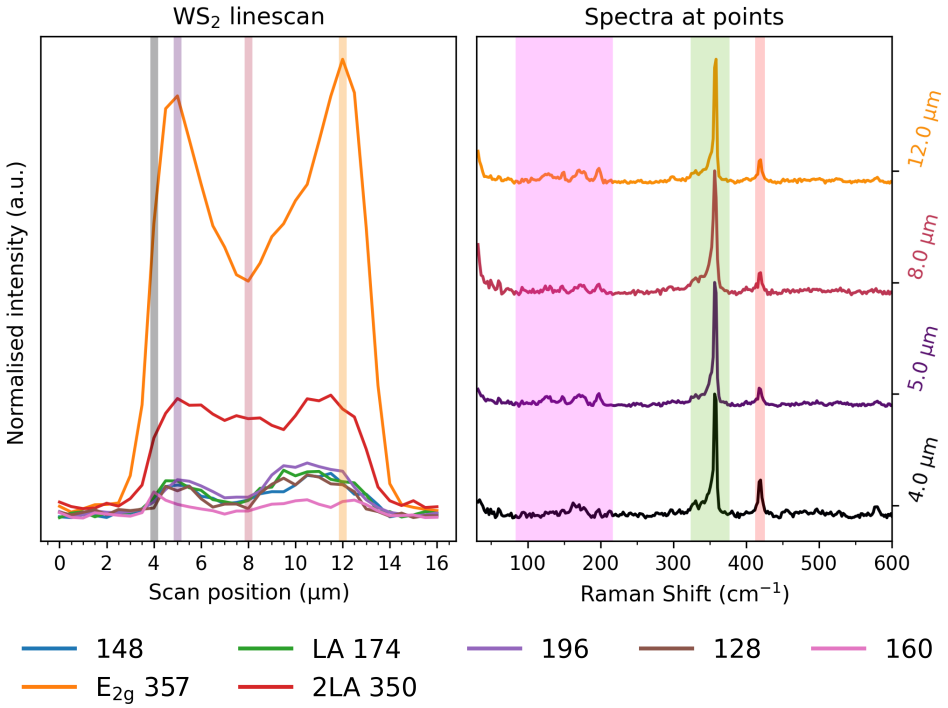

(a)

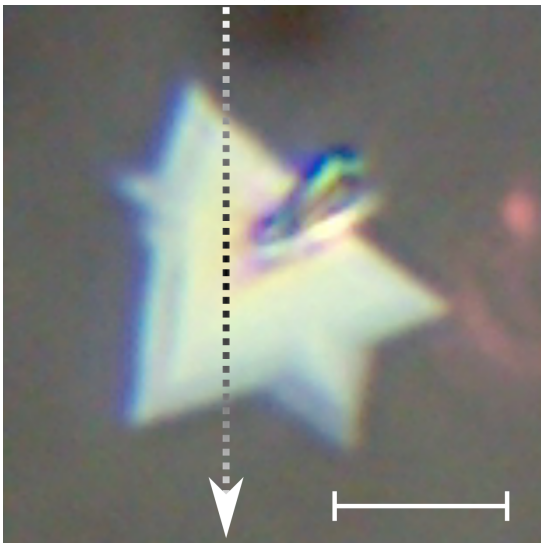

(b)

FIGURE 4.12: (a) Linescan and selected spectra at 785 nm excitation across a crystal of CVD WS_2, as shown in by the arrow in (b). Scale bar in (b) is 5 μm.

Moving on, Figure 4.12(b) shows a thick terraced crystal, which appears to have a relatively flat top surface, surrounded by terraced ridges as the layers below get larger. The linescan in (a) travels across the thickest section, as close to the center as possible without running over the section of seed crystal sticking out the side. This scan shows similar spikes at the edges as Figure 4.11, but are broader here likely due to the staggered layers. In this scan, there appears to be more activity from the acoustic phonon region, and Figure 4.13 zooms in to show this more clearly.

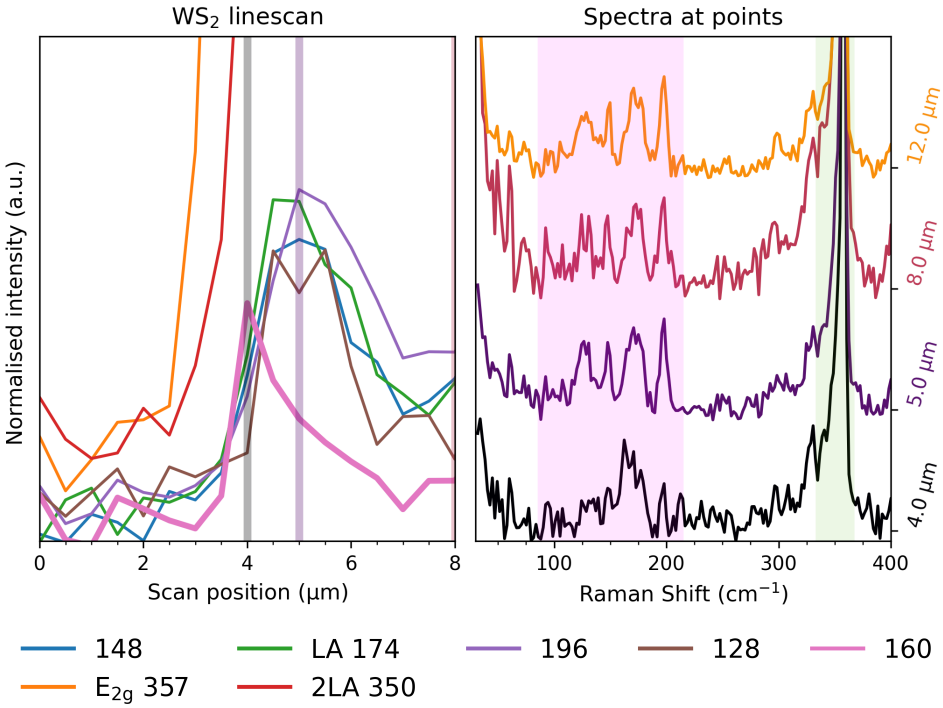

(a)

FIGURE 4.13: (a) Zoomed view of linescan in Figure 4.12 showing ordering of "edge" frequencies during linescan (left) and close-up of acoustic phonon region of the selected spectra (right).

Although weak and surrounded by noise, there are distinct peaks appearing in this region. In addition, the linescan is zoomed in to the points around 4 µm, and it is clear that one feature in particular around 160 cm^{-1} reaches a maximum before the rest. This behaviour is characteristic of the edge-activated K phonons in MoS_2, and suggests that this feature is also an edge-activated acoustic phonon. The other features in this region could be reasonably assigned to K, M, and Q acoustic phonons in the pDOS.

It is possible that the 160 cm^{-1} peak belongs to a mode that involves scattering to the Q_{CB} valley, which sits slightly lower in energy than the K_{CB} in few-layer and bulk WS_2.[227] Then, as the layer number increases and the Γ_{VB} point increases in energy, an indirect transition to the K_{CB} point becomes accessible and scattering to the Q_{CB} valley may be subsequently lost in favour of the $\overrightarrow{\Gamma K}$ pathway.

We can use low-temperature measurements to identify any features in this region arising from difference bands, as was done in Chapter 3 for MoS_2. However, Figure 4.14 shows that even at low-temperatures, most of the features this region remain, indicating that they do not belong to difference bands, but rather they must be first-order defect-mediated acoustic phonons and combinations of acoustic phonons. There are also differences between the spectra from two different crystals labelled LT-1 and LT-2. LT-1 shows a sharp feature at 73 cm^{-1} which is too low to be a K

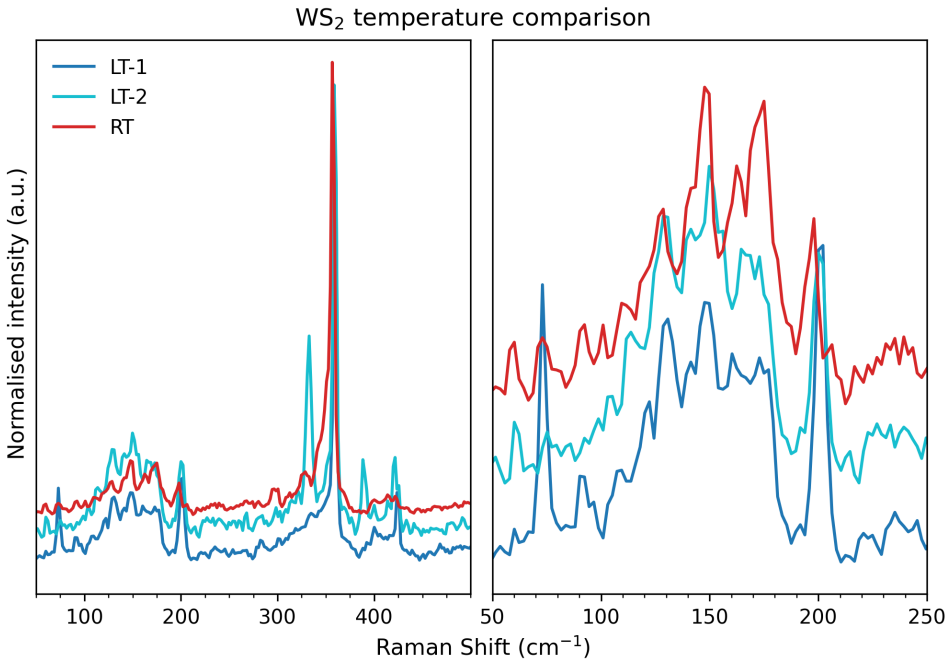

FIGURE 4.14: Comparison of the WS_2 modes at RT and LT (∼70 K), showing that most of the features below 200 cm^{-1} remain, indicating they are not difference bands, but instead must be first-order defect-mediated acoustic phonons, or second-order combinations of acoustic phonons.

or M phonon, but has the right frequency for a ZA(Q) phonon.[202] LT-2 has a sharp peak near 333 cm^{-1} which is only weakly present in the other spectra, and a feature around 388 cm^{-1} which is not shared by LT-1. The feature at and 421 cm^{-1} may be the A_{1g} fundamental mode, or a feature from the substrate. It appears that multiple resonance pathways are being accessed in these samples, which each appear to contribute a significant number of features to the spectra. It should be noted that these samples likely present a relatively disordered set of edges, suggesting that both $\overrightarrow{\Gamma M}$ and $\overrightarrow{\Gamma K}$ directions are being accessed in each spectrum.

It should be possible to extract these differences by carefully analysing the spectra of mechanically-exfoliated flakes and their ordered edges with respect to layer number. At 785 nm excitation, each pathway should be brought close to then out of resonance in sequence as layer number decreases, until in few-layers the last resonance is lost entirely (as in 4.11).

4.4 Conclusions

This chapter has explored several additional aspects of the indirect DRR mechanism - most of which form foundations for future work in this area. It has been shown that grain boundaries can also activate the defect modes in MoS_2, and the ability to detect them in this way represents a novel method for determining their location

and orientation in polycrystalline material. Polarization studies may reveal further details about how the grain boundaries scatter charge carriers, but this study is not feasible with our current setup due to the long collection times required, which possibly reflects a lower scattering probability at these boundaries than at edge defects. It has also been shown that the K point defect modes have an interesting reciprocal relationship with the general 2LA feature near 460 cm^{-1}, where increasing temperature favours the 2LA features until the K phonons are lost entirely. Moreover, this trend appears to affect the anti-Stokes scattered photons first, suggesting that an increase in temperature causes a shrinking of the band gap somewhere until a new resonance pathway opens. Further temperature controlled and tunable excitation experiments may help identify this scattering pathway. It has also been briefly shown that chemical modification of defective MoS_2 with thiol-containing ligands can lead to a quenching of the K phonons, which may be due to doping effects or as a consequence of blurring the edge boundary and a restriction on the wavevectors the edge can provide for scattering.

This chapter has also briefly explored the indirect resonance mechanism in some other TMD materials. While $MoSe_2$ appears to be in direct resonance at 785 nm excitation, WS_2 seems to have defect modes in thicker samples, while thin samples appear to have too large of a band gap to be resonant at this excitation energy. Low-temperature measurements indicate the modes observed are mostly first-order acoustic and second-order combinations, and suggests there may be multiple active indirect resonance pathways in these samples at this energy. The WS_2 samples were CVD grown, so further polarization dependent studies with thicker mechanically-exfoliated flakes and clear edges is expected to provide interesting results. Also untested at this stage is WSe_2, which is expected to have similar defect behaviour at 785 nm excitation as MoS_2, and will be worth investigating in the future.

Chapter 5

Methods and Materials

This chapter outlines the materials and methods used to construct the tube furnace and microscope, and synthesise and prepare samples for Raman analysis.

5.1 Materials

A list of the parts used in the construction of the microscope can be found at the end of this chapter (section 5.8).

The chemicals used throughout these methods were purchased from commercial vendors and used without purification unless otherwise stated.

The silicon and sapphire substrates were both purchased from SPI supplies (www.2spi.com). Natural MoS_2 crystals were also purchased from SPI, while synthetic MoS_2 which has highly oriented layers with much larger single-crystal sizes was purchased from 2D Semiconductors (www.2dsemiconductors.com). The silicon substrates are purchased pre-cut from a polished (one side only) silicon wafer as 5×5 mm squares, 0.525 mm thick. The sapphire substrates are 5×5 mm squares, 0.5 mm thick, and polished on both sides on the (001) crystallographic plane.

$MoSe_2$ crystals were supplied by Dr. Kim McKelvey at Victoria University of Wellington.

The tube furnace insulation is constructed from a mixture of Cemix Laitite refractory mortar, perlite, and pumice rocks. Furnace crucibles are made from Gorilla Fire Cement.

5.2 Synthetic Methods

5.2.1 Mechanical Exfoliation - Scotch Tape Method

Mechanically-exfoliated flakes are prepared using the "scotch tape" method in literature.[7,25] A crystal of MoS_2 (or other layered material) is pressed into a piece of scotch tape and peeled away. A thin piece of crystal will remain attached to the tape. Another section of the tape is then pressed into this crystal, and peeled away, leaving the original crystal divided. This process is repeated with other sections (on any of

the pieces of crystal at this point) until a satisfactorily thin sample is obtained. This is then pressed into a flat substrate, typically sapphire, and the non-sticky side of the tape is rubbed with a piece of soft plastic. The tape is then peeled away and flakes will be visible remaining on the substrate. Gentle rubbing causes less material to be deposited, and firm rubbing causes more to be deposited, but can also leave a significant amount of tape residue on the surface of the substrate, and cause large crystals to fracture and break apart.

5.2.2 Sonication

Nanoparticles of MoS_2 were synthesied using a common sonication technique in literature.[86,231,232] A horn sonicator, in our case a Misonix S-4000 Ultrasonic Processor (600 W, 20 kHz) is used to fracture MoS_2 flakes into smaller pieces though deliberately destructive sonication power. The cavitation induced by the sonicator creates intense shear and strain forces which damage the flakes and allow them to be ripped apart. The resulting solution is a mixture of different sized particles, dispersed in the solvent or slowly precipitating over time. This mixture is purified into fractions of different size distributions by centrifuging multiple times at sequentially higher speeds, collecting the pelleted material each time.

This method has been used with several common laboratory solvents, including: dimethylformamide (DMF), tetrahydrofuran (THF), acetonitrile (MeCN), ethanol/water, and chloroform. In the cases of DMF and THF, the breaking of the particles appeared to work better with a small amount of water in the sonication mixture. For chloroform, which is immiscible with water, the sonication did not yield much nanoparticle material. As such each solvent was actually a 4:1 mixture of the named solvent and water, respectively. It is possible that the water is involved with the fracturing process - perhaps catalytically, or as a reactant that binds via the oxygen atom to the newly formed edges.

Of these solvents, DMF was the most efficient at dispersing and fracturing MoS_2, while THF was almost as efficient at fracturing into smaller pieces, but was less efficient at dispersing, which in some cased facilitated purification as material precipitated quickly. Regardless of their efficiency, all solvents produced the same defect modes at the same frequencies, indicating that the solvent is not necessarily playing a role spectroscopically through doping or activation of the edges. This does not rule out activation via oxidation at the edges from water or oxygen in the air.

A general procedure for the sonication synthesis is as follows:

1. 50 mg of commercially obtained MoS_2 powder was weighed and added to a 50 mL plastic tube.

2. 25 mL of a 4:1 ratio of the desired solvent (e.g. DMF) to water was added to the tube.

3. This was sonicated for 10 minutes in a Bandelin SONOREX^{TM} Digital 10 P bath sonicator at 100 % power to partially disperse the material, before transferring to the horn sonicator.

4. The tube was clamped over a bath of ice-water slurry, and the tip of the sonicator horn was placed at approximately half the depth of the solvent in the tube. Parafilm® was wrapped around the the opening in the tube, with a hole for the horn to pass through to minimise solvent splash out out of the tube.

5. The sonicator was then run for at 100 % (600 W) power for 3 hours using an 8 mm diameter horn in pulse mode - 10 seconds on, 5 seconds off.

6. The sonicated solution was then centrifuged twice at each of the following speeds, collecting the pellets while the solvent was used in the next centrifugation. 2,000 rpm, 3,000 rpm, 5,000 rpm, 8,000 rpm, 11,000 rpm, 14,000 rpm.

7. The particles remaining in solution after the final centrifugation were dialysed into water using a membrane with 14,000 Dalton molecular weight cutoff.

8. The dialysed particles, now in water, were either processed further or freeze-dried to produce a fine powder.

5.2.3 Tube Furnace

I initially attempted to synthesise MoS_2 crystals using chemical vapour deposition (CVD) techniques to produce pure samples with ideal, straight edges. Given the difficulty finding we've had in finding single-layer material under the optical microscope, we had hoped it could be grown with CVD and observed as part of a terraced multi-layer crystal (see Figure E.1), where the bottom layer would be single-layer and could be observed from the pattern it leaves, or identified spectrally during linescans. While many of the results presented in this thesis were obtained from mechanically-exfoliated crystals, this was mainly for convenience, since the bulk flakes provided more sample in the laser focal volume, which yielded much faster collection times. This was particularly important for maintaining sample position while collecting data in the polarization studies with a fluctuating background temperature (see section 2.3.5 for thermal stability details). In addition, since there are two resonance pathways to discuss, they can both be discussed in the bulk flakes, but only one can be observed in the thin MoS_2 crystals produced by CVD. Nevertheless, the CVD results were very useful for helping uncover the mechanism along the way, and provide an apparatus for synthesis of other TMD materials (see section 4.3).

A diagram of the general reaction layout for MoS_2 synthesis is shown in Figure 5.1.

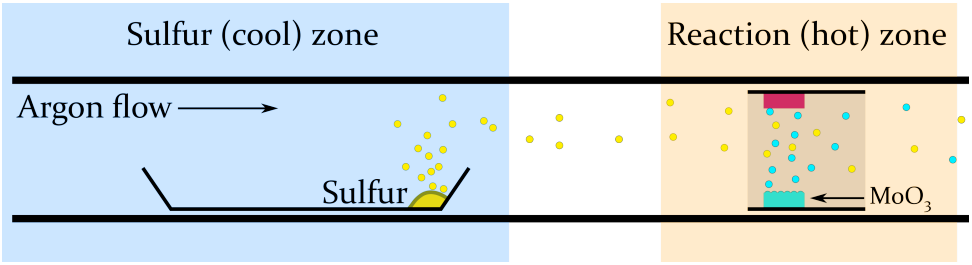

FIGURE 5.1: Schematic diagram showing the CVD process used to make MoS_2. Argon is flown from left to right through a sealed tube furnace, over evaporating sulfur which it carries to the hot-zone, where MoO_3 (blue rectangle) is being evaporated. The sulfur and MoO_3 mix and react, forming gaseous MoS_x which then deposits on the growth substrate (purple rectangle) and rearranges into crystalline MoS_2. Excess sulfur and MoO_3 either deposit on the walls of the tube past the hot-zone, or are carried by they argon flow out of the tube to a bubbler.

The actual synthetic method proved to be difficult to get right, and ultimately resulted in the construction of a specialised "mini-tube furnace" for TMD growth. One of the research groups in our department have two tube furnaces which they allowed us to use to synthesise TMDs. However, their furnaces are not ideal for our TMD synthesis. They are relatively large, and capped with steel flanges and valves which exhibit corrosion after exposure to the hot sulfur gas used in the synthesis. Furthermore, this sulfur gas condenses on the cool sections of the tube walls, and is an absolute nightmare to clean from these large tubes, as sulfur does not dissolve in common solvents. Cleaning these large tubes was therefore difficult, and the flanges took a long time to reassemble. In addition, other researchers use the tubes for creating sensitive catalysts, and the chances of contamination of their materials with our sulfur residue was high.

As such, we felt that a small furnace with a small quartz tube and ground-glass cone and socket joints ("quick-fit" style) would better suit our needs. It would be much quicker and easier to clean, the small size allows faster cooling for quicker experiment runs, and it gave us the opportunity to add a second heating zone, which is used to control the evaporation rate of the sulfur precursor independently from the reaction zone (although this is not required for all syntheses).

Rather than purchasing a new furnace, we realised we could create a simple proof-of-concept design using readily-available volcanic pumice rock. Figure 5.2 shows this early design, which uses a section of nichrome heating filament nestled below a cylindrical depression for a glass tube to sit. Separate rocks and filaments were used for the two heating zones, and each coil was hooked up to a bench-top lab power supplies to provide a heating current. Argon gas is flown through the tube to provide an inert atmosphere, and also serve as a carrier gas to flow the sulfur into

the reaction zone. The pumice rock provides good insulation and a tight fit around glass tube, which along with the small tube size meant only relatively low wattages were required to reach the hot-zone reaction temperature of 800 °C. The cool-zone (sulfur zone) is typically heated to approximately 200 °C.

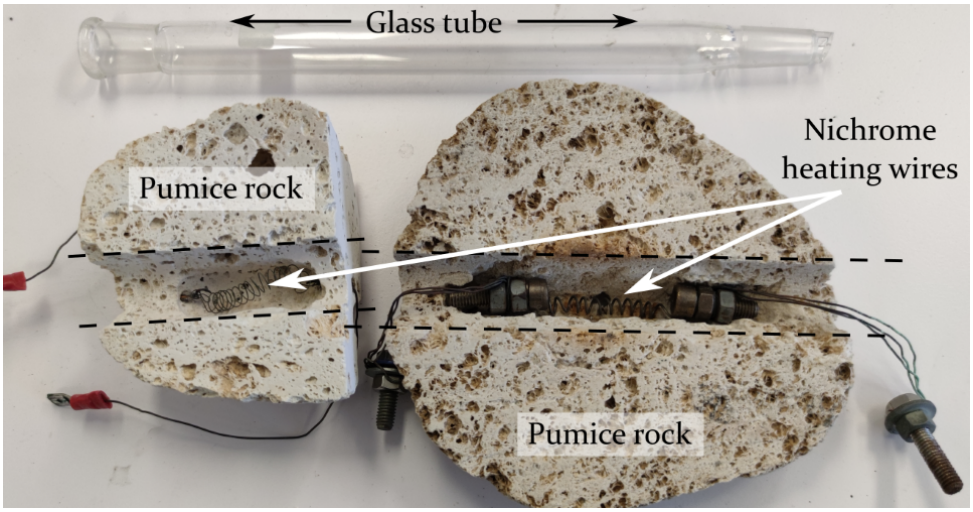

FIGURE 5.2: An initial prototype of a custom miniature tube furnace, using pumice rock with channels carved out to fit a cylindrical glass tube and for inserting nichrome wire filaments for heating. The top halves or lids of these "furnaces" are not shown, but feature a cylindrical cut-out that sits over the glass tube. The dotted lines indicate the cylindrical region for the glass tube to sit. The left section is the low-temperature zone, and the right section is the high-temperature zone.

At the hot-zone reaction temperature, borosilicate glass softens and is therefore not suitable as a tube material. Instead, we had a quartz tube made by Grant Franklin, the scientific glassblower based at Victoria University of Wellington. For this tube, a more robust design was implemented, which is shown in Figures 5.3 and 5.4. The furnace insulation was created using a 3D printed mould and a refractory cement mixture, filled out with more pumice rock. We considered using commercially available firebricks as the tube insulation, however casting in a mould provided the ability to easily customise the shape of the insulation interior to fit the filaments, and to direct airflow around the tube (see Figure 5.3).

Parameter Optimisation

The synthetic procedure is based on the reports in literature which use MoO_3 powder as the molybdenum source, and sulfur powder as the sulfur source.[233–236] Specifically, this procedure is adapted from Lin *et al.*, who use an inverted geometry where the growth substrate sits above the MoO_3 precursor substrate, and measure the effect

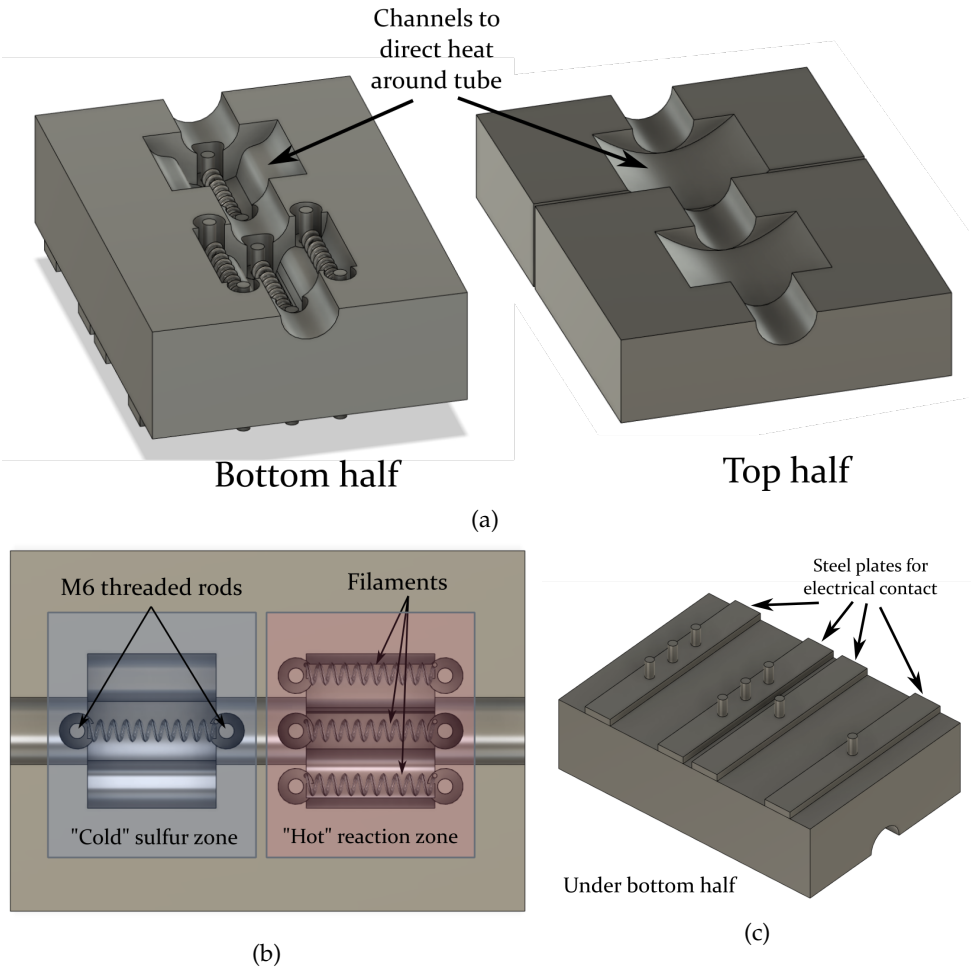

FIGURE 5.3: CAD design of the improved tube furnace. (a) Angled views of the bottom and top halves. (b) A top-down view showing the two heating zones and the filaments attached to threaded rods. (c) An underside view of the bottom half, showing how the rods contacting the filaments are connected together electrically through steel plates.

of the distance between the two on the growth.[233] They also demonstrate impressively large single-crystals, up to 300 µm across one side, which suggests the procedure should produce highly-crystalline material with well-ordered edges. The crucibles used in this setup are made using Gorilla Fire Cement Sealant and 3D printed moulds, which allows the precursor-to-substrate distance to be set for each crucible (pair). The design is shown in Figure 5.5, with the precursor substrate sitting on the bottom-half crucible, while the growth substrate sits inverted above this on grooves in the crucible lid (see section 5.2.3 for fabrication instructions). To change the separation distance, another crucible lid is used with the height at which the substrate is held being set in the mould design.

The CVD growth of MoS_2 is incredibly sensitive to the growth conditions, which include hot-zone temperature, relative concentrations of each precursor in the gas phase, total concentration of MoS_x clusters reaching the sample surface, and flow

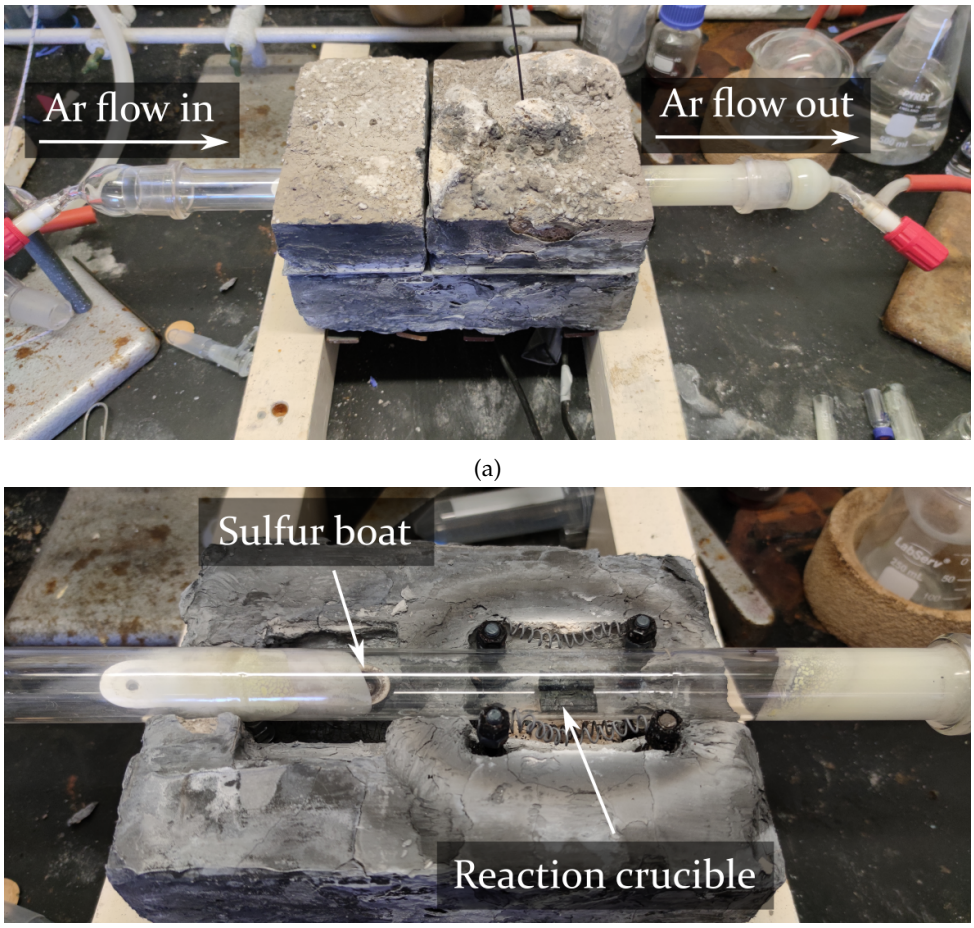

FIGURE 5.4: Photos of the fabricated tube furnace. (a) The full furnace with both top halves on. Argon flows in from the left via the ground glass gas fitting, and out through the right to a bubbler. A thermocouple can be seen as a thin black line extending vertically from the top of the furnace. (b) A view of the furnace with the top halves off, showing the positions of the sulfur boat (obscured by sulfur residue on the tube) and reaction crucible.

rate of carrier gas. The concentration of sulfur at the reaction site is a consequence of both sulfur zone temperature, total quantity/surface area of sulfur in that zone, and the flow rate. The MoO_3 gaseous concentration is dependent on the quantity of dried MoO_3 on the precursor substrate, the position and shape of this dried region relative to the growth substrate, and flow rate. A higher flow rate causes a concentration gradient for both the MoO_3 evaporating, and the MoS_x clusters that form in the hot-zone, with higher concentrations forming downstream. The total concentration of clusters at the growth surface can be optimised by changing the precursor-to-substrate distance with different crucibles.

Since our tube furnace will have different design to the ones used in literature, even the best attempts to follow their protocols will need some form of optimisation to compensate for these differences - particularly since many of the above variables

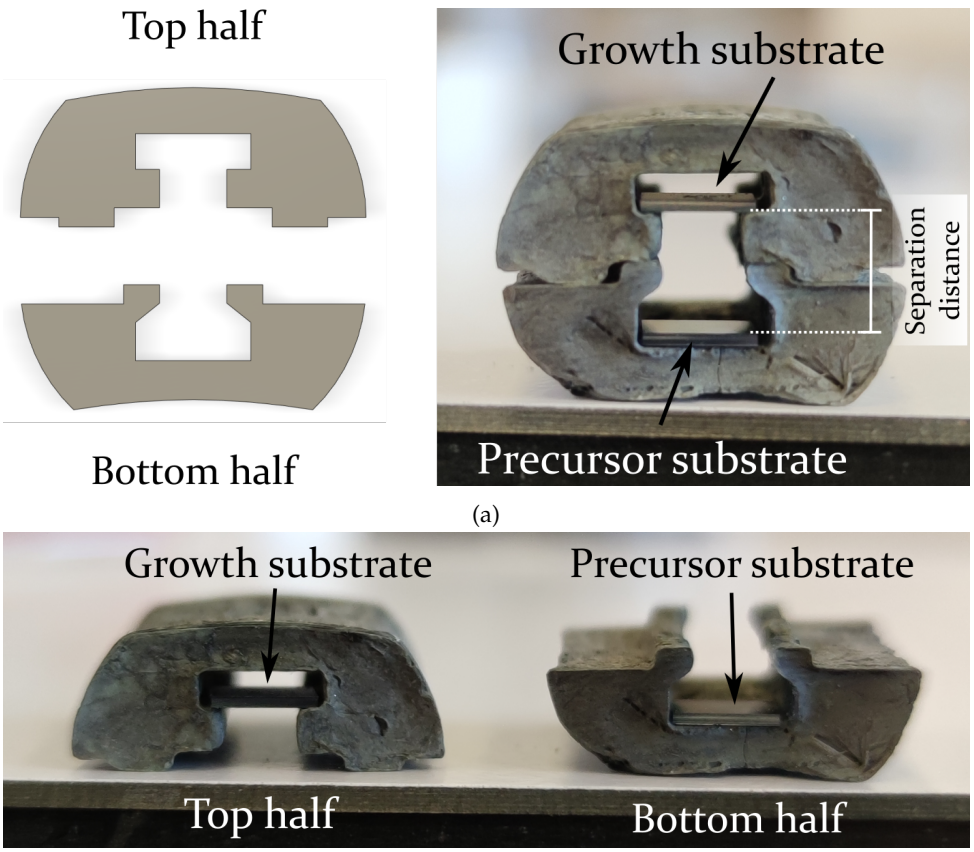

FIGURE 5.5: (a) Left shows a CAD drawing of the crucible shapes, and right shows the assembled crucible with the two substrates. The two halves are located together by the grooves that run the length of the crucible. (b) Another view showing the shape and length of the crucibles.

are interdependent. Consequently it took 24 experimental runs to optimise the parameters for our furnace and grow decent crystals. While all parameters play a role, the growth seems most sensitive to flow-rate and precursor to sample distance.

An example of MoS_2 growth at 6 mm precursor-to-substrate distance is given here:

1. 6 µL of 10 mg mL^{-1} MoO_3 powder in deionised water is dried onto a 5×5 mm chip of silicon using a hot plate set near 100 °C.

   (a) This volume is not enough to cover the chip, and will influence the growth. For instance, if a range of crystal sizes and thicknesses is wanted, the droplet should be placed against one edge of the chip, and this end should be oriented downstream below the growth substrate. This results in a concentration gradient of MoO_3, with higher concentrations forming downstream. This in turn causes a concentration gradient of MoS_x to form at the growth substrate (see Figure 5.6). The low-concentration

side will contain small crystals spaced far apart, the middle will have large crystals close together, and the high concentration will have interconnected and often multi-layer crystals covering the surface.

(b) To grow a more homogeneous patch of crystals, a volume around 20 µL should be used, with approximately the same mass of MoO_3 as above.

2. This chip is placed face up in the bottom half of the 6 mm crucible (see Figure 5.5).

3. A growth substrate (sapphire or silicon) chip is placed in the groove of the top half, with the growth surface face-down (facing the precursor chip).

4. The top half crucible is rested on the bottom half (Figure 5.5(a)) and this is slid into the quartz tube, centred on the hot-zone (Figure 5.4).

5. An aluminium oxide (alumina) crucible containing the sulfur powder (sulfur boat) is placed in the other end of the quartz tube, positioned approximately three-quarters of the way into the cool-zone region. From this position, the cool-zone does not need to be independently controlled, and will reach the correct temperature as the hot-zone reaches the reaction temperature. Note this position only applies to the timings stated in this particular procedure - if the reaction is to run for longer, the sulfur boat may need to be further back and the zone temperature may need independent control.

6. The gas flow ground glass sockets are placed on each end of the quartz tube. The inlet socket carrying the argon gas is placed on the left (sulfur side) and the outlet socket is placed on the right (hot-zone side). The outlet is passed through a bubbler of water to prevent back-flow of atmosphere down the tube at low flow rates.

7. The tube is purged with 200-300 $mL\,min^{-1}$ of argon gas for 10 minutes to remove any oxygen atmosphere.

8. The synthetic run begins by turning the low-voltage, high-current power supply up to 38 A. This spreads the current over the three hot-zone coils, and draws approximately 350 W of power. A timer is started and the flow rate is dropped to 150 $mL\,min^{-1}$.

9. The furnace heats rapidly and the temperature is monitored via a thermocouple inserted into the top half of the insulation over the hot-zone.

10. The thermocouple should read 600 °C between 6.5 and 7 minutes. At this point, the flow rate is dropped to 60 $mL\,min^{-1}$.

11. The thermocouple should read 720 °C between 12 and 13 minutes. At this point, a timer for 10 minutes is started and the reaction is considered underway. If it takes significantly longer to reach this temperature, the coils may need replacing.

12. The furnace is allowed to increase a further 10 °C to a thermocouple reading of 730 °C. At this temperature the crucible and sample are 80 °C hotter than this measurement (i.e. 810 °C). The temperature is held at this value by manually turning back the voltage throughout the run, which decreases amperage readout.

13. Once the 10 minute timer is up, the power supply is turned off. The current required to hold this temperature by the 10 minute mark after manually decreasing is around 28 A. Another timer is set for 5 minutes, during which time the furnace is allowed to cool naturally.

14. After 5 minutes, the sulfur zone insulation (top half) is removed. This is an important step, because while the furnace is cooling sulfur is still being evaporated and passed down the tube to the sample. If the insulation is not removed at this step, the sulfur stays warm enough to continue evaporating and can deposit on the sample and crucible halves. This can contaminate the sample, but also causes problems for the next run as the sulfur on the crucible will create sulfur gas near the sample at an early stage of growth, which can cause imperfect crystals to grow. Another timer is set for 15 minutes.

15. After 15 minutes the sulfur in the boat should have solidified, and the hotzone insulation (top half) can be removed. Note if the sulfur is still liquid, wait another 5 minutes and check again.

16. The timings are less important now as the sample will be below 300 °C. After 5-10 minutes, the the tube can be lifted out of the furnace and placed behind it to cool in the fume hood.

17. After another 10 minutes, the sample should be cool enough to remove. The argon flow is turned off and the crucible is removed. There should be faint yellow/green growth on sapphire substrates, but it can be difficult to see growth by eye on silicon substrates.

WS_2

The procedure for WS_2 growth uses the same timings and temperatures, but a significantly shorter precursor to growth substrate distance due to the much lower volatility of the WO_3 precursor. Instead of using two half crucibles, a single bottom half crucible is used, and the growth substrate is separated by a two stacks of strips of silicon wafer (see Figure 5.7). These are 0.5 mm thick, giving a total spacing of 1 mm. A concentration gradient can be introduced by using two wafers on one side of the crucible (1 mm high) and only one wafer on the other (0.5 mm high). The amount of precursor is 30 µL of 10 mg mL^{-1}, dried onto the back of a silicon chip. It is interesting to note that it is typically easier to produce high-quality and bigger

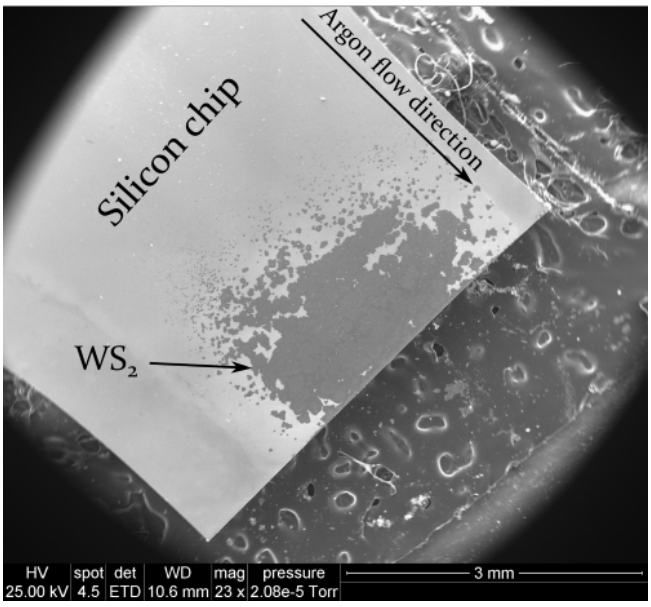

(a)

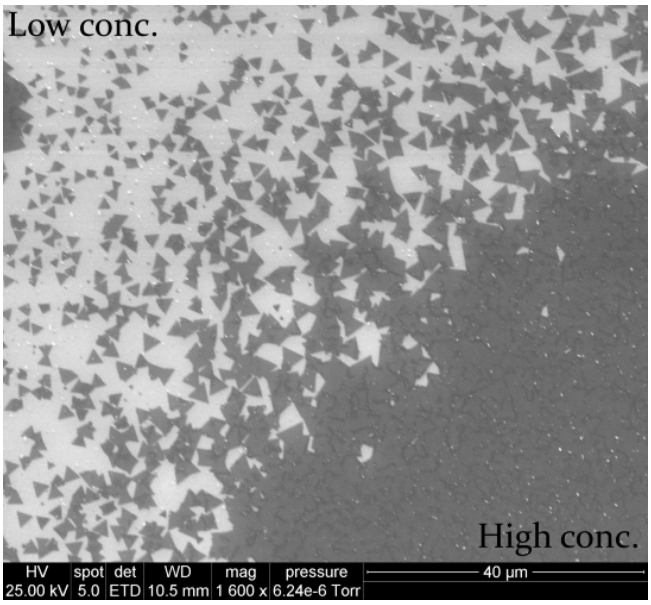

(b)

FIGURE 5.6: (a) Low-magnification SEM image of a concentration gradient in the gas phase resulting in a growth concentration gradient of crystals on a silicon chip. (b) A higher magnification SEM image showing the blending of crystal sizes and inter-crystal distance across a concentration gradient.

crystals of WS_2 than MoS_2, but that it is harder to cover a chip in WS_2 growth than MoS_2 growth, as the WS_2 tends to build up in clusters and around the edges, while MoS_2 can easily cover the full surface of a chip.

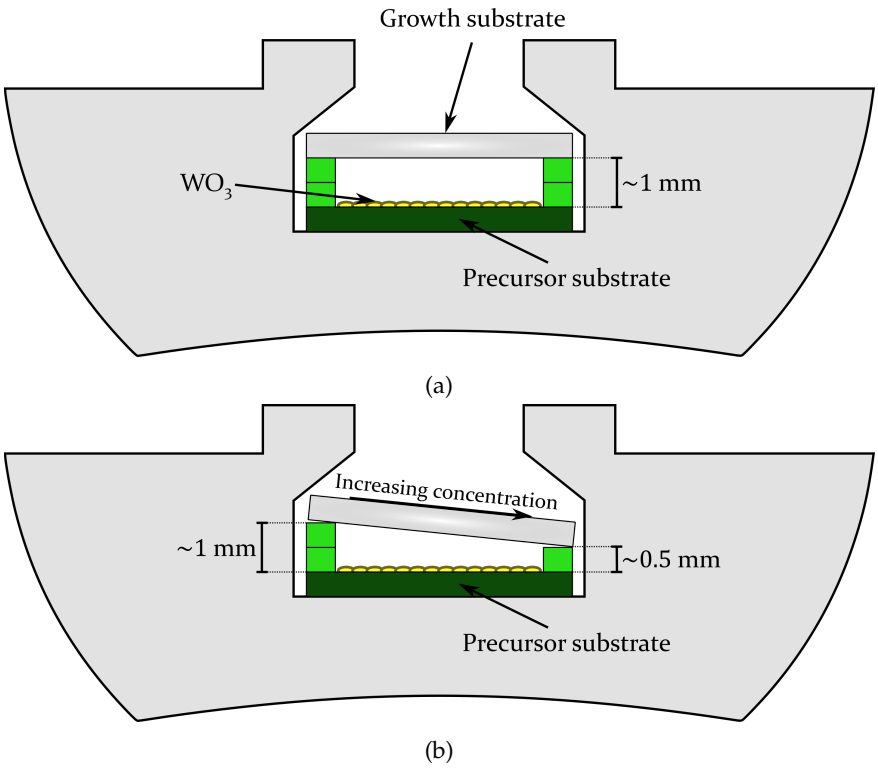

FIGURE 5.7: (a) Schematic of the WS_2 crucible assembly and the reduced precursor-to-substrate distance in this method. (b) Schematic showing an example of how the growth substrate can be tilted to introduce a gaseous WS_x concentration gradient across the growth substrate.

Crucible Fabrication

The crucibles are fabricated using Gorilla Fire Cement Sealant injected into a 3D printed mould - an example is shown in Figure 5.8. The interior of the moulds are filled with the refractory cement and left to dry overnight between 60 °C and 100 °C. This drives out some of the moisture and hardens the cement, but it is not yet set. Next the mould is removed by melting off the plastic. This is best achieved by wrapping the mould in aluminium foil with holes poked in the bottom, then hanging it over something to catch the melting plastic. I use a cylindrical drying oven in a vertical position with aluminium foil lining the base of the glassware, set between 200 °C and 250 °C. Note this should be done in a fume hood or under an extractor fan to expel the plastic fumes. After an hour or more the crucibles should be relatively clean and can be removed from the heat. Note a small amount of shrinkage of the crucibles can occur at this point. A quick scorching with a propane blowtorch helps remove the last of the plastic residue. The crucibles are scraped to remove flakes of excess refractory cement. These are then loaded into the tube furnace and slowly brought up to the standard reaction temperatures (800-900 °C) over 1-2 hours to drive off the last of the water in the cement. Note a small flow of gas through the tube helps to carry water vapour out of the hot-zone.

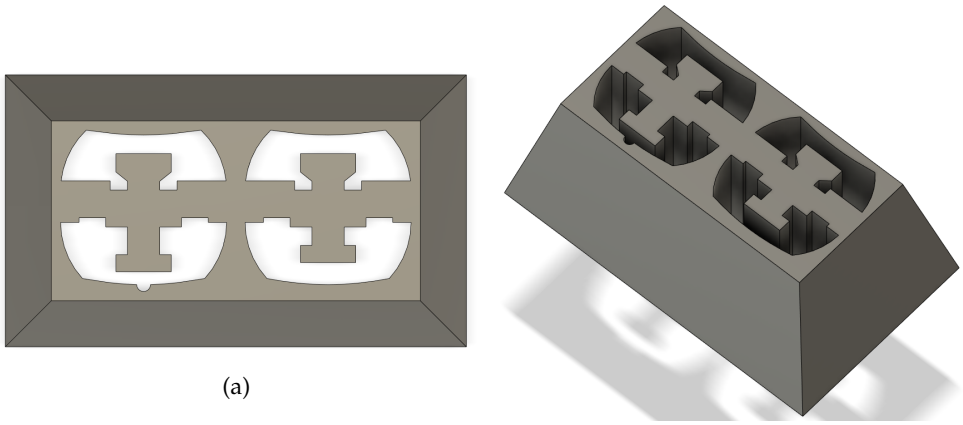

(a) (b)

FIGURE 5.8: Example of the moulds used to fabricate the tube furnace crucibles with set precursor-to-sample distances. (a) Top view and (b) side view.

5.3 Sample Preparation for Raman

5.3.1 Powders and Dispersed Sample

Dispersed/solvated samples can be dried onto a smooth steel or aluminium plate. This generally provides good thermal contact to minimise the effects of laser-induced heating at the sample, and the metal surfaces do not contribute Raman scattering. Powdered samples can be dispersed in solvent and prepared the same way, or they can be pressed into a metal plate using a flat surface, such as a glass microscope slide coverslip. Samples prepared in this way are often too thick to have good thermal dissipation, and care must be taken to avoid laser-induced heating affects such as annealing and oxidation at high (and sometimes low) laser powers.

These samples are typically placed below a 20-60$\times$ objective in air for Raman microscopy.

5.3.2 Sapphire and Silicon Substrates

Mechanically-exfoliated and CVD samples are prepared differently depending on the required magnification. For low-magnifications the samples are simply placed face up under the microscope objective. However, it is often desired for these samples to have the highest magnification (and NA) which gives the smallest spot size and highest collection efficiency. This is achieved with a 100$\times$ oil-immersion lens. In order to protect the sample from contamination by the oil, the sample has a 22 $\times$ 60 mm coverslip placed on top of it. However, this coverslip needs to be pinned down, otherwise the capillary forces generated by the oil and the microscope objective cause the lightweight coverslip to lift off the sample.

To mitigate this issue, the configuration shown in Figure 5.9 is used. the sample chip is placed face-up on the large paramagnetic steel disc used for mounting the

Linkam stage, and two old/used spacer chips of the same kind (sapphire or silicon, depending on the sample) are placed either side, separated approximately the same distance as the length of the coverslip. Two neodymium magnets are placed on top of the two spacer chips, and the magnetic force attracting the magnet to the stage pins the coverslip in place, at the right height for the sample.

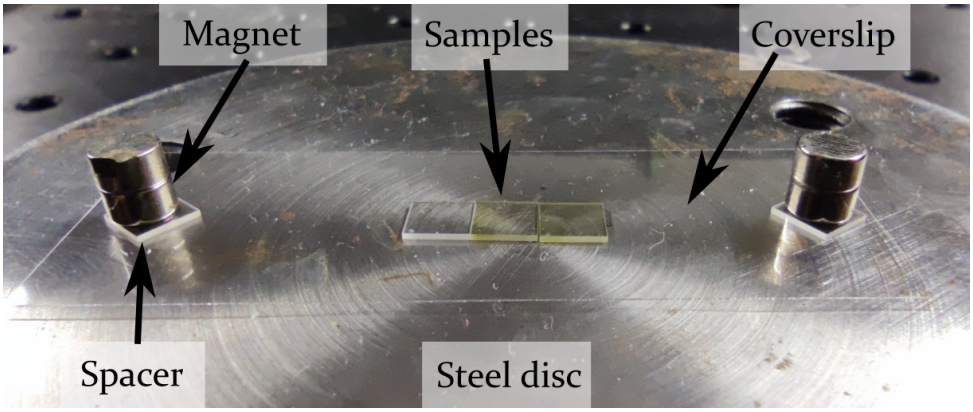

FIGURE 5.9: Photo of a set of CVD and mechanically-exfoliated samples on sapphire, as prepared for analysis with a 100× oil immersion objective. Note the yellow colouring is MoS_2 crystals, not microscope oil. Also note the machining lines (concentric circular markings) on the steel disc - these create an uneven surface which impacts the spot size of the microscope (discussed in the text).

It should be noted that placing a coverslip over the sample like this results in a small air gap between the sample and the coverslip, which reduces the efficiency of the objective due to the lower NA of air, and results in a slightly larger spot size. In addition, this air gap can vary in size across a sample, due to imperfections in the surface of the steel disc which can cause parts of the chip to be raised unevenly. This adds a degree of uncertainty to the maximum resolution of any linescan or map. Since the sapphire and silicon substrates are generally polished to a precise thickness, and coverslips are smooth on the nanoscale, the imperfections in the surface of the steel disc left by the machining process will largely determine the size of this air gap at any one point (see Figure 5.9 for these machining imperfections). Therefore, it would be a useful investment to have the steel disc surface precision ground to a smooth, flat finish.

5.3.3 Low-Temperature Stage

For low-temperature experiments samples are prepared on aluminium discs, either dried directly on the surface or mounted via carbon sticky tape for sapphire and silicon substrates. This disc is then centred in the Linkam stage. The aluminium disc acts as a thermal mass to help maintain low temperatures at the sample under high power. The disc height is also designed to bring the sample as close to the glass

window of the stage lid as possible so that higher NA objectives (with shorter focal lengths) can be used. However, care must be taken to ensure the sample height is not so thick that it comes into contact with the stage lid upon tightening.

5.4 Chemical Functionalisation

MoS_2 samples were chemically modified with thiol-containing molecules (ligands) to attempt to form chemical bonds to the sulfur vacancies at the edges via the thiol residues. The process involved simply stirring the sample and ligand together in an appropriate solvent, at an appropriate temperature, for some amount of time. Note that for these reactions it is not clear how much ligand is required to fully functionalise the MoS_2 material, since it is not clear how many edges and sites are actually available for modification. Therefore, while the starting material is weighed to provide a consistent amount of material for each reaction, the modifying ligand is typically a few milligrams or more, which is a large excess.

The starting material was defective MoS_2 synthesised using the sonication method above in DMF solvent - usually one of the lower speed centrifugation fractions as these represented a relatively large yield from the total starting material and still had clear defect modes in the Raman spectra. Mercaptoacetic acid (MAA), dodecanethiol (DDT), and thiophenol are all liquids at room temperature, so for these ligands the reaction was performed neat, with the ligand as the solvent. Approximately 5 mg of MoS_2 was weighed into a narrow 1 mL vial with a small magnetic stir bar. Then, approximately 200 µL of the ligand was added. The vial was sealed and the mixture was sonicated for 10 minutes in the bath sonicator at 100 % power to disperse the MoS_2. The vial was left to stir for 48 hours on a magnetic stir plate.

Thiobarbituric acid (TBA) and cysteamine (CA) are solids at room temperature, so these reactions were prepared following the protocols in Presolski *et al.*[223] Approximately 5 mg of MoS_2 was weighed into a 4 mL vial with a small magnetic stir bar. Approximately 5 mg of either TBA or CA was added to the vial, and dissolved in 1 mL of deionised water. The vial was sealed and the mixture was sonicated for 10 minutes in the bath sonicator at 100 % power. Then the vial was placed in an oil bath at 75 °C and stirred for 48 hours.

The workup and purification varied depending on the ligand. For MAA, TBA, and CA the sample was dialysed in deionised water for 48-72 hours, swapping the dialysate several times throughout this period. During dialysate swapping, the MoS_2 was (attempted to be) resuspended with sonication to help dissolve any ligand that may be trapped between aggregates of MoS_2.

For DDT and thiophenol, the mixture is diluted in THF and washed via centrifugation at 5000 rpm for 5 minutes, four times. Between each centrifugation, the MoS_2 is redispersed in the THF solvent by sonication for 5-10 minutes.

5.5 Data Processing

Data collected from the Raman microscopes are manipulated in a number of ways to clean up the data and prepare it for further analysis. Most of the data processing is done with custom Python code which I have written over the course of this PhD, and is available on request from myself or Prof. Mark Waterland.

Most of the data has been subject to a baselining procedure utilising a least-squares algorithm in the SciPy module for Python. SciPy also provides similar least-squares algorithms for optimising the fits of any function to a data set - and this was utilised in the peak fitting package written by myself, alongside various pieces of code from forums across the internet. The same algorithms were used to optimise fits for the $cos^2\theta$ dependencies of polarization data sets.

Background subtractions were performed as either raw subtractions of background spectra from the sample spectra, collected with the same acquisition time, or as normalised spectra to a particular background spectral feature (e.g. a sapphire peak around 419 cm^{-1} or 800 cm^{-1}.)

AFM image analysis was performed using Gwyddion SPM software under the GNU General Public License.

5.6 Computational Details

Electronic structure and symmetry decomposition calculations were performed using density functional theory implemented by Quantum ESPRESSO[237–239] via the generalised gradient approximation and Perdew-Burke-Ernzerhof functional (GGA-PBE).[240]

Valence electrons were described using a plane wave basis set with a 450 eV kinetic energy cut-off, and core electrons were accounted for using the projector augmented wave (PAW) method,[241] and a Monkhorst-Pack $12 \times 12 \times 4$ k-point grid was used to sample the Brillouin zone. Long-range non-covalent interactions were included using Grimme's semiempirical DFT-D2 correction.[242] The few-layer systems were constructed with 12 Å of vacuum either side of the structure in the c-axis to simulate an isolated environment, and used the 2D cutoff.[243] Fully relativistic pseudopotentials
(`S.rel-pbe-n-kjpaw_psl.1.0.0`, `Mo.rel-pbe-spn-kjpaw_psl.1.0.0`) were used in all calculations and were obtained from the precision standard solid-state pseudopotentials (SSSP).[244,245] An example input file for the relaxation step can be found in Appendix F.

5.7 Instrumentation and Equipment

Raman spectrographs and detectors: Teledyne Princeton Instruments Acton LS785 spectrograph and PIXIS400 camera/CCD detector for 785 nm Raman, and Teledyne Princeton Instruments FERGIE (current version is now called the IsoPlane 81) spectrograph and detector for other wavelengths in the visible.

Raman lasers: Solid-state diode lasers for 532 nm, 633 nm (Ondax inc., free-space), and 785 nm (Enwave Optronics, Inc., fiber-coupled) were used for almost all data collection, and a free-space 633 nm Helium-Neon gas laser was used for the sonication series samples.

Temperature-controlled stage: Linkam THMS600, generously on indefinite loan from Prof. Eric Le Ru at Victoria University of Wellington.

Bath ultrasonicator: Bandelin SONOREX^{TM} Digital 10 P.

Horn sonicator: Misonix S-4000 Ultrasonic Processor, 600 W 20 kHz operating frequency.

Centrifuges: Sigma 1-14 microcentrifuge, and Thermo Fisher Heraeus Multifuge^{TM} X1R centrifuge.

Atomic force microscope: Nanosurf easyScan 2. Silicon ContAl-G cantilevers were used in contact mode purchased from www.budgetsensors.com.

Scanning electron microscope: FEI Quanta 200 Environmental Scanning Electron Microscope (SEM) with EDAX X-ray detector module.

UV-vis: SINCO S-3100 UV-Vis spectrophotometer.

Infrared spectrometer: Thermo Fisher Nicolet 6700 FTIR with with Smart iTR attenuated total reflection (ATR) attachment with germanium crystal.

Beam profiler: gentec-eo BEAMAGE-3.0.

Computational resources: Quantum ESPRESSO v.6.8, New Zealand eScience Infrastructure (NeSI) allocation.

3D Printer: Prusa i3 MK3S fused-deposition modelling (FDM)

5.8 Microscope Construction

This section provides a list of the main materials and hardware used to construct the scanning Raman microscope and, where applicable, a cost estimate. The number of items is a recommended minimum, and a "+" symbol next to the number indicates that it is useful to have more for versatility in the assembly, redundancy, extra stability, or multiple lasers etc. Note the configuration listed is for one laser wavelength only (785 nm), and additional optics and hardware will be required for each separate wavelength utilised.

The sum of the the costs of the following table is approximately $16,250 USD. This represents the cost of building a scanning microscope from scratch, but does

not include the optical table, lasers, or detectors - which are in fact the most expensive parts by far. Nevertheless, a commercial microscope with sub-micron scanning capability, minus the detectors and lasers can still cost hundreds of thousands of dollars. In addition, for an optics lab looking to upgrade to scanning microscope capabilities, most of the expensive equipment will be on hand already.

TABLE 5.1: A summary of the parts used to build the scanning microscope and their estimated costs. An "*" indicates parts that we don't have, or have inferior versions of and would be a good upgrade or choice for new system.

Item	Number used	Supplier/part number	Approx. cost per unit (USD)
Hardware			
Nikon stage	1	unknown origin	
1.5 inch optical post (200 mm long)	6	ThorLabs P200/M	63.00
Half-inch optical posts (various lengths)	20+	ThorLabs TR50/M	7.00 at 50 mm
Half-inch post holders (various lengths)	7	ThorLabs PH50/M	9.00 at 50 mm
Aluminium breadboard (150×150 mm)	1	ThorLabs MB1515/M	55.00
Steel cage assembly rods (various lengths)	50+	ThorLabs ER6	9.00 at 6 inches
30 mm cage plate standard (thick)	10+	ThorLabs CP33T/M	25.00
30 to 60 mm cage plate adapter	4+	ThorLabs LCP33/M	44.00
30 mm removable segment cage plate (thick)	2+	ThorLabs CP45T/M	40.00
60 to 30 mm cage system right-angle adapter	1+	ThorLabs LCP30	46.00
30 mm cage system U-bench	1	ThorLabs CBB1/M	84.00
30 mm cage mounting bracket (compact)	2+	ThorLabs CP33B	16.00
Snap-on 30 mm cage mounting brackets	2+	ThorLabs CPMA4/M	35.00
Swivel base adapter (magnetic)	2+	ThorLabs UPHA	23.00
Gimbal mount 30 mm cage system (1-inch optics)	6+	ThorLabs KC45D	225.00
30 mm cage XY translator (1-inch optics)	5+	ThorLabs CXY1	192.00

Z-translation 30 mm cage mount (1-inch optics)	3+	ThorLabs SM1ZA	206.00
Pivoting quick-release 1-inch optic mount for 30 mm cage	0+	ThorLabs CP360R/M	104.00
Right-angle bracket (slots)	2+	ThorLabs AB90	29.00
Right-angle vertical bracket	2+	ThorLabs VB01/M	102.00
1.5-inch post mounting clamp with tapped holes	2+	ThorLabs C1511/M	76.00
Adjustable mounting base	2+	ThorLabs BA2TA2/M	28.00
Assorted screws, various lengths	1+	M6, M5, M4, M3/ThorLabs	300.00+
Optics			
Single mode fiber optic patch cable FC/PC (2 m)	1+	ThorLabs P1-780A-FC-2	100.00
Multi-mode 50 µm fiber optic path cable FC/PC (collection)(2 m)	1+	ThorLabs M42L02	80.00
Multi-mode 105 µm fiber optic path cable FC/PC (illumination)(2 m)	1+	ThorLabs M94L02	120.00
Fixed focus aspheric (or triplet*) fiber collimators	2+	ThorLabs F280FC-780 (TC06FC-780)	169.00 (456.00)
High-quality* oil-immersion objective lens	1+	ThorLabs RMS100X-O	1,256.00
Achromatic doublets, half and 1-inch, various focal lengths, various anti-reflective coatings	5+	ThorLabs AC254-50-A-ML	109.00 for 1-inch optics

1-inch round protected aluminium mirror	1+	ThorLabs PF10-03-G01	54.00
50:50 beam splitter (unmounted*)	2+	ThorLabs CCM5-BS016/M (BS004)	196.00 (183.00)
Linear polarizing filter (half-inch mounted)	2+	ThorLabs LPIRB050-MP2	283.00
Zero-order half wave plate (half-inch mounted)	1+	ThorLabs WPH05ME-780	272.00
Rotation mount (continuous) half-inch optics	2+	ThorLabs RSP05/M	80.00
Volume Bragg Grating notch filter	3+	OptiGrate	1,000
Volume Bragg Grating spectral filter	2+	OptiGrate	1,500
Electronics			
Stepper motors Nema 17	5+	StepperOnline	10.00
Stepper motor controller Duet 2 Ethernet	1+	Duet3D	182.00
3D printer - Prusa i3 MK3S+	1+	Prusa Research	1,000.00
Scanning microscope software	1	Waterland Group, Python/Open source code	Python is free!

Chapter 6

Conclusions

This thesis demonstrates the design principles of and methods for constructing a low-frequency scanning Raman microscope, capable of generating Raman linescans and spectral maps, and with the ability to quickly swap laser wavelengths to perform resonance Raman experiments. The design is modular, and fully modifiable to suit experimental needs, such as through the incorporation of specific polarization optics and additional equipment, including temperature controlled apparatus. In particular, this work showcases the capabilities of 3D printing as applied to the optics lab, for the construction of custom and complex optomechanical mounts and devices. This work has been enabled by the rapid development of 3D printing technology over the last decade, and the core design of the scanning components can be adapted to fit most, if not any, commercially designed stages. Therefore, this design offers an opportunity for researchers to modify their existing microscopes, or construct one from stock optical components, for a fraction of the cost of commercially available stages and scanning microscope setups. Furthermore, the scanning software, while rudimentary, is coded in relatively simple Python for ease of use, allowing complete control over the scanning protocols and unique automated experiment designs, such as high-throughput multi-sample collections, or integration with analysis code for automatic collection and spectral screening.

Using this Raman microscope, a unique double resonance Raman mechanism via the indirect transition of MoS_2 has been discovered and explored in detail, revealing a defect-mediated relaxation pathway that results in the appearance of intense features arising from single acoustic phonons and double resonance Raman combination bands. These defect modes exhibit a strong polarization dependence, owing to a requirement for momentum conservation under a backscatter condition at the crystal edges. This backscatter condition requires that defect scattering by armchair and zigzag edges involve single phonons from different high-symmetry points of the Brillouin zone. Specifically, a defect backscatter at an armchair edge results in the observation of phonons from the K and Q points, while at a zigzag edge M-point phonons are observed. However, due to a combination of symmetry constraints and a (not fully-resonant) pre-resonance to the M point at 785 nm excitation, single M point phonons are seldom observed. This pre-resonant pathway is

observed at both edge types, likely due to the strong electron-phonon coupling of a group of phonons at the M point, resulting in double resonance Raman combination bands and an overall enhancement to the entire spectrum at bulk MoS_2 edges. In thinner MoS_2 edges, the widening band gap causes the pre-resonant pathway to be lost, taking with it the whole spectrum enhancement but leaving clearly observable K and Q point phonons. It is likely that the peak near 188 cm^{-1} ($p2$) has multiple contributions from both K and Q phonons, and the use of a tunable excitation laser, electron-phonon coupling calculations, or variable temperature and/or pressure experiments should help resolve their specific contributions and reveal valuable information about the low-energy scattering dynamics in MoS_2.

A similar backscatter mechanism is known to provide defect modes for graphene, but there has not yet been any reports of a similar mechanism or modes for MoS_2 - with the exception of the phonon density of states features which arise as a consequence of a breakdown of the $q \approx 0$ selection rule in all crystalline materials. Therefore, this account demonstrates edge-specific resonant defect modes in MoS_2 for the first time, which are not only capable of quantifying defects but also determining the relative structures and orientation of these edges. This technique is expected to be an invaluable tool for the characterisation and development of catalytic MoS_2 materials for hydrogen evolution - for which the edges are the catalytic sites, and for MoS_2 nanomaterials, where edge structure is responsible for imparting unique properties to the materials. Furthermore, I have shown that these modes can be activated by grain boundaries, and this technique presents a novel approach to detecting them, and potentially other defects in polycrystalline MoS_2.

Having elucidated this mechanism in MoS_2, I have also shown that defect modes are accessible through indirect resonances in other TMDs, which should allow a wealth of electronic and structural information to be accessed in these materials as well. Their full characterisation and polarization dependencies have yet to be performed, which leaves an opportunity for future research. For this, it would be advantageous to seek the use of a tunable near-IR laser source and accompanying triple spectrograph, so that the extent of these observed and any additional resonances can be fully explored and characterised.

Chapter 7

Future Directions

7.1 MoS_2

The biggest limitation in this work is that we only have one infrared laser to use at 785 nm. Temperature has been exploited where possible to glean additional information, but only having the one laser has largely locked this analysis to a specific section of the BZ. As such, while the results presented in Chapter 3 cover the core theory of the indirect DRR in MoS_2, questions still remain which should be answered with additional infrared excitation energies, ideally in a tunable laser setup.

For instance, $p2$ ($\sim$188 cm^{-1}) is suspected to contain contributions from TA(K), ZA(K) and LA(Q) phonons, however their near-degeneracy prevents their resolution in the Raman spectra, even with peak fitting techniques. Scanning the excitation source should reveal an energy where the $\overrightarrow{\Gamma K}$ resonance pathway is lost but the $\overrightarrow{\Gamma Q}$ pathway remains, thereby favouring its resonance and revealing the respective K and Q phonon contributions.

Also of interest is the the M point resonance. It is expected that with an increasing excitation energy, the $\overrightarrow{\Gamma M}$ pathway will become fully resonant, and we may see a different set of modes appear. Note that the symmetry analysis given in section 3.2.5 indicates that only one of the LA branches at M has the correct symmetry to mediate the $\overrightarrow{\Gamma M}$ transition, so it is unlikely the TA(M) and ZA(M) will be observed. They may, however, become weakly allowed if symmetry is broken near the edge. Nevertheless, it would be interesting to see how an increasing excitation affects the final spectrum of disordered edges and powdered samples. For instance, since the K point resonance appears to be lost at higher temperatures (see section 4.2.1), we may observe a favouring of resonances from either the M point, K point, or neither. It is entirely possible that resonance with 785 nm excitation is somewhat inefficient for observing defect modes in MoS_2, where another energy may better meet the energy difference for the K point resonance. That being said, the tunable band-gap with layer number is still conveniently in resonance from bulk to bilayer with 785 nm excitation, meaning a laser energy that is more resonant at one particular thickness may not be resonant at another. This seems to be the case with WS_2 at 785 nm, where edge-resonant effects are not observed until samples become sufficiently thick (see

section 4.3), which is consistent with WS_2 having a similar band structure but with a slightly larger band gap.

7.1.1 Abandoned Syntheses

Throughout this research I tried many different synthetic methods in an attempt to create a library of nanomaterials to characterise. Unfortunately, many of the techniques either didn't provide the materials we wanted, or we did not have appropriate experimental apparatus to properly achieve the synthesis. It would be interesting to revisit these once the experimental conditions can be properly achieved. Some honorable mentions of abandoned synthetic pathways include:

- Quantum dot or "nanocluster" MoS_2 synthesis using an inverse-micelle method.[246–248] While there are many easier "quantum dot" synthesis methods in literature, the idea was that these clusters would grow inside the inverse micelles and present clean edges and homogeneous sizes to mitigate some of the inhomogeneous broadening effects I was observing in the Raman of quantum dot samples. However, these reactions are incredibly air sensitive, and I could not successfully synthesise them without a glove box.

- Nanoribbons of MoS_2 grown inside and confined by carbon nanotube "nanoreactors".[96,97] This was an interesting concept as a method for synthesising nanoribbons with well-defined edges. However, the syntheses call for long reaction times (weeks to months in ovens) and near ultra-high vacuum pressures. I was unsuccessful in synthesising these materials with modified conditions at vacuums around 10^{-3} mbar, and so this could be re-attempted if 10^{-6} mbar vacuums can be achieved.

- Using a diamond knife in a microtome to mechanically fracture nanoribbons of MoS_2.[249] While our research group has had successes in the past fabricating nanoribbons of graphene using this rather unconventional method, MoS_2 is a considerably softer bulk material, and did not cut well. This could be reattempted with a cryo-microtome at low-temperatures to make the MoS_2 more stiff and brittle, and more likely to fracture instead of crumple.

7.2 Defects

While edge defects of MoS_2 are well characterised in this work, we have only just scratched the surface of other defect analysis in MoS_2. Grain boundaries are an interesting type of defect, since they have sections of localised order, and their length and coordination geometry depends on the mismatch between two crystals. They may therefore have unique properties solely dependent on relative crystal position and orientation, rather than chemical composition.[104] Chapter 4 shows that grain

boundaries do indeed activate defect modes in MoS_2, but the exact nature of this activation - its polarization dependencies and how it varies as the boundary changes direction, are not yet understood. A detailed polarization study, coupled with some form of atomic resolution technique to determine grain boundary structure may reveal interesting geometry-dependent scattering effects, and could provide a means for characterising different types of grain boundaries. In addition, computational analysis of the states around the boundary structures might reveal additional states to/from which scattering may occur.

Point defects have also yet to be analysed. There are methods reported in literature for generating sulfur vacancies and various defects, typically employing some form of ion-beam irradiation or high-temperature, high-vacuum treatment.[121,250] It would be interesting to see how readily the essentially random scattering of these point and cluster defects can be identified by the backscatter mechanism. Then it would be useful to mathematically define the relationship between intensity and defect concentration for these resonant features, which should provide a more accurate tool for quantifying defects in MoS_2 materials.

7.3 Chemical Modification

As with the above defects, chemical modification of MoS_2 has only been examined in passing in Chapter 4, but it can be seen that modification with thiol-containing ligands can have significant affects on the defect mode intensities. It is unclear whether this is a result of a blurring of the well-defined edges, or a consequence of doping effects on the band structure. It would be interesting to perform a full study containing ligands with various electron donating and withdrawing properties to elucidate the mechanism. Results from such studies may provide insights into the processes which passivate the edges of MoS_2 during catalysis.

7.4 Other TMDs

Results from Chapter 4 indicate that there are defect-activated indirect resonance features in other common TMD materials. Each TMD has a similar but unique band structure, and the electronic properties differ for each material. As Chapter 4 demonstrated, 785 nm excitation will not be suitable for accessing the indirect transitions in all these materials, so either a tunable excitation source or a carefully selected range of laser wavelengths would be needed to identify and access resonant pathways. A full characterisation of the edge-dependent backscattering for each of these systems can be performed, as well as all the above tunable laser, defect investigation and modification studies. Since the physical and electronic properties of each TMD are unique, there may be a vast range of applications that benefit from a detailed analysis of the defect-mediated DRR phenomena.

In addition to the common TMDs, it is also possible to synthesise and fabricate TMD alloys and 2D van der Waals heterostructures. In alloys, some percentage of the constituent atoms are replaced with similar atoms in the series (Mo, W, S, Se, and Te) which changes the structural and electronic properties of the material.[64,251] In 2D heterostructures, the relative orientation and position of each layer alters the overall electronic properties, meaning new pathways in the band structure can form, leading to new excitonic transitions and electronic properties.[216–218] As such, it is expected that indirect resonance DRR investigations of these kinds of materials may yield interesting results.

7.5 Computational Studies

This work has only utilised computational analysis to obtain symmetry information for states in the band structure. However, in DRR literature computational analysis is a powerful, and at times necessary, complementary data set to help understand the complex scattering phenomena occurring in these materials. Future studies could also delve deeper into the computational analysis to calculate electron-phonon and exciton-phonon coupling constants for scattering pathways, and investigate absorption coefficients to identify ideal excitation energies.

7.6 Synchrotron Source

While highly-tunable excitation sources in the optics lab can be difficult or expensive to achieve, a synchrotron may provide a completely tunable, coherent, polarized source of electromagnetic radiation across visible and near-infrared wavelengths. Most modern synchrotrons are optimised for producing high-energy X-rays, but can utilise visible light beamlines for diagnostics or imaging purposes. In addition, synchrotron sources are typically much more intense than standard lab sources, and most facilities contain equipment for a variety of specialised experimental configurations, including temperature and pressure control. The high-intensity source can overcome low throughput issues associated with triple grating spectrometers and diminishing Raman scattering efficiencies in the near-infrared, and low-temperatures can be utilised to minimise sample damage. As such, a tunable resonance study utilising synchrotron radiation could rapidly obtain a full mapping of the indirect resonance pathways for a range of TMD materials - provided a suitable visible/near-infrared beamline can be accessed.

Appendix A

Raman Microscope Design Supplementary Figures

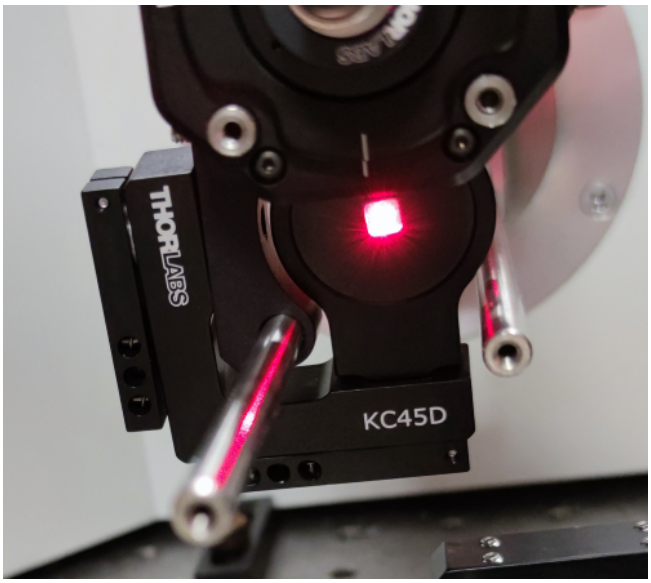

FIGURE A.1: Photo showing the glow of a VBG spectral filter due to Rayleigh scattering of divergent light passing through the filter. This light scatters in random directions and can eventually make it to the detector where it contributes to stray light artefacts.

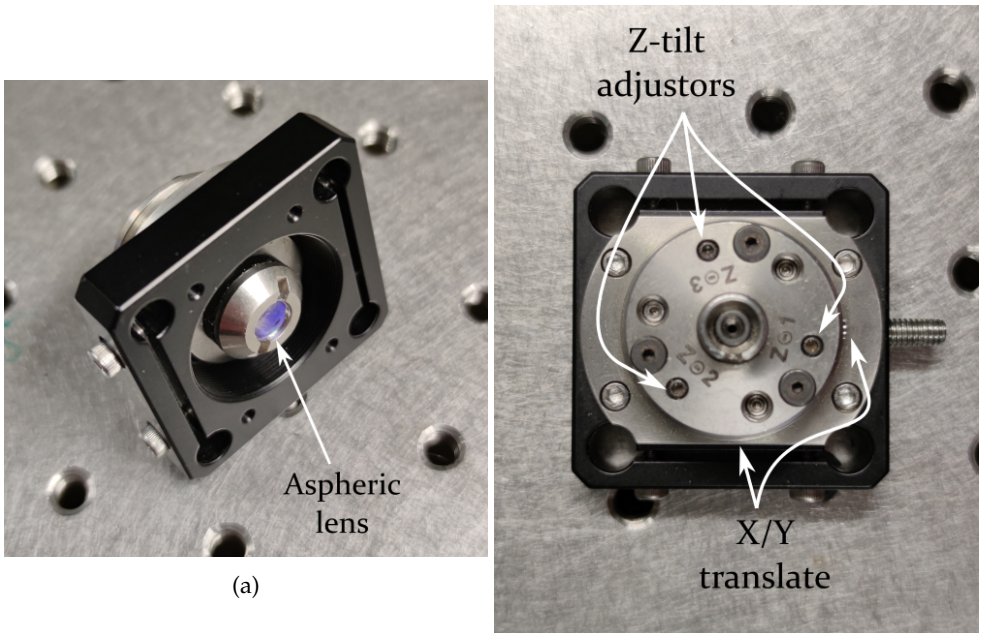

(a) (b)

FIGURE A.2: Photos of ThorLabs FiberPort adapters, designed for fiber coupling to/from single mode fibers with every alignment degree of freedom built into the housing (three-axis tilt, X/Y translate, Z-translate/focus). Unfortunately, the the Z-focus is achieved with a simultaneous adjustment of all three tilt axes - which is ridiculously difficult to do without ruining the axial alignment.

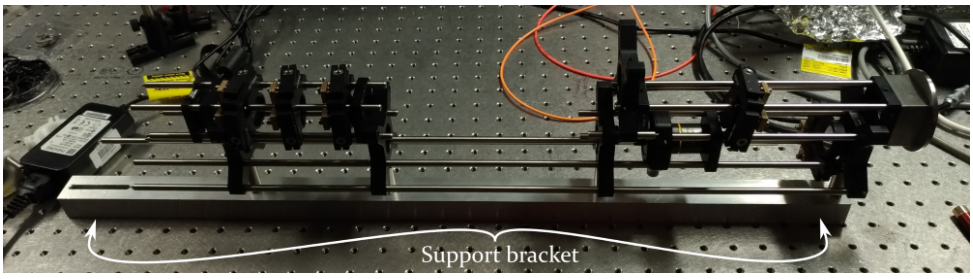

FIGURE A.3: An example of a bracing bracket used to keep long cage optics aligned without flexing under their own weight.

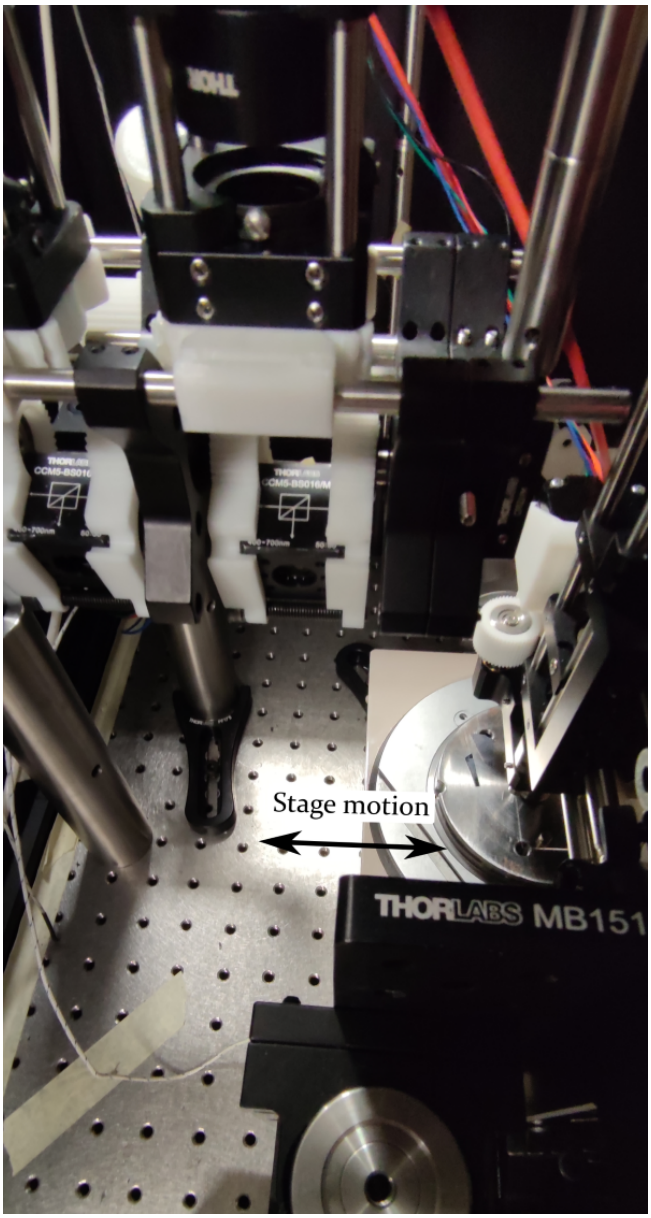

FIGURE A.4: An almost vertical perspective of the area underneath the swing optics of Section C, showing that the stage below prevents mounting of an additional support post on the right-hand side of Section C to the table.

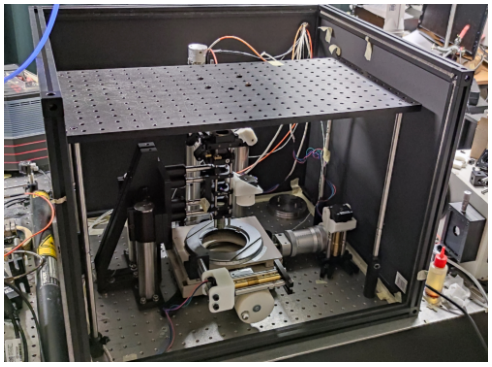

(a)

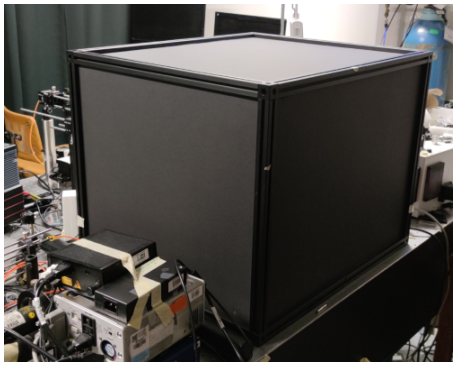

(b)

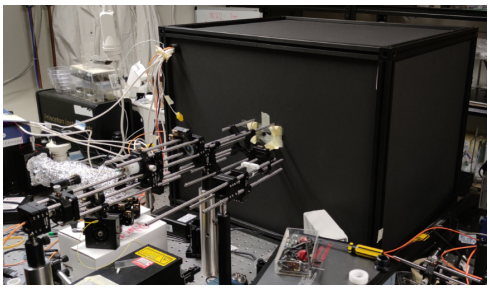

(c)

FIGURE A.5: (a) Thermal insulation box surrounding Sections C and D with the front and top walls off. The breadboard which runs over the top of Section D provides an anchor point for supporting Section C (see Figure 2.36), and provides a convenient location for the keyboard and mouse during sample alignment/positioning. (b) Side view of the closed box, with Sections A and B in the left background. (d) Back view of the box, with Sections A and B seen in the left foreground.

FIGURE A.6: The simple objective used for high-magnification Raman microscopy. Magnification = 100×, NA = 1.25, f ≈ 1.66 mm, clear aperture D ≈ 5 mm.

FIGURE A.7: A snap-on cage mount holding a half-inch rotation mount (see angle increments) and polarizing optic.

FIGURE A.8: A flexible mechanical coupling for mitigating run-out issues. Not used in the final designs due to backlash and hysteresis issues.

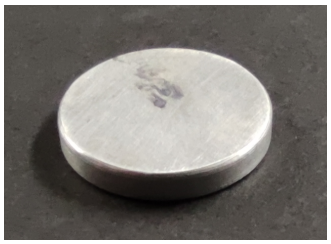

FIGURE A.9: An aluminium disc used for loading samples in the LT Linkam stage. The dark spot in the image is some MoS_2 powder pressed into the metal.

Appendix B

Symmetry Information for MoS_2

B.1 Transition Symmetry Analysis

This appendix lists symmetry information and tabulates combinations of phonons and states for analysis of allowed transitions. The symmetry information listed here is obtained from literature[171,202,203] and Quantum ESPRESSO (QE) computational outputs. Due to the band nesting ability of the indirect transitions, state symmetries are considered both at and either side of high symmetry points near band minima/maxima. Where a band is listed multiple times in the same table indicates differing irreducible representations for the states encompassed by the sampling range around the high symmetry points.

TABLE B.1: Phonon symmetries and irreducible representations from the M and K points of the BZ published by Linveh and Spanier.[171] Phonon frequencies (ν) are gathered from various reports in literature, and correspond to the frequencies at 0 K.

Mode	M point (D_{2h})	$\nu\ (cm^{-1})$	Mode	K point (D_{3h})	$\nu\ (cm^{-1})$
ZA′	B_{3g}	174	ZA′	A_2'	184
TA′	B_{1g}	160	TA′	A_2''	188
LA′	A_g	233	LA′	A_1'	237
ZA	B_{1u}	182	ZA	A_2'	185
TA	B_{3u}	156	TA	A_2''	190
LA	B_{2u}	235	LA	A_1'	234

TABLE B.2: The above phonon irreducible representations with wavevectors to the K and M points, reduced to the C_{2v} point group to match the symmetry (point group) of the VB states near Γ.

Mode	M point ($C_{2v}(x/y/z)$)	ν (cm^{-1})	Mode	K point (C_{2v})	ν (cm^{-1})
ZA′	$B_2/B_1/A_2$	174	ZA′	B_2	184
TA′	$A_2/B_2/B_1$	160	TA′	B_1	188
LA′	A_1	233	LA′	A_1	237
ZA	$A_1/B_1/B_2$	182	ZA	B_2	185
TA	$B_1/B_2/A_1$	156	TA	B_1	190
LA	$B_2/A_1/B_1$	235	LA	A_1	234

TABLE B.3: Irreducible representations of states near (but not at) the K point. There are two different sets of symmetries for the bands either side of the K point, as the bands move towards M and Γ respectively.

∼ Γ Band	Symm	Phonon	Symm	∼ K
24	B_1	A_2	B_2	27
24	B_1	B_1 (TA,TA′)	A_1	28
24	B_1	B_1 (TA,TA′)	A_1	27
24	B_1	A_1 (LA,LA′)	B_1	28
25	A_1	B_2 (ZA,ZA′)	B_2	27
25	A_1	A_1 (LA,LA′)	A_1	28
25	A_1	A_1 (LA,LA′)	A_1	27
25	A_1	B_1 (TA,TA′)	B_1	28
26	A_1	B_2 (ZA,ZA′)	B_2	27
26	A_1	A_1 (LA,LA′)	A_1	28
26	A_1	A_1 (LA,LA′)	A_1	27
26	A_1	B_1 (TA,TA′)	B_1	28

TABLE B.4: Irreducible representations of states near (but not at) the M point. There are two different sets of symmetries for the bands either side of the M point, as the bands move towards K and Γ respectively.

∼ Γ Band	Symm	Phonon	Symm	∼ M
24	B_1	A_1 (LA,LA′,TA,ZA)	B_1	27
24	B_1	A_1 (LA,LA′,TA,ZA)	B_1	28
24	B_1	B_1 (LA,TA,TA′ZA,ZA′)	A_1	27
24	B_1	A_2 (ZA′,TA′)	B_2	28
25	A_1	B_1 (LA,TA,TA′,ZA,ZA′)	B_1	27
25	A_1	B_1 (LA,TA,TA′ZA,ZA′)	B_1	28
25	A_1	A_1 (LA,LA′,TA,ZA)	A_1	27
25	A_1	B_2 (LA,TA,TA′,ZA,ZA′)	B_2	28
26	A_1	B_1 (LA,TA,TA′ZA,ZA′)	B_1	27
26	A_1	B_1 (LA,TA,TA′ZA,ZA′)	B_1	28
26	A_1	A_1 (LA,LA′,TA,ZA)	A_1	27
26	A_1	B_2 (LA,TA,TA′,ZA,ZA′)	B_2	28

TABLE B.5: Irreducible representations of the states at the M point. Multiple combinations of initial and final states are listed.

$\sim \Gamma$ Band	Symm	Phonon	Symm	M
24	B_1	A_2 (ZA',TA')	B_2	27
24	B_1	B_1 (LA,TA,TA'ZA,ZA')	A_1	27
24	B_1	A_1 (LA,LA',TA,ZA)	B_1	27
24	B_1	B_2 (LA,TA,TA',ZA,ZA')	A_2	28
24	B_1	A_2 (ZA',TA')	B_2	28
24	B_1	A_1 (LA,LA',TA,ZA)	B_1	28
25	A_1	B_2 (LA,TA,TA',ZA,ZA')	B_2	27
25	A_1	A_1 (LA,LA',TA,ZA)	A_1	27
25	A_1	B_1 (LA,TA,TA'ZA,ZA')	B_1	27
25	A_1	A_2 (ZA',TA')	A_2	28
25	A_1	B_2 (LA,TA,TA',ZA,ZA')	B_2	28
25	A_1	B_1 (LA,TA,TA'ZA,ZA')	B_1	28
26	A_1	B_2 (LA,TA,TA',ZA,ZA')	B_2	27
26	A_1	A_1 (LA,LA',TA,ZA)	A_1	27
26	A_1	B_1 (LA,TA,TA'ZA,ZA')	B_1	27
26	A_1	A_2 (ZA',TA')	A_2	28
26	A_1	B_2 (LA,TA,TA',ZA,ZA')	B_2	28
26	A_1	B_1 (LA,TA,TA'ZA,ZA')	B_1	28

TABLE B.6: Irreducible representations of the phonon modes at the Q point and their frequencies (approximate), obtained from QE computational outputs.

Mode	Q point (C_{2v})	ν (cm^{-1})
ZA'	A_2	107
ZA	B_2	110
TA'	B_1	136
TA	A_1	140
LA'	B_1	182
LA	A_1	185

TABLE B.7: Irreducible representations of states both at and near the Q point with C_{2v} symmetry. Unlike the K and M points, only one band (the CBM) drops in energy to form the local minima at the Q point, and as such only one band is considered for the final excited states. Conversely, three possible bands near Γ are considered for the initial states.

$\sim \Gamma$ Band	Symm	Phonon	Symm	$\sim$ K
24	B_1	B_1 (TA',LA')	A_1	27
25	A_1	A_1 (LA,TA)	A_1	27
26	A_1	A_1 (LA,TA')	A_1	27

B.2 Symmetry Decomposition Output

```
xk=(   0.00000,   0.00000,   0.00000  )

point group D_6h(6/mmm)
there are 12 classes
the character table:


E     2C6   2C3   C2    3C2'  3C2'' i     2S3   2S6   s_h   3s_d  3s_v
A_1g  1.00  1.00  1.00  1.00  1.00  1.00  1.00  1.00  1.00  1.00  1.00  1.00
A_2g  1.00  1.00  1.00  1.00 -1.00 -1.00  1.00  1.00  1.00  1.00 -1.00 -1.00
B_1g  1.00 -1.00  1.00 -1.00  1.00 -1.00  1.00 -1.00  1.00 -1.00  1.00 -1.00
B_2g  1.00 -1.00  1.00 -1.00 -1.00  1.00  1.00 -1.00  1.00 -1.00 -1.00  1.00
E_1g  2.00  1.00 -1.00 -2.00  0.00  0.00  2.00  1.00 -1.00 -2.00  0.00  0.00
E_2g  2.00 -1.00 -1.00  2.00  0.00  0.00  2.00 -1.00 -1.00  2.00  0.00  0.00
A_1u  1.00  1.00  1.00  1.00  1.00  1.00 -1.00 -1.00 -1.00 -1.00 -1.00 -1.00
A_2u  1.00  1.00  1.00  1.00 -1.00 -1.00 -1.00 -1.00 -1.00 -1.00  1.00  1.00
B_1u  1.00 -1.00  1.00 -1.00  1.00 -1.00 -1.00  1.00 -1.00  1.00 -1.00  1.00
B_2u  1.00 -1.00  1.00 -1.00 -1.00  1.00 -1.00  1.00 -1.00  1.00  1.00 -1.00
E_1u  2.00  1.00 -1.00 -2.00  0.00  0.00 -2.00 -1.00  1.00  2.00  0.00  0.00
E_2u  2.00 -1.00 -1.00  2.00  0.00  0.00 -2.00  1.00  1.00 -2.00  0.00  0.00


the symmetry operations in each class and the name of the first
element:

E        1
2C6      5    6
2C3      7    8
C2       2
3C2'     4   12   11
3C2''    3    9   10
i       13
2S3     17   18
2S6     19   20
s_h     14
3s_d    16   24   23
3s_v    15   21   22


Band symmetry, D_6h(6/mmm) point group:

e(  1 -  2) =    -50.90807  eV     2   --> A_1g
e(  1 -  2) =    -50.90807  eV     2   --> B_2u
e(  3 -  4) =    -25.12947  eV     2   --> B_1g
```

```
e(  3 -  4) =    -25.12947  eV     2   --> A_2u
e(  5 -  8) =    -24.93979  eV     4   --> E_2g
e(  5 -  8) =    -24.93979  eV     4   --> E_1u
e(  9 -  9) =     -4.26913  eV     1   --> A_1g
e( 10 - 10) =     -4.03748  eV     1   --> B_2u
e( 11 - 11) =     -3.03848  eV     1   --> B_1g
e( 12 - 12) =     -2.65394  eV     1   --> A_2u
e( 13 - 13) =      3.84773  eV     1   --> A_1g
e( 14 - 14) =      4.79165  eV     1   --> B_2u
e( 15 - 15) =      7.26026  eV     1   --> B_1g
e( 16 - 17) =      7.28589  eV     2   --> E_2g
e( 18 - 19) =      7.29770  eV     2   --> E_1u
e( 20 - 21) =      8.38299  eV     2   --> E_1g
e( 22 - 23) =      8.42372  eV     2   --> E_2u
e( 24 - 24) =      9.39835  eV     1   --> A_2u
e( 25 - 25) =      9.56579  eV     1   --> A_1g
e( 26 - 26) =     10.61791  eV     1   --> B_2u
e( 27 - 28) =     12.66375  eV     2   --> E_1g
e( 29 - 30) =     12.68820  eV     2   --> E_2u
e( 31 - 31) =     12.84659  eV     1   -->   ?

**********************************************

**********************************************

xk=(   0.00000,   0.01375,   0.00000  )

point group C_2v (mm2)
there are  4 classes
the character table:

E     C2    s_v   s_v'
A_1    1.00  1.00  1.00  1.00
A_2    1.00  1.00 -1.00 -1.00
B_1    1.00 -1.00  1.00 -1.00
B_2    1.00 -1.00 -1.00  1.00

the symmetry operations in each class and the name of the first
element:

E        1
C2       2
```

```
s_v      3
s_v'     4


Band symmetry, C_2v (mm2)  point group:

e(  1 -  2) =    -50.90801  eV     2   -->   2 A_1  D_1  S_1
e(  3 -  4) =    -25.12937  eV     2   -->   2 B_2  D_4  S_4
e(  5 -  6) =    -24.94030  eV     2   -->   ?
e(  7 -  8) =    -24.93990  eV     2   -->   ?
e(  9 -  9) =     -4.26703  eV     1   --> A_1  D_1  S_1
e( 10 - 10) =     -4.03540  eV     1   --> A_1  D_1  S_1
e( 11 - 11) =     -3.03751  eV     1   --> B_2  D_4  S_4
e( 12 - 12) =     -2.65321  eV     1   --> B_2  D_4  S_4
e( 13 - 13) =      3.85019  eV     1   --> A_1  D_1  S_1
e( 14 - 14) =      4.79406  eV     1   --> A_1  D_1  S_1
e( 15 - 15) =      7.25475  eV     1   --> B_2  D_4  S_4
e( 16 - 16) =      7.28089  eV     1   --> A_1  D_1  S_1
e( 17 - 17) =      7.28803  eV     1   --> B_1  D_3  S_3
e( 18 - 18) =      7.29284  eV     1   --> A_1  D_1  S_1
e( 19 - 19) =      7.29995  eV     1   --> B_1  D_3  S_3
e( 20 - 20) =      8.37339  eV     1   --> B_2  D_4  S_4
e( 21 - 21) =      8.37946  eV     1   --> A_2  D_2  S_2
e( 22 - 22) =      8.42029  eV     1   --> A_2  D_2  S_2
e( 23 - 23) =      8.42692  eV     1   --> B_2  D_4  S_4
e( 24 - 24) =      9.40354  eV     1   --> B_2  D_4  S_4
e( 25 - 25) =      9.56594  eV     1   --> A_1  D_1  S_1
e( 26 - 26) =     10.61380  eV     1   --> A_1  D_1  S_1
e( 27 - 27) =     12.66109  eV     1   --> B_2  D_4  S_4
e( 28 - 28) =     12.66723  eV     1   --> A_2  D_2  S_2
e( 29 - 29) =     12.68476  eV     1   --> B_2  D_4  S_4
e( 30 - 30) =     12.69256  eV     1   --> A_2  D_2  S_2
e( 31 - 31) =     12.84391  eV     1   -->   ?
```

Appendix C

Double Resonance Raman Supplementary Figures

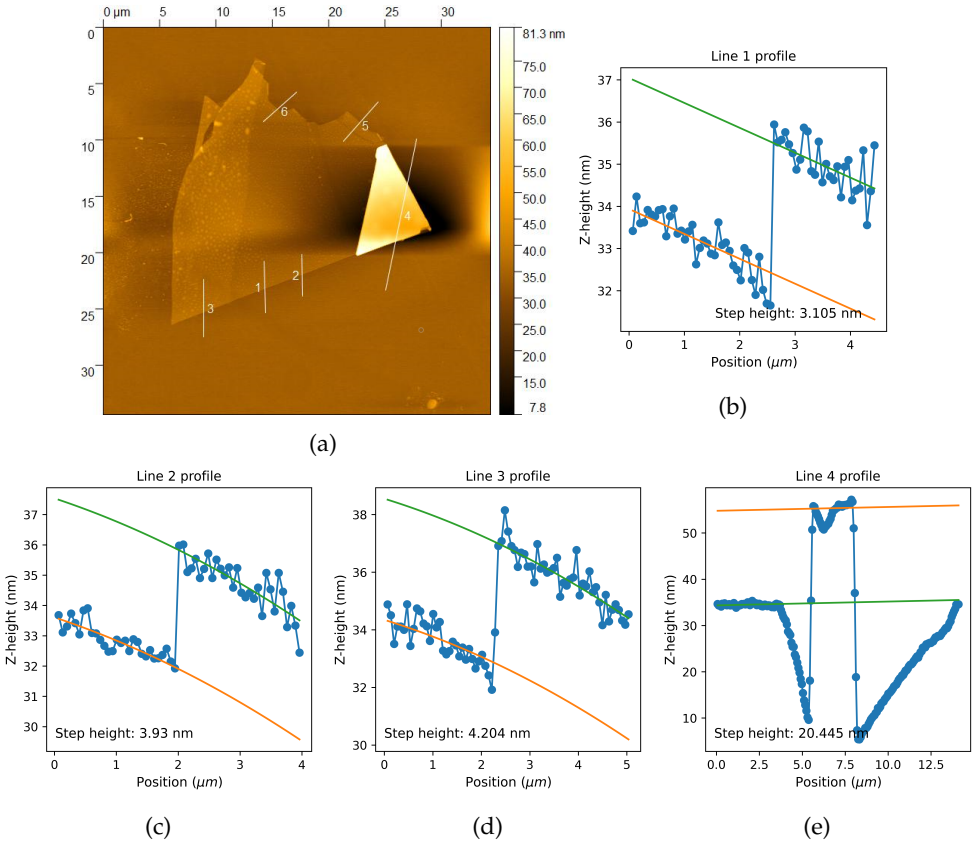

FIGURE C.1: (a) AFM image and (b-e) height profiles of the indicated lines in (a).

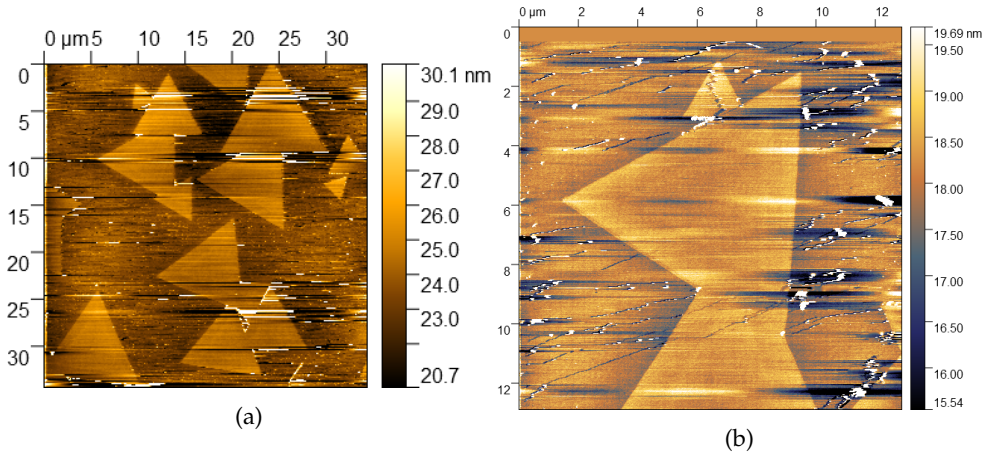

FIGURE C.2: AFM images of a sample of CVD-grown triangular crystals of MoS_2. Note there are many artefacts in these scans due to surrounding precursor and MoS_2 crystal seed deposits that get pushed/dragged by the AFM tip.

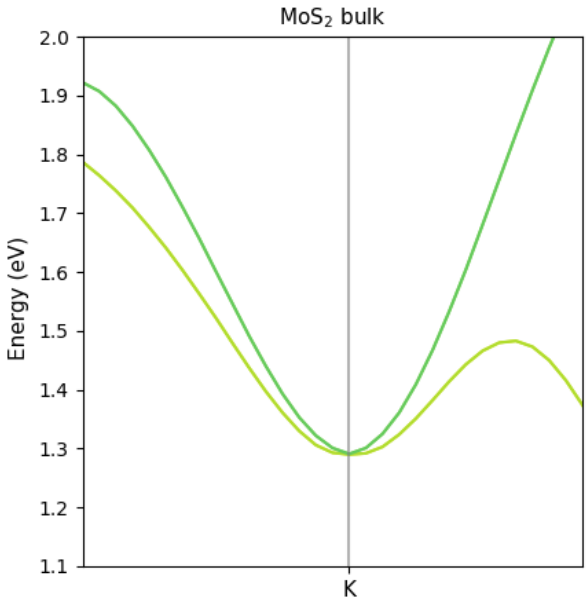

FIGURE C.3: A zoomed view of the band structure in the conduction band of bulk MoS_2 near the K point, showing two separate bands which may both be involved in the indirect transitions.

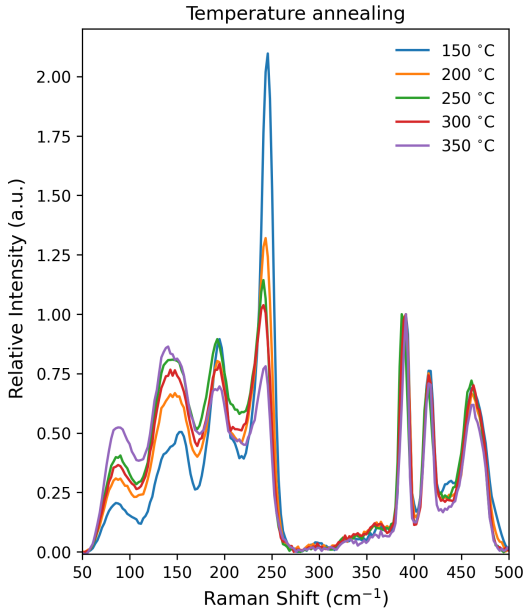

FIGURE C.4: Raman spectra of sonicated samples which have been subject to heating under high vacuum ($10^{-2} - 10^{-3}$ mbar) and various temperatures. The results indicate that the defect mode features are intrinsic to the sample and not a result of chemical contamination or doping effects from the solvent/surrounding environment.

Appendix D

Resonance Tuning Supplementary Info

D.1 Calibration of Temperature in MoS_2

In our current setup, we do not have the capability to accurately control the temperature of the sample. We can lower to liquid nitrogen temperatures at 70 K, and measure along the way, but we do not have the software required to hold at any temperature before this. For the same software reasons, we cannot heat the stage, but we can induce localised heating with laser power by deliberately preparing the samples in such a way that thermal dissipation is poor (i.e. freeze-drying). Then, using the thermal shifts of the fundamental A_{1g} and E_{2g} modes in MoS_2, we can determine the temperature of the parts of the sample contributing to Raman scattering.

To do this, we peakfit the A_{1g} and E_{2g} at a each power, then extract the peak positions and determine the magnitude of the shifts with respect to the modes at room temperature. We can then determine a change in temperature using the temperature coefficients in table D.1, as reported by Livneh and Steerer.[215] Figure D.6(a) shows the fundamental mode regions in Figure 4.5, and (b) shows peakfits of the room-temperature (blue) and largest shift at high power (red), and their shift with respect to each other. Figure D.7 shows the spectra in Figure 4.5 zoomed in on the defect mode region and offset for clarity.

TABLE D.1: Temperature shift data for the E_{2g} and A_{1g} modes of MoS_2, using increasing laser power as a proxy for temperature control.

Mode	Fitted shift (cm^{-1})	Temperature coefficient (cm^{-1}/K)	Estimated temperature difference (K)
E_{2g}	4.47	-0.0147	304.08
A_{1g}	3.68	-0.0123	299.19

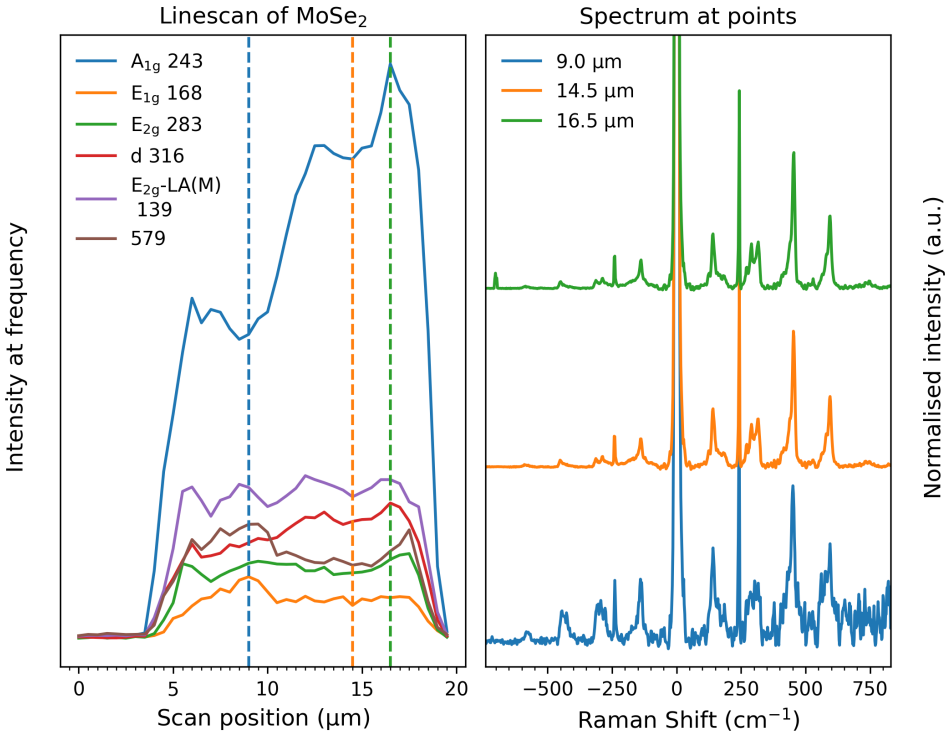

FIGURE D.1: Same linescan as Figure 4.9, showing the anti-Stokes region as well.

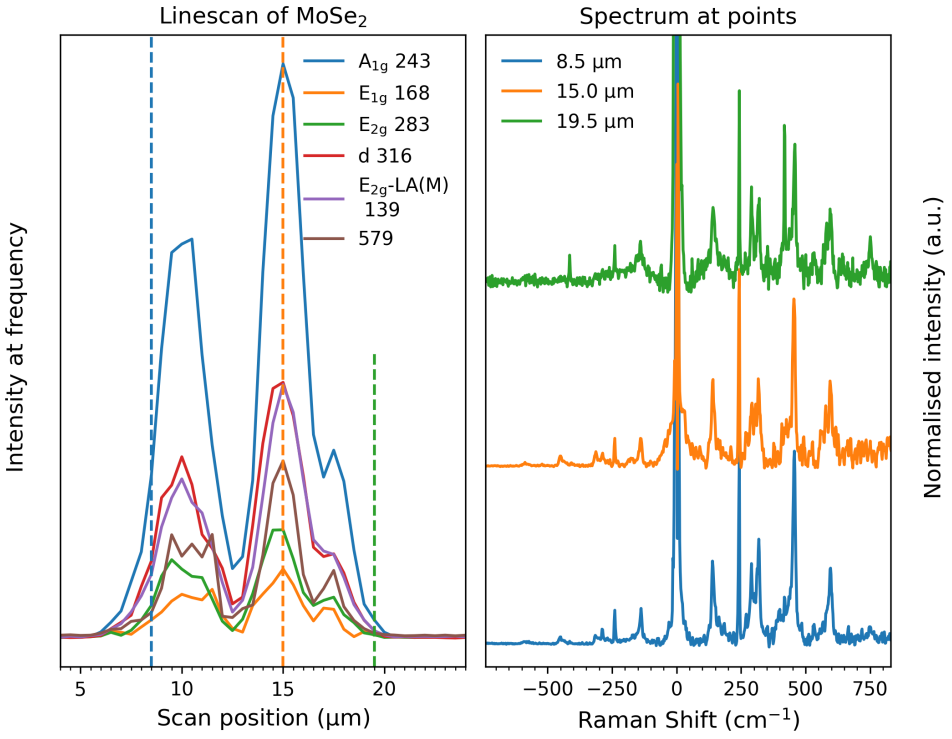

FIGURE D.2: Same linescan as Figure 4.10, showing the anti-Stokes region as well.

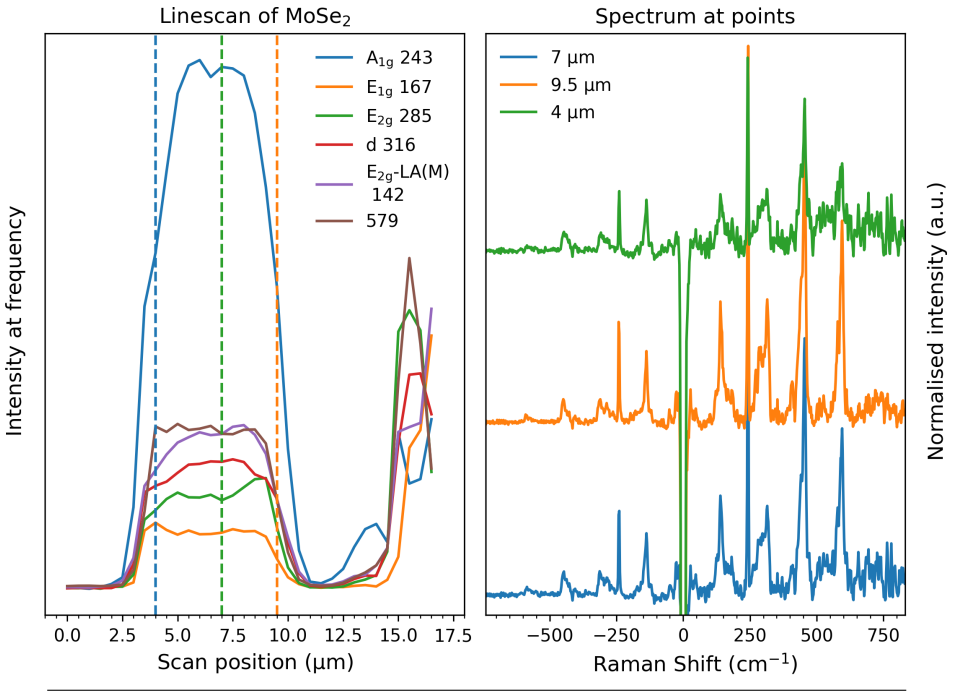

FIGURE D.3: Additional linescan of $MoSe_2$ flakes.

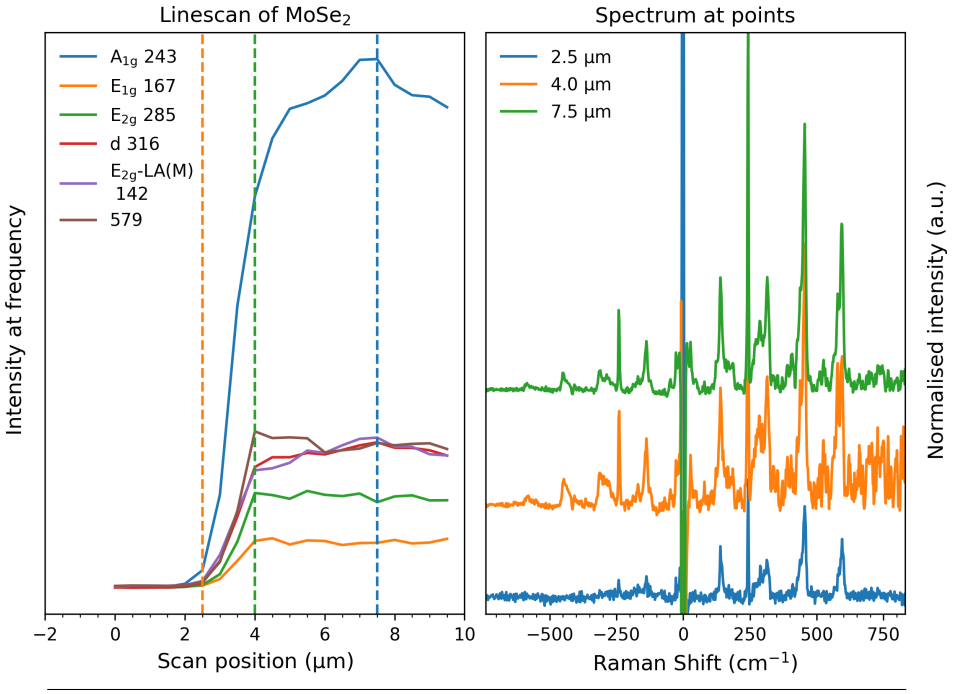

FIGURE D.4: Additional linescan of $MoSe_2$ flakes.

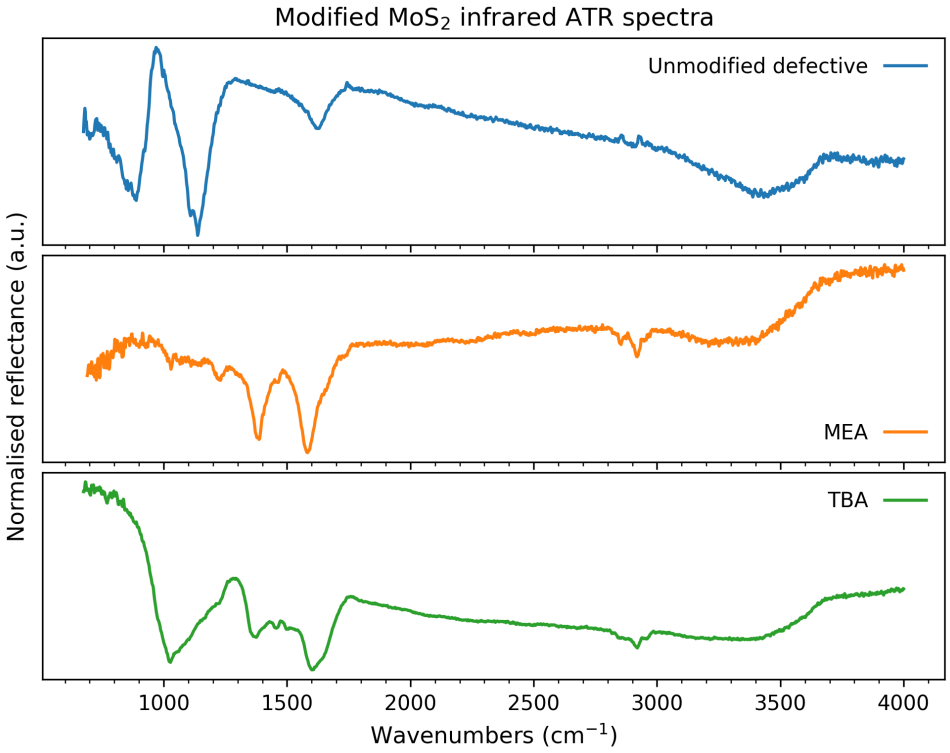

FIGURE D.5: Infrared attenuated total reflectance spectra of the modified MoS_2 materials in Figure 4.8.

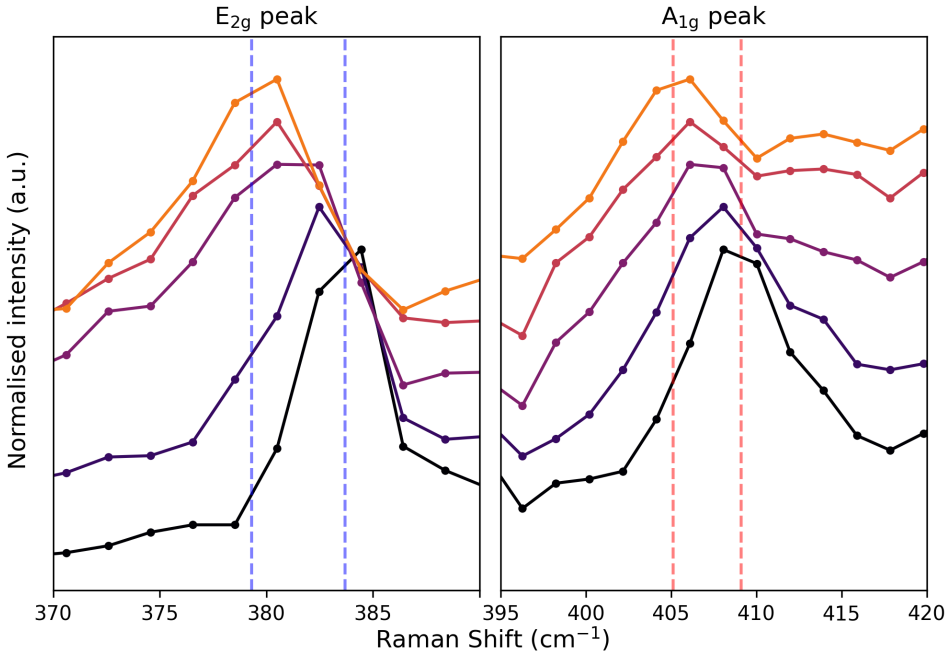

(a)

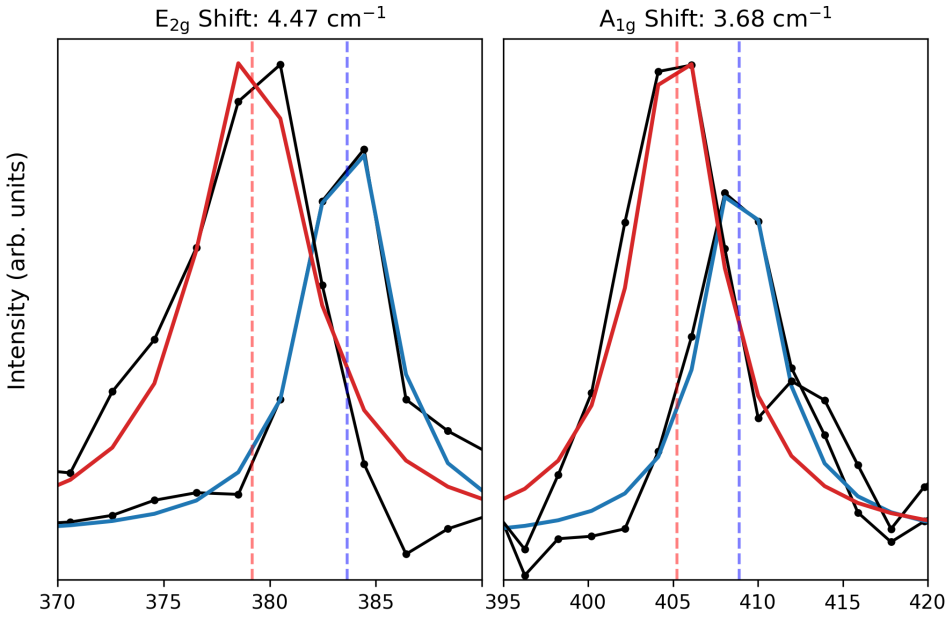

(b)

FIGURE D.6: (a) Zoom of the E_{2g} (left) and A_{1g} (right) modes for the select spectra in Figure 4.5, normalised and offset for clarity. (b) The lowest and highest laser powers correspond to the least and greatest shifts of each peak, plotted here and peakfit to extract the position value. The information is given in table D.1.

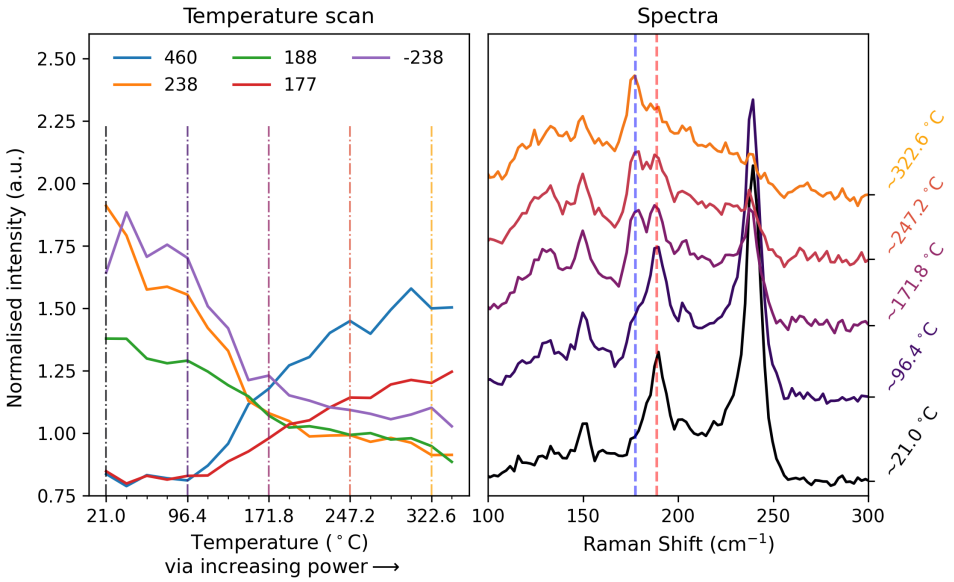

FIGURE D.7: Zoom of the defect mode region for the select spectra in 4.5, normalised to the E_{2g} and offset for clarity. The red and blue dashed lines show the frequencies of the TA(K) and A_{1g}-LA(M) modes respectively. The graph on the left now shows the TA(K) mode normalised to the A_{1g}-LA(M) to emphasise their reciprocal nature.

Appendix E

Methods Supplementary Info

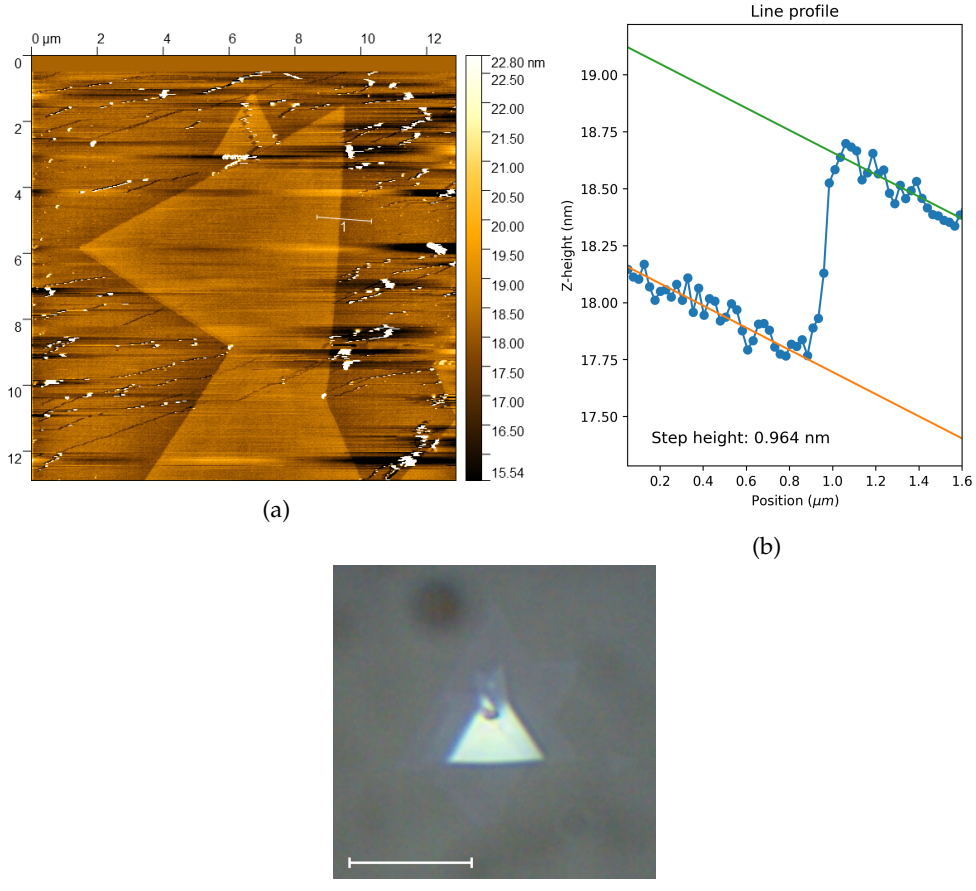

(a)

(b)

(c)

FIGURE E.1: (a) AFM image and (b) height-profile of the marked line in (a) of a CVD synthesised MoS_2 crystal on sapphire. The scales in (a) are in microns. The profile indicates either one or two layers, and although difficult to see and does not appear in the line profile, a faint brighter region is visible in the centre of crystal which suggests a third layer is growing on top, but has yet to reach the sides. (c) shows a similar example of a thicker terraced crystal. These terraced crystals may reveal the location of single-layer material by scanning near them - even if it is not necessarily visible under the optical microscope. Scale bar in (c) is 10 µm

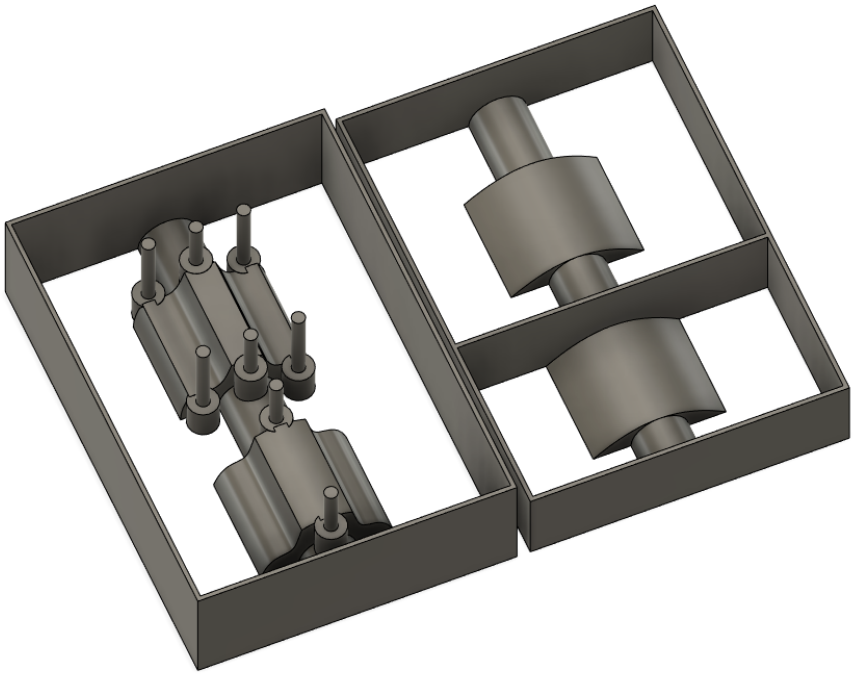

FIGURE E.2: The 3D printed moulds for casting the refractory cement in the shape of the tube furnace. Left is the bottom half, and right is the top half.

Appendix F

Quantum ESPRESSO Input Example

Below is an example of the input file for a Quantum ESPRESSO variable-cell relaxation calculation.

```
   &control
calculation  = 'vc-relax',
restart_mode = 'from_scratch',
prefix       = 'MoS2_6',
pseudo_dir   = '/home/max/QE6/pseudo',
outdir       = '../out',

wf_collect    = .true.
verbosity     = 'high'
forc_conv_thr = 1D-4
etot_conv_thr = 1D-6
/
&system
ibrav       = 4,
a = 3.1596,
c = 12.295,
nat         = 6,
ntyp        = 2,
ecutwfc     = 60,
ecutrho = 450,
occupations = 'smearing',
smearing = 'gaussian'
degauss     = 0.005
vdw_corr    = 'dft-d'
! lspinorb = .true.,
! noncolin = .true.,
! tot_charge  = 0.5
```

```
/
&electrons
conv_thr         = 1.0e-14
electron_maxstep = 100,
mixing_mode      = 'plain'
mixing_beta      = 0.7
/
&ions
ion_dynamics = 'bfgs'
/
&CELL
/

ATOMIC_SPECIES
S  32.065  S.pbe-n-kjpaw_psl.1.0.0.UPF
Mo 95.94  Mo.pbe-spn-kjpaw_psl.1.0.0.UPF

ATOMIC_POSITIONS {angstrom}
S  -0.00000158      1.82419682      10.78148550
S  1.57980158       0.91209704       4.63398550
S  1.57980158       0.91209704       1.51351450
S  -0.00000158      1.82419682       7.66101450
Mo -0.00000158      1.82419682       3.07375000
Mo 1.57980158       0.91209704       9.22125000

K_POINTS {automatic}
12 12 4 0 0 0
```

Appendix G

Introduction to Geometric Optics

G.1 Introduction to Geometric Optics

G.1.1 Plane Wave Propagation

A beam of monochromatic light propagating through a laboratory can be treated as a plane wave propagating through space, which spans the beam diameter.[252] A laser source typically produces a collimated beam, which means the diameter of the beam does not change (much) as it travels through space. Conversely, a light bulb is what we consider a point source, meaning it radiates light from some point in space. This light is not collimated - it diverges from the source, and is considered to behave as a radial wave (Figure G.1). A wavefront is an imaginary surface representing a set of points where the wave is in phase, which for a perfect plane wave can be any 2D slice perpendicular to the direction of propagation. For convenience, we can pick the points of maximum amplitude, and draw these as solid lines extending out from a source. Figure G.1 shows that for a radial wave, the wavefronts are curved surfaces of constant radius, and for a plane wave they are simply 2D planes in space. The shape of the wavefront therefore tells us whether the beam is converging, diverging, or collimated.

A general property of electromagnetic radiation is that the waves slow as they enter a medium of higher refractive index, and this allows us to change the shape of wavefronts. Figure G.2 shows that if we place a glass lens with the appropriate curvature in front of a point source, the points along the curved wavefront reach the curved lens at different radii from the source, so the wavefront is slowed differentially - first at the center line (dotted line in the figure), then outwards above and below. This causes the resulting wavefront inside the lens to flatten out and propagate in one direction like a plane wave. This plane wave will meet the flat back surface of the lens simultaneously across its wavefront and exit with its wavefront unperturbed. In essence, this lens has collimated a cone of the light emitted by the point source.

The reverse of the diagram is also true, such that if a plane wave enters the flat surface of the lens it will exit the curved surface with a radial wavefront, and hence

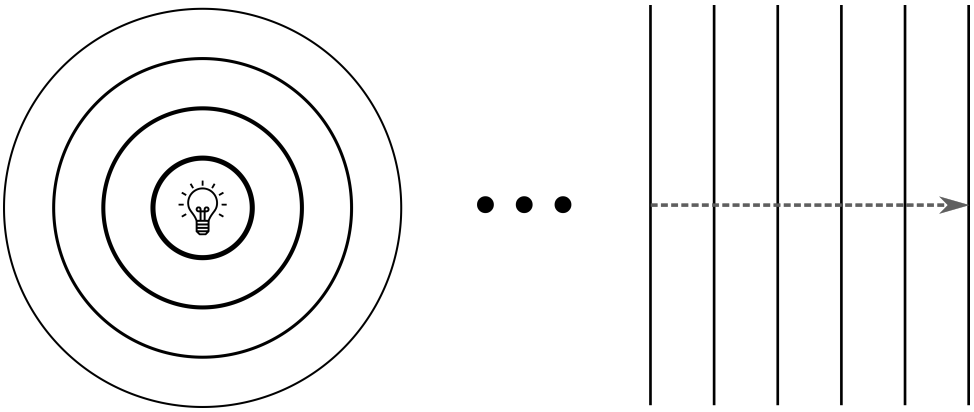

FIGURE G.1: Propagation behaviour of radial (left) and plane (right) waves. The solid circles on the left and vertical lines on the right represent the wavefronts of the two wave types. At large distances from a radial source, the wavefront curvature decreases such that they appear to be are plane waves.

focus to a point. Instead of drawing wavefronts it is convenient to use the Geometrical optics model of light propagation, which represents light as straight lines or rays travelling perpendicular to the wavefront at that point. When a ray reaches an optic such as a lens, the arrow changes direction to represent the reshaped wavefront (Figure G.2(b)). Collimated light is represented by parallel lines and diverging/converging light by non-parallel lines.

The refractive index of material is defined as

$$n = \frac{c}{v} \tag{G.1}$$

where c is the speed of light in a vacuum and v is the phase velocity of light in the medium. Snell's Law, shown in equation G.2, ties these concepts together and describes how light propagates from one medium to another, relating the angles of incidence and refraction, the phase velocities, and refractive indicies of each medium (see Figure G.3).[163]

$$\frac{sin\theta_2}{sin\theta_1} = \frac{v_2}{v_1} = \frac{n_1}{n_2} \tag{G.2}$$

Snell's Law forms the basis for many manipulations in the Raman laboratory. The most useful definition for us is

$$NA = nsin\theta \tag{G.3}$$

where NA is the numerical aperture of a system, n is the refractive index, and θ is typically the angle formed by a ray and the principal axis (central axis of the optic, see Figure G.4). The NA is a dimensionless variable which describes how aggressively light is focused or defocused by an optic. As such it finds use as a descriptor

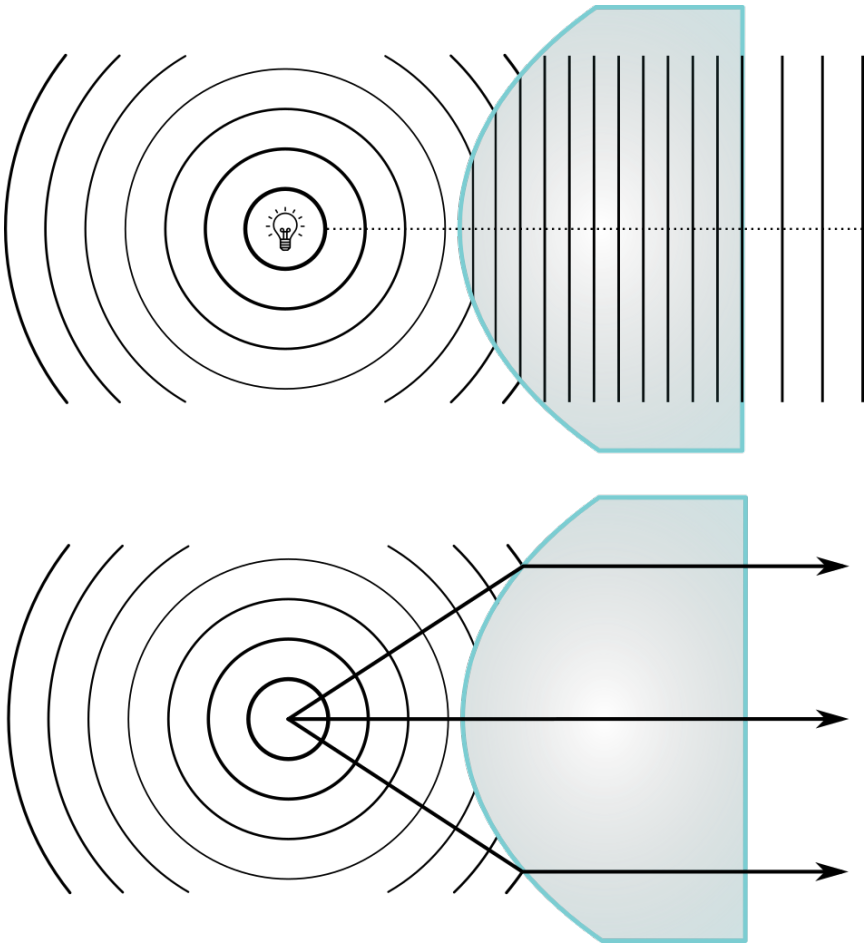

FIGURE G.2: (a) A radial wave emitted from a point source can be focused by placing a lens of the appropriate curvature at an appropriate distance from the source (the focal length). Upon entering the lens, the difference in refractive index and curved surface causes the wavefront to reshape into a straight line, representing a plane wave. (b) In the Geometrical optics model, the wavefront can be represented by vectors perpendicular to the tangent of the wavefront at that point.

of optical elements in many systems, including cameras, microscope objectives, fiber optic cables, and spectrographs. Figure G.4 shows how the focal length (f), lens diameter (D), and NA are related with respect to the cone of light shaped by a focusing lens. The angle θ is half the angle of the full-cone of light being focused or collimated by the lens. We can therefore also write the NA as a function of focal length and lens diameter

$$NA = n\,sin\theta = n\,sin\left[tan^{-1}\left(\frac{D}{2f}\right)\right] \approx n\frac{D}{2f} \tag{G.4}$$

where n in this case is the refractive index of air which is is ≈ 1.

Equation G.4 is perhaps the most useful equation for the Raman lab, as optics in their mounts are typically marked with their focal length (f) but not their NA. This is because the diameter D in equation G.4 is actually the beam diameter (not the lens

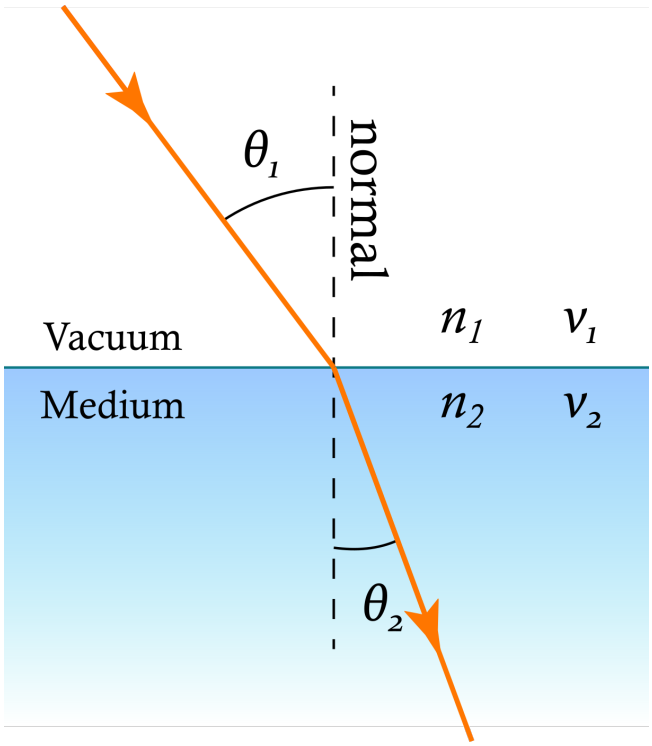

FIGURE G.3: Diagram of light refraction at an interface between two refractive indexes, n_1 and n_2, with phase velocities v_1 and v_2. θ_1 is the angle of incidence, with respect to the surface normal, and θ_2 is the angle of refraction with respect to the surface normal.

diameter), which means the actual NA of the optic in use is a function of the input beam diameter. Note how in G.4 the incoming rays do not completely fill the lens in the vertical direction. This means that the cone of light being focused has a smaller θ_{max} than the whole lens is capable of producing. Therefore a smaller input beam diameter results in a smaller half-cone angle and what will be referred to here as the "effective NA" (NA_{eff}). In order to maximise NA_{eff}, the lens must be entirely filled by the beam of light. This has important implications later on, as the laser spot size, and therefore scanning point-resolution at the sample, is a function of NA_{eff}.

When manipulating light in the lab it is important to consider the NA_{eff}. Having too small an NA_{eff} results in a larger spot, which is a problem when spatially filtering or focusing into a fiber, while too large an NA_{eff} results in a beam which disperses too aggressively, and can miss optics (see Figure G.5). Both of these situations typically result in throughput losses.

It might make sense to standardise or maximise laser beam diameters, so that one need not worry about NA_{eff}. However, as a general rule, it is best to minimise unnecessary optical elements in a system, as each element creates reflection losses, but also introduces aberrations into the beam itself.

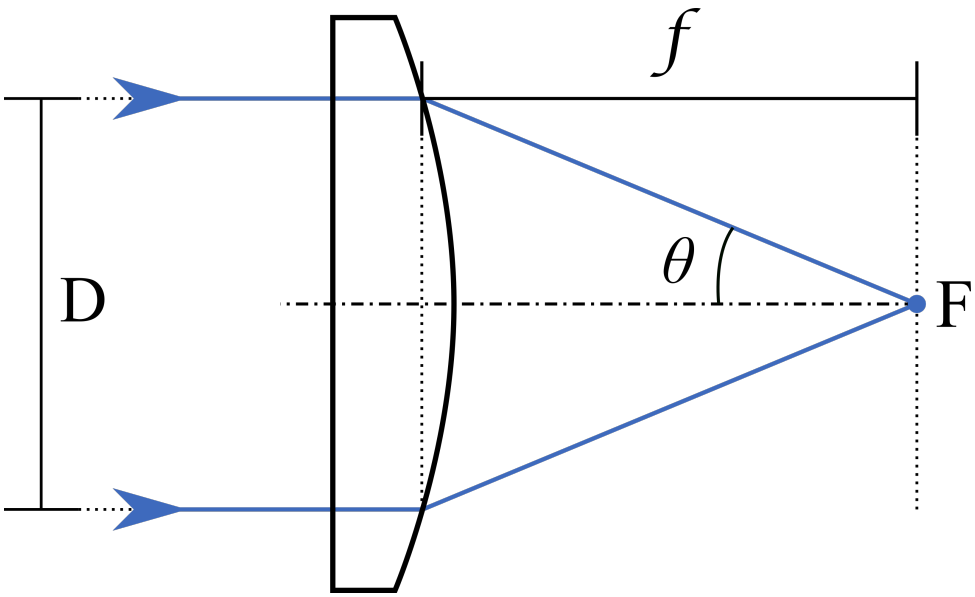

FIGURE G.4: Diagram of a lens focusing collimated light (arrows on the left), and labels of the variables in equation G.4. D is the beam diameter (of light), f is the focal length, θ is the maximum angle made by the focusing light rays and the principal axis (dot-dash line), and F is the focal point of the lens.

G.1.2 Optical Elements - Lenses

By utilising lenses of various different geometries, we can shape light in the laboratory to suit the desired application. Figure G.6 shows four kinds of simple spherical lenses, and how the light propagates through and out of them. Generally speaking, a convex lens will collimate a point source, while a concave lens will diverge a collimated beam. These lenses are referred to as spherical because their curvatures are achieved with spherical tools or machining techniques. They're simple and cheap to manufacture, but they do not accurately reconstruct the wavefront, and attempting to either focus or collimate with one of these will introduce spherical aberrations. For low-curvature lenses with relatively long focal lengths, the effects of spherical aberrations are small, so they can typically be used without much concern. However, for high quality results, we need to use more sophisticated lenses.

These can be compound elements with multiple lenses such as those found in microscope objectives and achromatic doublets, or aspheric lenses for monochromatic applications (e.g. laser beam shaping, fiber coupling).

A problem faced by optics is that they disperse the wavelengths of light passing through them, and different wavelengths end up focused at different points. The phase velocity of light is dependent on the refractive index, which itself is dependent on the wavelength or frequency of light, and so the angle of refraction changes with wavelength.

This property is responsible for the splitting of white light in to colours by prisms

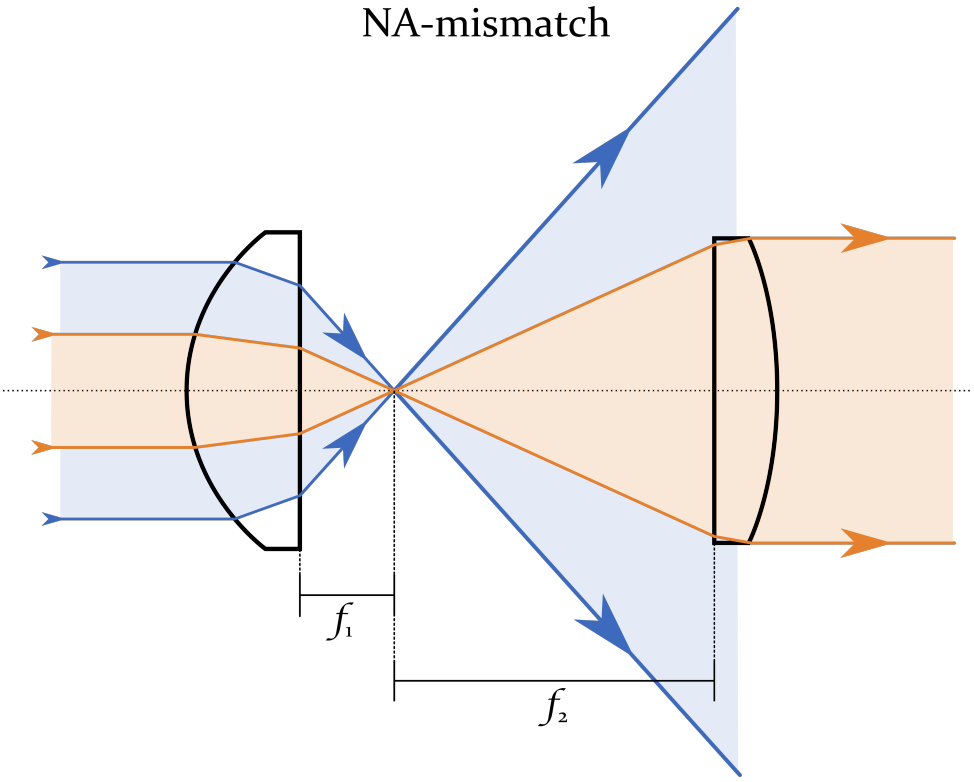

(a)

FIGURE G.5: An example of NA mismatch in the lab. A strongly focusing lens on the left (high NA, small f) causes the light to diverge quickly after crossing the focal point, and the long focal length lens on the right cannot collect all the light, and the blue rays are lost. Only the orange rays are collected by the lens, which corresponds to a smaller section of the input beam diameter.

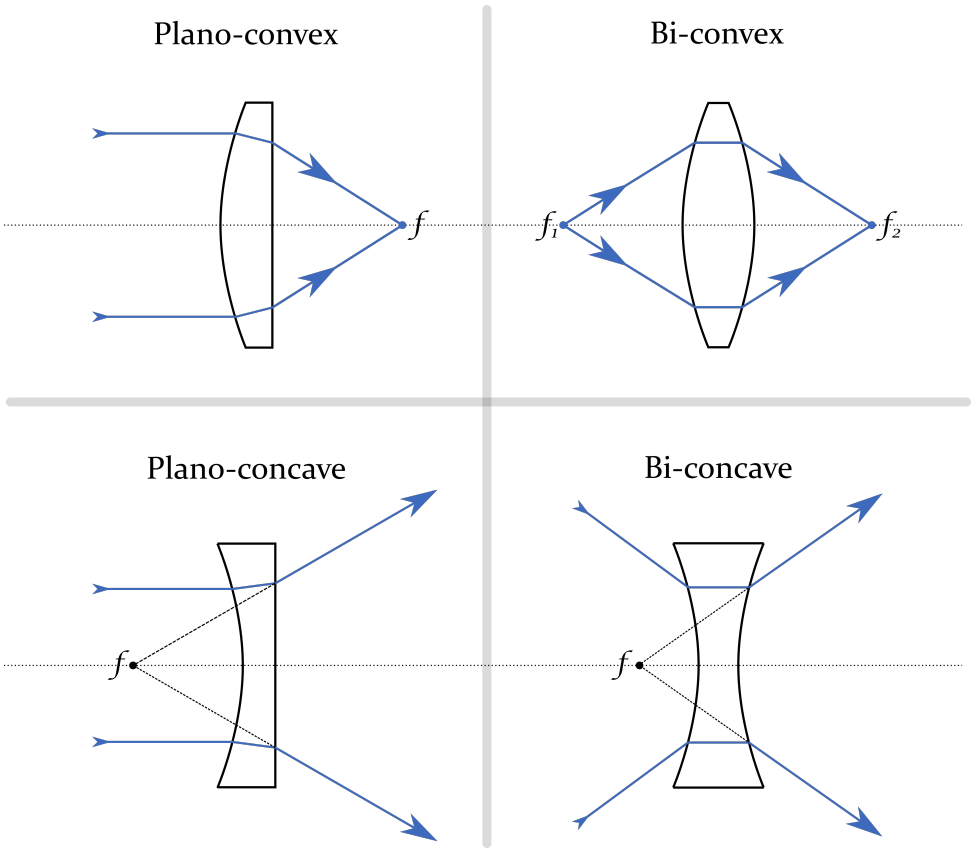

FIGURE G.6: Examples of four common lens shapes, which are used for different effects in the lab. Convex lenses cause collimated light to focus to a point, while concave lenses cause collimated light to diverge.

and rainbows. When not intended, the effects wavelength dispersion on a system is termed chromatic aberration.

Achromatic lenses and microscope objectives mitigate some of this effect by using two or more optical elements, made from materials with different refractive indexes and shaped such that the dispersion of the first lens is balanced/corrected for (for two wavelengths) by the second lens, whilst still focusing/defocusing light.

Aspheric lenses are designed to have the perfect shape for focusing monochromatic light to a diffraction-limited spot without introducing spherical aberrations. These are often desired when the smallest possible focused spot size is required, and are found in fiber coupling optics for monochromatic lasers. Because there is no chromatic correction, these lenses are not suitable for focusing or collimating polychromatic light of different wavelengths, such as Raman-scattered light.

There are several approximations which can be used to predict the spot size, depending on your choice of definitions for spot size. For a perfect truncated plane wave of diameter D and aberration-free optics, the diameter of the focused beam S can be given by:

$$S = \frac{4\lambda f}{D} \propto \frac{\lambda}{NA_{eff}} \tag{G.5}$$

where λ is the wavelength of light and f is the focal length of the lens.[160] We can see that the spot size is proportional to the wavelength of light, and inversely proportional to the NA_{eff}.

A more realistic spot size for the centre of the Airy disc formed by a diffraction-limited Gaussian beam by diffraction-limited optics with a known NA can be given by:

$$S = \frac{1.22\lambda}{NA_{eff}} \tag{G.6}$$

It is typically desired to keep spot sizes throughout the setup as small as possible to maximise spatial resolution and minimise beam divergence.

Bibliography

[1] K. S. Novoselov, D. Jiang, F. Schedin, T. J. Booth, V. V. Khotkevich, S. V. Morozov and A. K. Geim, *PNAS*, 2005, **102**, 10451–10453.

[2] S. Z. Butler, S. M. Hollen, L. Cao, Y. Cui, J. A. Gupta, H. R. Gutiérrez, T. F. Heinz, S. S. Hong, J. Huang, A. F. Ismach, E. Johnston-Halperin, M. Kuno, V. V. Plashnitsa, R. D. Robinson, R. S. Ruoff, S. Salahuddin, J. Shan, L. Shi, M. G. Spencer, M. Terrones, W. Windl and J. E. Goldberger, *ACS Nano*, 2013, **7**, 2898–2926.

[3] Q. H. Wang, K. Kalantar-Zadeh, A. Kis, J. N. Coleman and M. S. Strano, *Nat. Nanotechnol.*, 2012, **7**, 699–712.

[4] V. Podzorov, M. E. Gershenson, C. Kloc, R. Zeis and E. Bucher, *Appl. Phys. Lett.*, 2004, **84**, 3301–3303.

[5] B. Radisavljevic, A. Radenovic, J. Brivio, V. Giacometti and A. Kis, *Nat. Nanotechnol.*, 2011, **6**, 147–150.

[6] R. Wadhwa, A. V. Agrawal and M. Kumar, *J. Phys. D. Appl. Phys.*, 2021, **55**, 063002.

[7] Z. Yin, H. Li, H. Li, L. Jiang, Y. Shi, Y. Sun, G. Lu, Q. Zhang, X. Chen and H. Zhang, *ACS Nano*, 2012, **6**, 74–80.

[8] H. S. Lee, S.-W. Min, Y.-G. Chang, M. K. Park, T. Nam, H. Kim, J. H. Kim, S. Ryu and S. Im, *Nano Lett.*, 2012, **12**, 3695–3700.

[9] M. Fontana, T. Deppe, A. K. Boyd, M. Rinzan, A. Y. Liu, M. Paranjape and P. Barbara, *Sci. Rep.*, 2013, **3**, 1634.

[10] W. J. Yu, Y. Liu, H. Zhou, A. Yin, Z. Li, Y. Huang and X. Duan, *Nat. Nanotechnol.*, 2013, **8**, 952–958.

[11] A. Pospischil, M. M. Furchi and T. Mueller, *Nat. Nanotechnol.*, 2014, **9**, 257–261.

[12] K. Chang and W. Chen, *ACS Nano*, 2011, **5**, 4720–4728.

[13] K. Chang and W. Chen, *Chem. Commun.*, 2011, **47**, 4252–4254.

[14] C. Feng, J. Ma, H. Li, R. Zeng, Z. Guo and H. Liu, *Mater. Res. Bull.*, 2009, **44**, 1811–1815.

[15] Y. Zhang, Y. Zhang, H. Zhang, L. Bai, L. Hao, T. Ma and H. Huang, *Coord. Chem. Rev.*, 2021, **448**, 214147.

[16] M. Chhowalla, H. S. Shin, G. Eda, L.-J. Li, K. P. Loh and H. Zhang, *Nat. Chem.*, 2013, **5**, 263–275.

[17] D. Jariwala, V. K. Sangwan, L. J. Lauhon, T. J. Marks and M. C. Hersam, *ACS Nano*, 2014, **8**, 1102–1120.

[18] M. A. Py and R. R. Haering, *Can. J. Phys.*, 1983, **61**, 76–84.

[19] M. A. Lukowski, A. S. Daniel, F. Meng, A. Forticaux, L. Li and S. Jin, *J. Am. Chem. Soc.*, 2013, **135**, 10274–10277.

[20] R. I. Christy, *Thin Solid Films*, 1980, **73**, 299–307.

[21] T. Spalvins, *JMEP*, 1992, **1**, 347–351.

[22] M. Chhowalla and G. A. J. Amaratunga, *Nature*, 2000, **407**, 164–167.

[23] R. Rosentsveig, A. Gorodnev, N. Feuerstein, H. Friedman, A. Zak, N. Fleischer, J. Tannous, F. Dassenoy and R. Tenne, *Tribol. Lett.*, 2009, **36**, 175–182.

[24] J. M. Martin, C. Donnet, T. Le Mogne and T. Epicier, *Phys. Rev. B*, 1993, **48**, 10583–10586.

[25] D.-M. Tang, D. G. Kvashnin, S. Najmaei, Y. Bando, K. Kimoto, P. Koskinen, P. M. Ajayan, B. I. Yakobson, P. B. Sorokin, J. Lou and D. Golberg, *Nat. Commun.*, 2014, **5**, 3631.

[26] Q. Zhang, L. Mei, X. Cao, Y. Tang and Z. Zeng, *J. Mater. Chem. A*, 2020, **8**, 15417–15444.

[27] K.-G. Zhou, N.-N. Mao, H.-X. Wang, Y. Peng and H.-L. Zhang, *Angew. Chem. Int. Ed.*, 2011, **50**, 10839–10842.

[28] R. J. Smith, P. J. King, M. Lotya, C. Wirtz, U. Khan, S. De, A. O'Neill, G. S. Duesberg, J. C. Grunlan, G. Moriarty, J. Chen, J. Wang, A. I. Minett, V. Nicolosi and J. N. Coleman, *Adv. Mater.*, 2011, **23**, 3944–3948.

[29] M. B. Dines, *Mater. Res. Bull.*, 1975, **10**, 287–291.

[30] J. Zheng, H. Zhang, S. Dong, Y. Liu, C. Tai Nai, H. Suk Shin, H. Young Jeong, B. Liu and K. Ping Loh, *Nat. Commun.*, 2014, **5**, 2995.

[31] Y. Huang, Y. Sun, X. Zheng, T. Aoki, B. Pattengale, J. Huang, X. He, W. Bian, S. Younan, N. Williams, J. Hu, J. Ge, N. Pu, X. Yan, X. Pan, L. Zhang, Y. Wei and J. Gu, *Nat. Commun.*, 2019, **10**, 982.

[32] E. J. M. Hensen, V. H. J. De Beer and R. A. Van Santen, in *Transition Metal Sulphides: Chemistry and Catalysis*, ed. T. Weber, R. Prins and R. A. van Santen, Springer Netherlands, Dordrecht, 1998, pp. 169–188.

[33] C. T. Tye and K. J. Smith, *Top. Catal.*, 2006, **37**, 129–135.

[34] M. D. d. Valle, J. Cruz-Reyes, M. Avalos-Borja and S. Fuentes, *Catal. Letters*, 1998.

[35] J. P. Wilcoxon, T. R. Thurston and J. E. Martin, *NsM*, 1999, **12**, 993–997.

[36] P. C. K. Vesborg, B. Seger and I. Chorkendorff, *J. Phys. Chem. Lett.*, 2015, **6**, 951–957.

[37] G. Li, D. Zhang, Q. Qiao, Y. Yu, D. Peterson, A. Zafar, R. Kumar, S. Curtarolo, F. Hunte, S. Shannon, Y. Zhu, W. Yang and L. Cao, *J. Am. Chem. Soc.*, 2016, **138**, 16632–16638.

[38] Y. Li, H. Wang, L. Xie, Y. Liang, G. Hong and H. Dai, *J. Am. Chem. Soc.*, 2011, **133**, 7296–7299.

[39] T. F. Jaramillo, K. P. Jørgensen, J. Bonde, J. H. Nielsen, S. Horch and I. Chorkendorff, *Science*, 2007, **317**, 100–102.

[40] J. Kibsgaard, Z. Chen, B. N. Reinecke and T. F. Jaramillo, *Nat. Mater.*, 2012, **11**, 963–969.

[41] H. Vrubel, D. Merki and X. Hu, *Energy Environ. Sci.*, 2012, **5**, 6136–6144.

[42] H. I. Karunadasa, E. Montalvo, Y. Sun, M. Majda, J. R. Long and C. J. Chang, *Science*, 2012, **335**, 698–702.

[43] C. Ruffman, C. K. Gordon, J. T. A. Gilmour, F. D. Mackenzie and A. L. Garden, *Nanoscale*, 2021, **13**, 3106–3118.

[44] D. Voiry, M. Salehi, R. Silva, T. Fujita, M. Chen, T. Asefa, V. B. Shenoy, G. Eda and M. Chhowalla, *Nano Lett.*, 2013, **13**, 6222–6227.

[45] Q. Xiang, J. Yu and M. Jaroniec, *J. Am. Chem. Soc.*, 2012, **134**, 6575–6578.

[46] Z. H. Deng, L. Li, W. Ding, K. Xiong and Z. D. Wei, *Chem. Commun.*, 2015, **51**, 1893–1896.

[47] D. Merki, S. Fierro, H. Vrubel and X. Hu, *Chem. Sci.*, 2011, **2**, 1262–1267.

[48] J. D. Benck, Z. Chen, L. Y. Kuritzky, A. J. Forman and T. F. Jaramillo, *ACS Catal.*, 2012, **2**, 1916–1923.

[49] L. Wu, A. Longo, N. Y. Dzade, A. Sharma, M. M. R. M. Hendrix, A. A. Bol, N. H. de Leeuw, E. J. M. Hensen and J. P. Hofmann, *ChemSusChem*, 2019, **12**, 4383–4389.

[50] D. Merki, H. Vrubel, L. Rovelli, S. Fierro and X. Hu, *Chem. Sci.*, 2012, **3**, 2515–2525.

[51] H. Tributsch, *Berichte der Bunsengesellschaft für physikalische Chemie*, 1977, **81**, 361–369.

[52] A. B. Laursen, S. Kegnæs, S. Dahl and I. Chorkendorff, *Energy Environ. Sci.*, 2012, **5**, 5577–5591.

[53] X. Zong, H. Yan, G. Wu, G. Ma, F. Wen, L. Wang and C. Li, *J. Am. Chem. Soc.*, 2008, **130**, 7176–7177.

[54] K. K. Kam and B. A. Parkinson, *J. Phys. Chem.*, 1982, **86**, 463–467.

[55] R. Coehoorn, C. Haas, J. Dijkstra, C. J. F. Flipse, R. A. de Groot and A. Wold, *Phys. Rev. B*, 1987, **35**, 6195–6202.

[56] V. Grasso and G. Mondio, in *Electronic Structure and Electronic Transitions in Layered Materials*, ed. V. Grasso, Springer Netherlands, Dordrecht, 1986, pp. 173–288.

[57] W. Zhao, R. M. Ribeiro, M. Toh, A. Carvalho, C. Kloc, A. H. Castro Neto and G. Eda, *Nano Lett.*, 2013, **13**, 5627–5634.

[58] K. F. Mak, C. Lee, J. Hone, J. Shan and T. F. Heinz, *Phys. Rev. Lett.*, 2010, **105**, 136805.

[59] A. Splendiani, L. Sun, Y. Zhang, T. Li, J. Kim, C.-Y. Chim, G. Galli and F. Wang, *Nano Lett.*, 2010, **10**, 1271–1275.

[60] D. Y. Qiu, F. H. da Jornada and S. G. Louie, *Phys. Rev. Lett.*, 2013, **111**, 216805.

[61] D. Vaquero, V. Clericò, J. Salvador-Sánchez, A. Martín-Ramos, E. Díaz, F. Domínguez-Adame, Y. M. Meziani, E. Diez and J. Quereda, *Commun. Phys.*, 2020, **3**, 1–8.

[62] L. Wang, Z. Wang, H.-Y. Wang, G. Grinblat, Y.-L. Huang, D. Wang, X.-H. Ye, X.-B. Li, Q. Bao, A.-S. Wee, S. A. Maier, Q.-D. Chen, M.-L. Zhong, C.-W. Qiu and H.-B. Sun, *Nat. Commun.*, 2017, **8**, 13906.

[63] I. A. Eliseyev, A. I. Galimov, M. V. Rakhlin, E. A. Evropeitsev, A. A. Toropov, V. Y. Davydov, S. Thiele, J. Pezoldt and T. V. Shubina, *pss*, 2021, **15**, 2100263.

[64] A. Chaves, J. G. Azadani, H. Alsalman, D. R. da Costa, R. Frisenda, A. J. Chaves, S. H. Song, Y. D. Kim, D. He, J. Zhou, A. Castellanos-Gomez, F. M. Peeters, Z. Liu, C. L. Hinkle, S.-H. Oh, P. D. Ye, S. J. Koester, Y. H. Lee, P. Avouris, X. Wang and T. Low, *npj 2D Mater. Appl.*, 2020, **4**, 1–21.

[65] S. Mouri, Y. Miyauchi and K. Matsuda, *Nano Lett.*, 2013, **13**, 5944–5948.

[66] K. Burns, A. M. Z. Tan, A. Gabriel, L. Shao, R. G. Hennig and A. Aitkaliyeva, *J. Mater. Res.*, 2020, **35**, 949–957.

[67] S. Refaely-Abramson, D. Y. Qiu, S. G. Louie and J. B. Neaton, *Phys. Rev. Lett.*, 2018, **121**, 167402.

[68] A. Castellanos-Gomez, R. Roldán, E. Cappelluti, M. Buscema, F. Guinea, H. S. J. van der Zant and G. A. Steele, *Nano Lett.*, 2013, **13**, 5361–5366.

[69] J. Feng, X. Qian, C.-W. Huang and J. Li, *Nat. Photon.*, 2012, **6**, 866–872.

[70] H. Shi, H. Pan, Y.-W. Zhang and B. I. Yakobson, *Phys. Rev. B*, 2013, **87**, 155304.

[71] Q. Yue, Z. Shao, S. Chang and J. Li, *Nanoscale Res. Lett.*, 2013, **8**, 425.

[72] S. Tongay, J. Zhou, C. Ataca, J. Liu, J. S. Kang, T. S. Matthews, L. You, J. Li, J. C. Grossman and J. Wu, *Nano Lett.*, 2013, **13**, 2831–2836.

[73] F. K. Perkins, A. L. Friedman, E. Cobas, P. M. Campbell, G. G. Jernigan and B. T. Jonker, *Nano Lett.*, 2013, **13**, 668–673.

[74] Q. He, Z. Zeng, Z. Yin, H. Li, S. Wu, X. Huang and H. Zhang, *Small*, 2012, **8**, 2994–2999.

[75] D. J. Late, Y.-K. Huang, B. Liu, J. Acharya, S. N. Shirodkar, J. Luo, A. Yan, D. Charles, U. V. Waghmare, V. P. Dravid and C. N. R. Rao, *ACS Nano*, 2013, **7**, 4879–4891.

[76] J. Bonde, P. G. Moses, T. F. Jaramillo, J. K. Nørskov and I. Chorkendorff, *Faraday Discuss.*, 2008, **140**, 219–231.

[77] X. Chen and A. R. McDonald, *Adv. Mater.*, 2016, **28**, 5738–5746.

[78] P. Vishnoi, A. Sampath, U. V. Waghmare and C. N. R. Rao, *Chem. Eur. J.*, 2017, **23**, 886–895.

[79] D. M. Sim, M. Kim, S. Yim, M.-J. Choi, J. Choi, S. Yoo and Y. S. Jung, *ACS Nano*, 2015, **9**, 12115–12123.

[80] S. Presolski and M. Pumera, *Mater. Today*, 2016, **19**, 140–145.

[81] R. Anbazhagan, H.-J. Wang, H.-C. Tsai and R.-J. Jeng, *RSC Adv.*, 2014, **4**, 42936–42941.

[82] S. S. Chou, M. De, J. Kim, S. Byun, C. Dykstra, J. Yu, J. Huang and V. P. Dravid, *J. Am. Chem. Soc.*, 2013, **135**, 4584–4587.

[83] T. Liu, C. Wang, X. Gu, H. Gong, L. Cheng, X. Shi, L. Feng, B. Sun and Z. Liu, *Adv. Mater.*, 2014, **26**, 3433–3440.

[84] T. Liu, C. Wang, W. Cui, H. Gong, C. Liang, X. Shi, Z. Li, B. Sun and Z. Liu, *Nanoscale*, 2014, **6**, 11219–11225.

[85] T. Wang, R. Zhu, J. Zhuo, Z. Zhu, Y. Shao and M. Li, *Anal. Chem.*, 2014, **86**, 12064–12069.

[86] J. Ali, G. U. Siddiqui, K. H. Choi, Y. Jang and K. Lee, *J. Lumin.*, 2016, **169**, 342–347.

[87] H. D. Ha, D. J. Han, J. S. Choi, M. Park and T. S. Seo, *Small*, 2014, **10**, 3858–3862.

[88] H. Lin, C. Wang, J. Wu, Z. Xu, Y. Huang and C. Zhang, *New J. Chem.*, 2015, **39**, 8492–8497.

[89] J. Li and J.-J. Zhu, *Analyst*, 2013, **138**, 2506–2515.

[90] N. S. Arul and V. D. Nithya, *RSC Adv.*, 2016, **6**, 65670–65682.

[91] W. Qiao, S. Yan, X. Song, X. Zhang, Y. Sun, X. Chen, W. Zhong and Y. Du, *RSC Adv.*, 2015, **5**, 97696–97701.

[92] S. Xu, D. Li and P. Wu, *Adv. Funct. Mater.*, 2015, **25**, 1127–1136.

[93] M. J. Haastrup, M. H. R. Mammen, J. Rodríguez-Fernández and J. V. Lauritsen, *ACS Nano*, 2021, **15**, 6699–6708.

[94] X. Liu, T. Xu, X. Wu, Z. Zhang, J. Yu, H. Qiu, J.-H. Hong, C.-H. Jin, J.-X. Li, X.-R. Wang, L.-T. Sun and W. Guo, *Nat. Commun.*, 2013, **4**, 1776.

[95] H. Gu, L. Zhang, Y. Huang, Y. Zhang, W. Fan and T. Liu, *RSC Adv.*, 2016, **6**, 13757–13765.

[96] A. Botos, J. Biskupek, T. W. Chamberlain, G. A. Rance, C. T. Stoppiello, J. Sloan, Z. Liu, K. Suenaga, U. Kaiser and A. N. Khlobystov, *J. Am. Chem. Soc.*, 2016, **138**, 8175–8183.

[97] Z. Wang, H. Li, Z. Liu, Z. Shi, J. Lu, K. Suenaga, S.-K. Joung, T. Okazaki, Z. Gu, J. Zhou, Z. Gao, G. Li, S. Sanvito, E. Wang and S. Iijima, *J. Am. Chem. Soc.*, 2010, **132**, 13840–13847.

[98] J. R. Schaibley, H. Yu, G. Clark, P. Rivera, J. S. Ross, K. L. Seyler, W. Yao and X. Xu, *Nat. Rev. Mater.*, 2016, **1**, 1–15.

[99] Y. Liu, Y. Gao, S. Zhang, J. He, J. Yu and Z. Liu, *Nano Res.*, 2019, **12**, 2695–2711.

[100] D. Xiao, G.-B. Liu, W. Feng, X. Xu and W. Yao, *Phys. Rev. Lett.*, 2012, **108**, 196802.

[101] S. Wu, J. S. Ross, G.-B. Liu, G. Aivazian, A. Jones, Z. Fei, W. Zhu, D. Xiao, W. Yao, D. Cobden and X. Xu, *Nature Phys.*, 2013, **9**, 149–153.

[102] B. Zhu, H. Zeng, J. Dai, Z. Gong and X. Cui, *PNAS*, 2014, **111**, 11606–11611.

[103] B. R. Carvalho, Y. Wang, S. Mignuzzi, D. Roy, M. Terrones, C. Fantini, V. H. Crespi, L. M. Malard and M. A. Pimenta, *Nat. Commun.*, 2017, **8**, 14670.

[104] Z. Zhang, X. Zou, V. H. Crespi and B. I. Yakobson, *ACS Nano*, 2013, **7**, 10475–10481.

[105] Z. Yang, D. Gao, J. Zhang, Q. Xu, S. Shi, K. Tao and D. Xue, *Nanoscale*, 2014, **7**, 650–658.

[106] J. Zhang, J. M. Soon, K. P. Loh, J. Yin, J. Ding, M. B. Sullivian and P. Wu, *Nano Lett.*, 2007, **7**, 2370–2376.

[107] J. Zhou, J. Lin, H. Sims, C. Jiang, C. Cong, J. A. Brehm, Z. Zhang, L. Niu, Y. Chen, Y. Zhou, Y. Wang, F. Liu, C. Zhu, T. Yu, K. Suenaga, R. Mishra, S. T. Pantelides, Z.-G. Zhu, W. Gao, Z. Liu and W. Zhou, *Adv. Mater.*, 2020, **32**, 1906536.

[108] Q. Li, X. Zhao, L. Deng, Z. Shi, S. Liu, Q. Wei, L. Zhang, Y. Cheng, L. Zhang, H. Lu, W. Gao, W. Huang, C.-W. Qiu, G. Xiang, S. J. Pennycook, Q. Xiong, K. P. Loh and B. Peng, *ACS Nano*, 2020, **14**, 4636–4645.

[109] B. Schuler, D. Y. Qiu, S. Refaely-Abramson, C. Kastl, C. T. Chen, S. Barja, R. J. Koch, D. F. Ogletree, S. Aloni, A. M. Schwartzberg, J. B. Neaton, S. G. Louie and A. Weber-Bargioni, *Phys. Rev. Lett.*, 2019, **123**, 076801.

[110] Y. Wang, L. Deng, Q. Wei, Y. Wan, Z. Liu, X. Lu, Y. Li, L. Bi, L. Zhang, H. Lu, H. Chen, P. Zhou, L. Zhang, Y. Cheng, X. Zhao, Y. Ye, W. Huang, S. J. Pennycook, K. P. Loh and B. Peng, *Nano Lett.*, 2020, **20**, 2129–2136.

[111] S. Tongay, J. Suh, C. Ataca, W. Fan, A. Luce, J. S. Kang, J. Liu, C. Ko, R. Raghunathanan, J. Zhou, F. Ogletree, J. Li, J. C. Grossman and J. Wu, *Sci. Rep.*, 2013, **3**, 2657.

[112] P. K. Chow, R. B. Jacobs-Gedrim, J. Gao, T.-M. Lu, B. Yu, H. Terrones and N. Koratkar, *ACS Nano*, 2015, **9**, 1520–1527.

[113] C. Chakraborty, K. M. Goodfellow and A. N. Vamivakas, *Opt. Mater. Express, OME*, 2016, **6**, 2081–2087.

[114] Z. Wu, W. Zhao, J. Jiang, T. Zheng, Y. You, J. Lu and Z. Ni, *J. Phys. Chem. C*, 2017, **121**, 12294–12299.

[115] C. Ataca, H. Şahin, E. Aktürk and S. Ciraci, *J. Phys. Chem. C*, 2011, **115**, 3934–3941.

[116] R. Shidpour and M. Manteghian, *Chem. Phys.*, 2009, **360**, 97–105.

[117] L. Kou, C. Li, Z. Zhang and W. Guo, *ACS Nano*, 2010, **4**, 2124–2128.

[118] P. Lu, X. Wu, W. Guo and X. C. Zeng, *Phys. Chem. Chem. Phys.*, 2012, **14**, 13035–13040.

[119] Y. Li, D. Wu, Z. Zhou, C. R. Cabrera and Z. Chen, *J. Phys. Chem. Lett.*, 2012, **3**, 2221–2227.

[120] Y. Cai, G. Zhang and Y.-W. Zhang, *J. Am. Chem. Soc.*, 2014, **136**, 6269–6275.

[121] J. Hong, Z. Hu, M. Probert, K. Li, D. Lv, X. Yang, L. Gu, N. Mao, Q. Feng, L. Xie, J. Zhang, D. Wu, Z. Zhang, C. Jin, W. Ji, X. Zhang, J. Yuan and Z. Zhang, *Nat. Commun.*, 2015, **6**, 6293.

[122] R. Addou, L. Colombo and R. M. Wallace, *ACS Appl. Mater. Interfaces*, 2015, **7**, 11921–11929.

[123] S. Wang, G. D. Lee, S. Lee, E. Yoon and J. H. Warner, *ACS Nano*, 2016, **10**, year.

[124] F. Aryeetey, T. Ignatova and S. Aravamudhan, *RSC Adv.*, 2020, **10**, 22996–23001.

[125] S. H. Song, M.-K. Joo, M. Neumann, H. Kim and Y. H. Lee, *Nat. Commun.*, 2017, **8**, 2121.

[126] Y. Yang, W. Liu, Z. Lin, K. Zhu, S. Tian, Y. Huang, C. Gu and J. Li, *J. Phys. Chem. C*, 2020, **124**, 17418–17422.

[127] J. Ji, A. Zhang, J. Fan, Y. Li, X. Wang, J. Zhang, E. W. Plummer and Q. Zhang, *PNAS*, 2016, **113**, 2349–2353.

[128] T.-X. Huang, X. Cong, S.-S. Wu, K.-Q. Lin, X. Yao, Y.-H. He, J.-B. Wu, Y.-F. Bao, S.-C. Huang, X. Wang, P.-H. Tan and B. Ren, *Nat. Commun.*, 2019, **10**, 5544.

[129] Y. Guo, W. Zhang, H. Wu, J. Han, Y. Zhang, S. Lin, C. Liu, K. Xu, J. Qiao, W. Ji, Q. Chen, S. Gao, W. Zhang, X. Zhang and Y. Chai, *Sci. Adv.*, 2018, **4**, eaau6252.

[130] D. M. Basko, *Phys. Rev. B*, 2008, **78**, 125418.

[131] C. Casiraghi, A. Hartschuh, H. Qian, S. Piscanec, C. Georgi, A. Fasoli, K. S. Novoselov, D. M. Basko and A. C. Ferrari, *Nano Lett.*, 2009, **9**, 1433–1441.

[132] M. Kitajima, *Crit. Rev. Solid State Mater. Sci.*, 1997, **22**, 275–349.

[133] S. Mignuzzi, A. J. Pollard, N. Bonini, B. Brennan, I. S. Gilmore, M. A. Pimenta, D. Richards and D. Roy, *Phys. Rev. B*, 2015, **91**, 195411.

[134] D. Long, in *The Raman Effect*, John Wiley & Sons, Ltd, 2002, pp. 3–18.

[135] R. McCreery, in *Raman Spectroscopy for Chemical Analysis*, John Wiley & Sons, Ltd, 2000, pp. 1–14.

[136] F. Hu, L. Shi and W. Min, *Nat. Methods.*, 2019, **16**, 830–842.

[137] R. Merlin, A. Pinczuk and W. H. Weber, in *Raman Scattering in Materials Science*, ed. W. H. Weber and R. Merlin, Springer, Berlin, Heidelberg, 2000, pp. 1–29.

[138] Y.-S. Li and J. S. Church, *J. Food Drug Anal.*, 2014, **22**, 29–48.

[139] P. T. Mah, S. J. Fraser, M. E. Reish, T. Rades, K. C. Gordon and C. J. Strachan, *Vib. Spectrosc.*, 2015, **77**, 10–16.

[140] D. Long, in *The Raman Effect*, John Wiley & Sons, Ltd, 2002, pp. 303–335.

[141] P. J. Larkin, J. Wasylyk and M. Raglione, *Appl. Spectrosc.*, 2015, **69**, 1217–1228.

[142] S. Mosca, C. Conti, N. Stone and P. Matousek, *Nat. Rev. Methods Primers*, 2021, **1**, 1–16.

[143] R. Corporation, *Customs Border Protection Uses Raman*, 2022, `https://handhelds.rigaku.com/customs-border-protection-uses-raman`.

[144] A. P. Lister, W. J. Sellors, C. R. Howle and S. Mahajan, *Anal. Chem.*, 2021, **93**, 417–429.

[145] H. Scientific, *T64000 Triple Raman Spectrometer - HORIBA*, `https://www.horiba.com/es/scientific/products/raman-spectroscopy/raman-spectrometers/triple-raman-spectrometers/details/triple-raman-spectrometers-140/`.

[146] T. P. Instruments, *TriVista Spectrometer*, 2022, `https://www.princetoninstruments.com/products/trivista-family/trivista`.

[147] P. Ranzieri, A. Girlando, S. Tavazzi, M. Campione, L. Raimondo, I. Bilotti, A. Brillante, R. G. Della Valle and E. Venuti, *ChemPhysChem*, 2009, **10**, 657–663.

[148] L. Liang, J. Zhang, B. G. Sumpter, Q.-H. Tan, P.-H. Tan and V. Meunier, *ACS Nano*, 2017, **11**, 11777–11802.

[149] P. H. Tan, W. P. Han, W. J. Zhao, Z. H. Wu, K. Chang, H. Wang, Y. F. Wang, N. Bonini, N. Marzari, N. Pugno, G. Savini, A. Lombardo and A. C. Ferrari, *Nat. Mater.*, 2012, **11**, 294–300.

[150] F. Thouin, D. A. Valverde-Chávez, C. Quarti, D. Cortecchia, I. Bargigia, D. Beljonne, A. Petrozza, C. Silva and A. R. Srimath Kandada, *Nat. Mater.*, 2019, **18**, 349–356.

[151] I. S. T. Ltd., *Nano Edge Archives*, 2022, `https://www.iridian.ca/product-category/raman-filters/raman-edge-pass-filters-2/raman-nano-edge/`.

[152] E. Hecht, *Optics*, Pearson Education Limited, 5th edn., 2017.

[153] R. Paschotta, *RP Photonics Encyclopedia*, 2022, https://www.rp-photonics.com/encyclopedia.html.

[154] R. Paschotta, *Encyclopedia of Laser Physics and Technology*, Wiley VCH Verlag, 1st edn., 2008.

[155] I. Thorlabs, *Technical Resources - Thorlabs*, 2022, https://www.thorlabs.com/navigation.cfm?guide_id=2400.

[156] D. R. Paschotta, *Volume Bragg Gratings*, 2022, https://www.rp-photonics.com/volume_bragg_gratings.html.

[157] D. R. Paschotta, *Bragg Gratings*, 2022, https://www.rp-photonics.com/bragg_gratings.html.

[158] L. A. Ribeiro, S. F. Quirino, A. O. Toledo, C. L. Barbosa, O. Lisboa and J. U. Arruda, *AIP Conf. Proc.*, 2008, **1055**, 159–162.

[159] E. Hecht, in *Optics*, Pearson Education Limited, Harlow, Essex, England, 5th edn., 2017, pp. 96–158.

[160] K. Thyagarajan and A. Ghatak, in *Lasers: Fundamentals and Applications*, ed. K. Thyagarajan and A. Ghatak, Springer US, Boston, MA, 2011, pp. 263–275.

[161] E. O. Inc., *Gaussian Beam Propagation*, 2022, https://www.edmundoptics.com/knowledge-center/application-notes/lasers/gaussian-beam-propagation/.

[162] D. R. Paschotta, *Paraxial Approximation*, https://www.rp-photonics.com/paraxial_approximation.html.

[163] E. Hecht, in *Optics*, Pearson Education Limited, Harlow, Essex, England, 5th edn., 2017, pp. 96–158.

[164] I. Thorlabs, *Single Mode FC/PC Fiber Optic Patch Cables*, 2022, https://www.thorlabs.com/newgrouppage9.cfm?objectgroup_id=1362.

[165] C. Kittel, in *Introduction to Solid State Physics*, John Wiley & Sons, Inc., United States of America, 8th edn., 2005, pp. 89–104.

[166] D. Long, in *The Raman Effect*, John Wiley & Sons, Ltd, 2002, pp. 19–29.

[167] P. Y. Yu and M. Cardona, in *Fundamentals of Semiconductors: Physics and Materials Properties*, ed. P. Y. Yu and M. Cardona, Springer, Berlin, Heidelberg, 2010, pp. 1–15.

[168] P. Y. Yu and M. Cardona, in *Fundamentals of Semiconductors: Physics and Materials Properties*, ed. P. Y. Yu and M. Cardona, Springer, Berlin, Heidelberg, 2010, pp. 345–426.

[169] R. McCreery, in *Raman Spectroscopy for Chemical Analysis*, John Wiley & Sons, Ltd, 2000, pp. 149–219.

[170] P. Y. Yu and M. Cardona, in *Fundamentals of Semiconductors: Physics and Materials Properties*, ed. P. Y. Yu and M. Cardona, Springer, Berlin, Heidelberg, 2010, pp. 107–158.

[171] T. Livneh and J. E. Spanier, *2D Mater.*, 2015, **2**, 035003.

[172] J. Kim, J.-U. Lee and H. Cheong, *J. Phys. Condens. Matter.*, 2020, **32**, 343001.

[173] X. Zhang, X.-F. Qiao, W. Shi, J.-B. Wu, D.-S. Jiang and P.-H. Tan, *Chem. Soc. Rev.*, 2015, **44**, 2757–2785.

[174] R. T. Sam, T. Umakoshi and P. Verma, *Sci. Rep.*, 2020, **10**, 21227.

[175] K. Gołasa, M. Grzeszczyk, P. Leszczyński, C. Faugeras, A. a. L. Nicolet, A. Wysmołek, M. Potemski and A. Babiński, *Appl. Phys. Lett.*, 2014, **104**, 092106.

[176] H.-L. Liu, H. Guo, T. Yang, Z. Zhang, Y. Kumamoto, C.-C. Shen, Y.-T. Hsu, L.-J. Li, R. Saito and S. Kawata, *Phys. Chem. Chem. Phys.*, 2015, **17**, 14561–14568.

[177] H.-L. Liu, T. Yang, Y. Tatsumi, Y. Zhang, B. Dong, H. Guo, Z. Zhang, Y. Kumamoto, M.-Y. Li, L.-J. Li, R. Saito and S. Kawata, *Sci. Rep.*, 2018, **8**, 11398.

[178] L. M. Malard, M. A. Pimenta, G. Dresselhaus and M. S. Dresselhaus, *Phys. Rep.*, 2009, **473**, 51–87.

[179] R. N. Gontijo, G. C. Resende, C. Fantini and B. R. Carvalho, *J. Mater. Res.*, 2019, **34**, 1976–1992.

[180] A. Grüneis, R. Saito, G. G. Samsonidze, T. Kimura, M. A. Pimenta, A. Jorio, A. G. S. Filho, G. Dresselhaus and M. S. Dresselhaus, *Phys. Rev. B*, 2003, **67**, 165402.

[181] L. G. Cançado, M. A. Pimenta, B. R. A. Neves, M. S. S. Dantas and A. Jorio, *Phys. Rev. Lett.*, 2004, **93**, 247401.

[182] R. N. Gontijo, A. Gadelha, O. J. Silveira, R. W. Nunes, M. A. Pimenta, A. Righi and C. Fantini, *Phys. Rev. B*, 2021, **103**, 045411.

[183] J.-U. Lee, J. Park, Y.-W. Son and H. Cheong, *Nanoscale*, 2015, **7**, 3229–3236.

[184] C. Kittel, in *Introduction to Solid State Physics*, John Wiley & Sons, Inc., United States of America, 8th edn., 2005, pp. 393–426.

[185] R. N. Gontijo, T. Zhang, K. Fujisawa, A. L. Elías, M. A. Pimenta, A. Righi, M. Terrones and C. Fantini, *2D Mater.*, 2021, **8**, 035042.

[186] J.-H. Fan, P. Gao, A.-M. Zhang, B.-R. Zhu, H.-L. Zeng, X.-D. Cui, R. He and Q.-M. Zhang, *J. Appl. Phys.*, 2014, **115**, 053527.

[187] G. Kioseoglou, A. T. Hanbicki, M. Currie, A. L. Friedman and B. T. Jonker, *Sci. Rep.*, 2016, **6**, 25041.

[188] L. Sun, J. Yan, D. Zhan, L. Liu, H. Hu, H. Li, B. K. Tay, J.-L. Kuo, C.-C. Huang, D. W. Hewak, P. S. Lee and Z. X. Shen, *Phys. Rev. Lett.*, 2013, **111**, 126801.

[189] B. R. Carvalho, L. M. Malard, J. M. Alves, C. Fantini and M. A. Pimenta, *Phys. Rev. Lett.*, 2015, **114**, 136403.

[190] A. P. S. Gaur, S. Sahoo, J. F. Scott and R. S. Katiyar, *J. Phys. Chem. C*, 2015, **119**, 5146–5151.

[191] J.-m. Li, Y.-k. Yao, L.-h. Sun, X.-y. Shan, C. Wang and X.-h. Lu, *Chinese Phys. Lett.*, 2019, **36**, 048201.

[192] E. del Corro, A. Botello-Méndez, Y. Gillet, A. L. Elias, H. Terrones, S. Feng, C. Fantini, D. Rhodes, N. Pradhan, L. Balicas, X. Gonze, J.-C. Charlier, M. Terrones and M. A. Pimenta, *Nano Lett.*, 2016, **16**, 2363–2368.

[193] F. Dybała, M. P. Polak, J. Kopaczek, P. Scharoch, K. Wu, S. Tongay and R. Kudrawiec, *Sci. Rep.*, 2016, **6**, 26663.

[194] M. A. Pimenta, E. del Corro, B. R. Carvalho, C. Fantini and L. M. Malard, *Acc. Chem. Res.*, 2015, **48**, 41–47.

[195] H.-S. Tsai, Y.-H. Huang, P.-C. Tsai, Y.-J. Chen, H. Ahn, S.-Y. Lin and Y.-J. Lu, *ACS Omega*, 2020, **5**, 10725–10730.

[196] G. Y. Jia, Y. Liu, J. Y. Gong, D. Y. Lei, D. L. Wang and Z. X. Huang, *J. Mater. Chem. C*, 2016, **4**, 8822–8828.

[197] A. S. Barker and A. J. Sievers, *Rev. Mod. Phys.*, 1975, **47**, S1–S179.

[198] H. Yuan, X. Zhou, Y. Cao, Q. Bian, Z. Zhang, H. Sun, S. Li, Z. Shao, J. Hu, Y. Zhu, Z. Mao, W. Ji and M. Pan, *npj 2D Mater. Appl.*, 2019, **3**, 1–9.

[199] E. Rashba and G. E. Gurgenishvili, *Phys. Solid State*, 1962.

[200] P. Y. Yu, M. H. Pilkuhn and F. Evangelisti, *Solid State Commun.*, 1978, **25**, 371–373.

[201] M. Placidi, M. Dimitrievska, V. Izquierdo-Roca, X. Fontané, A. Castellanos-Gomez, A. Pérez-Tomás, N. Mestres, M. Espindola-Rodriguez, S. López-Marino, M. Neuschitzer, V. Bermudez, A. Yaremko and A. Pérez-Rodríguez, *2D Mater.*, 2015, **2**, 035006.

[202] A. Molina-Sánchez and L. Wirtz, *Phys. Rev. B*, 2011, **84**, 155413.

[203] H. Tornatzky, R. Gillen, H. Uchiyama and J. Maultzsch, *Phys. Rev. B*, 2019, **99**, 144309.

[204] N. Wakabayashi and R. M. Nicklow, in *Electrons and Phonons in Layered Crystal Structures*, ed. T. J. Wieting and M. Schlüter, Springer Netherlands, Dordrecht, 1979, pp. 409–464.

[205] S. K. Mahatha, K. D. Patel and K. S. R. Menon, *J. Phys. Condens. Matter*, 2012, **24**, 475504.

[206] C. Habenicht, R. Schuster, M. Knupfer and B. Büchner, *J. Phys. Condens. Matter.*, 2018, **30**, 205502.

[207] A. Koitzsch, A.-S. Pawlik, C. Habenicht, T. Klaproth, R. Schuster, B. Büchner and M. Knupfer, *npj 2D Mater. Appl.*, 2019, **3**, 1–9.

[208] S. K. Mahatha, A. S. Ngankeu, N. F. Hinsche, I. Mertig, K. Guilloy, P. L. Matzen, M. Bianchi, C. E. Sanders, J. A. Miwa, H. Bana, E. Travaglia, P. Lacovig, L. Bignardi, D. Lizzit, R. Larciprete, A. Baraldi, S. Lizzit and P. Hofmann, *Surf. Sci.*, 2019, **681**, 64–69.

[209] H. Li, Q. Zhang, C. C. R. Yap, B. K. Tay, T. H. T. Edwin, A. Olivier and D. Baillargeat, *Adv. Funct. Mater.*, 2012, **22**, 1385–1390.

[210] P. Y. Yu and M. Cardona, in *Fundamentals of Semiconductors: Physics and Materials Properties*, ed. P. Y. Yu and M. Cardona, Springer, Berlin, Heidelberg, 2010, pp. 243–344.

[211] J. Noffsinger, E. Kioupakis, C. G. Van de Walle, S. G. Louie and M. L. Cohen, *Phys. Rev. Lett.*, 2012, **108**, 167402.

[212] B. K. Ridley, *Quantum Processes in Semiconductors*, Oxford University Press, Oxford, 5th edn., 2013.

[213] M. C. Lucking, J. Bang, H. Terrones, Y.-Y. Sun and S. Zhang, *Chem. Mater.*, 2015, **27**, 3326–3331.

[214] J. Tang, Z. Wei, Q. Wang, Y. Wang, B. Han, X. Li, B. Huang, M. Liao, J. Liu, N. Li, Y. Zhao, C. Shen, Y. Guo, X. Bai, P. Gao, W. Yang, L. Chen, K. Wu, R. Yang, D. Shi and G. Zhang, *Small*, 2020, **16**, 2004276.

[215] T. Livneh and E. Sterer, *Phys. Rev. B*, 2010, **81**, 195209.

[216] A. K. Geim and I. V. Grigorieva, *Nature*, 2013, **499**, 419–425.

[217] N. Ubrig, E. Ponomarev, J. Zultak, D. Domaretskiy, V. Zólyomi, D. Terry, J. Howarth, I. Gutiérrez-Lezama, A. Zhukov, Z. R. Kudrynskyi, Z. D. Kovalyuk, A. Patané, T. Taniguchi, K. Watanabe, R. V. Gorbachev, V. I. Fal'ko and A. F. Morpurgo, *Nat. Mater.*, 2020, **19**, 299–304.

[218] M. Okada, A. Kutana, Y. Kureishi, Y. Kobayashi, Y. Saito, T. Saito, K. Watanabe, T. Taniguchi, S. Gupta, Y. Miyata, B. I. Yakobson, H. Shinohara and R. Kitaura, *ACS Nano*, 2018, **12**, 2498–2505.

[219] A. M. van der Zande, P. Y. Huang, D. A. Chenet, T. C. Berkelbach, Y. You, G.-H. Lee, T. F. Heinz, D. R. Reichman, D. A. Muller and J. C. Hone, *Nat. Mater.*, 2013, **12**, 554–561.

[220] D. Wang, H. Yu, L. Tao, W. Xiao, P. Fan, T. Zhang, M. Liao, W. Guo, D. Shi, S. Du, G. Zhang and H. Gao, *Nano Res.*, 2018, **11**, 6102–6109.

[221] S. Golovynskyi, I. Irfan, M. Bosi, L. Seravalli, O. I. Datsenko, I. Golovynska, B. Li, D. Lin and J. Qu, *Appl. Surf. Sci.*, 2020, **515**, 146033.

[222] O. O. Smirnova, I. A. Eliseyev, A. V. Rodina and T. V. Shubina, *J. Phys. Conf. Ser.*, 2020, **1482**, 012038.

[223] S. Presolski, L. Wang, A. H. Loo, A. Ambrosi, P. Lazar, V. Ranc, M. Otyepka, R. Zboril, O. Tomanec, J. Ugolotti, Z. Sofer and M. Pumera, *Chem. Mater.*, 2017, **29**, 2066–2073.

[224] E. Doni and R. Girlanda, in *Electronic Structure and Electronic Transitions in Layered Materials*, ed. V. Grasso, Springer Netherlands, Dordrecht, 1986, pp. 1–171.

[225] L. Liu, S. B. Kumar, Y. Ouyang and J. Guo, *IEEE Trans. Electron. Devices.*, 2011, **58**, 3042–3047.

[226] Y. Ding, Y. Wang, J. Ni, L. Shi, S. Shi and W. Tang, *Physica B: Condens. Matter.*, 2011, **406**, 2254–2260.

[227] A. Berkdemir, H. R. Gutiérrez, A. R. Botello-Méndez, N. Perea-López, A. L. Elías, C.-I. Chia, B. Wang, V. H. Crespi, F. López-Urías, J.-C. Charlier, H. Terrones and M. Terrones, *Sci. Rep.*, 2013, **3**, 1755.

[228] T. Sekine, M. Izumi, T. Nakashizu, K. Uchinokura and E. Matsuura, *J. Phys. Soc. Jpn.*, 1980, **49**, 1069–1077.

[229] T. J. Wieting, A. Grisel and F. Lévy, *Physica B+C*, 1980, **99**, 337–342.

[230] A. M. Stacy and D. T. Hodul, *J. Chem. Phys. Solids*, 1985, **46**, 405–409.

[231] A. O'Neill, U. Khan and J. N. Coleman, *Chem. Mater.*, 2012, **24**, 2414–2421.

[232] J. N. Coleman, M. Lotya, A. O'Neill, S. D. Bergin, P. J. King, U. Khan, K. Young, A. Gaucher, S. De, R. J. Smith, I. V. Shvets, S. K. Arora, G. Stanton, H.-Y. Kim, K. Lee, G. T. Kim, G. S. Duesberg, T. Hallam, J. J. Boland, J. J. Wang, J. F. Donegan, J. C. Grunlan, G. Moriarty, A. Shmeliov, R. J. Nicholls, J. M. Perkins, E. M. Grieveson, K. Theuwissen, D. W. McComb, P. D. Nellist and V. Nicolosi, *Science*, 2011.

[233] Z. Lin, Y. Zhao, C. Zhou, R. Zhong, X. Wang, Y. H. Tsang and Y. Chai, *Sci. Rep.*, 2015, **5**, year.

[234] A. Singh, M. Moun, M. Sharma, A. Barman, A. Kumar Kapoor and R. Singh, *Appl. Surf. Sci.*, 2021, **538**, 148201.

[235] Z. Liu, M. Amani, S. Najmaei, Q. Xu, X. Zou, W. Zhou, T. Yu, C. Qiu, A. G. Birdwell, F. J. Crowne, R. Vajtai, B. I. Yakobson, Z. Xia, M. Dubey, P. M. Ajayan and J. Lou, *Nat. Commun.*, 2014, **5**, 5246.

[236] M. O'Brien, N. McEvoy, T. Hallam, H.-Y. Kim, N. C. Berner, D. Hanlon, K. Lee, J. N. Coleman and G. S. Duesberg, *Sci. Rep.*, 2014, **4**, 7374.

[237] P. Giannozzi, S. Baroni, N. Bonini, M. Calandra, R. Car, C. Cavazzoni, D. Ceresoli, G. L. Chiarotti, M. Cococcioni, I. Dabo, A. D. Corso, S. d. Gironcoli, S. Fabris, G. Fratesi, R. Gebauer, U. Gerstmann, C. Gougoussis, A. Kokalj, M. Lazzeri, L. Martin-Samos, N. Marzari, F. Mauri, R. Mazzarello, S. Paolini, A. Pasquarello, L. Paulatto, C. Sbraccia, S. Scandolo, G. Sclauzero, A. P. Seitsonen, A. Smogunov, P. Umari and R. M. Wentzcovitch, *J. Phys. Condens. Matter.*, 2009, **21**, 395502.

[238] P. Giannozzi, O. Andreussi, T. Brumme, O. Bunau, M. B. Nardelli, M. Calandra, R. Car, C. Cavazzoni, D. Ceresoli, M. Cococcioni, N. Colonna, I. Carnimeo, A. D. Corso, S. de Gironcoli, P. Delugas, R. A. DiStasio Jr., A. Ferretti, A. Floris, G. Fratesi, G. Fugallo, R. Gebauer, U. Gerstmann, F. Giustino, T. Gorni, J. Jia, M. Kawamura, H.-Y. Ko, A. Kokalj, E. Küçükbenli, M. Lazzeri, M. Marsili, N. Marzari, F. Mauri, N. L. Nguyen, H.-V. Nguyen, A. Otero-de-la Roza, L. Paulatto, S. Poncé, D. Rocca, R. Sabatini, B. Santra, M. Schlipf, A. P. Seitsonen, A. Smogunov, I. Timrov, T. Thonhauser, P. Umari, N. Vast, X. Wu and S. Baroni, *J. Phys. Condens. Matter.*, 2017, **29**, 465901.

[239] P. Giannozzi, O. Baseggio, P. Bonfà, D. Brunato, R. Car, I. Carnimeo, C. Cavazzoni, S. de Gironcoli, P. Delugas, F. Ferrari Ruffino, A. Ferretti, N. Marzari, I. Timrov, A. Urru and S. Baroni, *J. Chem. Phys.*, 2020, **152**, 154105.

[240] J. P. Perdew, K. Burke and M. Ernzerhof, *Phys. Rev. Lett.*, 1996, **77**, 3865–3868.

[241] P. E. Blöchl, *Phys. Rev. B*, 1994, **50**, 17953–17979.

[242] S. Grimme, *J. Comput. Chem.*, 2006, **27**, 1787–1799.

[243] T. Sohier, M. Calandra and F. Mauri, *Phys. Rev. B*, 2017, **96**, 075448.

[244] G. Prandini, A. Marrazzo, I. E. Castelli, N. Mounet and N. Marzari, *npj Comput. Mater.*, 2018, **4**, 1–13.

[245] K. Lejaeghere, G. Bihlmayer, T. Björkman, P. Blaha, S. Blügel, V. Blum, D. Caliste, I. E. Castelli, S. J. Clark, A. D. Corso, S. d. Gironcoli, T. Deutsch, J. K. Dewhurst, I. D. Marco, C. Draxl, M. Dułak, O. Eriksson, J. A. Flores-Livas, K. F. Garrity, L. Genovese, P. Giannozzi, M. Giantomassi, S. Goedecker, X. Gonze, O. Grånäs, E. K. U. Gross, A. Gulans, F. Gygi, D. R. Hamann, P. J. Hasnip, N. A. W. Holzwarth, D. Iuşan, D. B. Jochym, F. Jollet, D. Jones, G. Kresse, K. Koepernik, E. Küçükbenli, Y. O. Kvashnin, I. L. M. Locht, S. Lubeck, M. Marsman, N. Marzari, U. Nitzsche, L. Nordström, T. Ozaki, L. Paulatto, C. J. Pickard, W. Poelmans, M. I. J. Probert, K. Refson, M. Richter, G.-M. Rignanese, S. Saha, M. Scheffler, M. Schlipf, K. Schwarz, S. Sharma, F. Tavazza, P. Thunström, A. Tkatchenko, M. Torrent, D. Vanderbilt, M. J. v. Setten, V. V. Speybroeck, J. M. Wills, J. R. Yates, G.-X. Zhang and S. Cottenier, *Science*, 2016.

[246] R. Doolen, R. Laitinen, F. Parsapour and D. F. Kelley, *J. Phys. Chem. B*, 1998, **102**, 3906–3911.

[247] J. P. Wilcoxon and G. A. Samara, *Phys. Rev. B*, 1995, **51**, 7299–7302.

[248] V. Chikan, M. R. Waterland, J. M. Huang and D. F. Kelley, *J. Chem. Phys.*, 2000, **113**, 5448–5456.

[249] N. Mohanty, D. Moore, Z. Xu, T. S. Sreeprasad, A. Nagaraja, A. A. Rodriguez and V. Berry, *Nat. Commun.*, 2012, **3**, 844.

[250] M. Liu, J. Shi, Y. Li, X. Zhou, D. Ma, Y. Qi, Y. Zhang and Z. Liu, *Small*, 2017, **13**, 1602967.

[251] Y. Chen, J. Xi, D. O. Dumcenco, Z. Liu, K. Suenaga, D. Wang, Z. Shuai, Y.-S. Huang and L. Xie, *ACS Nano*, 2013, **7**, 4610–4616.

[252] E. Hecht, in *Optics*, Pearson Education Limited, Harlow, Essex, England, 5th edn., 2017, pp. 18–44.